FLOW AND CONJUGATE HEAT TRANSFER STUDY OF WALL BOUNDED LAMINAR PLANE JET FLOWS

A Thesis
submitted in partial fulfillment of the
requirements for the Degree of
Doctor of Philosophy

by

P. Rajesh Kanna
(*Roll No. 01610303*)

under the guidance of

Dr. Manab Kumar Das

DEPARTMENT OF MECHANICAL ENGINEERING

Indian Institute of Technology Guwahati

GUWAHATI

JULY-2005

CERTIFICATE

It is certified that the work contained in this thesis entitled **Flow and Conjugate Heat Transfer study of Wall Bounded Laminar Plane Jet Flows** by **P. Rajesh Kanna,** a student of Department of Mechanical Engineering, Indian Institute of Technology, Guwahati for the award of the degree of Doctor of Philosophy has been carried out under my supervision and that this work has not been submitted elsewhere for a degree.

Manab Das 25/7/05

Dr. Manab Kumar Das
Associate Professor
Dept. of Mechanical Engineering
I.I.T. Guwahati

Dedicated to
To my mother *Late. Smt. Punnialakshmi*
&
To my grand mother *Late. Smt. Meenambal*

Acknowledgements

I am very much grateful to Dr. Manab Kumar Das, my thesis supervisor, for the invaluable guidance I have received during the research period. He has introduced me the specialization, computational fluid dynamics in the field of fluids and thermal. I am deeply indebted to him for his way of approaching problem, immense patience, utmost care and constant encouragement through out this work. With his excellent guidance the work has been reached to the present quality. I believe that the way he has shown is everlasting and fruitful in my career.

I am thankful to my doctoral committee members Dr. A.K. Dass, Dr. P. Mahanta and Dr. D.C. Dalal for giving their valuable suggestions and encouragement. I am thankful to my examiners, who helped me to shape myself to meet the requirement of a successful researcher. I am grateful to Dr. A.D. Sahashrabudhe, Deputy Director, IIT Guwahati and Dr. P.S. Robi, Head of the Mechanical Engineering Department, IIT Guwahati for providing the computational facilities and other devices to carry out this research. I am thankful to mechanical engineering department staff Mr. M. Pathak and Mr. Amal Kalita for their help and support during this research work. I am thankful to the head of the computer science department for permitting me to carry out some of the computations at computer science department servers. I am sincerely thankful to the institute for providing sufficient funds and grants to have this research work done successfully. I am thankful to the other faculty members, staff directly or indirectly motivated me to complete this thesis work.

I am very glad to take this opportunity to thank some of my friends. Mr. Sheik Karimulla who helped me the at the time of joining the institute. I thank Mr. Madhu Sudhana Rao, Mr. Amaresh Dalal and Mr. K. Rajesh who had healthy discussion during my stay in IIT. I would like to thank Mr. Sivasankar, Mr. Sivagurumurthy, Mr. Senthil Raja Mr. Suresh Kumar and Arul Prakash (IITK) who made easy my stay at the institute. I would like to thank my friends in maths department for extending help and encouragement. I would like to thank my colleagues Mr. Vishnu and Mr. Sunil who helped me to prepare this report in the present level. I thank my family members for their affection and moral support to carry out this research work smoothly. Last but not least I am thankful to cuisiner Mr. Krishna for his service throughout the stay in IIT. Every person is in need of God at every instant of life. I thank him, *Lord Murugan*, for giving me all the above.

Om Muruga Saranam

P. Rajesh Kanna
Dept. of Mechanical Engineering
I.I.T. Guwahati

July 2005

List of Publication from this thesis work

International Journal Paper

1. Kanna, P. R. and Das, M., K., Conjugate Forced Convection Heat Transfer from a Flat Plate by Laminar Plane Wall Jet Flow. *International Journal of Heat and Mass Transfer*, (48) 14, 2005. pp 2896-2910.

2. Kanna, P. R. and Das, M., K., Conjugate Heat Transfer Study of Two-Dimensional Laminar Incompressible Offset Jet Flows. *Numerical Heat Transfer. Part A. Applications*. Article in press, 2005.

3. Kanna, P. R. and Das, M., K., Numerical Simulation of Two-Dimensional Laminar Incompressible Offset Jet Flows. *International Journal for Numerical Methods in Fluids*, Article in press, 2005.

4. Kanna, P. R. and Das, M., K., A short note on the Reattachment Length for BFS Problem, Accepted for publication in *International Journal for Numerical Methods in Fluids*, 2005.

5. Kanna, P. R. and Das, M., K., Conjugate Heat Transfer Study of Two-Dimensional Laminar Incompressible Wall Jet under Backward-Facing Step. Resubmitted as Technical Note to *ASME Transactions* : *Journal of Heat Transfer*, 2005.

6. Kanna, P. R. and Das, M., K., Heat Transfer Study of Two-Dimensional

Laminar Incompressible Offset Jet Flows. Revised manuscript submitted to *Heat and Mass Transfer*, 2005.

7. Kanna, P. R. and Das, M., K., Numerical Simulation of Two-Dimensional Laminar Incompressible Wall Jet under Backward-Facing Step Flows. Communicated to *ASME Transactions : Journal of Fluids Engineering*, 2005.

8. Das, M., K. and Kanna, P. R, Study of Flow at High Re in a Lid Driven Cavity Problem. Communicated to *ASME Transactions : Journal of Fluids Engineering*, 2005.

9. Kanna, P. R. and Das, M., K., Conjugate Heat Transfer Study of Two-Dimensional Laminar Incompressible Wall Jet over Backward-Facing Step Flows: Effect of Geometry. Communicated to *ASME Transactions : Journal of Heat Transfer*, 2005.

10. Kanna, P. R. and Das, M., K., A note on Entrainment Boundary Condition: Wall Jet Problem. Communicated to *International Journal for Numerical Methods in Fluids*, 2005.

11. Kanna, P. R. and Das, M., K., Heat Transfer Study of Two-Dimensional Laminar Incompressible Wall Jet under Backward-Facing Step. Communicated to *Numerical Heat Transfer. Part A. Applications*, 2005.

Referred Conferences

1. Kanna, P. R. and Das, M., K., Conjugate Forced Convection Heat Transfer from A laminar Plane Wall Jet Flow. Presented in *17th National/6th ISHMT–ASME Heat and Mass Transfer Conference*, HMT-2004-C008, Jan. 5-7, 2004, IGCAR, Kalpakkam, India.

2. Kanna, P. R. and Das, M., K., Conjugate Forced Convection Heat Transfer From a Flat Plate by Laminar Plane Wall Jet Flow, *ASME Summer Heat Transfer conference*, July 17-22, 2005, San Francisco, CA, USA. Draft paper accepted.

3. Kanna, P. R. and Das, M., K., Conjugate Heat Transfer Study Of Two-Dimensional Laminar Incompressible Offset Jet Flows. *ASME Summer Heat Transfer conference*, July 17-22, 2005, San Francisco, CA, USA, Draft paper accepted.

4. Kanna, P. R. and Das, M., K., Flow and Heat Transfer Study Of Two-Dimensional Laminar Incompressible Offset Jet Flows, *ASME Summer Heat – ASME Summer Heat Transfer conference*, July 17-22, 2005, San Francisco, CA, USA. Draft paper accepted.

5. Kanna, P. R. and Das, M., K., Numerical Heat Transfer Study of Two-Dimensional Laminar Incompressible Offset Jet Flows. *18th National/7th ISHMT – ASME Heat and Mass Transfer Conference*, IIT, Guwahati Jan.2006. Abstract accepted. Full length paper is submitted.

Abstract

Depending upon the distance of the confining boundaries from the discharge, a jet can be analyzed as a free jet or a bounded one. If the boundaries (parallel to inlet axis) are sufficiently away from the origin of the jet, the flow is termed as a free jet. However, a bounded jet will occur when it interacts with a parallel wall. Bounded jet flows occur in many engineering applications such as environmental discharges, heat exchangers, fluid injection systems, cooling of combustion chamber wall in a gas turbine, automobile demister and others. Bounded jets can be classified into three types: (a) impinging jet aimed toward the boundary; (b) wall jet where fluid is discharged at the boundary; and (c) offset jet from a vertical wall of a stagnant pool issuing parallel to a horizontal solid wall. The present work is aimed to understand the flow and conjugate heat transfer characteristics of wall bounded laminar jet flows. The study is carried out for plane wall jet flow and offset jet flow. Another study covered is plane wall jet flow over backward facing step.

Glauert (1956) defined plane wall jet as a stream of fluid blown tangential along a plane wall. The wall jet consists of an inner region and an outer region. It is a combination of boundary layer flow over flat plate at inner region and plane free jet at outer region. The velocity profile has a point of inflexion. The surrounding medium of wall jet may be quiescent or co-flow or counter-flow depending upon the applications. Similarity solution for plane wall jet as well as radial wall jet for both laminar and turbulent cases were presented with the introduction of Glauert constant F.

Offset jet flow occurs when fluid is discharged from a slot in a vertical wall into the ambient near a horizontal solid boundary parallel to the inlet jet direction. Due to the entrainment of fluid between the jet and the bottom plate, there is a reduction of pressure in this region forcing the jet to deflect towards the boundary and eventually attach with it. This is called Coanda effect (Tritton, 1977). The offset jet flow features are different in various regions. In the near-field within a very short distance from the point of discharge, the jet flow is dominated by momentum and has the properties of a free jet. Attachment occurs when the jet is deflected towards an adjacent solid wall and tends to flow along the boundary. In the region around the attachment point, that is, the impingement region and part of the recirculation region, the jet can be partly characterized as an impingement jet. The offset jet becomes a wall jet in the far field. Other factors like free-stream velocity, ambient stratification, buoyancy (density difference), discharge orientation etc. further complicate the jet-boundary interaction and the behavior of an offset jet.

In another type of problem geometry, fluid is discharged from a slot along vertical wall into the ambient near a horizontal solid boundary parallel to the inlet jet direction. The flow passes through a step in the downstream direction and forms the wall jet over step flow situation. The flow kind is common in industrial applications like electronics cooling, high speed engine cooling etc.

The understanding of the flow behavior of wall bounded jet is important in engineering practices. If attachment is not desired for more mixing, a knowledge of calculation and design is required to prevent it. For a case where attachment is desirable, study of the involved variables is required so that a precise location of the attachment point and the containment of the flow can be established. A conjugate heat transfer problem occurs when the fluid regime is coupled with the conducting solid wall having finite thickness. The temperature and the heat fluxes at the solid-fluid interface are considered to be equal. This is referred to as the fourth-kind boundary condition. Conjugate heat transfer is involved in many applications like high speed jet engines, electronics cooling, film cooling of turbine blades, extrusion of materials etc.

In the present work, the flow features, non-conjugate heat transfer and conjugate heat transfer characteristics of wall jet, offset jet and wall jet over backward-facing step are investigated. Analytical solutions of the wall jet are available, based on the self similarity of velocity field (Schlichting and Gersten, 2000). However, these solutions are valid only far away from the jet inlet, and in most applications, the near-field development holds the key to important features of the jet flow. Therefore, the near-field development of a wall jet has been the subject of a lot of research in recent years.

In the present work an analytical solution is investigated for forced convection heat transfer from a laminar plane wall jet as conjugate case. Vynyycky et al. (1998) have presented a procedure to solve conjugate heat transfer from a flat plate problem. Similar approach has been used to solve the present situation. For $Re \gg 1$, boundary layer theory is used for the investigation. The problem has been solved for two classic cases such as $Pr \geq 1$ and $Pr \ll 1$. The conjugate model consists of considering the full Navier-Stokes equation in

the fluid medium and coupling of energy equations in the fluid and the slab through the interface boundary conditions. Closed-form relations are found for Nusselt number (Nu), average Nusselt number ($\overline{Nu}$) and conjugate interface boundary temperature (θ_b). The effects of the Reynolds number (Re), the Prandtl number (Pr), the thermal conductivity ratio (k) between the slab and the fluid medium and the slab aspect ratio (λ) are investigated on the heat transfer characteristics. The analytical results are compared with the full numerical results.

The steady state results are obtained as the asymptotic solution of an unsteady state equation. The unsteady state stream function-vorticity equation governing the incompressible laminar flow in non-dimensional form are solved by Alternate Direction Implicit (ADI) method. Clustered grids are used for the computations. From Taylor series expansion the temperature gradients are evaluated and substituted for heat flux equation at interface and the conjugate interface temperature at new time step is obtained. To validate the developed code, two-dimensional lid-driven square-cavity flow problem (Ghia et al., 1982) and the backward-facing flow problem (Armaly et al., 1983, Gartling, 1990 and Dyne and Heinrich, 1992) have been solved. Sudden expansion flow problem is solved and compared with Durst et al. (1993). For split domain problem, L-shape lid driven cavity Oosterlee et al. (1993) and backward-facing step with upstream channel Barton (1997) are solved and results compared with them. Excellent agreement has been obtained with the benchmark solutions reported in the above references. The laminar plane wall jet problem then has been solved and the computed velocity profiles are compared with the similarity solutions of Glauert (1956) and the experimental results of Quintana et al. (1997) in a similar way as represented by Seidel (2001). It is observed that at different downstream locations x/h, a good agreement amongst them has been obtained. The non-conjugate heat transfer case has been solved for Prandtl number (Pr) equal to 1.4 and compared in a similar way for five downstream locations.

Flow and heat transfer characteristics are studied for an offset jet flow. Reynolds number and offset ratio are taken into account for finding the reattachment length and centerline velocity decay. Effect of Prandtl number is considered for the heat transfer study. It is noticed that the peak Nusselt number is falling downstream of the reattachment location. The conjugate heat transfer study of an offset jet flow is carried out to find the effect of slab thickness, conductivity ratio, Re and Pr. Here the bottom wall is kept constant temperature and side walls are insulated. Results are presented for interface temperature, local Nusselt number distribution and average Nusselt number.

The flow and heat transfer study of plane wall jet over backward-facing step are presented in detail. It is noticed that when the step length is increased the recirculation eddy size is reduced. The wall jet region results are compared with similarity solution and Quintana et al. (1997) and are in good agreement with them. It is found that peak Nusselt number is coming near the inlet due to heavy entrainment and the second peak Nusselt number is occurring after the reattachment location. The conjugate heat transfer has been studied to find the effect of properties of fluid and solid and effect of geometry. Reynolds number, Prandtl number, conductivity ratio, length of the step (l), height of the step (s) and thickness of the bottom solid wall (w) are the parameters considered for study. When $Re = 600$, the isotherms are deflected towards the bottom wall and have become denser near the recirculation region. It is observed that thermal gradients in the normal direction are following linear trend whereas in streamwise direction non-linear trend is occurred. In streamwise direction isotherm is reduced to a minimum value and further downstream direction is increased. In fluid region it is noticed that at higher k, isotherm has become less sensitive in the fluid whereas in the solid wall, the are sensitive to the k values considered for study. Local Nusselt number distribution for different k values are reported. Results have been compared with non-conjugate case. Effect of geometry is studied in detail.

Contents

List of figures xix

List of tables xxvii

Nomenclature xxx

Abbreviations xxxiv

1 Introduction **1**

1.1 Introduction 1

1.2 Objectives of the Present Work 10

1.3 Proposed Contents of the Thesis 11

2 Numerical Procedure **13**

2.1 Conjugate Heat Transfer 19

2.2 Validation of the Code 21

3 Conjugate Heat Transfer Study: Plane Wall Jet Flow **23**

3.1 Introduction 23

3.2 Basic Equations 24

3.2.1 Quasi-two-dimensional analogue: 36

3.3 Numerical Solution 39

3.4 Validation of the Numerical Procedure 41

3.5 Grid Independence Study 41

3.6 Results and Discussion 44

3.7 Conclusions: 52

4 Simulation of Incompressible Offset Jet Flows 53

4.1 Introduction 53

4.2 Mathematical Formulation 55

4.3 Validation of the Numerical Procedure 59

4.4 Grid Independent Study 60

4.5 Results and Discussion 61

4.6 Conclusions 78

5 Heat Transfer Study: Offset Jet Flows 81

5.1 Introduction 81

5.2 Mathematical Formulation 82

5.3 Validation of the Numerical Procedure 84

5.4 Grid Independent Study 84

5.5 Results and Discussion 85

5.6 Conclusions 98

6 Conjugate Heat Transfer Study: Offset Jet Flows 101

6.1 Introduction 101

6.2 Mathematical Formulation 102

6.3 Grid Independent Study 106

6.4 Results and Discussion 110
6.5 Conclusions 123

7 Study of Wall Jet Over Backward-facing Step 125
7.1 Introduction 125
7.2 Mathematical Formulation 127
7.3 Validation of the Code 131
7.4 Grid Independent Study 131
7.5 Results and Discussion 132
7.6 Conclusions 147

8 Heat Transfer Study: Wall Jet Flow Over Backward-Facing Step 149
8.1 Introduction 149
8.2 Mathematical formulation 150
8.3 Grid Independence Study 154
8.4 Results and Discussion 154
8.5 Conclusions 168

9 Conjugate Study: Wall Jet Flow Over Backward-Facing Step - Part 1 169
9.1 Introduction 169
9.2 Mathematical Formulation 170
  9.2.1 Interface boundary condition 173
9.3 Grid Independent Study 176
9.4 Results and Discussion 177

9.5 Conclusions 196

10 Conjugate Study: Wall Jet Flow Over Backward-Facing Step - Part 2 **197**

10.1 Introduction 197

10.2 Results and Discussion 199

10.3 Conclusions 216

11 Conclusion and Scope for the Future Work **219**

11.1 Summary 219

11.2 Scope for the Future work 221

Appendix **223**

A Lid Driven Cavity Problem **223**

B Backward-Facing Step Flow Problem **227**

C Plane Wall Jet Flow Problem **231**

D Sudden Expansion Flow Problem **233**

E L- Shape Lid Driven Cavity Problem **237**

F Backward-Facing Step Flow with Upstream Channel **241**

References **245**

List of Figures

1.1 Schematic of plane wall jet flow: Non-conjugate 2

2.1 Interface boundary grids 20

3.1 Combination of a wall jet with solid wall 24
3.2 Grid independence for y-direction grids: $Re = 500, Pr = 1.4$ . . 42
3.3 Computational domain 43
3.4 Isotherm patterns within the solid slab for various parameters by numerical simulations 48
3.5 Local Nusselt number (Nu) for different parameters 49
3.6 Conjugate interface temperature (θ_b) for various parameters . . 50
3.7 Average Nusselt number for various parameters ($\overline{Nu}$) 51

4.1 Schematic diagram and boundary conditions in an offset jet problem 56
4.2 Grid independence study: OR=1.0 60
4.3 Velocity vector and stream trace plot (a-e), (f) u_{max} distribution, $Re = 600, OR = 1.0$ 67
4.4 Effect of offset ratio and Re on the streamline pattern 68

4.5 Effect of offset ratio and Re on the streamline pattern: 69
4.6 Velocity vector (a-c) and the recirculation eddy (d-f), $Re = 300$ 70
4.7 Centerline velocity: $OR = 1.5$ 71
4.8 Comparison of reattachment length with Re and OR. 72
4.9 Recirculation eddy structure for various Re and OR 73
4.10 Effect of OR and Re on entrainment: u-velocity contour plot . . 74
4.11 Local u velocity comparison 75
4.12 u - velocity component for various Re and OR 76
4.13 Vorticity distribution along the bottom wall 77

5.1 Schematic diagram and boundary conditions in a offset jet problem 82
5.2 Grid independence study: $Pr = 1.4, OR = 1.0$ 85
5.3 $Pr = 1.0$: Effect of offset ratio and Re Isotherm contour: (a)-(c) $Re = 200$, (d)-(f) $Re = 300$, (g)-(i) $Re = 400$ 91
5.4 $Pr = 1.0$: Effect of offset ratio and Re Isotherm contour: (a)-(c) $Re = 500$, (d)-(f) $Re = 600$ 92
5.5 Effect of Pr Isotherm contour: $OR = 1.5$ 93
5.6 Downstream location temperature contour: Fig. a-c, $Re = 300$, Fig. d-f, $Re = 600$ 94
5.7 Nusselt number variation for Re 95
5.8 Effect of Pr on Nusselt number 96
5.9 Effect of OR on Nusselt number: $Re = 500$ 97
5.10 Maximum Nusselt number. $OR = 1$ 98

6.1 Schematic diagram and boundary conditions in an offset jet problem 103

6.2 Grid independence study, $(Pr = 1.4, OR = 1.0)$ 108
6.3 Typical grids used for offset jet. 109
6.4 Isotherm contour: Effect of Re. $(Pr = 1, k = 5, S/h = 5)$ 114
6.5 Isotherm contour: Effect of Pr. $(Re = 300, k = 5, S/h = 5)$ . . . 115
6.6 Isotherm contour: Effect of solid slab thickness. $(Re = 300, Pr = 1, k = 1)$ 116
6.7 Isotherm contour: Effect of conductivity ratio. $(Re = 300, Pr = 1, S/h = 10)$ 117
6.8 Isotherm contour: Effect of Re. $(Pr = 1, k = 5, S/h = 5)$ 118
6.9 Isotherm contour: Effect of Pr. $(Re = 300, k = 5, S/h = 5)$ . . . 119
6.10 Isotherm contour: Effect of solid slab thickness. $(Re = 300, Pr = 1, k = 1)$ 119
6.11 Isotherm contour: Effect of conductivity ratio. $(Re = 300, Pr = 1, S/h = 10)$ 120
6.12 Conjugate interface temperature (θ_b): Effect of $Re, Pr, S/h, k$ . . 121
6.13 Local Nusselt number (Nu): Effect of $Re, Pr, S/h, k$ 122

7.1 Schematic diagram and boundary conditions in a wall jet under backward-facing step problem 129
7.2 Streamline contour 139
7.3 Vorticity contour 140
7.4 Effect of Re on wall vorticity: $l = 2h, s = 1h$ 141
7.5 Effect of step length on wall vorticity: $Re = 400, s = 1h$ 142
7.6 Effect of step height on wall vorticity: $Re = 400, l = 2h$ 143
7.7 Similarity profile $Re = 400, l = 2h, s = 1h$ 144

7.8 Effect of step height on upstream velocity at $x = 1h$: $Re = 400, l = 2h$ 145
7.9 Local maximum u velocity: $l = 2h, s = 1h$ 146
7.10 Reattachment length for different geometry and Reynolds number: $(l = 0h, s = 1h$ [74]) 146

8.1 Schematic diagram and boundary conditions in a wall jet under backward-facing step problem 151
8.2 Typical grids used for the computation. 155
8.3 Effect of Re on Isotherm contour: 160
8.4 Effect of Pr on Isotherm contour:$Re = 400, l = 2h, s = 1h$ . . . 161
8.5 Effect of step length on Isotherm contour: $Re = 400, Pr = 1.0, s = 1h$ 162
8.6 Effect of step height on Isotherm contour: $Re = 400, Pr = 1.0, l = 2h$ 163
8.7 Local Nusselt number distribution along step length, AB 163
8.8 Local Nusselt number distribution along step height, BC 164
8.9 Local Nusselt number distribution along bottom wall, CD . . . 164
8.10 Effect of upstream geometry on local Nusselt number along bottom wall, CD 165
8.11 Downstream u velocity and temperature similarity profile . . . 166
8.12 Effect of upstream geometry on average Nusselt number 167

9.1 Schematic diagram and boundary conditions in a wall jet over backward-facing step problem 171
9.2 Clustered grids used for the computation. 177

9.3 Effect of Re in fluid region ($Pr = 1, k = 5, l = 2h, s = 1h, w = 1h$). 184

9.4 Effect of Re in solid wall ($Pr = 1, k = 5, l = 2h, s = 1h, w = 1h$). 185

9.5 Effect of Pr in fluid region ($Re = 400, k = 5, l = 2h, s = 1h, w = 1h$). 186

9.6 Effect of Pr in solid wall. ($Re = 400, k = 5, l = 2h, s = 1h, w = 1h$). 187

9.7 Isotherm contour: Effect of conductivity ratio in fluid region ($Re = 400, Pr = 1, l = 2h, s = 1h, w = 1h$). 188

9.8 Effect of conductivity ratio in solid wall ($Re = 400, Pr = 1, l = 2h, s = 1h, w = 1h$). 189

9.9 Conjugate interface temperature: Effect of Re. ($Pr = 1, k = 5, l = 2h, s = 1h, w = 1h$) 190

9.10 Conjugate interface temperature: Effect of Pr. ($Re = 400, k = 5, l = 2h, s = 1h, w = 1h$) 191

9.11 Conjugate interface temperature: Effect of k. ($Re = 400, Pr = 1, l = 2h, s = 1h, w = 1h$) 192

9.12 Local Nusselt number: Effect of Re. ($Pr = 1, k = 5, l = 2h, s = 1h, w = 1h$) 193

9.13 Local Nusselt number: Effect of Pr. ($Re = 400, k = 5, l = 2h, s = 1h, w = 1h$) 194

9.14 Local Nusselt number: Effect of k. ($Re = 400, Pr = 1, l = 2h, s = 1h, w = 1h$). Non-conjugate study - [76] 195

10.1 Schematic diagram and boundary conditions 200

10.2 Clustered grids used for the computation. 200

10.3 Temperature in the solid region: Effect of l. ($Re = 400, Pr = 1, k = 5, s = 1h, w = 1h$). 207

10.4 Temperature in the solid region: Effect of s. ($Re = 400, Pr = 1, k = 5, l = 2h, w = 1h$). 208

10.5 Temperature in the solid region: Effect of w. ($Re = 400, Pr = 1, k = 5, l = 2h, s = 1h$). 209

10.6 Conjugate interface temperature: Effect of l. ($Re = 400, Pr = 1, k = 5, s = 1h, w = 1h$). 210

10.7 Conjugate interface temperature: Effect of s. ($Re = 400, Pr = 1, k = 5, l = 2h, w = 1h$). 211

10.8 Conjugate interface temperature: Effect of w. ($Re = 400, Pr = 1, k = 5, l = 2h, s = 1h$). 212

10.9 Local Nusselt number distribution: Effect of l. ($Re = 400, Pr = 1, k = 5, s = 1h, w = 1h$). 213

10.10 Local Nusselt number distribution: Effect of s. ($Re = 400, Pr = 1, k = 5, l = 2h, w = 1h$). 214

10.11 Local Nusselt number distribution: Effect of w. ($Re = 400, Pr = 1, k = 5, l = 2h, s = 1h$). 215

A.1 Schematic diagram with boundary condition of lid driven cavity problem. PV-Primary vortex, BL-Bottom left vortex, BR-Bottom right vortex, TL-Top left vortex. 224

A.2 Vertical centerline u- velocity passing through geometric center. Open symbols [59], close symbol [80] and line patterns are present results 224

A.3 Horizontal centerline v- velocity passing through geometric center. Open symbols [59], close symbol [80] and line patterns are present results 225

A.4 Moving wall vorticity. Open symbols [59], close symbol [80] and line patterns are present results 225

A.5 Left wall separation points. Open symbols are Barragy and Carrey [81] and line patterns are present results 226

B.1 Schematic diagram and boundary conditions in a BFS problem . 227

B.2 Primary vortex reattachment length for various Re. 228

B.3 Comparison of numerical solution with benchmark results. O -Gartling [34], Δ -Dyne and Heinrich [36] and present: —— x=3, - - - x=7, ... x=15 229

C.1 Comparison of results with similarity solution for $Re = 500$: Plane Wall jet flow. 232

D.1 Plane sudden-expansion flow problem: a part of the domain, Durst et al. [28] 234

D.2 Comparison of normalised u velocity profiles for $Re = 70$, Durst et al. [28] 235

D.3 Comparison of normalised u velocity profiles for $Re = 610$, Durst et al. [28] 235

E.1 Schematic diagram and boundary conditions of L-shape lid driven cavity flow problem [60]. 238
E.2 Velocity profiles along CL1 and CL2. 239

F.1 Backward-facing step flow with upstream channel problem. (Domain shown near the step) 243
F.2 Reattachment length for different Reynolds number: Parabolic inlet profile 244

List of Tables

5.1 Average Nusselt number: $Re = 200$ 89

5.2 Average Nusselt number: $Re = 300$ 89

5.3 Average Nusselt number: $Re = 400$ 90

5.4 Average Nusselt number: $Re = 500$ 90

5.5 Average Nusselt number: $Re = 600$ 90

6.1 Grid independence study ($Pr = 1.0$): Value of $\overline{Nu}$ for $S/h = 5$. 106

6.2 Grid independence study ($Pr = 1.0$): Value of $\overline{Nu}$ for $S/h = 10$ 107

6.3 Average Nusselt number: $Re = 300$, $S/h = 5$ 113

6.4 Average Nusselt number: $Re = 300$, $S/h = 10$ 113

6.5 Average Nusselt number: $Re = 600$, $S/h = 5$ 113

6.6 Average Nusselt number: $Re = 600$, $S/h = 10$ 114

7.1 Effect of Re on wall jet similarity region distance. $l = 2h, s = 1h$ 136

7.2 Effect of step length on wall jet similarity region distance. $Re = 300, s = 1h$ 137

7.3 Effect of step height on wall jet similarity region distance. $Re = 300, l = 2h$ 137

7.4 Effect of step length on primary vortex reattachment length. Percentage of reduction from $l = 1h$: $s = 1h$ 137

7.5 Effect of step height on primary vortex reattachment length. Percentage of variation from $s = 1h$: $s = 1h$ 137

8.1 Grid independence study: Value of $\overline{Nu}$: $Re = 400, Pr = 1.0, l = 2h$ 154

8.2 Peak Nusselt number: $Re = 400, Pr = 1, s = 1h$ 159

8.3 Peak Nusselt number: $Re = 400, Pr = 1, l = 2h$ 159

9.1 Grid independence study: Value of $\overline{Nu}$. ($Re = 400, Pr = 1, l = 2h, s = 1h, w = 1h$) 176

9.2 Average Nusselt number: Effect of Re. ($Pr = 1, k = 5, l = 2h, s = 1h, w = 1h$) 182

9.3 Average Nusselt number: Effect of Pr. ($Re = 400, k = 5, l = 2h, s = 1h, w = 1h$) 182

9.4 Average Nusselt number: Effect of k. ($Re = 400, Pr = 1, l = 2h, s = 1h, w = 1h$) 182

10.1 Minimum temperature. ($Re = 400, Pr = 1, k = 5, s = 1h, w = 1h$) 201

10.2 Average Nusselt number: Effect of l. ($Re = 400, Pr = 1, k = 5, s = 1h, w = 1h$) 206

10.3 Average Nusselt number: Effect of s. ($Re = 400, Pr = 1, k = 5, l = 2h, w = 1h$) 206

10.4 Average Nusselt number: Effect of w. ($Re = 400, Pr = 1, k = 5, l = 2h, s = 1h$) 206

F.1 Primary vortex reattachment length: (ER=0.25,Re=500) 242
F.2 Primary vortex reattachment length: (ER=0.75,Re=200) 243

Nomenclature

A	constant
a	thickness of the slab, m
b	length of the slab, m
h	inlet slot height, m
i	x-direction grid point
j	y-direction grid point
k_f	thermal conductivity of the fluid, W/m-^{0}K
k_s	thermal conductivity of the slab, W/m-^{0}K
k	thermal conductivity ratio, k_s/k_f
l	step length, m
L	Length of the slab, m
n	normal direction
Nu	local Nusselt number
$\overline{Nu}$	average Nusselt number
Pr	Prandtl number, $\frac{\nu}{\alpha}$
Re	Reynolds number for the fluid
S	thickness of the slab, m
Q	constant
T_c	constant bottom wall temperature, ^{0}C
T_∞	constant ambient temperature, ^{0}C
T_w	constant bottom wall temperature, ^{0}C
$\bar{t}$	dimensional time, s
t	nondimensional time

$\bar{u}, \bar{v}$	dimensional velocity components along (x, y) axes, m/s
u_r	dimensionless resultant velocity
u, v	dimensionless velocity components along (x, y) axes
$\overline{U}$	inlet mean velocity, m/s
U_∞	ambient velocity of fluid, m/s
x_1	Reattachment length, m
$\bar{x}, \bar{y}$	dimensional Cartesian co-ordinates along and normal to the plate, m
x, y	dimensionless Cartesian co-ordinates along and normal to the plate

Greek symbols

α	thermal diffusivity, m^2/s
γ	constant
ΔT	temperature difference, $T_c - T_\infty$, ^{0}C
δ	wall jet boundary layer thickness
ε	convergence criterion
η	similarity variable
θ	dimensionless temperature
θ_0	constant
$\bar{\theta}_b$	dimensionless average boundary temperature
θ_b	dimensionless average boundary temperature
κ	clustering parameter
$\bar{\theta}_b$	dimensionless average boundary temperature
θ_b	dimensionless boundary temperature
θ_s	dimensionless temperature in the solid wall
λ	aspect ratio a/b
ν	kinematic viscosity, m^2/s
σ	dimensionless constant
τ	dimensionless constant
χ	constant
ν	kinematic viscosity
ψ	dimensionless stream function
ω	dimensionless vorticity

Subscripts

f	fluid
max	maximum
s	solid
w	wall
b	interface
f	fluid
s	solid
w	wall
∞	ambient condition

Abbreviations

ADI	alternate direction implicit
2*D*	two dimensional
DNS	direct numerical simulations
RANS	Reynolds average Navier Stokes
OR	offset ratio

Chapter 1

Introduction

1.1 Introduction

Depending upon the distance of the confining boundaries from the discharge, a jet can be analyzed as a free jet or a bounded one. If the boundaries (parallel to inlet axis) are sufficiently away from the origin of the jet, the flow is termed as a free jet. However, a bounded jet will occur when it interacts with a parallel wall. Bounded jet flows occur in many engineering applications such as environmental discharges, heat exchangers, fluid injection systems, cooling of combustion chamber wall in a gas turbine, automobile demister and others. Bounded jets can be classified into three types: (a) impinging jet aimed toward the boundary; (b) wall jet where fluid is discharged at the boundary; and (c) offset jet from a vertical wall of a stagnant pool issuing parallel to a horizontal solid wall.

Glauert [1] defined plane wall jet as a stream of fluid blown tangential along a plane wall (Fig. 1.1). The wall jet consists of an inner region and an outer region. It is a combination of boundary layer flow over flat plate at inner region and plane free jet at outer region [2]. The surrounding medium of wall jet may be quiescent or co-flow or counter-flow depending upon the applications. Similarity solution for plane wall jet as well as radial wall jet for both laminar and turbulent cases were presented with the introduction of Glauert constant *'F'* [1].

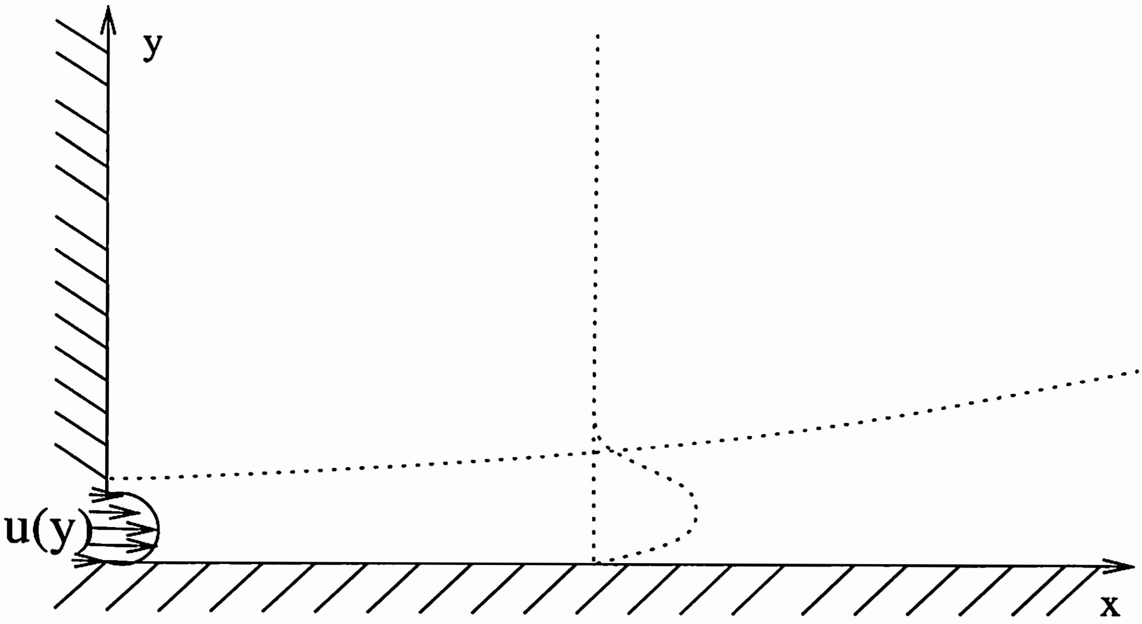

Figure 1.1: Schematic of plane wall jet flow: Non-conjugate

Offset jet flow occurs when fluid is discharged from a slot in a vertical wall into the ambient near a horizontal solid boundary parallel to the inlet jet direction. Due to the entrainment of fluid between the jet and the bottom plate, there is a reduction of pressure in this region forcing the jet to deflect towards the boundary and eventually attach with it. This is called Coanda effect [3]. The offset jet flow features are different in various regions. In the near-field within a very short distance from the point of discharge, the jet flow is dominated by momentum and has the properties of a free jet. Attachment occurs when the jet is deflected towards an adjacent solid wall and tends to flow along the boundary. In the region around the attachment point, that is, the impingement region and part of the recirculation region, the jet can be partly characterized as an impingement jet. The offset jet becomes a wall jet in the far field. Other factors like free-stream velocity, ambient stratification, buoyancy (density difference), discharge orientation etc. further complicate the jet-boundary interaction and the behavior of an offset jet.

In some cases fluid is discharged from a slot along horizontal wall into the ambient near a horizontal solid boundary parallel to the inlet jet direction. The plane wall jet passes over a step in the downstream direction and forms the wall jet over step flow situation. The flow kind is common in industrial applications like electronics cooling, high speed engine cooling etc. In offset jet flow once the jet ejects into ambient, Coanda effect takes place. Below the jet, recirculation eddy will be present and above it entrainment will occur. Before the wall jet flows over a backward-facing step flow, the jet ejects/spreads over a horizontal wall and Coanda effect occurs only after the jet flows over the step. Upto this distance it behaves like a plane wall jet. The huge entrainment naturally occurs near the jet entry and not in the downstream direction of the bottom wall. This makes significant changes in the flow physics and in the heat transfer mechanism.

The understanding of the flow behavior of wall bounded jet is important in engineering practices. If attachment is not desired for more mixing, a knowledge of calculation and design is required to prevent it. For a case where attachment is desirable, study of the involved variables is required so that a precise location of the attachment point and the containment of the flow can be established.

Experimental study is carried out with air as fluid by Seban and Back [4] for turbulent wall jet. They have compared the predicted velocity and temperature profiles with experimental values. Schwarz and Caswell [5] have studied laminar incompressible wall jet and found exact solutions for temperature for constant wall temperature as well as constant heat flux case. They have reported the length of virtual origin for wall jet. Chun and Schwarz [6] studied the stability of wall jet subjected to small disturbances. The critical Reynolds number based on boundary layer thickness and inlet mean velocity is about 57. The unsteady heat transfer study on laminar wall jet is reported by Gorla [7]. The Prandtl number considered is in the range of 0.01 to 1000. The closed form solution for temperature has been presented. Experimental study was carried by Bajura and Catalano [8] with water as fluid to study the transition in two-dimensional plane wall jet. The investigation is mainly focused on vortex formation on inner layer and outer shear layer of the wall jet. The theoretical as well as experimental study on stability of laminar wall jet is presented by Tsuji et al. [9]. They found that the subharmonic of a predominant disturbance velocity component appear in the non-linear region. Paige [10] carried out a study to quantify transition in the augmented flow and measure the effects of free stream velocity and slot height on transition. He has presented a relationship to define the transition point based on local Reynolds number which is based on local maximum velocity and boundary layer thickness. Shih and Gogineni [11] investigated the effects of using a low-frequency, high-amplitude external acoustic excitation on a wall jet. Oguz [12] has studied different jet configuration and reported that for annular wall jets the length of the inner gaseous region is found to be finite depending on the Froude number.

Amitay and Cohen [13] have reported the effects of wall blowing and suction on the stability characteristics of a laminar incompressible two-dimensional plane wall jet. Cohen et al. [14] did work on transition of wall jets subjected to blowing and suction. Quintana et al. [15] experimentally investigated the mean and fluctuating characteristics of a plane unsteady laminar wall jet for constant wall temperature. Streamwise velocity and temperature profiles are compared with similarity results. They found that the variations in temperature is significant in the inner region of wall jet. Laminar steady flow of wall jet in a large width cavity is studied by Homan and Soo [16] by stream function vorticity formulation. They used Alternate Direction Implicit (ADI) method to solve the governing equations. They reported recirculation region for different tank width to inlet height ratio and Reynolds number ranging from 10 to 50. They noticed that the large recirculation cell is located immediately above the wall jet boundary layer. Instability and receptivity of laminar wall jets are studied by Tumin and Aizatulin [17].

Seidel [18] has done numerical work to find the effect of high amplitude forcing on laminar and turbulent wall jet over a heated flat plate. Seidel has used DNS for laminar case and RANS for turbulent wall jet. Marzouk et al. [19] numerically studied the momentum and heat transfer in a pulsed plane laminar free jet and wall jet. They have investigated that the pulsation does not modify the flow parameters in the region of the established regime, but it does accelerate the initial development of the jet and improve the diffusion and the entrainment in the first diameters. Recently, Bhattacharjee and Loth [20] simulated laminar and transitional cold wall jets. They have investigated the significance of three different inlet profiles viz. parabolic, uniform and ramp and presented the detailed results of time-averaged wall jet thickness and temperature distribution. They used RANS approach for higher Reynolds number and DNS approach for three-dimensional wall jet.

The stability of 2D free jets was studied experimentally by Sato [21] and Sato and Sakao [22]. Theoretical analyses for axisymmetric free jets were carried out by Batchelor and Gill [23] and Cohen and Wygnanski [24]. Sarma et al. [25] have studied 2D incompressible jet development inside a duct in the laminar flow regime for cases with and without entrainment of ambient fluid. Chiriac and Ortega [26] numerically studied the steady and unsteady flow and heat transfer in a confined slot jet as a laminar case. Chattopadhyay [27] numerically investigated the Nusselt number distribution for laminar impinging annular jets. He found that the Nusselt number of annular jets are about 20% lower than circular jets for the same mass and momentum efflux. Durst et al. [28] carried out experiments and numerical study on symmetric sudden expansion flow problem. The downstream velocity profiles are presented for different Reynodls number and comparisons made between predicted results with experimental results and they found good agreement between them. Two dimensional experimental study is carried out by Holland and Liburdy [29] on heated turbulent offset jets. They compared the results with heated wall jet at downstream location. Kim et al. [30] have reported flow and heat transfer characteristics of wall attaching offset jet. They reported for wide range of offset ratio and Reynolds number ranging from 6500 to 39000. They have presented correlations for local Nusselt number distribution. Gu [31] presented a two-dimensional unsteady model for submerged turbulent offset jet. The local maximum velocity decay, jet trajectory and velocity profiles are presented in detail. Cho and Park [32] reported the steady and unsteady computation of upwash jet. For the steady flow computation was obtained by integrating RANS equations. For unsteady computation standard $k-\epsilon$ eddy viscosity model was used. They found the $k-\epsilon$ model resulted in a periodically oscillating flow.

Backward-facing step flow problem is treated as a benchmark problem for the past few decades. The detailed study on this problem was presented by Armaly et al. [33]. Size of recirculation eddies and downstream velocity profiles for wide range of Reynolds number are presented in detail. Discrepancy found between predicted and measured reattachment length was due to the experimental flow loses its two-dimensionality at higher Reynolds number (> 400). Benchmark results were presented by Gartling [34] for backward-facing step flow problem for $Re = 800$. The inlet channel effect on step flow problem is studied by Barton [35]. He found that the primary vortex length is reduced if an upstream channel is presented in the step flow. Dyne and Heinrich [36] reported the downstream temperature profile and Nusselt number distribution for step flow problem for the case of $Re = 800$, $Pr = 0.7$. Kondoh et al. [37] reported the heat transfer study of backward-facing step for wide range of Re, Pr and expansion ratio. Their reattachment length is more than the benchmark results of Barton ([35]). While solving for a three-dimensional backward-facing step flow problem, Biswas et al. [38] have observed and reported about the evolution of wall jet-like structure in the streamwise and spanwise direction. The self-similarity profile for the streamwise velocity (u) is observed in a plane at a distance of 1.08 away from the sidewall arising due to the sudden expansion near the step. For the spanwise velocity (w), it is at x=6 and 8 which is the culmination of the generation of the w velocity component from the side wall. Abu-Mulaweh et al. [39] presented velocity and temperature distributions, local Nusselt number and size of recirculation for mixed convection laminar flow over a forward-facing step problem. They reported that the opposing buoyancy force affects significantly the location and length of the recirculating flow region downstream of the step as well as local Nusselt number.

A conjugate heat transfer problem occurs when the fluid regime is coupled with the conducting solid wall of finite thickness. The temperature and the heat fluxes at the solid-fluid interface are considered to be equal. This is referred to as the fourth-kind boundary condition [40]. Conjugate heat transfer is involved in many applications like high speed jet engines, electronics cooling, film cooling of turbine blades, extrusion of materials etc. Conjugate heat transfer is getting more attention by the researchers for the past two decades. Many publications are devoted to conjugate heat transfer on flat plate [41–44].

Vynnycky et al. [45] presented closed form relations for interface temperature, local Nusselt number and average Nusselt number for laminar flow over a flat plate as conjugate case. Chiu et al. [46] studied conjugate heat transfer of horizontal channel both experimentally and numerically. They found that the parametric study of operational parameters related to the conjugate heat transfer revealed that the addition of conjugate heat transfer significantly affects the temperature and heat transfer rates at the surface of the heated region. Rao et al. [47] presented the results for laminar mixed convection with surface radiation from a vertical plate with a heat source as conjugate case. They solved the governing equations by stream function vorticity formulation. Jilani et al. [48] presented finite difference solution for conjugate heat transfer study on heat generating vertical cylinder. Steady [49] and unsteady [50] conjugate heat transfer from a cylinder in laminar flow are presented by Juncu. He carried out the numerical investigation for Reynolds number ranging from 2 to 20. He followed ADI method for solving the governing equation.

In the present work, the flow features, non-conjugate heat transfer and conjugate heat transfer characteristics of plane wall jet, offset jet and wall jet over backward-facing step are investigated. Analytical solutions of the wall jet are available, based on the self similarity of velocity field [1, 51]. However, these solutions are valid only far away from the jet inlet, and in most applications, the near-field development holds the key to important features of the jet flow. Therefore, the near-field development of a wall jet has been the subject of a lot of research in recent years.

Although many studies have been conducted on wall jet, some of the characteristics yet to be explored. The available literature on theoretical simulation of plane laminar offset jet flows are somewhat limited. The case of an entraining jet located near the jet discharge, which occur in several practical applications, has not been studied. The conjugate heat transfer is not carried for wall attaching offset jet. The present investigation aim to study the effect of Reynolds number, Prandtl number and slab thickness on local Nusselt number, peak Nusselt number location and interface temperature.

1.2 Objectives of the Present Work

The following situations are considered for carrying out the research.

- Closed form solution for conjugate heat transfer of laminar incompressible plane wall jet flow.
- Validating the closed form solution for conjugate heat transfer of plane wall jet flow by numerical simulation.
- Flow and heat transfer study of laminar incompressible offset jet flow.
- Conjugate heat transfer study of laminar incompressible offset jet flow.
- Flow and heat transfer study of laminar incompressible wall jet over backward-facing step flow.
- Conjugate heat transfer study of laminar incompressible wall jet over backward-facing step flow.

1.3 Proposed Contents of the Thesis

The thesis is planned to include the following chapters. Chapter 1 will cover the introduction and literature study. Chapter 2 will discuss about the numerical procedure to find the hydrodynamic solution, heat transfer solution for constant bottom wall temperature and conjugate heat transfer solution. Chapter 3 will discuss the closed form solution and comparisons with numerical simulation for conjugate plane wall jet problem. Chapter 4 will discuss the hydrodynamic study of an offset jet flow problem. Chapter 5 will discuss the heat transfer study of an offset jet. Chapter 6 will discuss the conjugate heat transfer study of an offset jet. Chapter 7 will discuss the hydrodynamic study of wall jet flow over backward-facing step. Chapter 8 will discuss the heat transfer of wall jet flow over backward-facing step. Chapter 9 and 10 will discuss the conjugate heat transfer of wall jet flow over backward-facing step. chapter 11 will cover the conclusion and scope of the work.

Chapter 2

Numerical Procedure

This chapter describes the governing equations and numerical procedure to solve the problems considered here. The two-dimensional incompressible Navier-Stokes equations in cartesian coordinates in primitive variable form are [52],

Continuity

$$\frac{\partial \hat{u}}{\partial \hat{x}} + \frac{\partial \hat{v}}{\partial \hat{y}} = 0 \tag{2.1}$$

x momentum

$$\frac{\partial \hat{u}}{\partial \hat{t}} + \hat{u}\frac{\partial \hat{u}}{\partial \hat{x}} + \hat{v}\frac{\partial \hat{u}}{\partial \hat{y}} = -\frac{1}{\rho}\frac{\partial \hat{p}}{\partial \hat{x}} + \nu\left(\frac{\partial^2 \hat{u}}{\partial \hat{x}^2} + \frac{\partial^2 \hat{u}}{\partial \hat{y}^2}\right) \tag{2.2}$$

y momentum

$$\frac{\partial \hat{v}}{\partial \hat{t}} + \hat{u}\frac{\partial \hat{v}}{\partial \hat{x}} + \hat{v}\frac{\partial \hat{v}}{\partial \hat{y}} = -\frac{1}{\rho}\frac{\partial \hat{p}}{\partial \hat{y}} + \nu\left(\frac{\partial^2 \hat{v}}{\partial \hat{x}^2} + \frac{\partial^2 \hat{v}}{\partial \hat{y}^2}\right) \tag{2.3}$$

Energy equation:

$$\frac{\partial T}{\partial \hat{t}} + \hat{u}\frac{\partial T}{\partial \hat{x}} + \hat{v}\frac{\partial T}{\partial \hat{y}} = \nu\left(\frac{\partial^2 T}{\partial \hat{x}^2} + \frac{\partial^2 T}{\partial \hat{y}^2}\right) \tag{2.4}$$

The stream function and vorticity are defined as:

$$\hat{u} = \frac{\partial \hat{\psi}}{\partial \hat{y}}; \ \hat{v} = -\frac{\partial \hat{\psi}}{\partial \hat{x}}; \ \nabla^2 \hat{\psi} = -\hat{\omega} \tag{2.5}$$

The x momentum and y momentum equations are combined by substituting the stream function and vorticity formulation Eq. 2.5 in Eq. 2.1-2.3 and the pressure term can be eliminated. The resultant equations are,

Streamfunction equation:

$$\nabla^2 \hat{\psi} = -\hat{\omega} \tag{2.6}$$

Vorticity transport equation:

$$\frac{\partial \hat{\omega}}{\partial \hat{t}} + \hat{u}\frac{\partial \hat{\omega}}{\partial \hat{x}} + \hat{v}\frac{\partial \hat{\omega}}{\partial \hat{y}} = \nu\left(\frac{\partial^2 \hat{\omega}}{\partial \hat{x}^2} + \frac{\partial^2 \hat{\omega}}{\partial \hat{y}^2}\right) \tag{2.7}$$

The unsteady state stream function - vorticity equation in non-dimensional conservative form are

Streamfunction equation

$$\nabla^2 \psi = -\omega \tag{2.8}$$

Vorticity equation

$$\frac{\partial \omega}{\partial t} + \frac{\partial (u\omega)}{\partial x} + \frac{\partial (v\omega)}{\partial y} = \frac{1}{Re}\nabla^2 \omega \tag{2.9}$$

Energy equation

$$\frac{\partial \theta_f}{\partial t} + \frac{\partial (u\theta_f)}{\partial x} + \frac{\partial (v\theta_f)}{\partial y} = \frac{1}{RePr}\nabla^2 \theta_f \tag{2.10}$$

The subscript f in the energy equation made for fluid. The following non-dimensional variables are used for obtaining the equations (2.8-2.10).

$$x = \frac{\hat{x}}{h}, \quad y = \frac{\hat{y}}{h}, \quad u = \frac{\hat{u}}{\bar{u}}, \quad v = \frac{\hat{v}}{\bar{u}}, \quad \psi = \frac{\hat{\psi}}{h\bar{u}}, \quad \omega = \frac{h\hat{\omega}}{\bar{u}}, \quad Re = \frac{h\bar{u}}{\nu}, \quad Pr = \frac{\nu}{\alpha} \quad \hat{\theta} = \frac{T - T_\infty}{T_\infty - T_w}, \quad t = \frac{\hat{t}}{(h/\bar{u})}$$

h - is the inlet slot height; u - horizontal velocity component; v - normal velocity component; Re - Reynolds number based on inlet mean velocity.

The computational domain considered here is clustered cartesian grids. For unit length, the grid space at i^{th} node is given by the expression [53],

$$x_i = \left(\frac{i}{i_{max}} - \frac{\kappa}{\vartheta} sin\left(\frac{i\vartheta}{i_{max}}\right)\right) \tag{2.11}$$

$\vartheta = 2\pi$ stretches both end of the domain whereas $\vartheta = \pi$ clusters more grid points near one end of the domain. κ varies between 0 to 1. When it approaches 1 more points fall near the end.

The unsteady vorticity transport equation 2.9 in time is solved by Alternate Direction Implicit method (ADI). The central differencing scheme is followed for both the convective as well as the diffusive terms (Roache [54]). It is first order accurate in time and second order accurate in space $O(\Delta t, \Delta x^2, \Delta y^2)$, and is unconditionally stable. It consists of two half time-steps.

The first half time-step:

$$\frac{\omega_{i,j}^{n+\frac{1}{2}} - \omega_{i,j}^{n}}{\Delta t/2} + Lx(u\omega)_{i,j}^{n+\frac{1}{2}} + Ly(v\omega)_{i,j}^{n} - \frac{1}{Re}(Lxx(\omega)_{i,j}^{n+\frac{1}{2}} + Lyy(\omega)_{i,j}^{n}) = 0 \tag{2.12}$$

The second half time-step:

$$\frac{\omega_{i,j}^{n+1} - \omega_{i,j}^{n+\frac{1}{2}}}{\Delta t/2} + Lx(u\omega)_{i,j}^{n+\frac{1}{2}} + Ly(v\omega)_{i,j}^{n+1} - \frac{1}{Re}(Lxx(\omega)_{i,j}^{n+\frac{1}{2}} + Lyy(\omega)_{i,j}^{n+1}) = 0 \tag{2.13}$$

where,

$$\begin{aligned} Lx(u\omega)_{i,j} &= \frac{(u\omega)_{i+1,j} - (u\omega)_{i-1,j}}{\Delta x_i + \Delta x_{i-1}}; \\ Ly(v\omega)_{i,j} &= \frac{(v\omega)_{i,j+1} - (v\omega)_{i,j-1}}{\Delta y_j + \Delta y_{j-1}} \end{aligned} \tag{2.14}$$

$$\begin{aligned} Lxx(\omega)_{i,j} &= \frac{\omega_{i-1,j} - 2\omega_{i,j} + \omega_{i+1,j}}{\Delta x_i * \Delta x_{i-1}}; \\ Lyy(\omega)_{i,j} &= \frac{\omega_{i,j-1} - 2\omega_{i,j} + \omega_{i,j+1}}{\Delta y_j * \Delta y_{j-1}} \end{aligned} \tag{2.15}$$

Equations (2.12 and 2.13) are rearranged to give the following equations

(2.16 and 2.17).

$$\begin{aligned}
-(C_x u^n_{i-1,j} + S_x)\omega^{n+\frac{1}{2}}_{i-1,j} + (1+2S_x)\omega^{n+\frac{1}{2}}_{i,j} - (-C_x u^n_{i+1,j} + S_x)\omega^{n+\frac{1}{2}}_{i+1,j} \\
= (C_y v^n_{i,j-1} + S_y)\omega^n_{i,j-1} + (1-2S_y)\omega^n_{i,j} \\
+(-C_y v^n_{i,j+1} + S_y)\omega^n_{i,j+1} \qquad (2.16)
\end{aligned}$$

$$\begin{aligned}
-(C_y v^n_{i-1,j} + S_y)\omega^{n+1}_{i,j-1} + (1+2S_y)\omega^{n+1}_{i,j} - (-C_y v^n_{i,j+1} + S_y)\omega^{n+1}_{i,j+1} \\
= (C_x u^n_{i-1,j} + S_x)\omega^{n+\frac{1}{2}}_{i-1,j} + (1-2S_x)\omega^{n+\frac{1}{2}}_{i,j} \\
+(-C_x u^n_{i+1,j} + S_x)\omega^{n+\frac{1}{2}}_{i+1,j} \qquad (2.17)
\end{aligned}$$

where $C_x = \frac{\Delta t}{2(\Delta x_i+\Delta x_{i-1})}$, $C_y = \frac{\Delta t}{2(\Delta y_j+\Delta y_{j-1})}$, $S_x = \frac{\Delta t}{Re}\frac{1}{\Delta x_i*(\Delta x_i+\Delta x_{i-1})}$, $S_y = \frac{\Delta t}{Re}\frac{1}{\Delta y_j*(\Delta y_j+\Delta y_{j-1})}$

The discretization of Eq. (2.8) is given by:

$$Lxx(\psi) + Lyy(\psi) = -\omega_{i,j} \qquad (2.18)$$

The velocity components are updated by the following equations:

$$\begin{aligned}
u = \frac{\partial\psi}{\partial y} &= \frac{\psi_{i,j+1} - \psi_{i,j-1}}{\Delta y_j + \Delta y_{j-1}} \qquad (2.19) \\
v = -\frac{\partial\psi}{\partial x} &= \frac{\psi_{i+1,j} - \psi_{i-1,j}}{\Delta x_i + \Delta x_{i-1}} \qquad (2.20)
\end{aligned}$$

The velocities which appear in Eqs. 2.16 and 2.17 are calculated at n^{th} time level while advancing to the $(n+1)^{th}$ time level. Because of this approximation in the nonlinear terms, the second order accuracy of the method is somewhat lost. However, something of the second-order accuracy of the linearized system is retained if the velocity field is slowly varying (Roache [54]). The Poisson Eq. (2.18) is solved explicitly by five point Gauss-Seidel methods. Thom's vorticity condition has been used to obtain the wall vorticity as given below.

$$\omega_w = -\frac{2\left(\psi_{w+1} - \psi_w\right)}{\Delta n^2} \tag{2.21}$$

where Δn is the grid space normal to the wall. It has been shown by Napolitano et al. [55] and Huang and Wetton [56] that convergence in the boundary vorticity is actually second order for steady problems and for time-dependent problems when $t > 0$. Roache [54] has reported that for a Blausius boundary-layer profile, numerical test verify that this first-order form is more accurate than second-order form.

The Poisson equation (2.8) is solved explicitly by five point Gauss-Seidel methods. For different problem and different *Re* different constant time step is used for the prediction. The results obtained for lower *Re* steady-state solution have been used as initial guess value for high *Re* flow for stream function and vorticity. This is based on the procedure given by Comini et al. [57]. It has been observed that for coarse grids, larger time step can be used whereas for fine grids, the solution diverges with large time step. While selecting κ, time step also needs to be considered. The maximum vorticity error behavior is complicated as explained by Roache [54]. While marching in time for the solution, it has been observed that the maximum vorticity error gradually decreases. It then increases drastically finally decreases asymptotically leading to steady-state solution. The convergence criteria to be set in such a way that it should not terminate at false stage. At steady state, the error reaches the asymptotic behavior. Here it is set as sum of vorticity error reduced to either the convergence criteria ε or large total time.

For vorticity,

$$\sum_{i,j=1}^{i_{max},j_{max}} \left|\omega_{i,j}^{t+\triangle t} - \omega_{i,j}^{t}\right| < \varepsilon \tag{2.22}$$

The heat transfer is study is carried out for non-conjugate case. For fluid region the energy equation Eq. 2.10 is solved by ADI method. For temperature, convergence criteria as non-conjugate case,

$$\sum_{i,j=1}^{i_{max},j_{max}} \left|\theta_{f\ i,j}^{t+\triangle t} - \theta_{f\ i,j}^{t}\right| < \varepsilon \tag{2.23}$$

2.1 Conjugate Heat Transfer

The conjugate heat transfer exists when the solid body is having finite thickness. The interface grid is shown in Figure 2.1. The energy equation in fluid region and solid region are solved simultaneously in conjugate heat transfer case. For solid region, the energy equation for solving conjugate case,

$$\frac{\partial \theta_s}{\partial t} - \frac{1}{RePr}\nabla^2\theta_s = 0 \tag{2.24}$$

The slab energy equation is written in transient non-dimensionalised form.

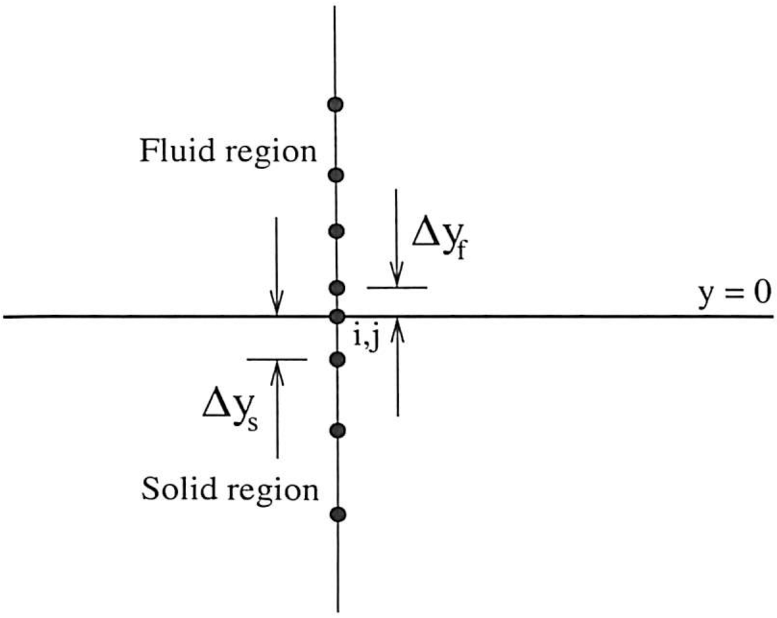

Figure 2.1: Interface boundary grids

The point to note here is that the second term (Eq. 2.24) contains Re and Pr. They appear because of the type of non-dimensionalisation. Similar form of equation has been given by Chiu et al [46]. The conjugate boundary conditions along interface are

$$k_s \left(\frac{\partial \theta_s}{\partial y}\right)_{y=0} = k_f \left(\frac{\partial \theta_f}{\partial y}\right)_{y=0}$$

$$\text{and} \quad \theta_f = \theta_s \quad \text{at} \quad \text{interface} \quad y = 0, \quad 0 < x \leq x_{max} \tag{2.25}$$

From Taylor series expansion the temperature gradients are evaluated and substituted in equations (2.10), (2.24) and (2.25). Simplifying, the conjugate interface temperature at new time step is,

$$
\begin{aligned}
\theta_{i,j}^{t+\Delta t} &= \theta_{i,j}^{t} + \frac{2\Delta t}{RePr(\Delta y_f + k\Delta y_s)}\left[\frac{1}{2}(\Delta y_f + k\Delta y_s)\right. \\
&\quad \left(\frac{\theta_{f,i+1,j} - 2\theta_{f,i,j} + \theta_{f,i-1,j}}{\Delta x_i * \Delta x_{i-1}}\right) - k\frac{\theta_{s,i,j} - \theta_{s,i,j-1}}{\Delta y_s} \\
&+ \left.\frac{\theta_{f,i,j+1} - \theta_{f,i,j}}{\Delta y_f}\right]^t
\end{aligned}
\tag{2.26}
$$

Here k is the conductivity ratio $(k_s/k_f.)$

Convergence criteria for temperature: conjugate case,

$$\sum_{i,j=1}^{i_{max},j_{max}} \left(\left|\theta_{s\ i,j}^{t+\Delta t} - \theta_{s\ i,j}^{t}\right| + \left|\theta_{f\ i,j}^{t+\Delta t} - \theta_{f\ i,j}^{t}\right| \right) < \varepsilon \tag{2.27}$$

Along solid wall constant stream lines are assumed based on inlet flow. At jet inlet, parabolic profile is assumed. At the outlet in the downstream direction, stream-wise gradients are assumed to be zero. At the entrainment boundary, normal velocity gradient is zero [58]. The details of the discretized form of the boundary conditions will be given along with particular problems solved in various chapters.

2.2 Validation of the Code

To validate the developed code, two-dimensional lid-driven square-cavity flow problem (Ghia et al. [59]) is solved and centerline u velocity and v velocity and moving wall vorticity are compared with benchmark results and found good agreement with them. To simulate inflow and outflow of fluid flow problem, the backward-facing flow problem has been solved. The downstream velocity profiles are compared with Gartling [34]. The laminar plane wall jet problem then has been solved and the computed velocity profiles are compared with the similarity solutions of Glauert [1] and the experimental results of Quintana et al. [15] in a similar way as represented by Seidel [18]. It is observed that at different downstream locations a good agreement amongst them has been obtained. The non-conjugate heat transfer case has been solved for Pr=1.4 and compared in a similar way. Further the conjugate study for laminar plane wall jet flow is carried out. To validate the recirculation eddy length measurement backward-facing step flow problem results are compared with (Armaly et al. [33], Gartling [34]). Heat transfer study is carried out in backward-facing step flow problem and results are compared with Dyne and Heinrich [36]. Sudden expansion flow problem is solved and compared with Durst et al [28]. After testing these problems offset jet flow problem is studied. For validating split domain procedure L shape lid driven cavity (Oosterlee et al. [60]) and backward-facing step with upstream channel (Barton [35]) are solved. Excellent agreement has been obtained with the benchmark solutions reported in the above references. The details are presented in Appendices.

Chapter 3

Conjugate Heat Transfer Study: Plane Wall Jet Flow

3.1 Introduction

This chapter describes the closed form solution for laminar plane wall jet flow as a conjugate case and numerical validation of the same. The present study is motivated by the cooling of heated slabs due to laminar plane wall jet flow. These type of conjugate heat transfer situations are found in electronics cooling, refrigerated air curtain, paper industry, electrical motor cooling etc. Here, a conjugate heat transfer by a two-dimensional laminar plane wall jet flow over a solid slab has been considered. An analytical solution has been presented for $Pr \ll 1$ and $Pr \geq 1$ cases with k, Re and λ as the parameters. The analytical solution has been compared and validated with a numerical solution. For this purpose, the problem has also been solved numerically with stream function-vorticity method considering it to be an unsteady-state formulation.

The integration in time has been allowed till a steady-state solution is obtained.

3.2 Basic Equations

Consider the steady two-dimensional heat transfer over a rectangular slab of finite thickness. A jet of fluid strikes the wall parallely, which is submerged in the same fluid thus developing wall jet. A schematic representation of the domain is shown in Fig. 3.1. The slab thickness is $-a \leq y \leq 0$ and the length is $\frac{-b}{2} \leq x \leq \frac{b}{2}$. The fluid has uniform temperature and velocity at inlet (i.e. $x = -\frac{1}{2}$). The bottom of the wall is maintained at constant temperature, $T_c > T_\infty$. The other ends of the wall are thermally insulated. It is assumed that the temperature gradient of solid wall in axial direction is negligible while comparing temperature gradient in normal direction, which is consistent with

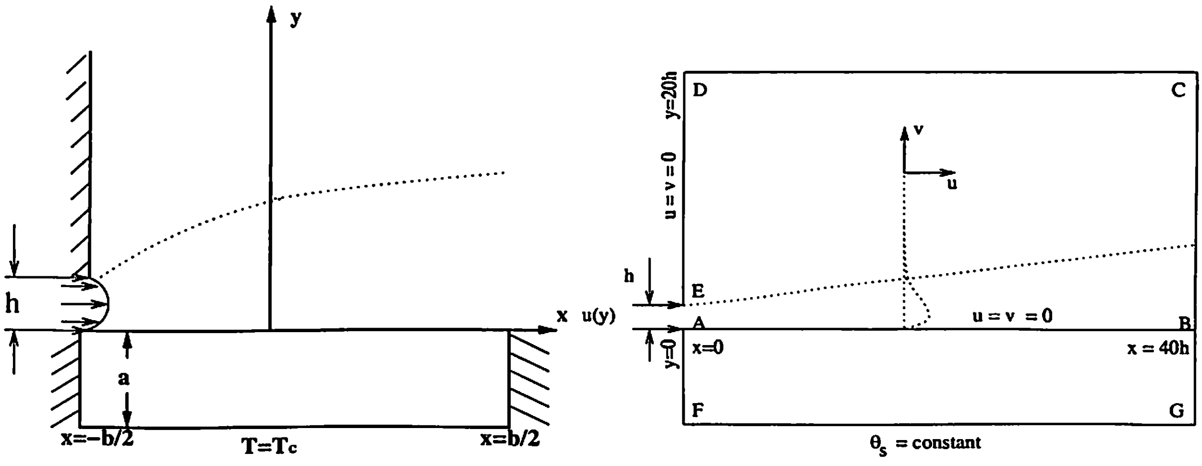

(a) Schematic diagram

(b) Coordinate system and boundary condition

Figure 3.1: Combination of a wall jet with solid wall

boundary layer theory. The surrounding of the fluid is assumed as quiescent regime. Following non-dimensional variables are used to express the problem.

$$\hat{x} = \frac{x}{b}, \hat{y} = \frac{y}{b}, \hat{u} = \frac{u}{U_\infty}\frac{1}{\sqrt{Re}}, \hat{v} = \frac{v}{U_\infty}\frac{1}{\sqrt{Re}}, \hat{\psi} = \frac{\psi}{bU_\infty},$$

$$\hat{\omega} = \frac{b\omega}{U_\infty}\frac{1}{\sqrt{Re}}, \hat{\theta}_f = \frac{T_f - T_\infty}{\Delta T}, \hat{\theta}_s = \frac{T_s - T_\infty}{\Delta T} \tag{3.1}$$

where $\Delta T = T_c$ - T_∞ and ψ is the stream function which is defined by

$$u = \frac{\partial \psi}{\partial y}, v = -\frac{\partial \psi}{\partial x} \tag{3.2}$$

The equations governing the vorticity and energy transport for the fluid (dropping the hats for all the variables for clarity)

$$\nabla^2 \psi = -\omega \tag{3.3a}$$

$$u\frac{\partial \omega}{\partial x} + v\frac{\partial \omega}{\partial y} = \frac{1}{Re^{3/2}}\nabla^2 \omega \tag{3.3b}$$

$$u\frac{\partial \theta_f}{\partial x} + v\frac{\partial \theta_f}{\partial y} = \frac{1}{PrRe^{3/2}}\nabla^2 \theta_f \tag{3.3c}$$

and for the conductive slab

$$\nabla^2 \theta_s = 0 \tag{3.3d}$$

where ∇^2 is the Laplacian in Cartesian co-ordinates (x, y). The boundary conditions for equations (3.3a)-(3.3d) are

$$\psi = \frac{\partial \psi}{\partial y} = 0 \text{ on } y = 0 \ \ |x| \leq \frac{1}{2} \tag{3.4a}$$

$$\theta_s = \theta_f \quad \text{on} \quad y = 0 \quad |x| \leq \frac{1}{2} \tag{3.4b}$$

$$\frac{\partial \theta_f}{\partial y} = k\frac{\partial \theta_s}{\partial y} \quad \text{on} \quad y = 0 \quad |x| \leq \frac{1}{2} \tag{3.4c}$$

$$\frac{\partial \theta_s}{\partial x} = 0 \quad \text{on} \quad x = \pm\frac{1}{2} \quad -\lambda \leq y \leq 0 \tag{3.4d}$$

$$\theta_s = 1 \quad \text{on} \quad y = -\lambda \quad |x| \leq \frac{1}{2} \tag{3.4e}$$

$$\theta_f \to 0 \quad \text{as} \quad y \to \infty \quad |x| \leq \frac{1}{2} \tag{3.4f}$$

$$\frac{\partial \psi}{\partial y} \to 0 \quad \text{as} \quad y \to \infty \quad |x| \leq \frac{1}{2} \tag{3.4g}$$

$$\omega \to 0 \quad \text{as} \quad y \to \infty \quad |x| \leq \frac{1}{2} \tag{3.4h}$$

The local Nusselt number is

$$Nu = -\left(\frac{\partial \theta_f}{\partial y}\right)_{y=0}, \quad |x| \leq \frac{1}{2} \tag{3.5}$$

The average Nusselt number is defined as,

$$\overline{Nu} = \int_{-1/2}^{1/2} Nu \, dx \tag{3.6}$$

While finding out the closed form solution for the energy equation, it is mandatory to obtain the similarity solution for the momentum equation. The solution proceeded for two classical cases such as Pr approaches infinity and Pr approaches zero. Pr number is the ratio of momentum transport property and thermal transport property of fluid in forced convection heat transfer [51]. For high Pr fluid, the thermal boundary layer thickness is smaller than viscous boundary layer thickness and vice versa. For $Pr \ll 1$, the viscous boundary layer can be ignored while calculating thermal boundary layer. Whereas for $Pr \geq 1$, within the thermal boundary layer region velocity depends on y. Liquid metals come under the family of $Pr \ll 1$ while oils are having $Pr \geq 1$. If the non-dimensional temperature at entry of slab fluid interface (-1/2, 0) is denoted as θ_0, then its value varies from 0 to 1. When $\theta_0 = 0$, heat is transferred to the flow at leading edge which is a singular point. This is valid for $Pr \geq 1$ and $Pr \ll 1$.

$Pr \geq 1$

Case I: For $\theta_0 > 0$ the suitable scalings are

$$\psi = Re^{-3/4}\Psi, \omega = Re^{3/4}\Omega, y = Re^{-3/4}Y \tag{3.7}$$

With this new scalings, equations (3.3a)-(3.3c) become

$$\frac{\partial^2 \Psi}{\partial Y^2} = -\Omega \tag{3.8a}$$

$$\frac{\partial \Psi}{\partial Y}\frac{\partial \Omega}{\partial X} - \frac{\partial \Psi}{\partial X}\frac{\partial \Omega}{\partial Y} = \frac{\partial^2 \Omega}{\partial Y^2} \tag{3.8b}$$

$$Pr\left(\frac{\partial \Psi}{\partial Y}\frac{\partial \theta_f}{\partial X} - \frac{\partial \Psi}{\partial X}\frac{\partial \theta_f}{\partial Y}\right) = \frac{\partial^2 \theta_f}{\partial Y^2} \tag{3.8c}$$

From equations (3.8a) and (3.8b), we eliminate Ω and integrate once with respect to Y to obtain

$$\frac{\partial \Psi}{\partial Y}\frac{\partial^2 \Psi}{\partial X \partial Y} - \frac{\partial \Psi}{\partial X}\frac{\partial^2 \Psi}{\partial Y^2} = \frac{\partial^3 \Psi}{\partial Y^3} \tag{3.9}$$

where $X = x + 1/2$. The boundary layer begins at $X = 0$. The boundary conditions relevant to the above equations are

$$\Psi = \frac{\partial \Psi}{\partial Y} = 0 \quad \text{on} \quad Y = 0 \quad X \geq 0 \tag{3.10a}$$

$$\theta_f = \theta_s \quad \text{on} \quad Y = 0 \quad 0 \leq X \leq 1 \tag{3.10b}$$

$$\frac{\partial \theta_f}{\partial Y} = \frac{1}{\sigma} \frac{\partial \theta_s}{\partial y} \quad \text{on} \quad Y = 0 \quad 0 \leq X \leq 1 \tag{3.10c}$$

where $\sigma = \frac{Re^{3/4}}{k}$ is a dimensionless parameter. Since uniform stream at ambient temperature is passing through the inlet slot, appropriate conditions at entry are

$$\frac{\partial \Psi}{\partial Y} = 1 \quad \text{at} \quad X = 0 \tag{3.11a}$$

$$\theta_f = 0 \quad \text{as} \quad X = 0 \tag{3.11b}$$

To evaluate the analytical solution, we transform the basic equations (3.9)-(3.11b) using similarity variable of Glauert [1]

$$\Psi = X^{1/4} F(X, \zeta), \quad \zeta = \frac{Y}{4X^{3/4}}, \; \theta_f(X, Y) = G(X, \zeta) \tag{3.12}$$

Equations (3.9) and (3.8c) are reduced to

$$F''' + 2F'^2 + FF'' = 4X \left(F' \frac{\partial F'}{\partial X} - F'' \frac{\partial F}{\partial X} \right) \tag{3.13a}$$

$$\frac{G''}{Pr} + FG' = 4X \left(F' \frac{\partial G}{\partial X} - G' \frac{\partial F}{\partial X} \right) \tag{3.13b}$$

where the prime denotes differentiation with respect to ζ. The boundary conditions in terms of F and G are,

$$F = F' = 0 \quad \text{on} \quad \zeta = 0 \tag{3.14a}$$

$$\theta_s = G \quad \text{on} \quad \zeta = 0 \tag{3.14b}$$

$$\frac{\partial \theta_s}{\partial y} = \frac{1}{4X^{3/4}}\sigma G' \quad \text{on} \quad \zeta = 0 \tag{3.14c}$$

$$F' \to 0, \quad G \to 0 \quad \text{as} \quad \zeta \to \infty \tag{3.14d}$$

Let $X \to 0$, and we arrive at the ordinary differential equations

$$F''' + 2F'^2 + FF'' = 0 \tag{3.15a}$$

$$\frac{G''}{Pr} + FG' = 0 \tag{3.15b}$$

subject to

$$F = F' = 0 \quad \text{on} \quad \zeta = 0 \tag{3.16a}$$

$$F' \to 0 \quad G \to 0 \quad \text{as} \quad \zeta \to \infty \tag{3.16b}$$

with the equation (3.14b) replaced as

$$G = \theta_0 \quad \text{on} \quad \zeta = 0 \tag{3.16c}$$

It is observed that the continuity of heat flux at interface at $X = 0$, further the canonical substitution $G = \theta_0 \hat{G}$ the equation (3.14c) becomes

$$\frac{\partial \theta_s}{\partial y} = \frac{1}{4X^{3/4}}\sigma\theta_0 \hat{G}'(0) \tag{3.17}$$

The heat flux has singularity at $X \to 0$. We remove it using plane polar coordinates (r, ϕ) as follows,

$$X = r\cos\phi \quad y = r\sin\phi$$

The boundary conditions (3.4d) and (3.17) become,

$$\frac{\partial \theta_s}{\partial \phi} = 0 \quad \text{on} \quad \phi = -\frac{\pi}{2} \tag{3.18a}$$

$$\frac{\partial \theta_s}{\partial \phi} = \frac{1}{4}\sigma\theta_0 \hat{G}'(0)\, r^{1/4} \quad \text{on} \quad \phi = 0 \tag{3.18b}$$

A harmonic function which satisfies these boundary condition is

$$\hat{\theta}_s(r, \phi) = A r^{1/4} sin\frac{\phi}{2} \tag{3.19}$$

where,

$$A = -\frac{1}{\sqrt{2}}\sigma\theta_0 \hat{G}'(0) \tag{3.20}$$

The singularity at $r = 0$ is removed by defining $\theta_s = \hat{\theta}_s + \theta_s^*$. So θ_s^* satisfies

$$\nabla^2 \theta_s^* = 0 \tag{3.21}$$

subject to

$$\theta_s^* = \theta_0 \hat{G} - \hat{\theta}_s \quad y = 0 \;\; 0 \le X \le 1 \tag{3.22a}$$

$$\frac{\partial \theta_s^*}{\partial y} = \frac{\sigma \theta_0 \hat{G}'}{4X^{3/4}} - \frac{\partial \hat{\theta}_s}{\partial y} \;\; \text{on} \;\; y = 0 \;\; 0 \le X \le 1 \tag{3.22b}$$

$$\frac{\partial \theta_s^*}{\partial X} = 0 \;\; \text{on} \;\; X = 0 \quad -\lambda \le y \le 0 \tag{3.22c}$$

$$\frac{\partial \theta_s^*}{\partial X} = -\frac{\partial \hat{\theta}_s}{\partial y} \;\; \text{on} \;\; X = 1 \quad -\lambda \le y \le 0 \tag{3.22d}$$

$$\theta_s^* = 1 - \hat{\theta}_s \;\; \text{on} \;\; y = -\lambda \;\; 0 \le X \le 1 \tag{3.22e}$$

Case II:

For the case $\theta_0 = 0$, the similarity variables have small changes as follows

$$\Psi = X^{1/4} F(X, \zeta), \quad \theta_f = X^{3/4} G(X, \zeta), \quad \zeta = \frac{Y}{4X^{3/4}} \tag{3.23}$$

The basic governing equations become

$$F''' + 2F'^2 + FF'' = 4X \left(F' \frac{\partial F'}{\partial X} - F'' \frac{\partial F}{\partial X} \right) \tag{3.24a}$$

$$\frac{G''}{Pr} + FG' - 3F'G = 4X \left(F' \frac{\partial G}{\partial X} - G' \frac{\partial F}{\partial X} \right) \tag{3.24b}$$

subject to the boundary conditions for $0 \le X \le 1$

$$F = F' = 0 \;\; \text{on} \;\; \zeta = 0 \tag{3.25a}$$

$$\theta_s = X^{3/4} G \;\; \text{on} \;\; \zeta = 0 \tag{3.25b}$$

$$\frac{\partial \theta_s}{\partial y} = \frac{\sigma G'}{4X^{3/4}} \quad \text{on} \quad \zeta = 0 \tag{3.25c}$$

$$F' \rightarrow 0, \quad G \rightarrow 0 \quad as \quad \zeta \rightarrow \infty \tag{3.25d}$$

Let $X \rightarrow 0$. Equations (3.24a) and (3.24b) become

$$F''' + FF'' + 2F'^2 = 0 \tag{3.26a}$$

$$\frac{G''}{Pr} + FG' - 3F'G = 0 \tag{3.26b}$$

subject to

$$F = F' = 0 \quad \text{on} \quad \zeta = 0 \tag{3.27a}$$

$$F' \rightarrow 0, \quad G \rightarrow 0 \quad \text{as} \quad \zeta \rightarrow \infty \tag{3.27b}$$

Equations (3.26a) and (3.26b) are same as the expressions given by Schwarz and Caswell [5]. An extra boundary condition is availed for being canonical forms $G = Q\hat{G}$ as solutions to above equations. The unknown constant Q can be found from the continuity of heat flux at $Y = 0$ from the solution of θ_s.

Now the boundary conditions are

$$\hat{G}'(0) = -1 \tag{3.28a}$$

$$\theta_s = X^{3/4} Q\hat{G} \quad \text{on} \quad y = 0 \quad 0 \leq X \leq 1 \tag{3.28b}$$

$$\frac{\partial \theta_s}{\partial y} = \frac{1}{4}\sigma \hat{G}' Q \quad \text{on} \quad y = -\lambda \quad 0 \leq X \leq 1 \tag{3.28c}$$

$$\theta_s = 1 \quad \text{on} \quad y = 0 \quad 0 \leq X \leq 1 \tag{3.28d}$$

$$\frac{\partial \theta_s}{\partial X} = 0 \quad \text{on} \quad X = 1, 0 \quad -\lambda \leq y \leq 0 \tag{3.28e}$$

Pr ≪ 1

For lower Prandtl number the thermal boundary layer thickness is higher than viscous boundary layer. According to this, change in scaling is done in y coordinate only and is given by,

$$y = Pr^{-1} Re^{-3/4} Y$$

The boundary layer equations for fluid field are now

$$\frac{\partial \Psi}{\partial Y}\frac{\partial^2 \Psi}{\partial Y \partial X} - \frac{\partial \Psi}{\partial X}\frac{\partial^2 \Psi}{\partial Y^2} = 0 \tag{3.29a}$$

$$\frac{\partial \Psi}{\partial Y}\frac{\partial \theta_f}{\partial X} - \frac{\partial \Psi}{\partial X}\frac{\partial \theta_f}{\partial Y} = \frac{\partial^2 \theta_f}{\partial Y^2} \tag{3.29b}$$

From the above, one obtains

$$\Psi \equiv Y \tag{3.30a}$$

$$\frac{\partial \theta_f}{\partial X} = \frac{\partial^2 \theta_f}{\partial Y^2} \tag{3.30b}$$

subject to

$$\theta_f = \theta_s \quad \text{on} \quad Y = 0 \quad 0 \leq X \leq 1 \tag{3.31a}$$

$$\frac{\partial \theta_s}{\partial y} = \sigma \frac{\partial \theta_f}{\partial Y} \quad \text{on} \quad Y = 0 \quad 0 \leq X \leq 1 \tag{3.31b}$$

$$\theta_f \to 0 \quad \text{as} \quad Y \to \infty \tag{3.31c}$$

$$\theta_f = 0 \quad \text{at} \quad X = 0 \tag{3.31d}$$

where $\sigma = \frac{Pr Re^{3/4}}{k}$. While considering $\theta_0 > 0$, the discontinuity exists when $\theta_0 > 0$ at $X = 0, Y = 0$, which is overcome by coordinate transformation as given below.

$$\eta = \frac{Y}{X^{1/2}}, \quad S = X^{1/2} \tag{3.32}$$

From equations (3.29b) and (3.30b),

$$\frac{\partial^2 \theta_f}{\partial \eta^2} = \frac{1}{2}\left(S\frac{\partial \theta_f}{\partial S} - \eta\frac{\partial \theta_f}{\partial \eta}\right) \tag{3.33}$$

subject to

$$\theta_s = \theta_f \quad \text{on} \quad \eta = 0 \quad 0 \leq S \leq 1 \tag{3.34a}$$

$$\frac{1}{\sigma}\frac{\partial \theta_s}{\partial y} = \frac{1}{S}\frac{\partial \theta_f}{\partial \eta} \quad \text{on} \quad \eta = 0 \quad 0 \leq S \leq 1 \tag{3.34b}$$

$$\theta_f \to 0 \quad \text{as} \quad \eta \to \infty \tag{3.34c}$$

Now equation (3.31d) is replaced by considering the limits of equations (3.33)-(3.34c) and let $S \to 0$, one obtains an ordinary differential equation

$$\frac{d^2\theta_f}{d\eta^2} + \frac{\eta}{2}\frac{d\theta_f}{d\eta} = 0 \tag{3.35}$$

subject to

$$\theta_f \to 0 \quad \text{as} \quad \eta \to \infty \tag{3.36a}$$

$$\theta_f = 0 \quad \text{on} \quad \eta = 0 \tag{3.36b}$$

which leads to solution

$$\theta_f = \theta_0 erfc\left(\frac{\eta}{2}\right) \tag{3.37}$$

The $erfc(X)$ denotes the complementary error function defined by $erfc(X) = \frac{2}{\sqrt{\pi}}\int_X^\infty e^{-s^2}\, ds$. Subsequently, one arrives at

$$\frac{\partial \theta_s}{\partial y} \sim \frac{\sigma\theta_0}{\sqrt{\pi X}} \quad \text{on} \quad y = 0 \quad \text{as} \quad X \to 0 \tag{3.38}$$

By analogy with equations (3.17) and (3.20), one should take

$$A = \frac{1}{\sqrt{2\pi}}\sigma\theta_0 \tag{3.39}$$

When $\theta_0 = 0$, there is no singularity at $X = 0, Y = 0$. Considering the solid slab, it is assumed that the axial conduction is negligible compared with normal direction and thus,

$$\frac{\partial^2 \theta_s}{\partial y^2} = 0 \tag{3.40}$$

After integrating, one obtains

$$\theta_s(X, y) = \frac{\theta_b(X) - 1}{\lambda} y + \theta_b(X) \tag{3.41}$$

which leads to equation (3.30b) subject to equations (3.31c) and (3.31d). The normal direction temperature gradients are balanced at interface, and

$$\frac{\partial \theta_f}{\partial Y} = \tau(\theta_f - 1) \tag{3.42}$$

where $\tau = k/\left(\lambda Pr Re^{3/4}\right)$

With reference to Carslaw and Jaeger [61], the solution for θ_f for $0 \leq X \leq 1$ can be written as

$$\theta_f(X, Y) = erfc\left(\frac{\eta}{2}\right) - e^{\left(\tau Y + \tau^2 X\right)} erfc\left(\frac{\eta}{2} + \tau\sqrt{X}\right) \tag{3.43}$$

Setting $Y = 0$, the interface temperature is given by,

$$\theta_b = 1 - e^{\tau^2 X} erfc\left(\tau\sqrt{X}\right) \tag{3.44}$$

3.2.1 Quasi-two-dimensional analogue:

To find out the temperature distribution in solid wall, the boundary condition at interface is needed. So the average conjugate boundary temperature and the average Nusselt number are evaluated. The average conjugate boundary temperature, $\bar{\theta}_b$ is defined as

$$\bar{\theta}_b = \int_0^1 \theta_b\left(X,0\right)\ dX \tag{3.45}$$

Averaging (3.41) over $0 \leq X \leq 1$ gives

$$\theta_s\left(y\right) = \frac{\bar{\theta}_b - 1}{\lambda} y + \bar{\theta}_b \tag{3.46}$$

Integrating equation (3.14c) over $0 \leq X \leq 1$ and using equation (3.46), one obtains

$$\frac{k}{\lambda}\left(\bar{\theta}_b - 1\right) = Re^{3/4}\bar{\theta}_b\hat{G}'\left(0\right) \tag{3.47}$$

where $\hat{G}'\left(0\right)$ depends on Pr only. For large value of Pr, $\hat{G}'\left(0\right)$ are evaluated using *Simpson's one–third rule* numerical integration and approximated value arrived at by least square method as given below.

$$G'\left(0\right) = 0.3236Pr^{1/3} \tag{3.48}$$

Rearranging equation (3.47)

$$\bar{\theta}_b = \frac{1}{1+\mu} \tag{3.49}$$

where

$$\mu = \frac{\lambda}{k}\frac{Pr^{1/3}Re^{3/4}}{3.09} \tag{3.50}$$

From (3.4c) and averaging (3.41) over $0 \leq X \leq 1$, the average Nusselt number is given by

$$\overline{Nu} = \frac{k}{\lambda}\frac{\mu}{(1+\mu)} \tag{3.51}$$

The case for $Pr \ll 1$ proceeds in a similar way except in place of equation (3.47), the expression is given by

$$\frac{k\left(\bar{\theta}_b - 1\right)}{\lambda} = \frac{2}{\sqrt{\pi}} Pr Re^{3/4} \bar{\theta}_b \tag{3.52}$$

$\bar{\theta}_b$ and $\overline{Nu}$ are same as above except in place of equation (3.50), μ is given by

$$\mu = \frac{2}{\sqrt{\pi}} \frac{\lambda Pr Re^{3/4}}{k} \tag{3.53}$$

Since the temperature at interface is non-uniform and the temperature profiles are self-preserving

$$\theta_b(x) = \chi\left(x + \frac{1}{2}\right)^{\gamma} \quad \frac{-1}{2} \leq x \leq \frac{1}{2} \tag{3.54}$$

The value of $'\gamma'$ is obtained from Schwarz and Caswell [5] and $'\chi'$ is constant flux given by

$$\chi \int_{-1/2}^{1/2} \left(x + \frac{1}{2}\right)^{\gamma} dx = \bar{\theta}_b \tag{3.55}$$

With known $\bar{\theta}_b$ and χ, $\theta_b(X)$ can be found. Now the Dirchlet problem for

θ_s subject to equations (3.4d), (3.4e) and

$$\theta_s = \theta_b\left(x\right) \quad \text{on} \quad y = 0 \quad \frac{-1}{2} \leq x \leq \frac{1}{2} \tag{3.56}$$

gives a series form of solution (Vynnycky et al. [45])

$$\theta_s\left(x, y\right) = \frac{-y}{\lambda} + 2\left(\gamma + 1\right)\bar{\theta}_b \sum_{n=1}^{\infty} I_n \frac{\sinh n\pi(y+\lambda)}{\sinh n\pi\lambda} \cos n\pi(x + \frac{1}{2}) \tag{3.57}$$

where, $I_n = \int_0^1 x^\gamma \cos n\pi x dx$

The heat flux at the conjugate boundary is then

$$\left(\frac{\partial \theta_s}{\partial y}\right)_{y=0} = \frac{-1}{\lambda} + 2\left(\gamma + 1\right)\bar{\theta}_b \pi \sum_{n=1}^{\infty} I_n \coth n\pi\lambda \cos n\pi(x + \frac{1}{2}) \tag{3.58}$$

3.3 Numerical Solution

The governing equations for two-dimensional laminar incompressible plane wall jet flow are in non-dimensional form Eq. 2.8 and Eq. 2.9 are solved. Further Eq. 2.10 and Eq. 2.24 are solved simultaneously subject to Eq. 2.25. The energy equation in fluid regime and solid regime are solved simultaneously. The slab energy equation is written in transient non-dimensionalised form. The point to note here is that the second term (Eq. 2.24) contains Re and Pr. They appear because of the type of non-dimensionalisation. Similar form of equation has been given by Chiu et al.[46].

The unsteady vorticity transport equation 2.9 in time is solved by Alternate Direction Implicit scheme(ADI). Constant time step 0.001 is used for the entire calculation. Here the convergence is set as sum of error is less than the convergence criteria ε, or a large total time is elapsed. The convergence criteria is set for Eq. 2.9 as $\varepsilon < 10^{-4}$, for Eq. 2.10 as $\varepsilon < 10^{-4}$ and for Eq. 2.24 as $\varepsilon < 10^{-6}$.

The inlet slot height $h = 0.5$ is assumed. At the bottom wall and the left side wall, constant stream lines are assumed based on inlet flow. At the outlet in the downstream direction, stream-wise gradients are assumed to be zero. At the entrainment boundary, normal velocity gradient is zero [58]. The detailed boundary conditions are given (Fig. 3.1(b)).

$$\text{at AE}, u(y) = 12y - 24y^2; \quad \psi(y) = 6y^2 - 8y^3; \quad \omega(y) = 48y - 12; \tag{3.59a}$$

$$\text{along ED}, \quad u = v = 0; \quad \psi = 0.50; \quad \omega = -\frac{2\psi_w - 2\psi_{w+1}}{\Delta x^2} \tag{3.59b}$$

$$\text{along AB}, \quad u = v = 0; \quad \psi = 0; \quad \omega = -\frac{2\psi_{w+1}}{\Delta y^2} \tag{3.59c}$$

$$\text{along BC}, \quad \frac{\partial u}{\partial x} = 0; \frac{\partial v}{\partial x} = 0 \tag{3.59d}$$

$$\frac{\partial^2 \psi}{\partial x^2} = 0; \quad \frac{\partial \omega}{\partial x} = 0 \tag{3.59e}$$

$$\text{along CD}, \quad \frac{\partial u}{\partial y} = 0 \tag{3.59f}$$

$$\text{along AF}, \text{BG}, \quad \frac{\partial \theta_s}{\partial x} = 0 \tag{3.59g}$$

$$\text{along FG}, \quad \theta_s = 1 \tag{3.59h}$$

$$\text{along CD}, \quad \theta_f = 0 \tag{3.59i}$$

$$\text{along DE, BC}, \quad \frac{\partial \theta_f}{\partial x} = 0 \tag{3.59j}$$

3.4 Validation of the Numerical Procedure

To validate the numerical procedure the plane wall jet flow is solved as non-conjugate case. The results are compared with similarity solution and experimental results [15] and found good agreement among them. The details are presented in Appendix C.

3.5 Grid Independence Study

The computational domain used has a size of 40 times the slot height in downstream direction and 20 times slot height in normal direction. To ensure that the parabolic inlet velocity profile falls exactly on the slot height, uniform grid points are used near the wall up to the slot height and beyond slot height clustered grids are used. The computational domain considered here are clustered cartesian grids. In Eq. 2.11 $\kappa = 0.7$ and $\vartheta = \pi$ is used for generating the grid points. A series of grid independence study has been done to find the optimum grid points in both directions. In x - direction the following grid systems are considered $75 \times 49, 101 \times 49, 125 \times 49$ and found that the average Nu variation is less than 1 % between the 101×49 and 125×49 grid points. Further in y-direction $101 \times 43, 101 \times 49, 101 \times 59, 101 \times 67, 101 \times 77$ and 101×101 grid systems are tested (Fig. 3.2). It is concluded that the grid refinement level 5

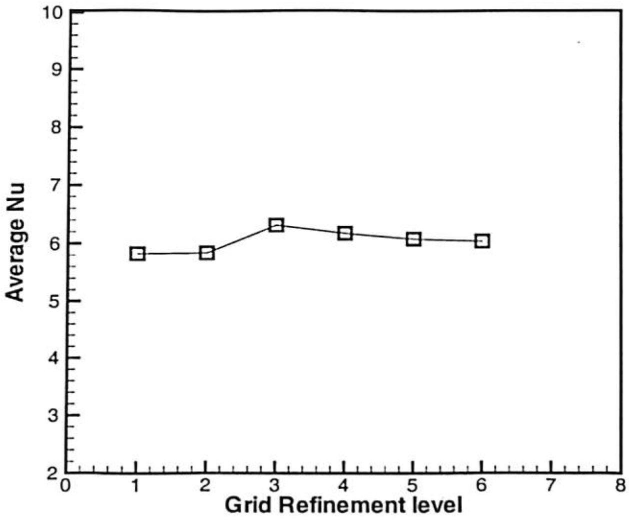

Figure 3.2: Grid independence for y-direction grids: $Re = 500, Pr = 1.4$

(101×77) will be used for the entire calculations. In the downstream direction the clustering function used for slab is same as that of the fluid regime whereas uniform grids are used in the y-direction for both cases $\lambda = 0.25$ and $\lambda = 1$. Typical computational grids are shown in Fig. 3.3(a)-3.3(c).

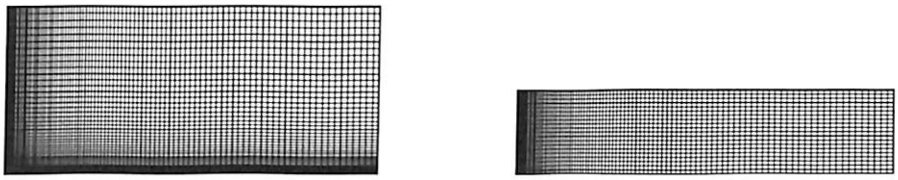

(a) Grids in the fluid regime (101x77, $\kappa = 0.7$)

(b) Grids in the slab regime (101x21, $\lambda = 0.25$)

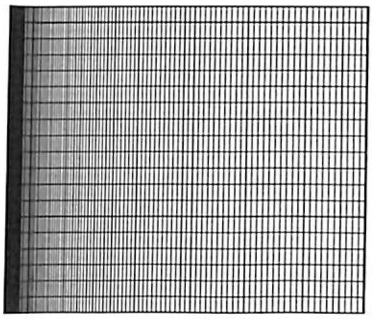

(c) Grids in the slab regime (101x21, $\lambda = 1.0$)

Figure 3.3: Computational domain

3.6 Results and Discussion

The present study is focused on finding a closed form relation for forced convection laminar plane wall jet as conjugate case and comparing the analytical results with numerical results. Four non-dimensional parameters (Re, Pr, λ, k) are considered for analysis. Higher complementary error function and exponential function values are evaluated using *Maple* 7.00 software [62]. For $Pr \ll 1$, it is approximated as $Pr = 0.01$ and for $Pr \geq 1$ it is approximated as $Pr = 100$. Results are evaluated for aspect ratios, $\lambda = 0.25$ and $\lambda = 1$, whereas thermal conductivity ratios are taken as $k = 1, 2, 5$ and 20 following Vynnycky et al. [45]. The maximum Re considered here for the study is 700, after which transition is expected [20].

For Figs. 3.5-3.6, different symbols are used to represent Nu and θ_b obtained by analytical results and different line patterns are used to represent the numerical results. For Fig. 3.7, the style is reversed.

The slab temperature contours are shown in Figs. (3.4(a)-3.4(h)). Results are presented for Re (= 500) case. Low Pr (= 0.01) and high Pr (= 100) cases are considered with $k = 1$ and $k = 20$. For $Pr = 0.01$ and $k = 1$ (Fig. 3.4(a)), more temperature drop occurs near the inlet, than in the downstream locations. The nature of the isotherms shows that there are heat fluxes in the negative longitudinal and transverse directions near the inlet. However, there is no longitudinal variation of temperature in the downstream location signifying that only transverse variation exists. With the increases in conductivity ratio k, heat transfer increases across the slab and the gradient in normal direction is larger than axial direction (Fig. 3.4(b)), which agrees with our assumption about the conductivity of the slab. It is worthwhile to remember that if k is larger, it behaves like an isothermal slab. At high Pr, a thin thermal boundary layer develops over the interface. Most of the temperature drop occurs across the solid for both the cases. That is why the isotherm in the slab near the interface (Figs. 3.4(c) and 3.4(d)) has a smaller value compared to Figs. 3.4(a) and 3.4(b). At high Pr, the contours are less variant in the downstream direction. In other words, the temperature gradient in the longitudinal direction is much smaller than that in the transverse direction. The slab is behaving like one-dimensional heat conduction in y-direction. The isotherm plots for aspect ratio $\lambda = 1$ are shown in Figs. 3.4(e)-3.4(h). For low Pr case (Figs. 3.4(e), 3.4(f)), the two-dimensionality nature of the isotherms are observed. However, in the high Pr case (Figs. 3.4(g), 3.4(h)), this nature is almost absent except a small region in the top-left corner.

The variations of the local Nu are shown in Figs. (3.5(a)-3.5(f)) for the parameters $Re = 500$, $Pr = 0.01, 100$, $\lambda = 0.25, 1.0$ and for a range of k values lying between, and including, those used for Fig. 3.4. The numerically computed values are given for these ranges whereas the semi-analytic results are plotted for those cases where the computations are possible. At leading edge, due to large thermal gradient, Nu is greater than the rest of the length. Entrainment also causes this large gradient. The Nu comparison showed good agreement between the two methods, Figs. (3.5(a) - 3.5(d)). Since the viscous boundary layers are dominant for high Pr fluid, the heat transfer is nearly one-dimensional (Fig. 3.4(c),3.4(d),3.4(g) and 3.4(h)) and Nu (numerical) is constant except near the leading edge. The approximation of constant-flux is expected to provide a reasonable result for $Pr \geq 1$ provided $k < 2$ (Vynnycky et al. [45]). However, as shown in Fig. (3.5(e)-3.5(f)), there are some discrepancies which need further investigation.

Figs. 3.6(a)-3.6(d) show the non-dimensional conjugate boundary temperature for different parameters. The values considered are: $Re = 500, Pr = 0.01$ and 100, $\lambda = 0.25$ and 1.0, $k = 1, 2, 5$ and 20. For $Pr \ll 1$, θ_b is evaluated analytically from equation (3.44) which is a closed-form relation. The analytical results are found to be in very good agreement with the numerical results (Figs. 3.6(a) and 3.6(b)). There is some discrepancy between the analytical and computed profiles near the leading edge. It has been observed that near the inlet, the computed velocity profile differ from the similarity velocity profile due to the entrainment effect. So the discrepancy for θ_b profiles may be attributed to the above reason and the assumptions in employing the boundary conditions (Eqns. 3.11a and 3.11b) for the starting of the boundary layer (Vynnycky et al. [45]). For high Pr fluid (Figs. 3.6(c) and 3.6(d)), θ_b is linearly varying at leading edge. In this case, thermal boundary layer thickness is smaller than viscous boundary layer. The predicted value is closer to the numerical value at the downstream locations whereas there is some discrepancy near the leading edge. θ_b, which is related to θ_s by the uniqueness property of the Dirichlet problem, is calculated by the constant-flux approximation (Eq. 3.54). The discrepancy at leading edge may be due to the presence of two-dimensionality of heat flux as shown by the isotherms (Figs. 3.4(c),3.4(d),3.4(g),3.4(h)).

Finally average Nusselt number dependency with Re and the comparisons with the predicted results have been presented in (Figs. 3.7(a)-3.7(d)). Average Nusselt number is expressed in terms of μ as given in equation (3.51). For low Pr (=0.01), there is a good agreement between the analytical and computed results (Figs. 3.7(a)-3.7(b)) except at k=20, Pr=0.01, λ=1.0 (Fig. 3.7(b)). It is found that higher aspect ratio reduces average $\overline{Nu}$. Boundary layer region becomes thinner at a higher Re. As expected, higher Re leads to higher $\overline{Nu}$ for the same λ and k values. The difference in local Nu as discussed earlier is reflected in the average Nusselt number for high Pr. The analytical results are not matching with the numerical results for $k > 1$ which needs further investigation.

(a) $Re = 500, Pr = 0.01, k = 1, \lambda = 0.25$ (b) $Re = 500, Pr = 0.01, k = 20, \lambda = 0.25$

(c) $Re = 500, Pr = 100.0, k = 1, \lambda = 0.25$ (d) $Re = 500, Pr = 100.0, k = 20, \lambda = 0.25$

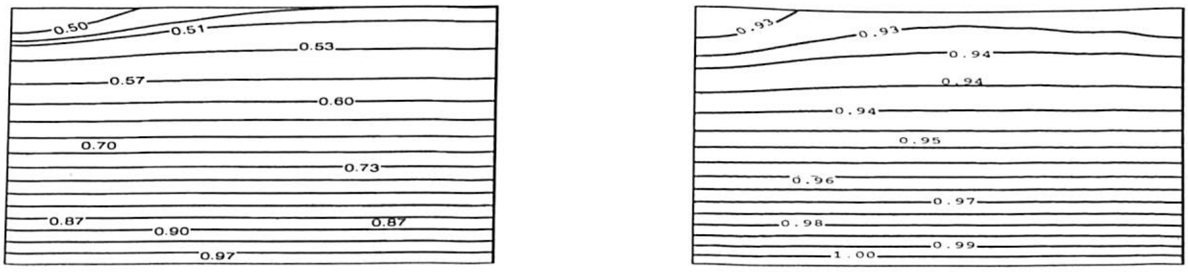

(e) $Re = 500, Pr = 0.01, k = 1, \lambda = 1.0$ (f) $Re = 500, Pr = 0.01, k = 20, \lambda = 1.0$

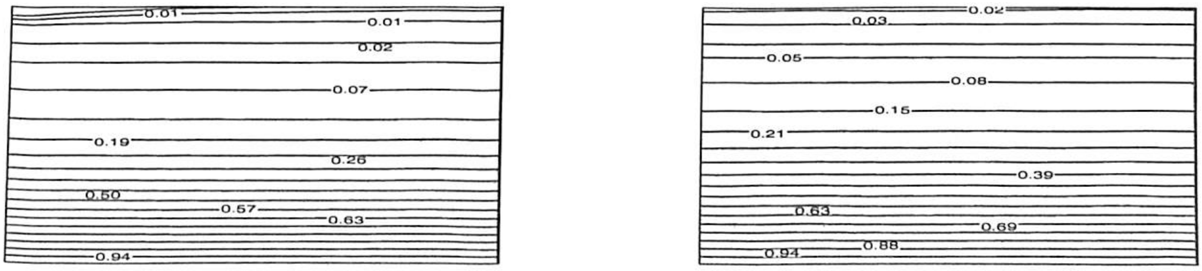

(g) $Re = 500, Pr = 100.0, k = 1, \lambda = 1.0$ (h) $Re = 500, Pr = 100.0, k = 20, \lambda = 1.0$

Figure 3.4: Isotherm patterns within the solid slab for various parameters by numerical simulations

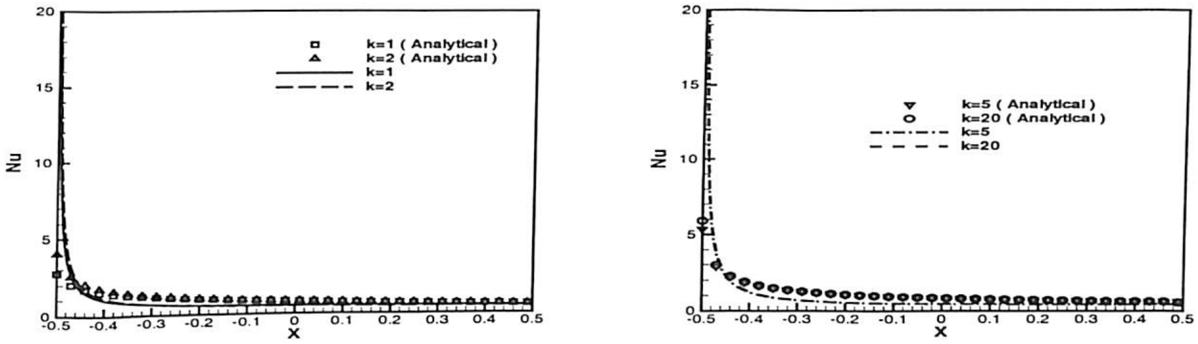

(a) $Re = 500, Pr = 0.01, \lambda = 0.25$ (b) $Re = 500, Pr = 0.01, \lambda = 0.25$

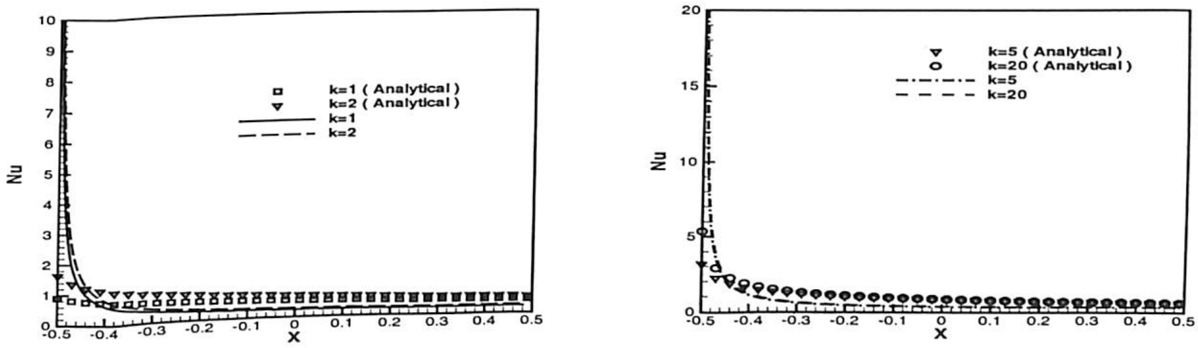

(c) $Re = 500, Pr = 0.01, \lambda = 1.0$ (d) $Re = 500, Pr = 0.01, \lambda = 1.0$

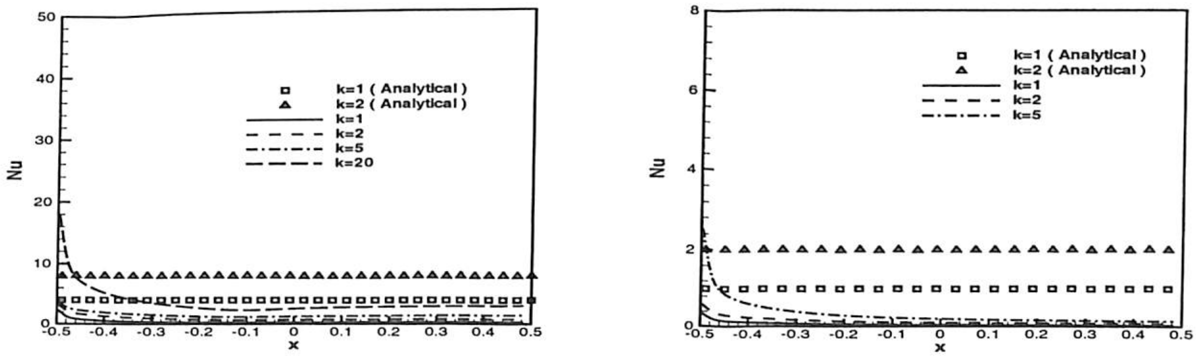

(e) $Re = 500, Pr = 100.0, \lambda = 0.25$ (f) $Re = 500, Pr = 100.0, \lambda = 1.0$

Figure 3.5: Local Nusselt number (Nu) for different parameters

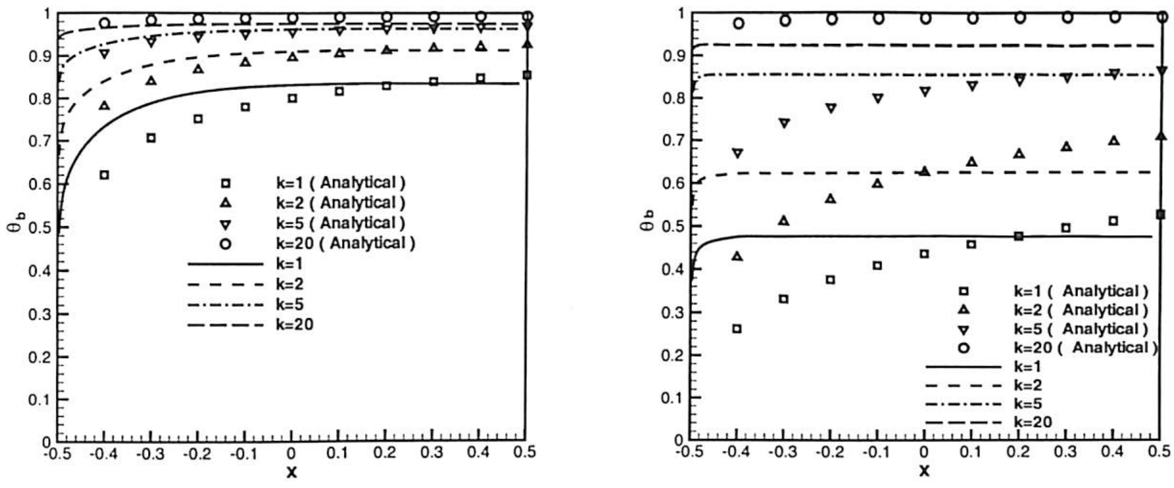

(a) $Re = 500, Pr = 0.01, \lambda = 0.25$ (b) $Re = 500, Pr = 0.01, \lambda = 1.0$

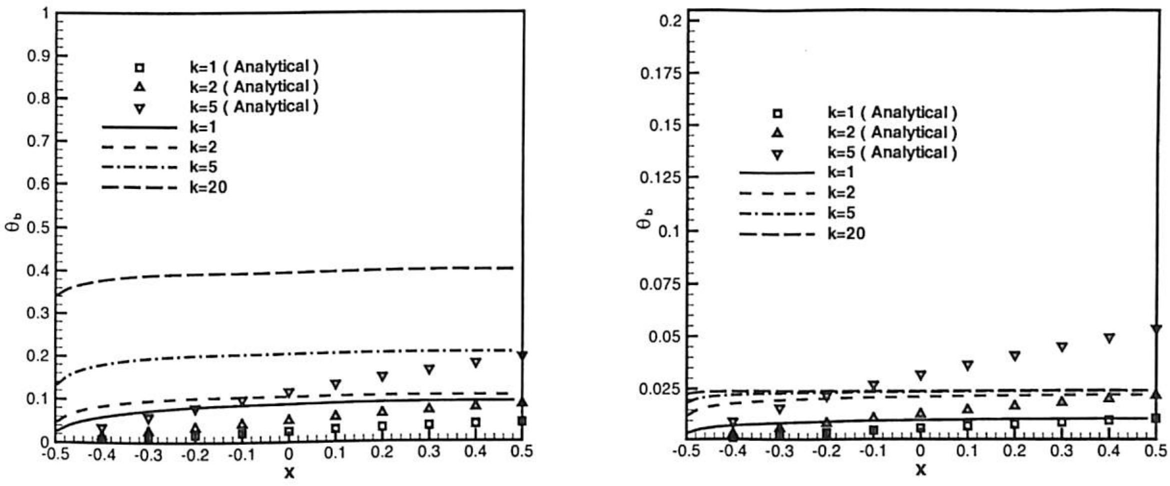

(c) $Re = 500, Pr = 100.0, \lambda = 0.25$ (d) $Re = 500, Pr = 100.0, \lambda = 1.0$

Figure 3.6: Conjugate interface temperature (θ_b) for various parameters

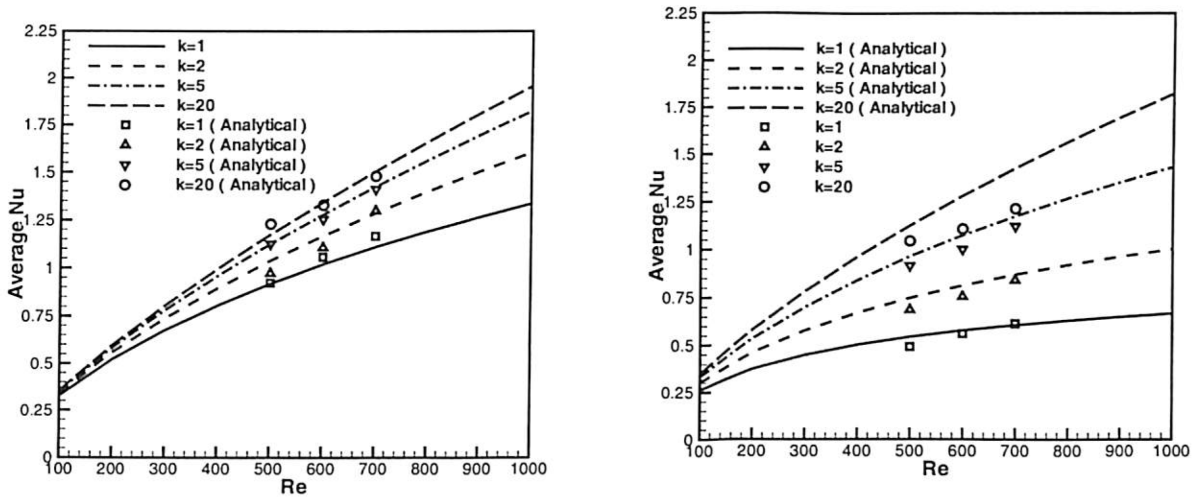

(a) $Pr = 0.01, \lambda = 0.25$ (b) $Pr = 0.01, \lambda = 1.0$

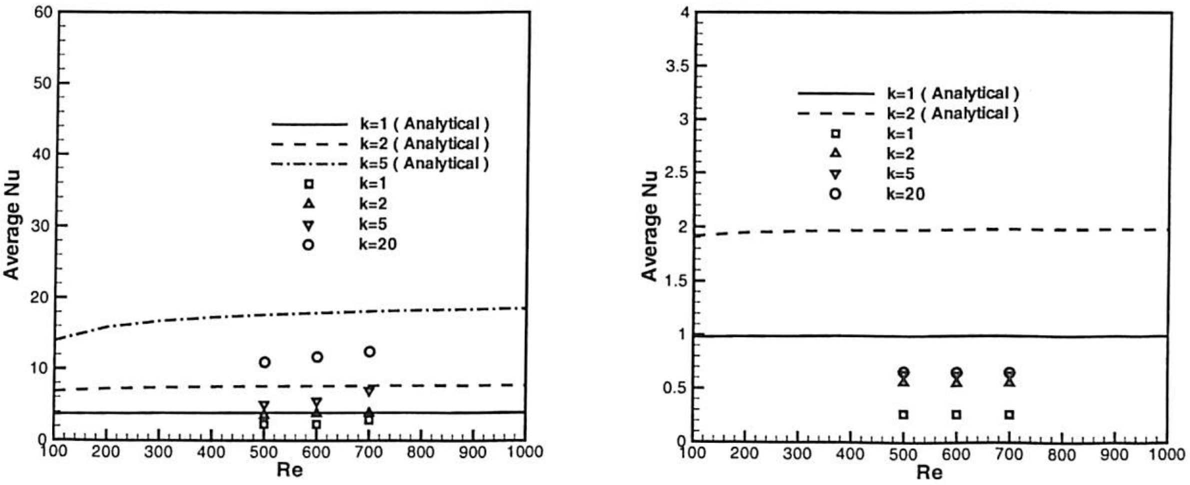

(c) $Pr = 100.0, \lambda = 0.25$ (d) $Pr = 100.0, \lambda = 1.0$

Figure 3.7: Average Nusselt number for various parameters ($\overline{Nu}$)

3.7 Conclusions:

In the present work, two-dimensional laminar incompressible plane wall jet heat transfer problem has been solved analytically as well as numerically for conjugate case. Four non-dimensional parameters (Re, Pr, k, λ) are considered for analysis. Closed-form solutions have been found for local Nusselt number, conjugate boundary interface temperature and average Nusselt number. For $Pr \ll 1$, heat flow depends on $(Re^{\frac{3}{4}} Pr/k,\ \lambda)$ while for $Pr \geq 1$, the relevant parameter set is $(Re^{\frac{3}{4}} Pr^{\frac{1}{3}}/k,\ \lambda)$. $\overline{\theta}_b$ can be reduced, via equation (3.49), to a function of just one parameter. The governing momentum and energy equations have been solved by stream function-vorticity method treating the problem as unsteady and for a wide range of the above non-dimensional parameters. Detailed results have been reported for two cases such as $Pr \ll 1$ and $Pr \geq 1$. Average Nusselt number relation is found in a simple form. Singularity exists at leading edge of the conducting wall. Good agreement is found for low Pr model between the two methods. It can be said that the analytical model performs well for low Pr fluid. For high Pr fluid. analytical solution of Nusselt number relation is giving reasonable results for $k \leq 2$ and this needs further investigation.

Acknowledgements

The present results are published in *International Journal of Heat and Mass Transfer*. The helpful comments of the reviewers of the journal are sincerely acknowledged.

Chapter 4

Simulation of Incompressible Offset Jet Flows

4.1 Introduction

In the present work, the flow features and entrainment characteristics of offset jets are investigated. Analytical solutions of the wall jet are available, based on the self similarity solution of the velocity field by Glauert [1] and Schlichting and Gersten [51]. However, these solutions are valid only far away from the jet inlet, and in most applications, the near-field development holds the key to important features of the jet flow. Therefore, the near-field development of a wall jet has been the subject of a lot of research in recent years.

The mean velocity profile in the longitudinal and transverse directions and the similarity nature are experimentally observed by Chandrasekhara Swamy and Bandyopadhyay [63] for a three-dimensional (3D) wall jet. The wall jet was generated by tangential flow of air from one-half of a round nozzle on to a smooth flat plate in a stagnant surrounding. Though the work was carried out for a 3D case, the observations presented are relevant to the present work. Cohen et al. [14] did work on the transition of wall jets subjected to blowing and suction. The purpose was to find out the effect of suction and blowing as the alternative controlling method for 2D incompressible wall jet instead of heating and cooling process. Amitay and Cohen [13] have reported the effects of wall blowing and suction on the stability characteristics of a laminar incompressible two-dimensional plane wall jet. They have reported that blowing and suction has the opposite effect on the viscous and inviscid instability modes. Quintana et al. [15] experimentally investigated the mean and fluctuating characteristics of a plane unsteady laminar wall jet for constant wall temperature. Seidel [18] has done numerical work to find out the effect of high amplitude forcing on laminar and turbulent wall jet over a heated flat plate. Seidel has used DNS for laminar case and RANS for turbulent wall jet. Recently, Bhattacharjee and Loth [20] simulated laminar and transitional cold wall jets. They have investigated the significance of three different inlet profiles viz. parabolic, uniform and ramp and presented the detailed results of time-averaged wall jet thickness and temperature distribution. They used RANS approach for higher Reynolds number and DNS approach for three-dimensional wall jet.

The stability of 2D free jets was studied experimentally by Sato [21] and Sato and Sakao [22]. Theoretical analysis for axisymmetric free jets was carried out by Batchelor and Gill [23] and Cohen and Wygnanski [24]. Sarma et al. [25] have studied 2D incompressible jet development inside a duct in the laminar flow regime for cases with and without entrainment of ambient fluid. While solving for a three-dimensional backward-facing step flow problem, Biswas et al. [38] have observed and reported about the evolution of wall jet-like structure in the streamwise and spanwise direction. The self-similarity profile for the streamwise velocity (u) is observed in a plane at a distance of 1.08 away from the sidewall arising due to the sudden expansion near the step. For the spanwise velocity (w), it is at x=6 and 8 which is the culmination of the generation of the w velocity component from the side wall.

Although many studies have been conducted on wall jet, the available literature on theoretical simulation of plane laminar offset jet flows are somewhat limited. The case of an entraining jet located near the jet discharge, which occur in several practical applications, has not been studied. In the present study, a time marching incompressible flow solver has been applied for simulating the flow features of offset jets for a range of aspect ratios and Reynolds number.

4.2 Mathematical Formulation

An incompressible two-dimensional laminar offset jet is considered. For the sake of simplicity, the jet is assumed to be isothermal and having the same density as the ambient fluid. Also, the velocity profile at the jet inlet is taken as parabolic. The governing equations are in non-dimensional form Eq. 2.8 and Eq. 2.9 are solved.

The unsteady vorticity transport equation (2.9) in time is solved by Alternate Direction Implicit scheme(ADI). The details of ADI is presented in Chapter 2.

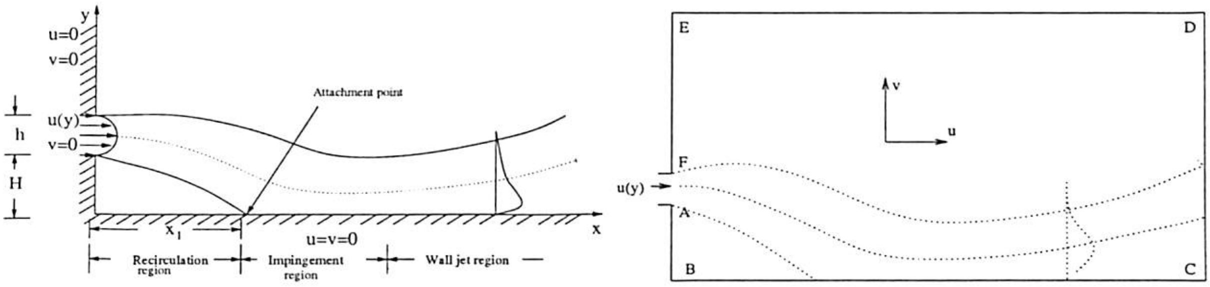

(a) schematic of the problem

(b) Computational domain

Figure 4.1: Schematic diagram and boundary conditions in an offset jet problem

The boundary conditions needed for the numerical simulation have been prescribed. For an offset jet with entrainment, the following dimensionless conditions have been enforced as shown in Fig. 4.1(b). The inlet slot height is assumed as, $h = 0.05$.

At the jet inlet, along AF (Fig. 4.1(b)),

$$u(y) = 120y - 2400y^2; \;\; \omega(y) = 4800y - 120; \; \psi(y) = 60y^2 - 800y^3 \quad (4.1a)$$

Along FE, BA and BC due to no-slip condition,

$$u = v = 0 \qquad (4.1b)$$

Along ED,

$$\frac{\partial u}{\partial y} = 0 \text{ and } \frac{\partial v}{\partial y} = 0 \tag{4.1c}$$

At downstream boundary the condition of zero first-derivative has been applied for velocity components. This condition implies that the flow has reached a developed condition. Thus, at (CD),

$$\frac{\partial u}{\partial x} = \frac{\partial v}{\partial x} = 0 \tag{4.1d}$$

Similar type of boundary conditions have been used by Gu [31] and Al-Sanea [64], [65]. For comparison and validation with available experimental and numerical work, two cases namely, plane wall jet and plane sudden-expansion flow problems have been solved. In the second case, all the walls except the inlet and the outlet are solid. Thus there is no entrainment from the atmosphere and the boundary conditions are no-slip for these surfaces.

At the bottom wall and the left side wall, constant stream lines are assumed based on inlet flow. At the outlet in the downstream direction, stream-wise gradients are assumed to be zero. At the entrainment boundary, normal velocity gradient is zero [58].

The detailed boundary conditions are,

along FE (Fig. 4.1(b)),

$$\omega(y) = \frac{2(\psi_w - \psi_{w+1})}{\triangle x_1 * \triangle x_1}; \ \psi = 0.05 \tag{4.2a}$$

along BA,

$$\omega(y) = \frac{2(0-\psi_{w+1})}{\triangle x_1 * \triangle x_1};\ \psi = 0 \tag{4.2b}$$

along BC,

$$\omega(x) = \frac{2(0-\psi_{w+1})}{\triangle y_1 * \triangle y_1};\ \psi = 0 \tag{4.2c}$$

along ED,

$$\frac{\partial^2 \psi}{\partial x \partial y} = 0 \tag{4.2d}$$

$$\psi_{i,j} = \psi_{i-1,j} + \psi_{i,j-1} - \psi_{i-1,j-1} \tag{4.2e}$$

$$u_{i,j} = u_{i,j-1} \tag{4.2f}$$

$$v_{i,j} = v_{i,j-1} \tag{4.2g}$$

$$\omega_{i,j} = \frac{(v_{i+1,j} - v_{i-1,j})}{(\Delta x_i + \Delta x_{i-1})} \tag{4.2h}$$

Along CD,

$$\psi_{i,j} = \psi_{i-1,j} + \psi_{i,j-1} - \psi_{i-1,j-1} \tag{4.2i}$$

$$\omega_{i,j} = \omega_{i-1,j} \tag{4.2j}$$

$$u_{i,j} = u_{i-1,j} \tag{4.2k}$$

$$v_{i,j} = v_{i-1,j} \tag{4.2l}$$

Equation 4.2d is also followed by Rao et al. [47] for entrainment boundary.

For *Re*=200, a time step of 0.0001 is used. The results obtained for lower

Re steady-state solution have been used as initial guess value for high *Re* flow for stream function and vorticity. Thus a higher time step of 0.001 is used for *Re* >200. This is based on the procedure given by Comini et al. [57]. The convergence criteria is set as sum of vorticity error in Eq. 2.22 is reduced to either $\varepsilon < 10^{-4}$ or large total time.

4.3 Validation of the Numerical Procedure

To validate the numerical procedure for solving offset jet flow problem, backward-facing step flow and sudden expansion flow problems are solved. The backward-facing step flow problem is solved for different Reynolds number and primary vortex reattachment length is compared with Armaly et al. [33], Barton [35] and Bhattacharjee and Loth [20]. The results are presented in Appendix B. The downstream location u velocity profiles are compared with [34]. It is found that the agreement is good with the benchmark results. Sudden expansion flow is simulated for Durst et al. [28] geometry (Appendix D). The downstream u velocity profiles are compared with their results for $Re = 70$ and $Re = 610$. Discrepancy is found between the present simulation with their results in few locations for $Re = 610$. This may be attributed due to the round off error/discretization error as discussed by Sarma et al. [25].

4.4 Grid Independent Study

The domain has been chosen as 30×h in stream wise direction and 20×h in normal direction. The computational domain considered here are clustered cartesian grids. In Eq.2.11 $\kappa = 0.7$ and $\theta = \pi$ is used for generating the grid points. Systematic grid refinement study is carried with 39×31, 51×41, 61×61, 71×61, 81×81 and 101×101 (Fig. 4.2(a)). Grid refinement level 5 is used for the entire computations. The grids are clustered in stream wise direction whereas in normal direction up to $3\times h$ height, grids are arranged uniformly and above this region, they are clustered. Typical grids are shown in Fig. 4.2(b).

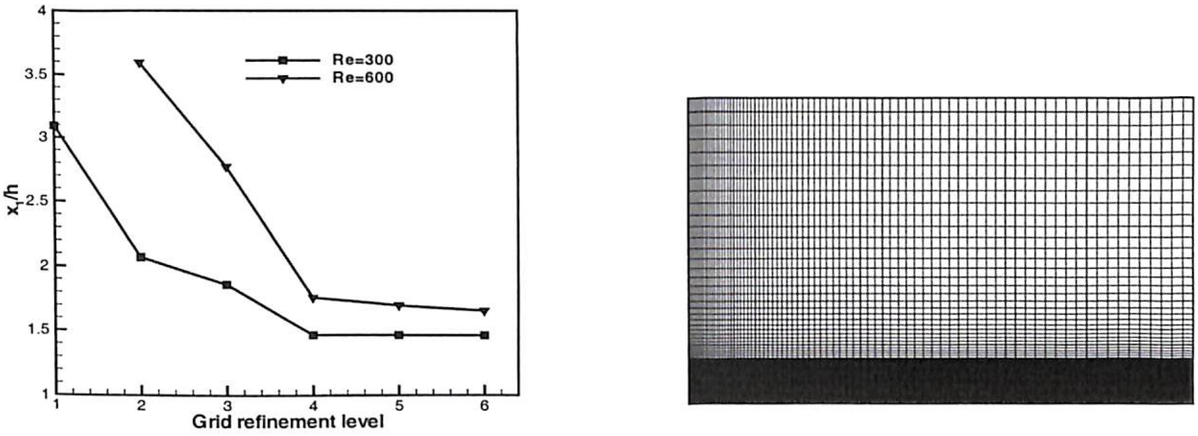

(a) Different grid systems

(b) Clustered grids

Figure 4.2: Grid independence study: OR=1.0

4.5 Results and Discussion

Flow separates at the corner and reattaches at the bottom of the wall due to Coanda effect. This length is called the reattachment length (x_1, Fig. 4.1(a)). The entire region can be sub-divided into three sub-regions as recirculation region, impingement region and wall jet region. To understand the flow physics two parameters considered here are Re ($Re = \overline{U}h/\nu$) and offset ratio (OR). Offset ratio is defined as the ratio of step height (H) to inlet slot height (h). Results are presented here for three OR viz. $OR = 0.5$, $OR = 1.0$, $OR = 1.5$ which Re is varied from 200 to 600 in steps of 50. Since the clustered grids are used for the computations, *Tecplot* 9.0 [66] is used for extracting the values for particular location.

In the problem of a nonbuoyant offset jet, a slot jet is discharged parallel to a solid wall. After leaving the nozzle, the jet curves towards the boundary and attaches to it, enclosing an eddying region of separated flows as shown in Fig. 4.1(a). This phenomenon, known as the Coanda effect, is caused by the reduction of pressure on the inner side of the jet due to entrainment of fluid by the jet. Flow fields, velocity profiles, jet trajectories and attachment length (cavity length) are investigated through detailed velocity measurements. Presented in Fig. 4.3 are numerically simulated velocity vectors representing the flow fields of an offset jet at various time levels for an offset ratio of 1.0 and Reynolds number 600. It can be seen that the initial action of the offset jet that enters the stationary ambient fluid is similar to that of a free jet, entraining fluid from the ambient and forming pair of vortices on two sides of the jet at $t = 350$ (Fig. 4.3(a)). A recirculation contained by the lower portion of the jet, the bottom, and the vertical wall is established by the entraining effect of the jet. Evidence of a secondary recirculation in the lower region at this stage is also shown in Fig. 4.3(b) at a time $t = 750$. The jet is deflected towards the bottom boundary to which the jet is closer due to the Coanda effect at a larger time ($t = 10000$, Fig. 4.3(c) and at $t = 20000$, Fig. 4.3(d)). The flow (attachment and recirculation) achieves its steady state at $t = 30000$. The secondary recirculation near the bottom boundary is pushed downstream and disappears after the flow becomes stable (Fig. 4.3(e)).

During the process of flow establishment, the entrainment of ambient fluid is reduced along the inner edge due to a finite volume of fluid and enhanced along the outer edge of the jet, eventually causing attachment of the jet to the boundary. The surrounding fluid above the jet being entrained into the jet is replenished by ambient fluid in the farther field. A recirculation contained by the upper part of the jet, the top boundary, and the vertical wall is formed as shown in Fig. 4.3(a). This upper vortex, which is initially ($t = 350$) above the jet and symmetric to the lower one about the jet centerline, moves downstream and stretches in the horizontal direction during the flow attachment and stabilization. A back flow is expected to occur at the upper portion of the outflow boundary to complete the large upper recirculation. Transient results of normalised u_{max} is shown in Fig. 4.3(f). It is noticed that the solution reaches steady state condition gradually. However there are few oscillations at $t = 10000$ and $t = 20000$. Further investigation in time show that the solution becomes time independent at $t = 30000$. It is ensured by computing upto large total time of $t = 10^5$.

Fig. 4.4 and Fig. 4.5 illustrate the stream lines plots for various Re and OR. It is observed that while Re increases, the size of recirculation eddy increases. Also it is noticed that similar effect is obtained when OR is increased. At exit, the stream lines become parallel and thus our assumption for fully developed flow is satisfied. It is of interest to note that the streamline pattern for $Re = 200$, $OR = 0.5$ (4.4(a)) is different from others. The main flow is unable to overcome the friction and thus is spreading in the normal direction. Similar observations have been made by Chiriac and Ortega [26] for low Re case in a confined slot jet impingement flow. Near the bottom wall, streamlines are less denser in order to satisfy the no-slip conditions along the walls. However the streamlines are denser throughout the impingement region. A part of the entrainment streamlines are passed towards the jet ejecting location and it shears with outer layer of the main flow. A close view of the recirculation eddies for $Re = 300$ and $OR = 0.5, 1.0$ and 1.5 are shown with velocity vector plot in Fig. 4.6. The location of u_{max} for the entire length of the domain is shown in Fig. 4.7(a). The y/h location is gradually falling down towards the bottom wall and after reattachment point it increases in rest of the domain length. This is attributed due to the jet deflection upto the reattachment point because of the Coanda effect. After that, it spreads in the downstream direction like a wall jet. The jet trajectory is defined as the position of locus of maximum centerline velocity as given by [31] and shown in Fig. 4.7(b). Variation of the jet centerline velocity with distance is shown in Fig. 4.7(c). The jet centerline velocity decreases gradually in downstream direction. However at high Re (=600), a small kink is presented after the reattachment point. It is attributed by the decrease in pressure after the reattachment of the jet.

The dependency of x_1/h with Re and OR is shown in Fig. 4.8. The reattachment length has an increasing trend with Re with a falling rate of increase within the range of Re considered. It is noticed that the center of the eddy moves away from the solid walls with Re and OR. However it is observed that the x direction variation is higher if Re increases while y direction variation is higher if OR increases (Fig. 4.9).

Entrainment occurs when a jet ejects into quiescent medium. Low pressure is created above and below, near the mouth of the jet ejection. The ambient fluid flows towards it and shear with the main flow. This phenomena is well captured in the present computations (Fig. 4.10). The negative u velocity contours show the ambient fluid flow towards low pressure zone created by the ejection of the jet. It is noticed that this flow rate is increased when OR is increased, and it increases markedly with Re. The agreement of the numerical solution with wall jet similarity solution is expected where the u velocity turns positive in everywhere in the normal direction. The region from reattachment point to this length is called impingement region. After impingement, the pressure of the main flow starts to decrease in this region. The decay of normalized local u_{max} is shown in Fig. 4.11(a). The decay of u_{max}/U_{max} is linear and independent of OR in the recirculation region. However it is higher for low Re. This is mainly due to the sudden expansion and interaction of the jet with ambient entrainment fluid. Further downstream the decay follows common behavior for various OR and Re. It is noticed that at higher OR, decay becomes independent of OR but a function of Re.

The computed u velocity profile at different downstream locations are compared with the similarity solution and experimental results of Quintana et al. [15] for laminar wall jet. It shows very good agreement with them (Fig. 4.11(b)). It satisfies the momentum flux, *Glauert* constant for laminar wall jet ([1]). Local u velocity is compared for different Re and OR at $x/h = 20$ (Fig. 4.11(c)). When OR increases for a particular Re, an increase in local u_{max} is attributed due to large reattachment length which reduces the decay of u-velocity. However the difference is reduced at higher OR. It is observed that the jet spreads more in the normal direction for low Re than at high Re. Spreading of jet is demonstrated near the impingement region by u velocity profile (Fig. 4.12). u_{max} is not much affected by OR in this particular region (refer Fig. 4.12(a)- 4.12(c)). At low Re, jet spreads more at particular location, for example $x/h = 5$ which is evident from Fig. 4.12(d)-4.12(f). This is due to the relatively less amount of momentum being carried by a lower Re case. An increase in u_{max} is obvious when Re increases.

The bottom wall vorticity distributions for different Re with OR=1.0 are shown in (Fig. 4.13(a)). Near the impingement region the vorticity variations are large while in downstream direction it becomes independent of x. It is noticed that while Re increases the normal u velocity gradient is increased, which influences the vorticity in the negative direction. Also the wall vorticity is higher (in negative side) because the velocity gradient near the wall is higher.

Fig. 4.13(b) shows the wall vorticity distribution for various OR and Re=350. Also it is noticed that the OR affects the vorticity upto the impingement region and further downstream, vorticity becomes independent of OR. This implies that the adjustment of the non-uniformity created by offset is complete near the outlet.

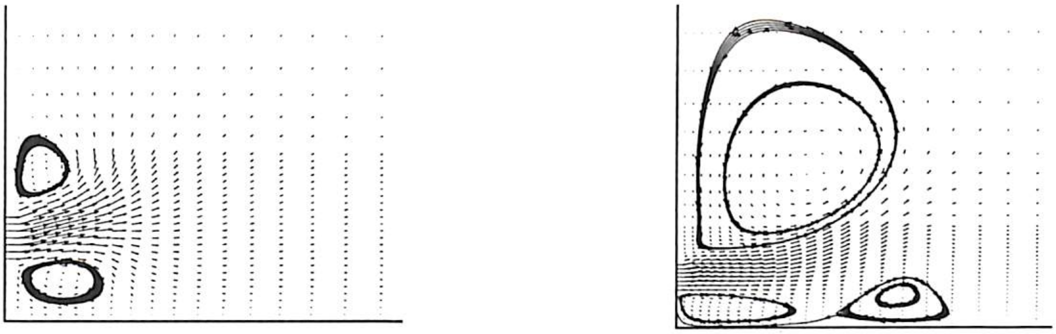

(a) $t = 350$ (b) $t = 750$

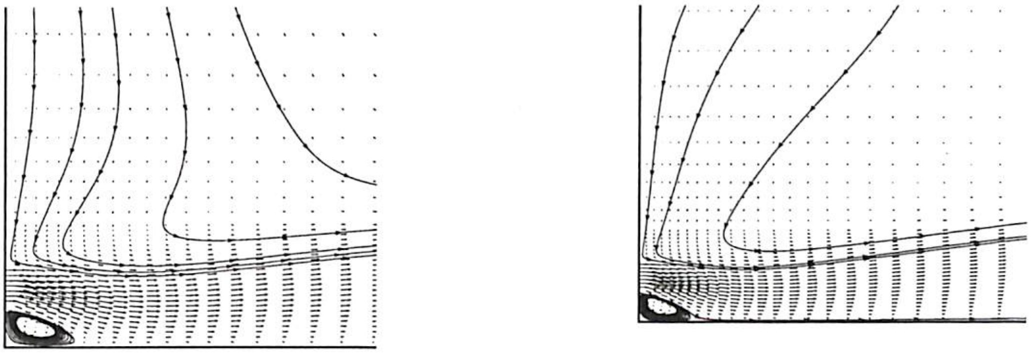

(c) $t = 10000$ (d) $t = 20000$

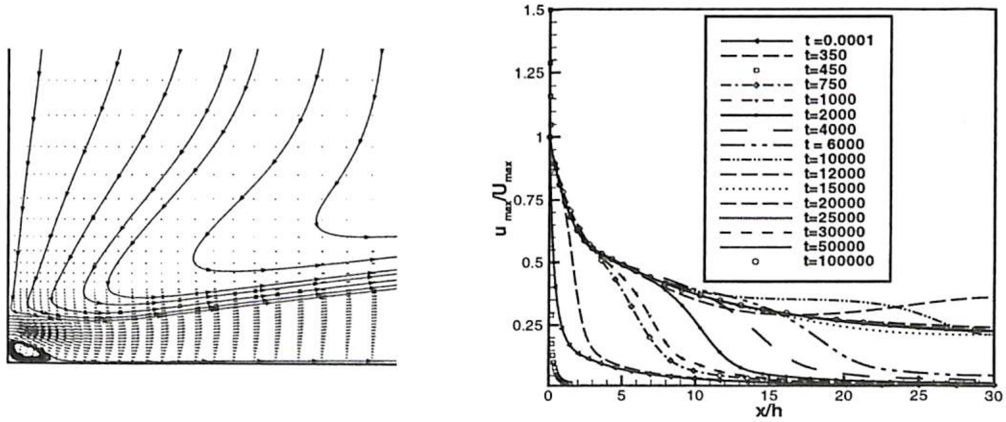

(e) $t = 3 * 10^4$ (f) Transient results of local u-max: $Re = 600, OR = 1.0$

Figure 4.3: Velocity vector and stream trace plot (a-e), (f) u_{max} distribution, $Re = 600, OR = 1.0$

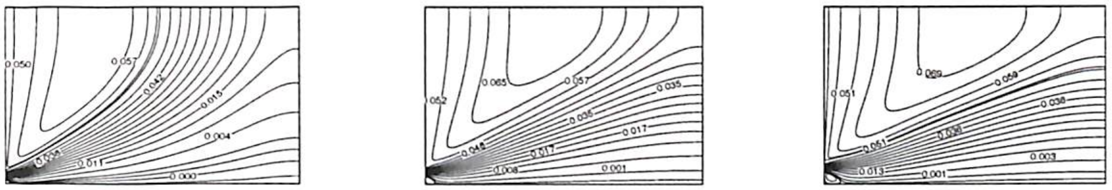

(a) $Re = 200$, $OR = 0.5$ (b) $Re = 200$, $OR = 1.0$ (c) $Re = 200$, $OR = 1.5$

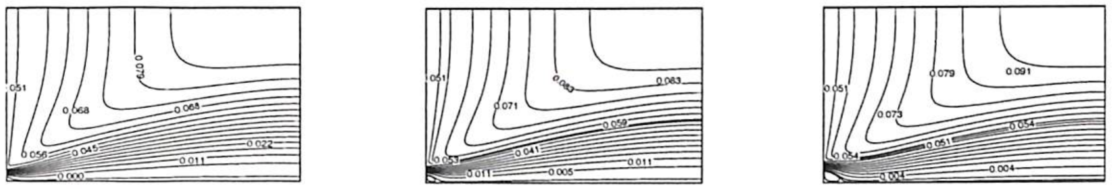

(d) $Re = 300$, $OR = 0.5$ (e) $Re = 300$, $OR = 1.0$ (f) $Re = 300$, $OR = 1.5$

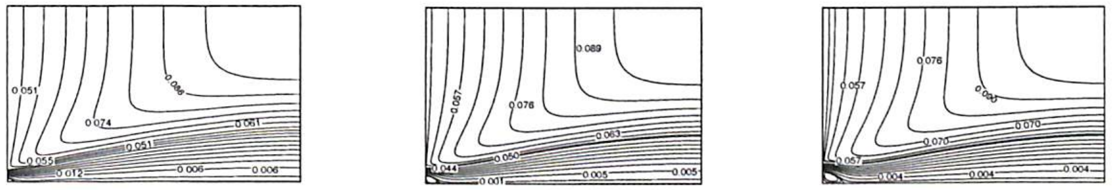

(g) $Re = 400$, $OR = 0.5$ (h) $Re = 400$, $OR = 1.0$ (i) $Re = 400$, $OR = 1.5$

Figure 4.4: Effect of offset ratio and Re on the streamline pattern

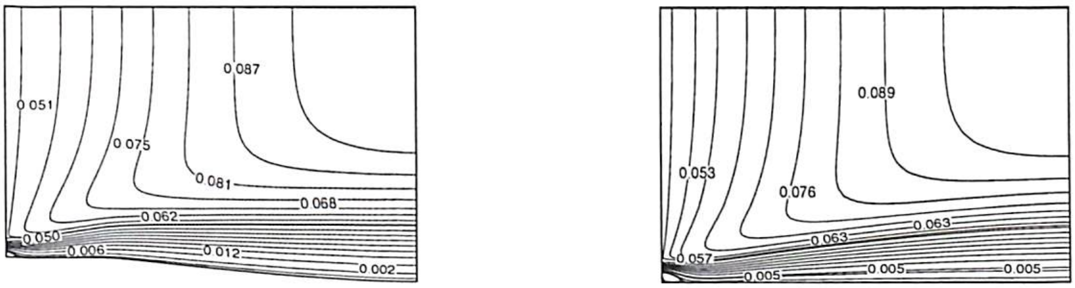

(a) $Re = 500$, $OR = 0.5$

(b) $Re = 500$, $OR = 1.0$

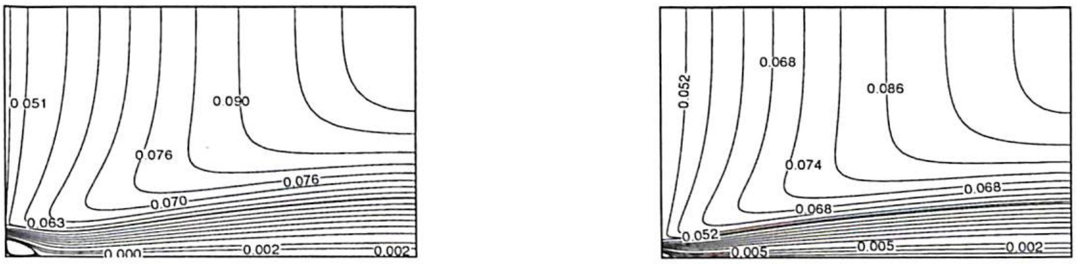

(c) $Re = 500$, $OR = 1.5$

(d) $Re = 600$, $OR = 0.5$

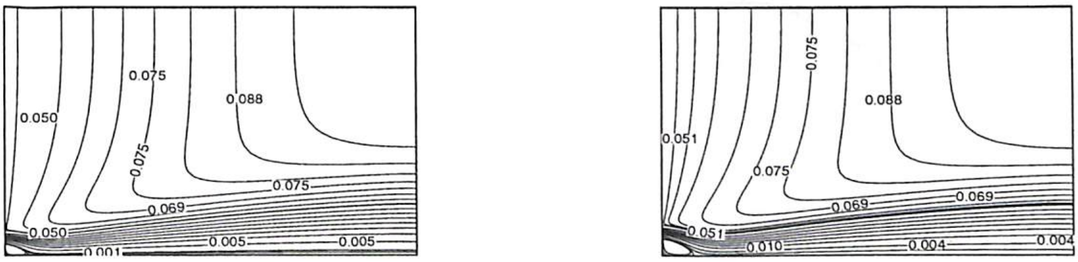

(e) $Re = 600$, $OR = 1.0$

(f) $Re = 600$, $OR = 1.5$

Figure 4.5: Effect of offset ratio and Re on the streamline pattern:

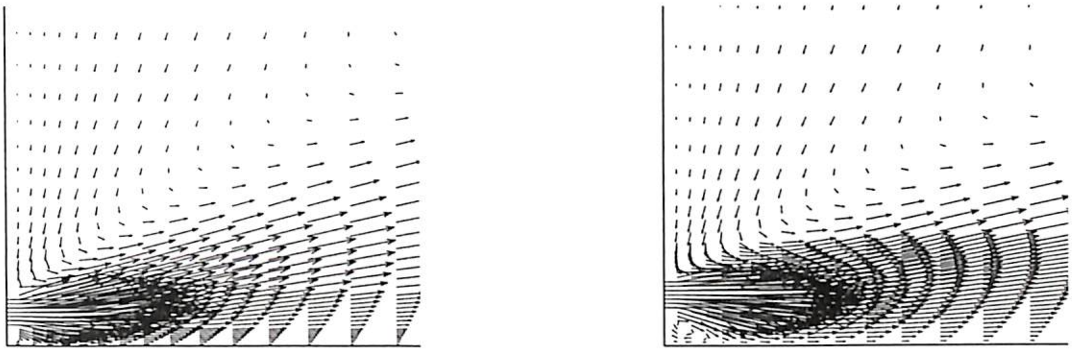

(a) $OR = 0.5$ (b) $OR = 1.0$

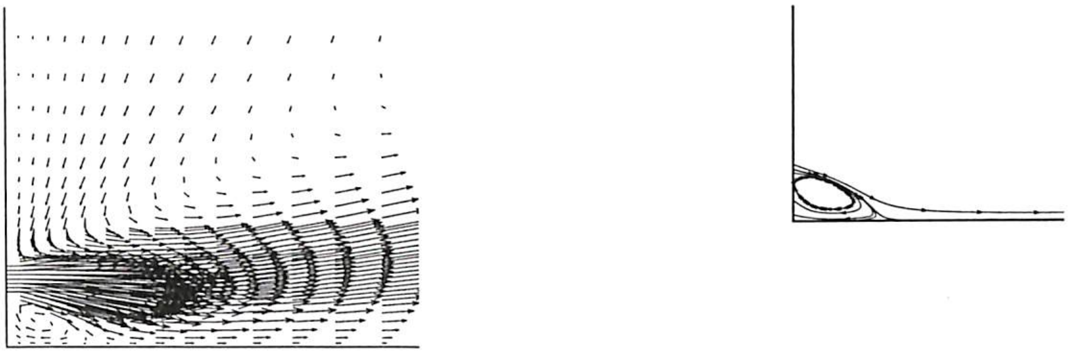

(c) $OR = 1.5$ (d) $OR = 0.5$

(e) $OR = 1.0$ (f) $OR = 1.5$

Figure 4.6: Velocity vector (a-c) and the recirculation eddy (d-f), $Re = 300$

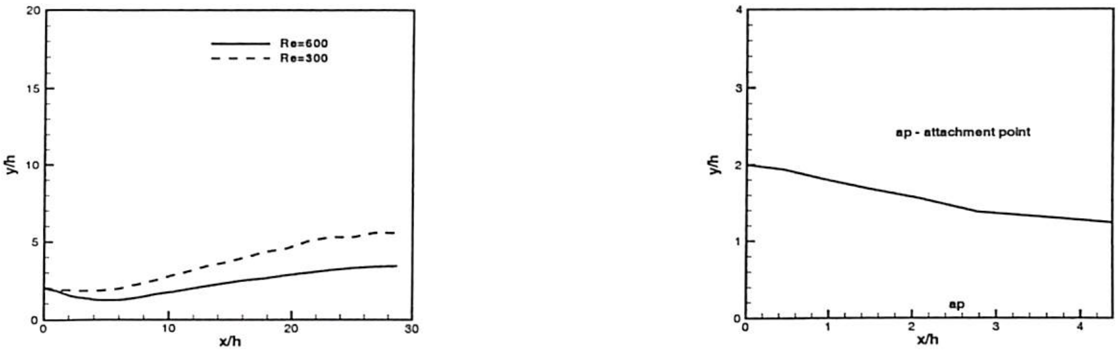

(a) u_{max} location

(b) u_{max} trajectory: $Re = 600$

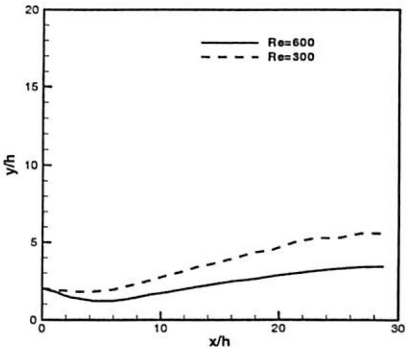

(c) Centerline velocity

Figure 4.7: Centerline velocity: $OR = 1.5$

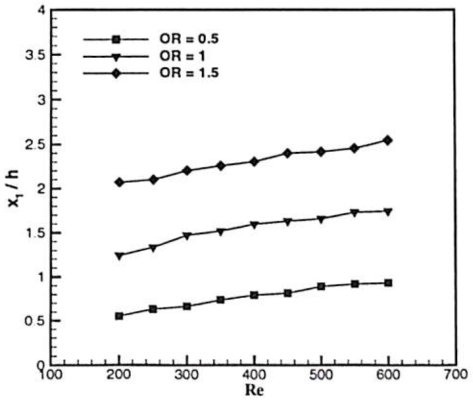

Figure 4.8: Comparison of reattachment length with *Re* and *OR*.

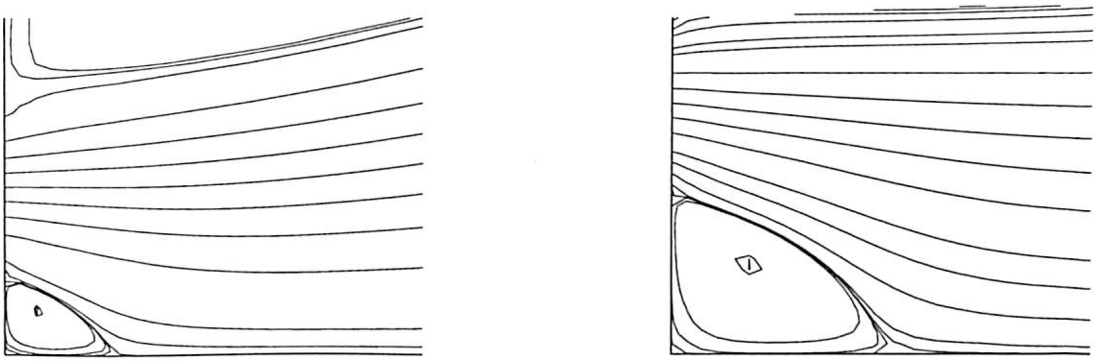

(a) $Re = 400$, OR=0.5 (b) $Re = 400$, OR=1.0

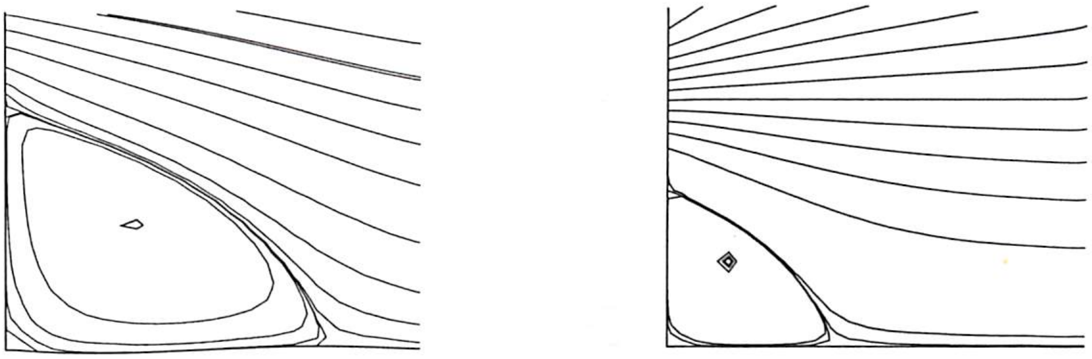

(c) $Re = 400$, OR=1.5 (d) $Re = 200$, OR $= 1.0$

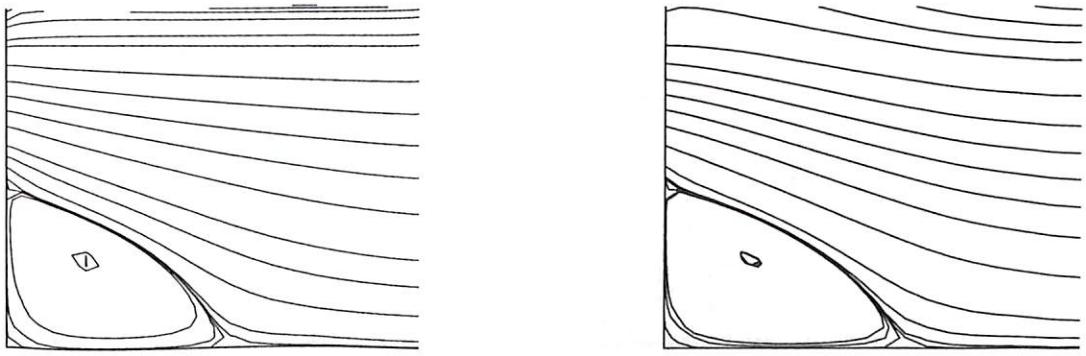

(e) $Re = 400$, OR $= 1.0$ (f) $Re = 600$, OR $= 1.0$

Figure 4.9: Recirculation eddy structure for various Re and OR

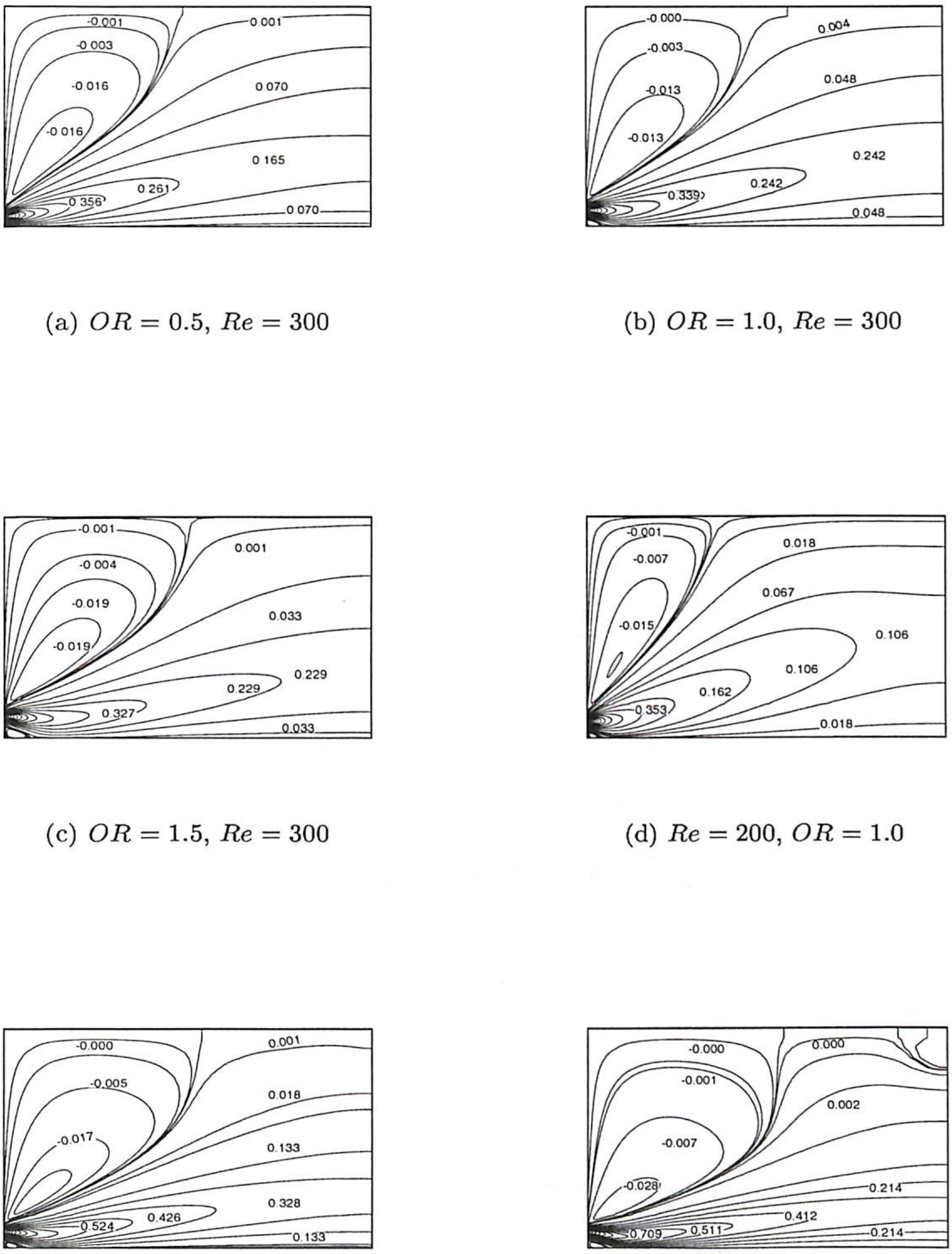

(a) $OR = 0.5$, $Re = 300$

(b) $OR = 1.0$, $Re = 300$

(c) $OR = 1.5$, $Re = 300$

(d) $Re = 200$, $OR = 1.0$

(e) $Re = 400$, $OR = 1.0$

(f) $Re = 600$, $OR = 1.0$

Figure 4.10: Effect of OR and Re on entrainment: u-velocity contour plot

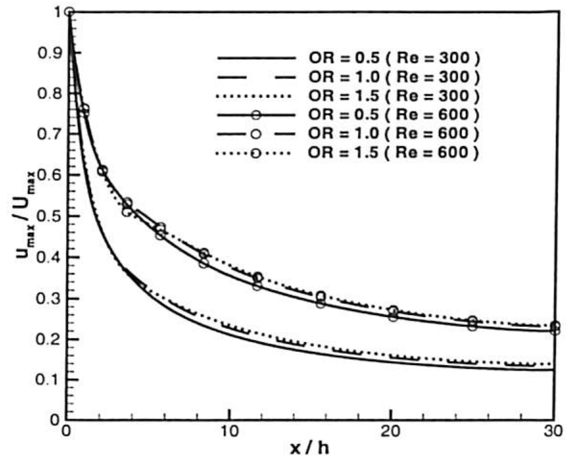

(a) Local u maximum velocity decay

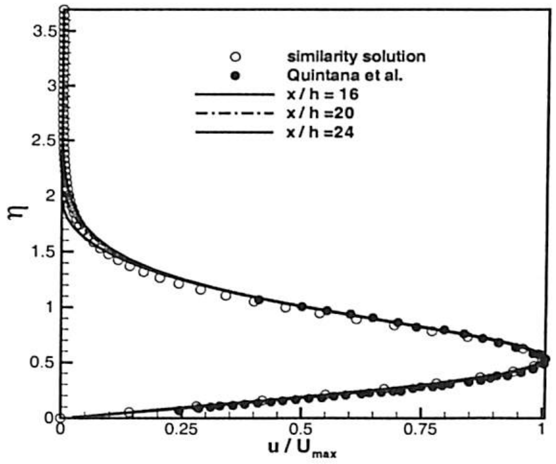

(b) Comparison of u - velocity profile. ($Re = 300,\ OR = 1$)

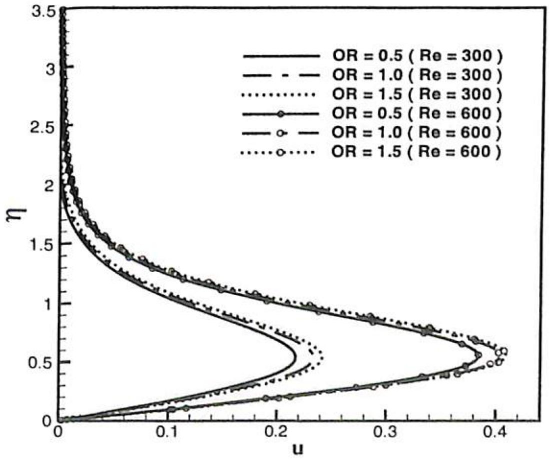

(c) u - velocity at wall jet region ($x/h = 20$)

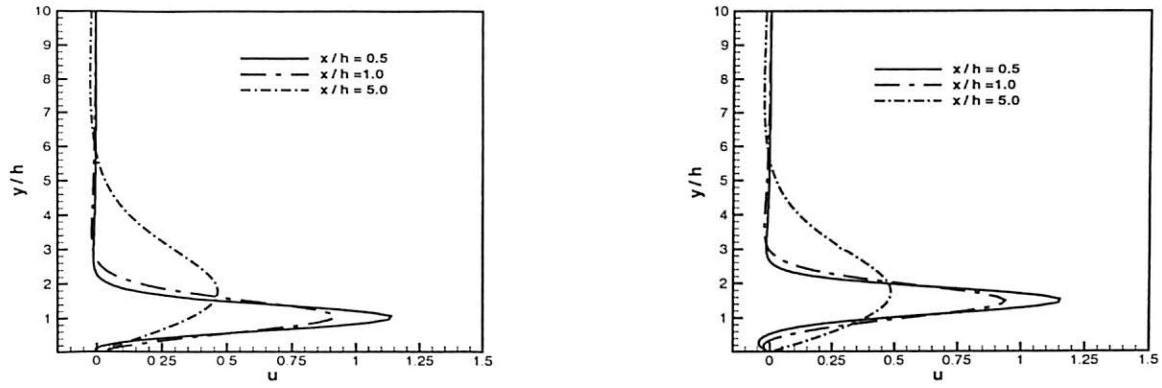

(a) $Re = 300$, OR=0.5 (b) $Re = 300$, OR=1.0

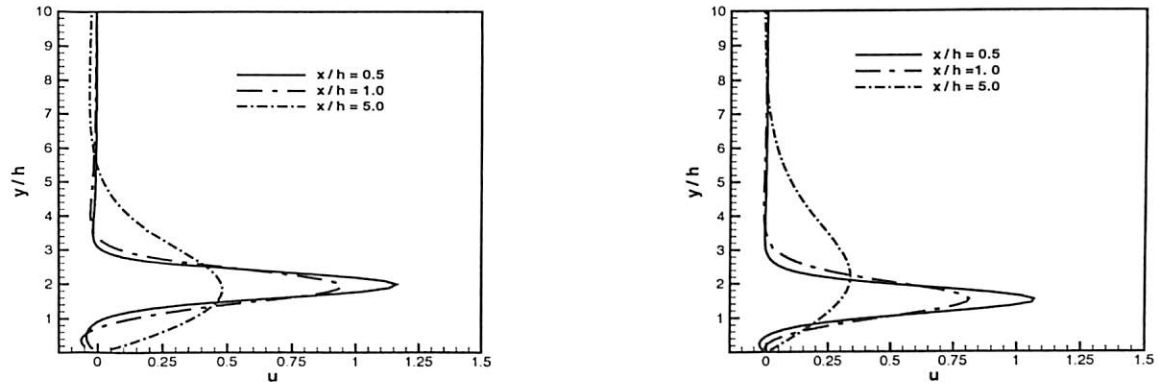

(c) $Re = 300$, OR=1.5 (d) $Re = 200$, OR $= 1.0$

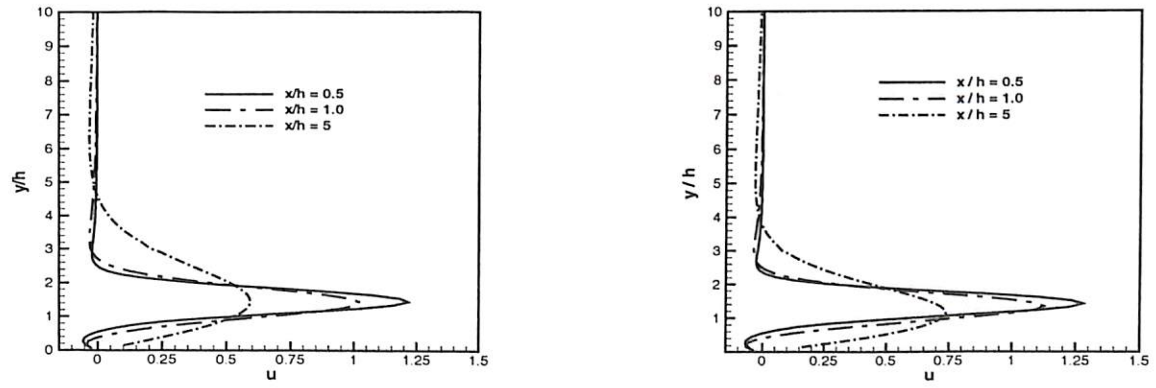

(e) $Re = 400$, OR $= 1.0$ (f) $Re = 600$, OR $= 1.0$

Figure 4.12: u - velocity component for various Re and OR

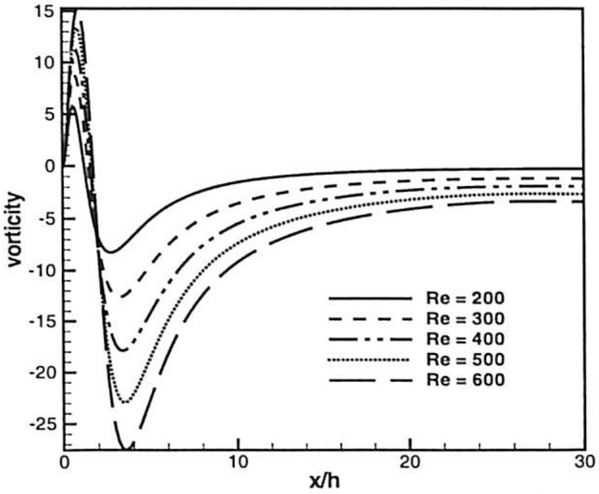

(a) $OR = 1.0$

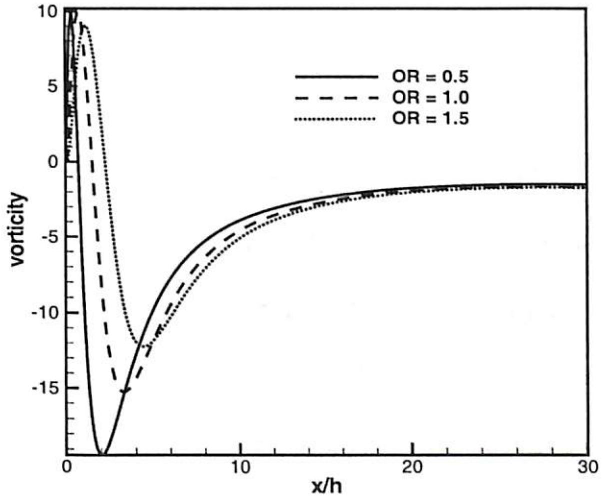

(b) $Re = 350$

Figure 4.13: Vorticity distribution along the bottom wall

4.6 Conclusions

Two-dimensional incompressible nonbuoyant offset jet is solved by stream function and vorticity formulation considering the problem as asymptotic solution to the transient equation. The flow characteristics like strength of recirculation eddy, impingement length, decay of local velocity and wall jet region are studied in details by varying Re and offset jet ratio. The transient results show the nature of vortex generation, it's movement with respect to time, disappearance of the outside vortex and attainment of the final steady-state distribution. The location of u_{max} is presented. The entrainment is increased for high Re and it is less affected with change in OR. The reattachment length has an increasing trend with Re with a falling rate of increase within the range of Re considered. The center of recirculation shifts significantly in the downstream direction with increase in Re. However it moves in the normal direction if OR is increased. The decay rate of u is not much affected by OR near the impingement region. However at high OR solution becomes independent of OR. Far downstream direction, flow behaves like a wall jet flow. The similarity u velocity profiles are having excellent agreement with experimental and numerical predictions. A shift in normal direction is observed in u_{max} while OR increases. The boundary layer thickness is smaller while Re increases. The bottom wall vorticity is considerably affected near the impingement region. In far downstream it becomes independent of a particular Re. The absolute vorticity value increases with an increase in Re.

Acknowledgement

The present results are accepted for publication in *International Journal for Numerical Methods in Fluids.* The helpful comments of the reviewers of the journal are sincerely acknowledged.

Chapter 5

Heat Transfer Study: Offset Jet Flows

5.1 Introduction

This chapter discusses the heat transfer characteristics of offset jet flow. For heat transfer study different Reynolds numbers, Prandtl numbers and offset ratios are considered. The heat transfer results are presented in terms of isotherm contour, Nusselt number and average Nusselt number. The peak Nusselt number value is presented for different Reynolds number and Prandtl number. The effect of Reynolds number and offset ratio on temperature, Nusselt number and average Nusselt number are presented in detail.

5.2 Mathematical Formulation

An incompressible two-dimensional laminar offset jet is considered. For the sake of simplicity, the jet is assumed to be isothermal and having the same density and temperature as the ambient fluid. Also, the velocity profile at the jet inlet is taken as parabolic. The step is assumed to be adiabatic condition. The governing equations are in non-dimensional form Eq. 2.8, Eq. 2.9 and Eq. 2.10 are solved.

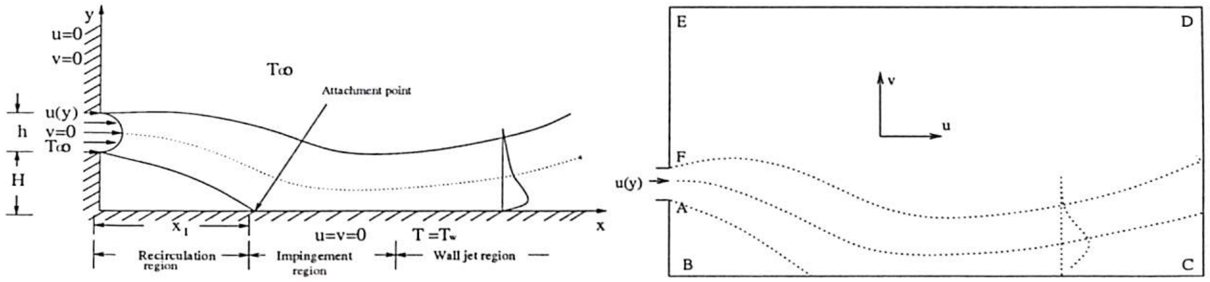

(a) schematic of the problem (b) Computational domain

Figure 5.1: Schematic diagram and boundary conditions in a offset jet problem

The schematic of the problem is shown in Fig. 5.1(a). The boundary conditions needed for the numerical simulation have been prescribed. For an offset jet with entrainment, the following dimensionless conditions have been enforced as shown in Fig. 5.1(b). The inlet slot height (AF) is assumed as, $h = 0.05$.

At the jet inlet, along AF (Fig. 5.1(b)),

$$u(y) = 120y - 2400y^2; \quad \omega(y) = 4800y - 120; \quad \psi(y) = 60y^2 - 800y^3 \quad (5.1a)$$

Along FE, BA and BC due to no-slip condition,

$$u = v = 0 \tag{5.1b}$$

Along ED,

$$\frac{\partial u}{\partial y} = 0 \text{ and } \frac{\partial v}{\partial y} = 0 \tag{5.1c}$$

Along BC,

$$\theta = 1 \tag{5.1d}$$

Along BA adiabatic,

$$\frac{\partial \theta}{\partial x} = 0 \tag{5.1e}$$

Along FE and ED ambient condition is assumed for θ. At downstream boundary the condition of zero first-derivative has been applied for velocity components. This condition implies that the flow has reached a developed condition. Thus, at CD,

$$\frac{\partial u}{\partial x} = \frac{\partial v}{\partial x} = \frac{\partial \theta}{\partial x} = 0 \tag{5.1f}$$

The Nusselt number and average Nusselt number expressions are given by:

$$Nu(x) = -\frac{\partial \theta}{\partial y}|_{y=0} \tag{5.2}$$

$$\overline{Nu} = \frac{1}{L}\int_0^L Nu(x)dx \tag{5.3}$$

The solution of the velocity field is done initially (Chapter 4). Using this velocity field, the energy equation is solved. For the computation time step 0.01 is used for $Pr = 1.0, 100.0$, whereas for $Pr = 0.01$, time step 0.0001 is used. At steady state, the error reaches the asymptotic behavior. Here it is set as sum of temperature error from consecutive iteration reduced to either the convergence criteria (Eq. 2.23, $\varepsilon < 10^{-4}$) or a large total time is elapsed.

5.3 Validation of the Numerical Procedure

The hydrodynamic solution for offset jet flow is validated in chapter 4. To validate the heat transfer numerical procedure, heat transfer in backward-facing step flow is solved and results are compare with Dyne and Heinrich [36]. The downstream temperature profiles of [36] are having good agreement with the present simulations. The details are presented in Appendix B.

5.4 Grid Independent Study

The domain has been chosen as $30\times h$ in streamwise direction and $20\times h$ in normal direction. The computational domain considered here are clustered cartesian grids (Fig. 5.2(b)). In Eq. 2.11 $\kappa = 0.7$ and $\theta = \pi$ is used for generating the grid points. Systematic grid refinement study is carried with

51×41, 61×61, 71×61, 81×81 and 101×101 (Fig. 5.2(a)). Grid refinement level 4 is used for the entire computations. The grids are clustered in stream wise direction whereas in normal direction up to $3\times h$ height, grids are arranged uniformly and above this region, they are clustered. Typical grids are shown in Fig. 5.2(b). The unsteady energy equation (2.10) in time is solved by Alternate Direction Implicit scheme(ADI).

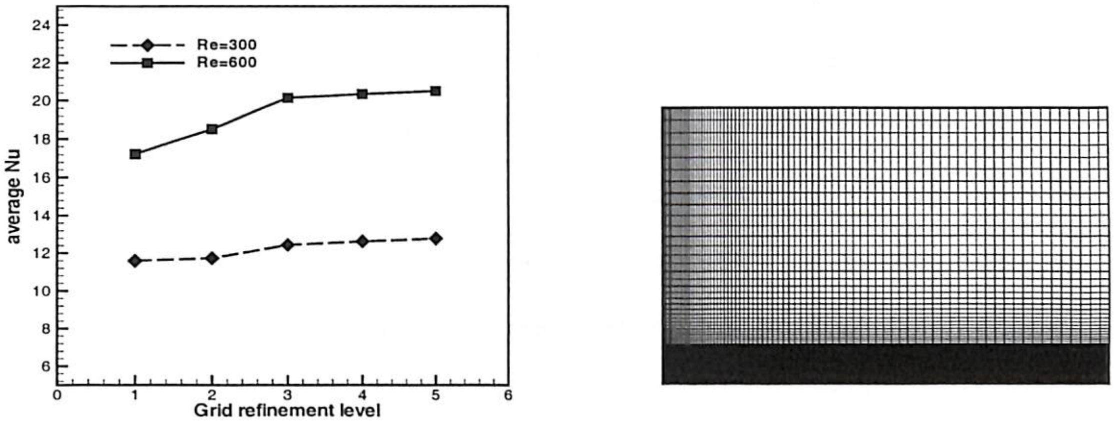

(a) Different grid systems

(b) Typical grids used for offset jet

Figure 5.2: Grid independence study: $Pr = 1.4, OR = 1.0$

5.5 Results and Discussion

Flow separates at the corner and reattaches at the bottom of the wall due to Coanda effect. This length is called reattachment length (x_1, Fig. 5.1(a)). The entire region can be sub-divided into three regions as recirculation region, impingement region and wall jet region. The heat transfer study has been done with three parameters considered here are Re $(=\overline{U}h/\nu)$, Pr and offset ratio

(OR). Offset ratio is defined as the ratio of step height (H) to inlet slot height (h). Results are presented here for three OR viz. $OR = 0.5$, $OR = 1.0$, $OR = 1.5$, Re varying from 200 to 600 in steps of 100 and $Pr = 0.01, 1, 100$. Since the clustered grids are used for the computations, *Tecplot* 9.0 [66] is used for extracting the values for particular location.

In the problem of a nonbuoyant offset jet, a slot jet is discharged parallel to a solid wall. The jet and surrounding medium is having same properties. After leaving the nozzle, the jet curves towards the boundary and attaches to it, enclosing an eddying region of separated flows as shown in Fig. 5.1(a). This phenomenon, known as the Coanda effect, is caused by the reduction of pressure on the inner side of the jet due to entrainment of fluid by the jet. The detailed heat transfer results are presented for isotherm contour, Nusselt number and average Nusselt number for wide range of Re, Pr and OR.

Fig. 5.3 and Fig. 5.4 show the isotherm lines for all the computed results for $Pr = 1.0$. When $Re = 200$, the isotherms penetrate in the far field region for OR=0.5 (Fig. 5.3(a)). This diffusion of heat implies that the convection is very small because the amount of entrainment is very small. With increase in OR (Fig. 5.3(c)) and increase in Re (Fig. 5.4(f)), the isotherms get concentrated near the wall, convection starts dominating. When Re is increased isotherm lines are compressed near the bottom wall. This is due to the jet spread rate in normal direction is decreased at high Re and OR. When Re is increased to 600, a depression in the isotherms is noticed. This is due to the reattachment of the jet where recirculation is more and the wall jet boundary layer starts developing. The influence of Pr is shown in Fig. 5.5 for $OR = 1.5$. Low Pr conduction heat transfer is dominant and at high Pr convection is dominant [37]. It is evident in the present results (Fig. 5.5). Fig. 5.5(a) and Fig. 5.5(d) show the isotherm of low Pr fluid. Here the heat transfer is occurred in the entire solution domain. For the low Pr fluid, conduction is dominant mode of heat transfer and the heat is transferred to the quiescent medium. At $Pr = 100$ (Fig. 5.5(c) and Fig. 5.5(f)), heat transfer occurs in the thin boundary layer of the main flow where the temperature gradient is high. Fig. 5.5(b) and Fig. 5.5(e) show the intermediate effect of both kind of heat transfer in the domain.

Non-dimensional temperature distribution at various downstream locations are presented in Fig. 5.6(a)-5.6(f). The results are presented for three regions: at within recirculation region, at reattachment location and at developing region (Fig. 5.6(a)-5.6(c)) for different Pr while OR is kept constant as 1. For low Pr, at $x/h = 0.5$ location, the temperature profile clearly shows the effect of recirculation flow (Fig. 5.6(a)). A relatively high temperature gradient is obtained because of this effect. At reattachment location and further downstream, the temperature gradient is decreasing. This is due to the flow development and gradual formation of wall jet. For $Pr = 1$, the temperature gradient is maximum at $x/h = 1.47$ (i.e. reattachment location) (Fig. 5.6(b)). For high $Pr(=100)$, at $x/h = 0.5$, a kink in the temperature contour is observed. Further downstream, at $x/h = 1.47$, maximum temperature gradient is observed. Influence of OR on temperature are shown in Fig. 5.6(d)- Fig. 5.6(f) for $Re = 600, Pr = 1.0$. In recirculation region, when OR is increased, the thermal layer thickness is higher in normal direction. It is noticed that at reattachment location similar trend is existing (Fig. 5.6(e)). Further downstream location the contour becomes independent of OR (Fig. 5.6(f)).

The interesting heat transfer property, Nusselt number is presented in details as a function of Re, Pr and OR. Fig. 5.7(a)-5.7(c) show the influence of Re on Nu with constant $OR = 1.0$. In general when Re is increased, Nu also increases. However, at low Pr this increment is less (Fig. 5.7(a)). The peak value of Nu is occurred near the reattachment location 5.7(b)-5.7(c). It shifts in downstream direction when Re is increased since the reattachment length is also increased. Further in downstream direction Nu decreases monotonically. Nu becomes invariant in wall jet region. It is noticed that the these profiles are self similar. The effect of Pr is presented in Fig. 5.8. The Nusselt number gradually increases upto reattachment location and further it decreases monotonically. This trend is common for any Re and OR. With increase in Pr, the heat transfer from the surface also increases. The effect of OR on Nusselt number is presented in Fig. 5.9 for $Re = 500$ and different Pr. It is noticed that when OR is increased, Nu is decreased. Near the jet exit due to rapid boundary layer growth, the temperature gradient is larger and which attributes to the high Nu (Fig. 5.9(a)). At $Pr = 1$, the peak Nu is decreased significantly for every OR changes. The peak value is moved in downstream direction. However it shows less variation at high Pr (Fig. 5.9(c)).

Maximum Nusselt number for different Re is presented in Fig. 5.10. Maximum Nusselt number is increased when Re is increased. However it is less

Table 5.1: Average Nusselt number: $Re = 200$

	$Pr = 0.01$	$Pr = 1.0$	$Pr = 100.0$
OR=0.5	2.822451	6.228781	28.968498
OR=1.0	2.297369	5.902078	28.839270
OR=1.5	2.390450	6.426655	32.280045

Table 5.2: Average Nusselt number: $Re = 300$

	$Pr = 0.01$	$Pr = 1.0$	$Pr = 100.0$
OR=0.5	2.883698	9.792087	47.390442
OR=1.0	2.592962	9.658308	48.085781
OR=1.5	2.205287	8.564577	43.522179

sensitive for low Pr. At high Pr it is increased rapidly when Re is increased.

Summary of the bulk mean property is given from Table 5.1 - Table 5.5 in detail. It is noticed that average Nu is increased when Re is increased for particular OR.It is noticed that average Nu is increased when Pr is increased for particular OR. When OR is increased $\overline{Nu}$ is decreased. However it is noticed that for high Pr, when OR is increased from 0.5 to 1.0, $\overline{Nu}$ is slightly increased and further decreased for $OR = 1.5$. For Re=200 (Table 5.1), with increase of OR from 0.5 to 1.0, $\overline{Nu}$ decreases whereas it increases when OR is further increased. For Re=300-600 (Table 5.2-Table 5.5), $\overline{Nu}$ gradually decreases with increase in OR for $Pr = 0.01$ and 1. However, for Pr=100, $\overline{Nu}$ increases and then decreases with gradual increase in OR. These kind of behavior needs further investigation.

Table 5.3: Average Nusselt number: $Re = 400$

	$Pr = 0.01$	$Pr = 1.0$	$Pr = 100.0$
OR=0.5	2.898741	12.303842	59.566738
OR=1.0	2.639623	12.178701	61.196480
OR=1.5	2.246418	10.794498	56.009968

Table 5.4: Average Nusselt number: $Re = 500$

	$Pr = 0.01$	$Pr = 1.0$	$Pr = 100.0$
OR=0.5	2.976373	14.499768	70.358238
OR=1.0	2.687608	14.398809	72.947220
OR=1.5	2.233061	12.772109	67.628464

Table 5.5: Average Nusselt number: $Re = 600$

	$Pr = 0.01$	$Pr = 1.0$	$Pr = 100.0$
OR=0.5	3.134441	20.209028	80.096924
OR=1.0	2.713668	16.371225	83.662781
OR=1.5	2.330573	14.573236	78.514282

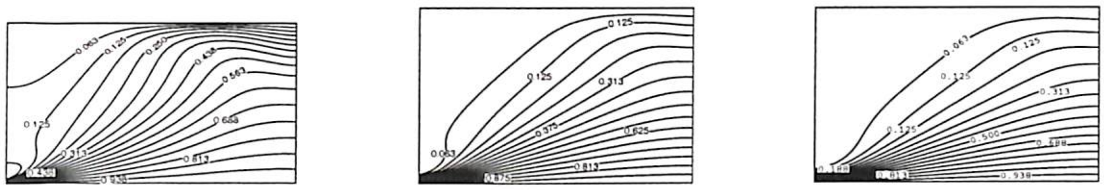

(a) $Re = 200$, $OR = 0.5$ (b) $Re = 200$, $OR = 1.0$ (c) $Re = 200$, $OR = 1.5$

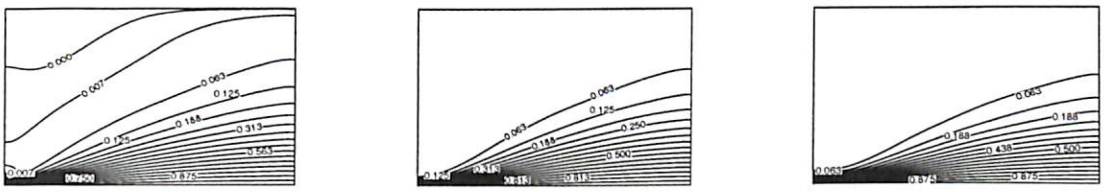

(d) $Re = 300$, $OR = 0.5$ (e) $Re = 300$, $OR = 1.0$ (f) $Re = 300$, $OR = 1.5$

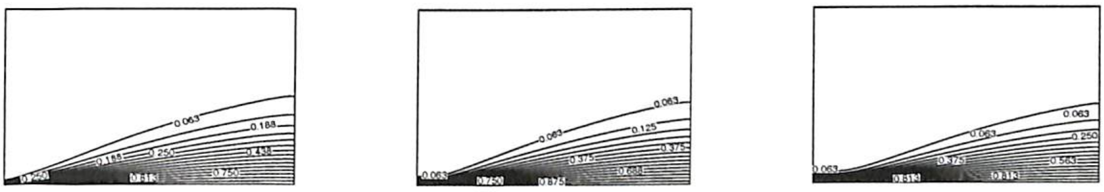

(g) $Re = 400$, $OR = 0.5$ (h) $Re = 400$, $OR = 1.0$ (i) $Re = 400$, $OR = 1.5$

Figure 5.3: $Pr = 1.0$: Effect of offset ratio and Re Isotherm contour: (a)-(c) $Re = 200$, (d)-(f) $Re = 300$, (g)-(i) $Re = 400$

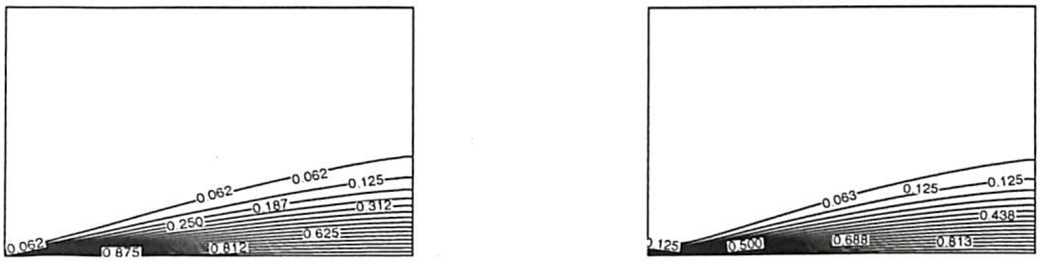

(a) $Re = 500$, $OR = 0.5$ (b) $Re = 500$, $OR = 1.0$

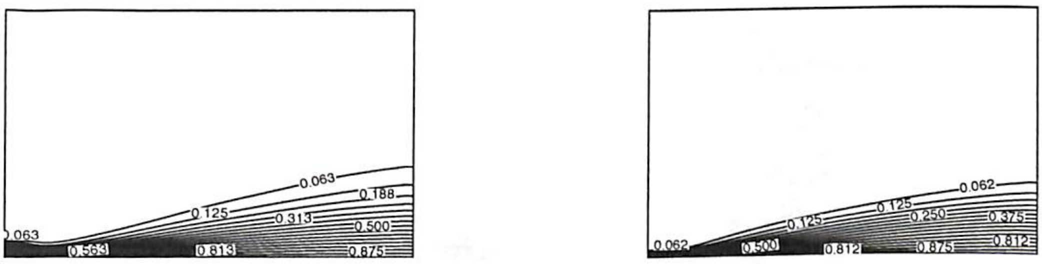

(c) $Re = 500$, $OR = 1.5$ (d) $Re = 600$, $OR = 0.5$

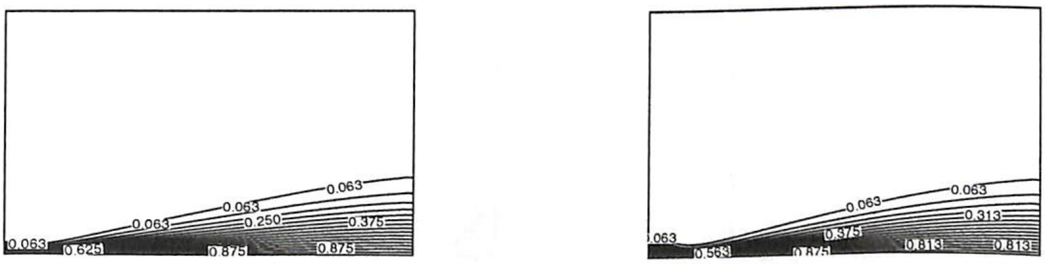

(e) $Re = 600$, $OR = 1.0$ (f) $Re = 600$, $OR = 1.5$

Figure 5.4: $Pr = 1.0$: Effect of offset ratio and Re Isotherm contour: (a)-(c) $Re = 500$, (d)-(f) $Re = 600$

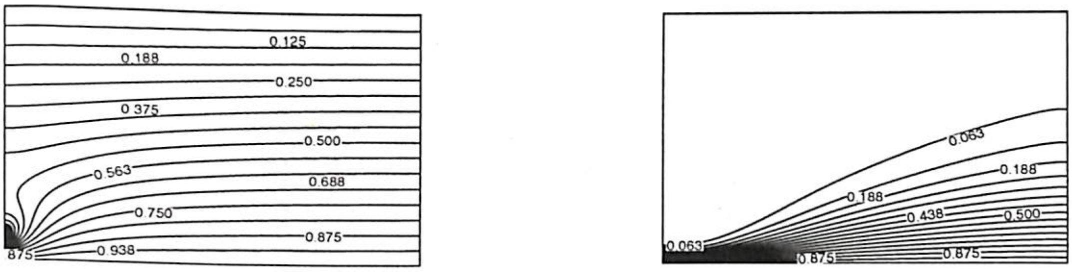

(a) $Re = 300, Pr = 0.01$

(b) $Re = 300, Pr = 1.0$

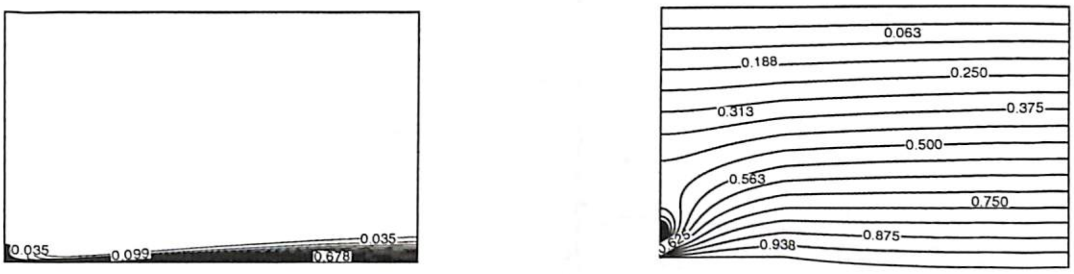

(c) $Re = 300, Pr = 100$

(d) $Re = 600,\ Pr = 0.01$

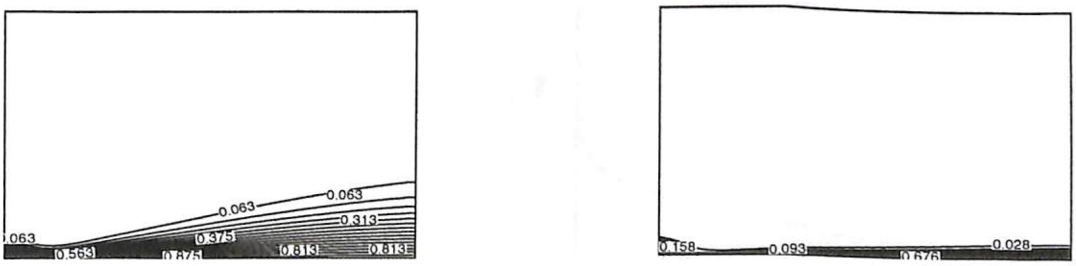

(e) $Re = 600,\ Pr = 1.0$

(f) $Re = 600,\ Pr = 100.0$

Figure 5.5: Effect of Pr Isotherm contour: $OR = 1.5$

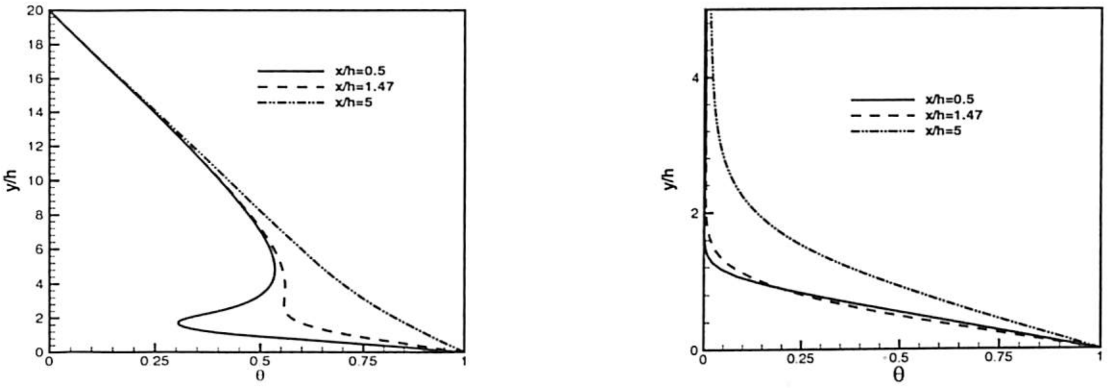

(a) $Pr = 0.01, OR = 1.0$ (b) $Pr = 1, OR = 1.0$

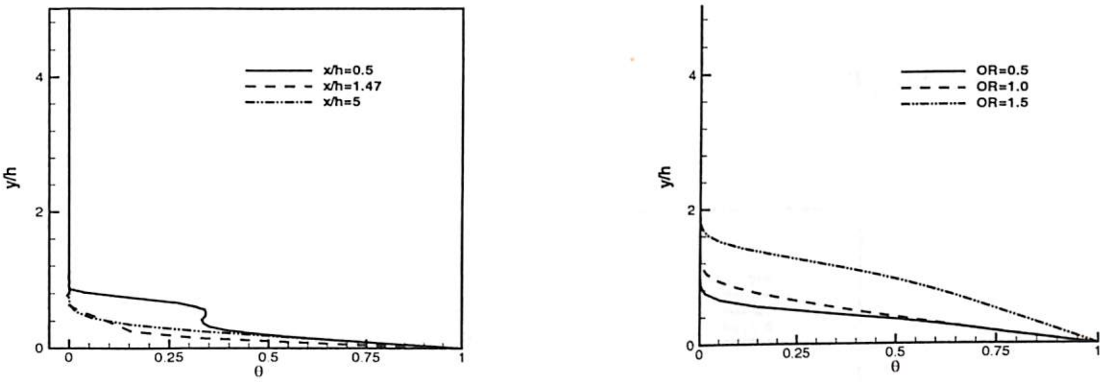

(c) $Pr = 100, OR = 1.0$ (d) $Pr = 1, x/h = 0.5$

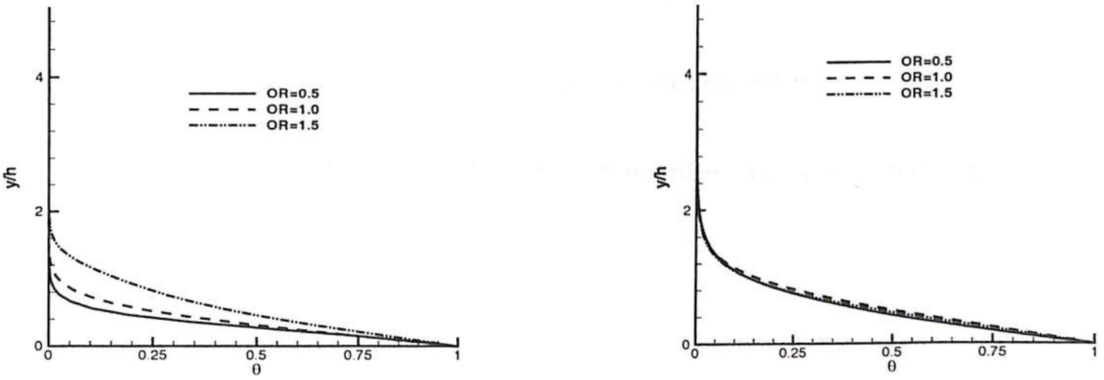

(e) $Pr = 1, x/h = 1.75$ (f) $Pr = 1, x/h = 5.0$

Figure 5.6: Downstream location temperature contour: Fig. a-c, $Re = 300$, Fig. d-f, $Re = 600$

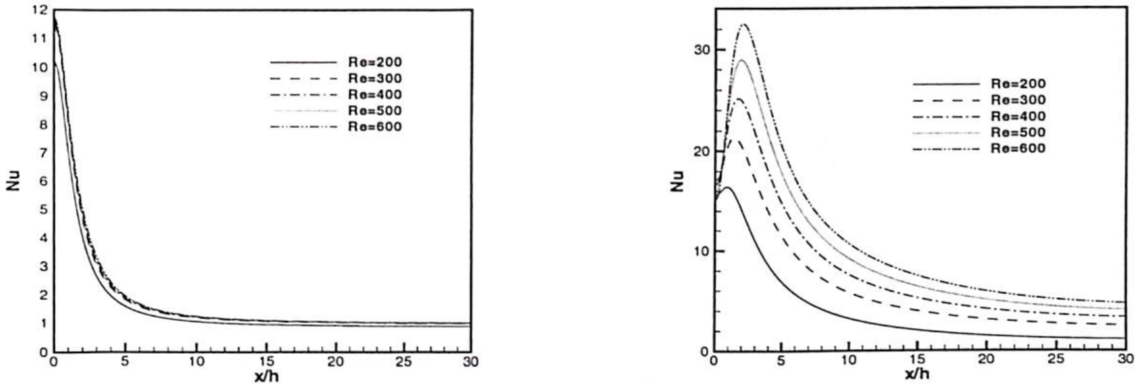

(a) $Pr = 0.01, OR = 1.0$ (b) $Pr = 1, OR = 1.0$

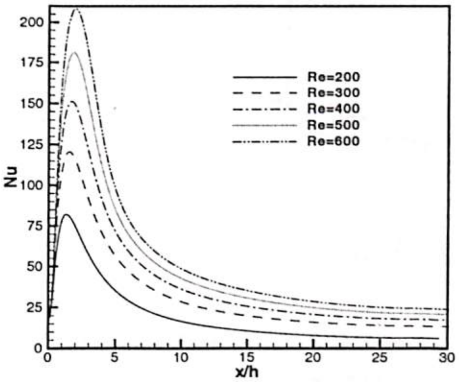

(c) $Pr = 100, OR = 1.0$

Figure 5.7: Nusselt number variation for Re

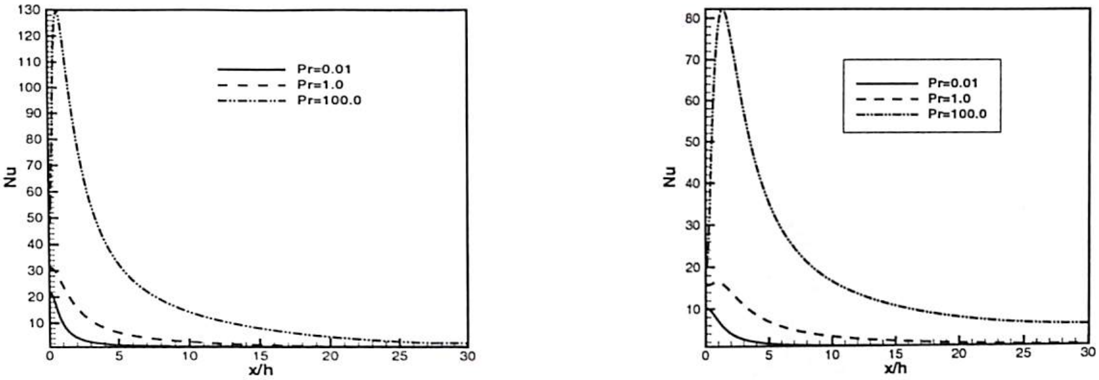

(a) $Re = 200, OR = 0.5$ (b) $Re = 200, OR = 1.0$

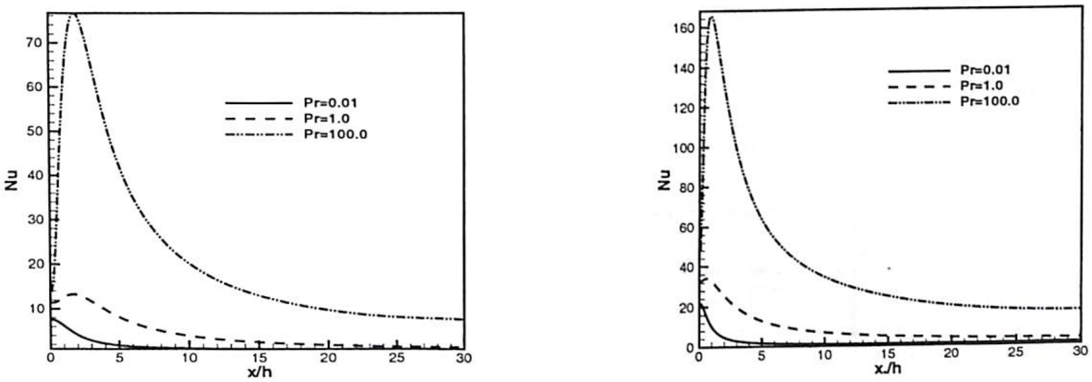

(c) $Re = 200, OR = 1.5$ (d) $Re = 400, OR = 0.5$

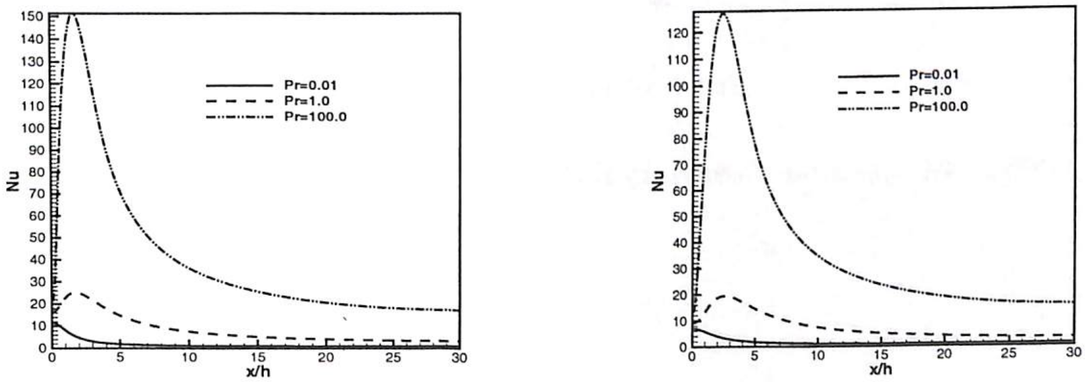

(e) $Re = 400, OR = 1.0$ (f) $Re = 400, OR = 1.5$

Figure 5.8: Effect of Pr on Nusselt number

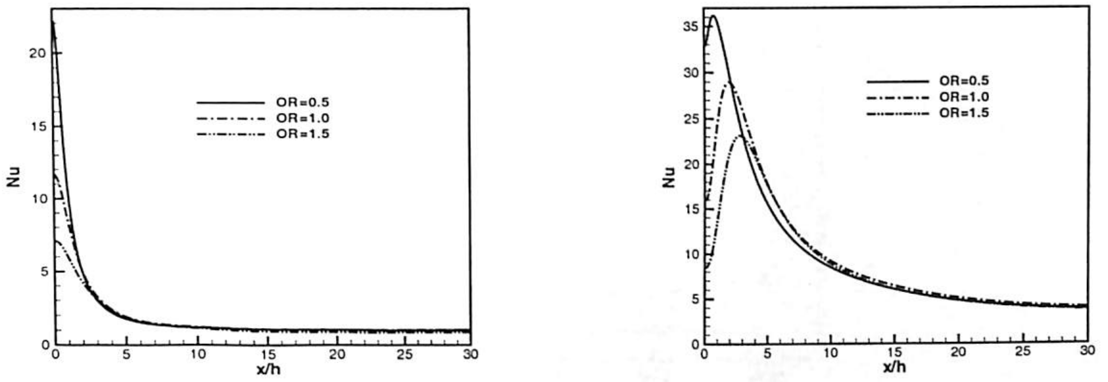

(a) $Pr = 0.01$ (b) $Pr = 1$

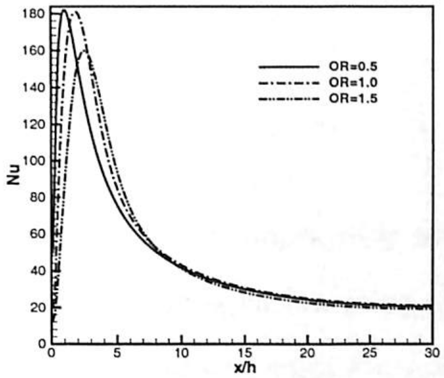

(c) $Pr = 100$

Figure 5.9: Effect of OR on Nusselt number: $Re = 500$

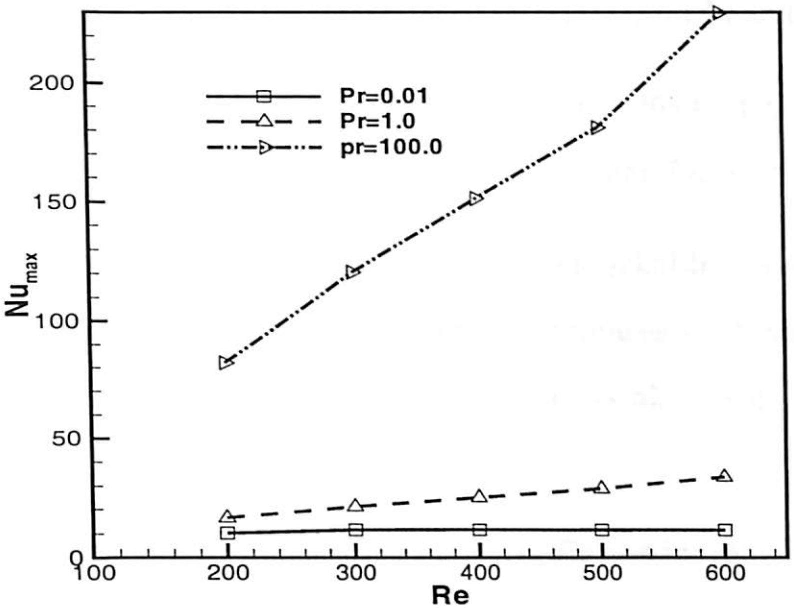

Figure 5.10: Maximum Nusselt number. $OR = 1$

5.6 Conclusions

Heat transfer study of two-dimensional incompressible nonbuoyant offset jet is carried out by solving the momentum equation using stream function and vorticity formulation. Heat transfer characteristics are systematically studied in detail by varying three parameters viz. Re, Pr and OR.

- For low Re and Pr, the isotherms penetrate in the far field because conduction effect is high. With increase in Re, convection starts dominating which results in concentration of isotherms near the wall.

- For same Re, increase in Pr leads to clustering of isotherms near the wall. At the attachment point, a significant depression of isotherms are observed signifying occurrence of maximum heat transfer.

- In the recirculation region, significant effect of thermal boundary layer is observed for Pr=0.01 and 100 whereas for Pr=1.0, it is absent.
- For a particular OR, there is a remarkable increase in maximum Nu with increase in Pr. However, it decreases with the increase in OR. The relative increase in Nu_max with Re is also large for Pr=100 compared to Pr=0.01 and 1.
- Average Nu is increased when Re, Pr are increased. It is decreased when OR is increased.

Chapter 6

Conjugate Heat Transfer Study: Offset Jet Flows

6.1 Introduction

This chapter discuss the heat transfer characteristics of offset jet flow as conjugate case. Rahman et al. [67] have studied conjugate heat transfer of a high Pr fluid jet impinging on a solid substrate containing electronics on the opposite surface.

Sahoo and Sharif [68] have studied mixed convection of a heated surface by impinging slot jets in two different configurations. In one case the jet issuing in the downward direction and in the other case it is issuing in vertically upward direction. The heat transfer process has been studied in the mixed-convection regime. Kanna and Das [69] have investigated the closed form solution for laminar plane wall jet and compared the results with simulated results. They studied the problem in connection with four parameters (Re, Pr, λ and k).

However, these solutions are valid only far away from the jet inlet, and in most applications, the near-field development holds the key to important features of the jet flow. Therefore, the near-field development of a wall jet has been the subject of considerable research in recent years. To the authors best knowledge, the conjugate heat transfer study of the plane laminar offset jet has not been carried out so far. In the present work, the conjugate heat transfer in connection with four parameters $Re, Pr, S/h$ and k are investigated (Fig. 6.1(a)). The bottom of the slab is maintained at a constant higher temperature. The conduction in the slab and convection heat transfer in the fluid are computed for various parameters and reported.

6.2 Mathematical Formulation

An incompressible two-dimensional laminar offset jet is considered. For the sake of simplicity, the jet inlet temperature is assumed to be isothermal and having the same density and temperature as the ambient fluid. Also, the velocity profile at the jet inlet is taken as parabolic. The step is assumed to be adiabatic condition. The solid slab bottom is kept at constant temperature and side walls of the slab are insulated. The governing equations are in non-dimensional form Eq. 2.8, Eq. 2.9, Eq. 2.10 and Eq. 2.24 are solved.

The computational domain considered here are clustered cartesian grids (Fig. 6.3). In Eq. 2.11 $\kappa = 0.7$ and $\theta = \pi$ is used for generating the grid points. The unsteady energy equation (2.10) in time is solved by Alternate Direction Implicit scheme (ADI). The boundary conditions needed for the nu-

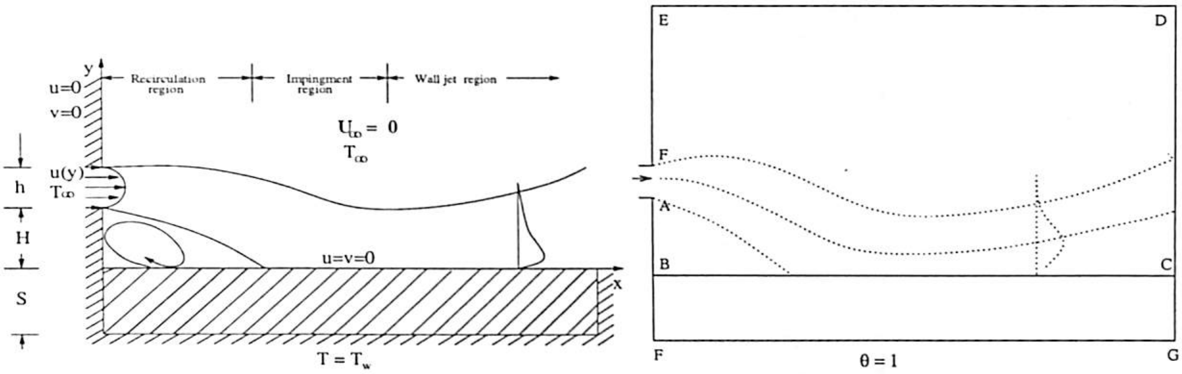

(a) Schematic of the problem

(b) Computational domain

Figure 6.1: Schematic diagram and boundary conditions in an offset jet problem

merical simulation have been prescribed. For an offset jet with entrainment, the following dimensionless conditions have been enforced as shown in Fig. 6.1(b). The inlet slot height is assumed as, $h = 0.05$.

At the jet inlet, along AF (Fig. 6.1(b)),

$$u(y) = 120y - 2400y^2; \quad \omega(y) = 4800y - 120; \; \psi(y) = 60y^2 - 800y^3 \quad (6.1a)$$

Along FE, BA and BC due to no-slip condition,

$$u = v = 0 \quad (6.1b)$$

Along ED,

$$\frac{\partial u}{\partial y} = 0 \text{ and } \frac{\partial v}{\partial y} = 0 \quad (6.1c)$$

Along FG,

$$\theta = 1 \tag{6.1d}$$

Along BA adiabatic,

$$\frac{\partial \theta}{\partial x} = 0 \tag{6.1e}$$

Along FE and ED ambient condition is assumed for θ. At downstream boundary the condition of zero first-derivative has been applied for velocity components. This condition implies that the flow has reached a developed condition. Thus, at CD,

$$\frac{\partial u}{\partial x} = \frac{\partial v}{\partial x} = \frac{\partial \theta}{\partial x} = 0 \tag{6.1f}$$

For the solid slab side walls, BF and CG are treated as adiabatic, where

$$\frac{\partial \theta}{\partial x} = 0 \tag{6.1g}$$

For the interface boundary Eq. 2.26 is used for finding the temperature for the next time level. The Nusselt number and average Nusselt number expressions are given by:

$$Nu(x) = -\frac{\partial \theta}{\partial y}|_{y=0} \tag{6.2}$$

$$\overline{Nu} = \frac{1}{L}\int_0^L Nu(x)dx \tag{6.3}$$

With known hydrodynamic solution (Chapter 4), the energy equation in fluid region as well as solid region are solved simultaneously for the new time level. The energy equation (Eq. 2.10) is disretised with central difference scheme for both convective and diffusive terms. It is solved by ADI method. The unsteady solid slab energy equation (Eq. 2.24) is discretised by central difference scheme and solved by Gauss-Seidel method. For particular time step, Eq. 2.24 is solved with guess interface value. Then the interface Eq. 2.26 is solved with new slab temperature values. Then the calculated interface value is used to compute fluid energy Eq. 2.10. The solution is checked for the global convergence .

Solution approaches steady-state asymptotically while the time reaches infinity. The energy equation in fluid regime and solid regime are solved simultaneously. For the computation, time step 0.01 is used for $Pr = 1.0, 100.0$, whereas for $Pr = 0.01$, time step 0.0001 is used. At steady state, the error reaches the asymptotic behavior. Here it is set as sum of temperature error from consecutive iteration reduced to either the convergence criteria Eq. 2.27 $\varepsilon < 10^{-6}$ or large total time.

6.3 Grid Independent Study

The domain has been chosen as $30 \times h$ in stream wise direction and $20 \times h$ in normal direction. Systematic grid refinement study is carried out with $51{\times}41$, $61{\times}61$, $71{\times}61$, $81{\times}81$ and $101{\times}101$ (Fig. 6.2) for non-conjugate heat transfer study by the same authors (Kanna and Das [70]). Grid refinement level 4 is sufficient for the entire computations in the fluid region. The grids are clustered in streamwise direction whereas in normal direction up to $3{\times}h$ height, grids are arranged uniformly and above this region, they are clustered. Typical grids are shown in Fig. 6.3. Since the interface is common for solid as well as fluid region, in x direction the same clustered grids are used for the solid slab. However in y direction uniform grid points are used. Grid points 21, 41, 61 are tested for $Re = 300, Re = 600$ and $S/h = 5$ and $S/h = 10$. It is seen from Table 6.1 and Table 6.2 that for the grid points 41, the variation in $\overline{Nu}$ is less than 1% and is selected for the entire computations.

Table 6.1: Grid independence study ($Pr = 1.0$): Value of $\overline{Nu}$ for $S/h = 5$

S/h=5	Re=300	Re=600
21	7.281502	10.651847
41	7.280468	10.652081
61	7.287588	10.652626

Table 6.2: Grid independence study ($Pr = 1.0$): Value of $\overline{Nu}$ for $S/h = 10$

S/h=10	Re=300	Re=600
21	5.903205	7.8472017
41	5.940445	7.9831901
61	5.941521	7.9860273

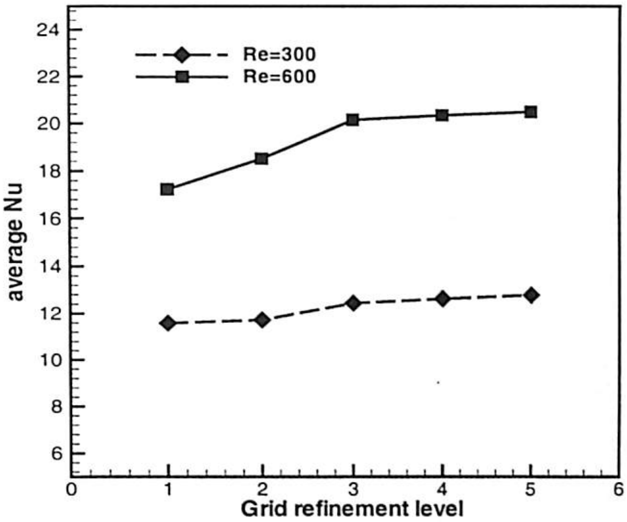

Figure 6.2: Grid independence study, $(Pr = 1.4, OR = 1.0)$

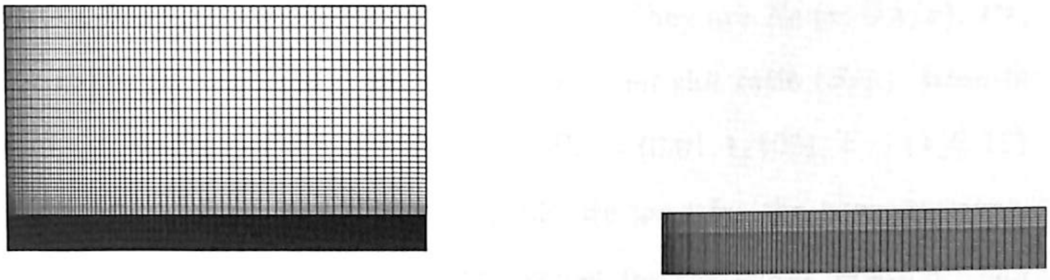

(a) Grids for fluid region (81 × 81)

(b) Grids for solid region (81 × 41): S/h=5

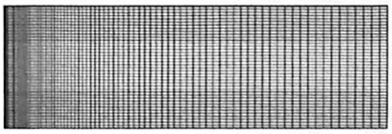

(c) Grids for solid region (81 × 41): S/h=10

Figure 6.3: Typical grids used for offset jet.

6.4 Results and Discussion

Flow separates at the corner and reattaches at the bottom of the wall due to Coanda effect. This length is called reattachment length (x_1, Fig. 6.1(a)). The entire region can be sub-divided into three regions as recirculation region, impingement region and wall jet region. The conjugate heat transfer study has been done with four parameters considered here. They are Re ($=\overline{U}h/\nu$), Pr, conductivity ratio (k) and solid slab thickness to jet slot ratio (S/h). Results are presented for values of Re = (300, 600), Pr = (0.01, 1, 100), k = (1, 5, 10) and S/h = (5, 10). Since the clustered grids are used for the computations, *Tecplot* 9.0 [66] is used for extracting the values for particular location. The detailed conjugate heat transfer results are presented for isotherm contour (θ), conjugate interface temperature (θ_b), Nusselt number (Nu) and average Nusselt number ($\overline{Nu}$) for the above cases.

The effect of four parameters, $Re, Pr, S/h, k$ on isotherm contours are presented for fluid region in Figs. 6.4 - 6.7. At low Re, jet spreads more in normal direction because the momentum flux is small compared to downstream direction frictional forces. Since the surrounding is quiescent, the jet spreads more at Re = 300 than at Re = 600. This is reflected on heat transfer (Fig. 6.4). Thermal boundary layer thickness for Re = 300 is higher than for Re = 600. For low Pr, thermal diffusivity is more. For high Pr fluid, thermal boundary layer thickness is small (Fig. 6.5(c)). The solid slab thickness affects the heat transfer in fluid region. Fig. 6.6 shows the isotherms in the fluid region. The interface temperature is decreased when the slab thickness is increased. The conductivity ratio (k) effects are demonstrated in Fig. 6.7. When k increases from 1 to 5, the interface temperature is also increased as expected leading to an increase in heat transfer (Fig. 6.7(b)). With further increase in k, there is an increase in the heat transfer (Fig. 6.7(c)). Effect of the four parameters on isotherms in the solid slab heat transfer are shown in Figs. 6.8 - 6.11. At high Re, the heat transfer coefficient in the fluid is high and thus the temperature drop in the slab is reduced (Fig. 6.8). The two-dimensionality in the solid slab is clearly shown. Thus the flow property Re affects heat transfer in solid. The variation of temperature in the slab is significant near the recirculation region (Figs. 6.8-6.11). When Pr increases, heat transfer in the solid slab is increased (Fig. 6.9). That is why a large drop in temperature is observed for $Pr = 100$. Since Re is constant, the velocity boundary layer is constant. However, the reduction in thermal diffusivity leads to thin thermal boundary layer and increased heat transfer. In downstream direction the contours become linear implying that the velocity boundary layer is developed. Slab thickness has an opposing impact on the heat transfer (Fig. 6.10). Solid slab acts as a resistance to heat transfer. Increase in slab thickness means increase in resistance and thus the heat transfer is reduced. The effect of k is presented in Fig. 6.11(a)-6.11(c). When k is increased, for the same fluid, the thermal conductivity of the slab is increased. The heat transfer is increased as expected. The two-dimensionality effects of isotherm in the slab is magnified at high k.

The conjugate interface temperature (θ_b) is presented in Fig. 6.12. The interface temperature is decreased upto reattachment point and again it increases in the downstream direction. It is observed that at $x/h = 30$, the profile becomes nearly parallel to x-axis implying that developed condition has been reached. When Re is increased θ_b is decreased (Fig. 6.12(a)). This means that according to Newton's law of cooling, the convective heat transfer is increased. At low Pr, the interface temperature reaches higher value (Fig. 6.12(b)). When Pr is increased the recirculation region interface temperature is decreased. The effect of solid slab thickness is shown in Fig. 6.12(c). The θ_b is reduced for higher value because the thermal resistance is more. For different k, θ_b is presented in Fig. 6.12(d). The θ_b is increased while k is increased. However it is noticed that the increase in heat transfer is sensitive at lower k values. The Nusselt number dependency on $Re, Pr, S/h$ and k is presented in detail in Fig. 6.13. With the increase in Re, Nusselt number is also increased. It reaches maximum value at reattachment point (Fig. 6.13(a)). The local Nusselt number is increased when Pr is increased. At $Pr = 0.01$, the Nusselt number becomes constant at wall jet region (Fig. 6.13(b)). Nusselt number is decreased when the slab thickness is increased (Fig. 6.13(c)). It follows the same trend for the entire downstream direction. The effect of k on local Nusselt number is presented in Fig. 6.13(d). It increases upto reattachment location and further decreased in the downstream direction. For high k values, Nusselt number is also high. However at downstream location, Nu becomes independent of k.

The summary of all the results are presented as variation of average Nusselt number ($\overline{Nu}$), shown in Table 6.3 - Table 6.6. Average Nusselt number is increased when k is increased for particular Pr. It is increased when Pr

Table 6.3: Average Nusselt number: $Re = 300$, $S/h = 5$

	$k = 1$	$k = 5$	$k = 10$
Pr=0.01	1.66835	2.230470	2.447401
Pr=1.0	3.666914	7.280468	8.30109
Pr=100	5.264887	18.422281	26.619541

Table 6.4: Average Nusselt number: $Re = 300$, $S/h = 10$

	$k = 1$	$k = 5$	$k = 10$
Pr=0.01	1.291796	2.083944	2.355951
Pr=1.0	2.282489	5.940445	7.380750
Pr=100	2.807344	11.511204	18.696224

is increased (Table 6.3). Comparing Table 6.3 and Table 6.4 average Nusselt number is decreased when solid slab thickness is increased. For high Re, average Nusselt number is also increased and similar trend is observed for Pr and S/h.

Table 6.5: Average Nusselt number: $Re = 600$, $S/h = 5$

	$k = 1$	$k = 5$	$k = 10$
Pr=0.01	1.743853	2.391801	2.531147
Pr=1.0	4.368432	10.652427	12.936015
Pr=100	5.754236	22.586895	35.617054

Table 6.6: Average Nusselt number: $Re = 600,\ S/h = 10$

	$k = 1$	$k = 5$	$k = 10$
Pr=0.01	1.369124	2.231438	2.2446594
Pr=1.0	2.524857	7.983190	10.807432
Pr=100	3.004654	13.143439	22.721922

(a) $Re = 300$ (b) $Re = 600$

Figure 6.4: Isotherm contour: Effect of Re. ($Pr = 1, k = 5, S/h = 5$)

(a) $Pr = 0.01$ (b) $Pr = 1$

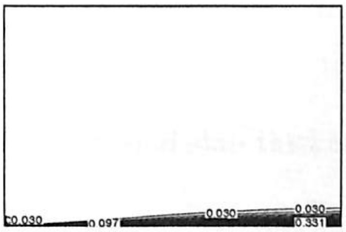

(c) $Pr = 100$

Figure 6.5: Isotherm contour: Effect of Pr. $(Re = 300, k = 5, S/h = 5)$

(a) $S/h = 5$

(b) $S/h = 10$

Figure 6.6: Isotherm contour: Effect of solid slab thickness. ($Re = 300, Pr = 1, k = 1$)

(a) $k = 1$ (b) $k = 5$

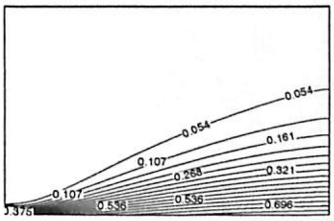

(c) $k = 10$

Figure 6.7: Isotherm contour: Effect of conductivity ratio. ($Re = 300, Pr = 1, S/h = 10$)

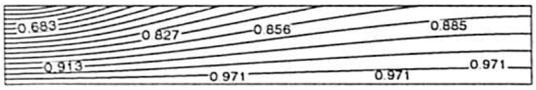

(a) $Re = 300$

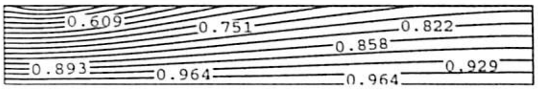

(b) $Re = 600$

Figure 6.8: Isotherm contour: Effect of Re. $(Pr = 1, k = 5, S/h = 5)$

(a) $Pr = 0.01$

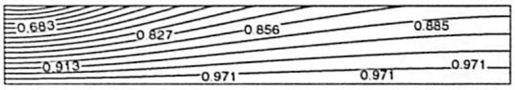

(b) $Pr = 1$

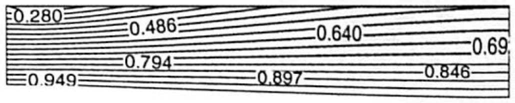

(c) $Pr = 100$

Figure 6.9: Isotherm contour: Effect of Pr. ($Re = 300, k = 5, S/h = 5$)

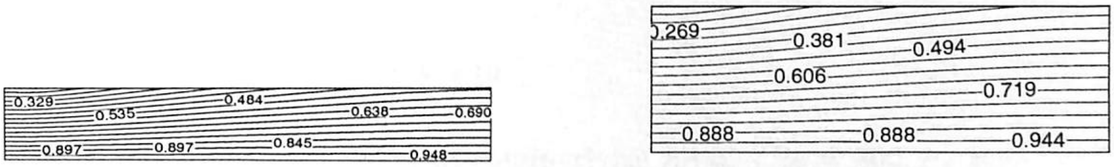

(a) $S/h = 5$

(b) $S/h = 10$

Figure 6.10: Isotherm contour: Effect of solid slab thickness. ($Re = 300, Pr = 1, k = 1$)

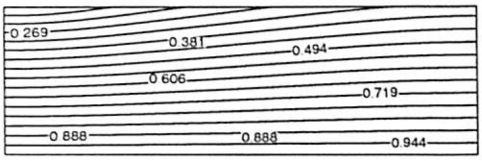

(a) $k = 1$

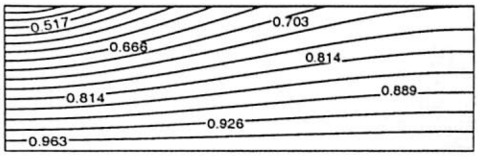

(b) $k = 5$

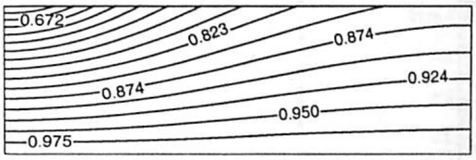

(c) $k = 10$

Figure 6.11: Isotherm contour: Effect of conductivity ratio. ($Re = 300, Pr = 1, S/h = 10$)

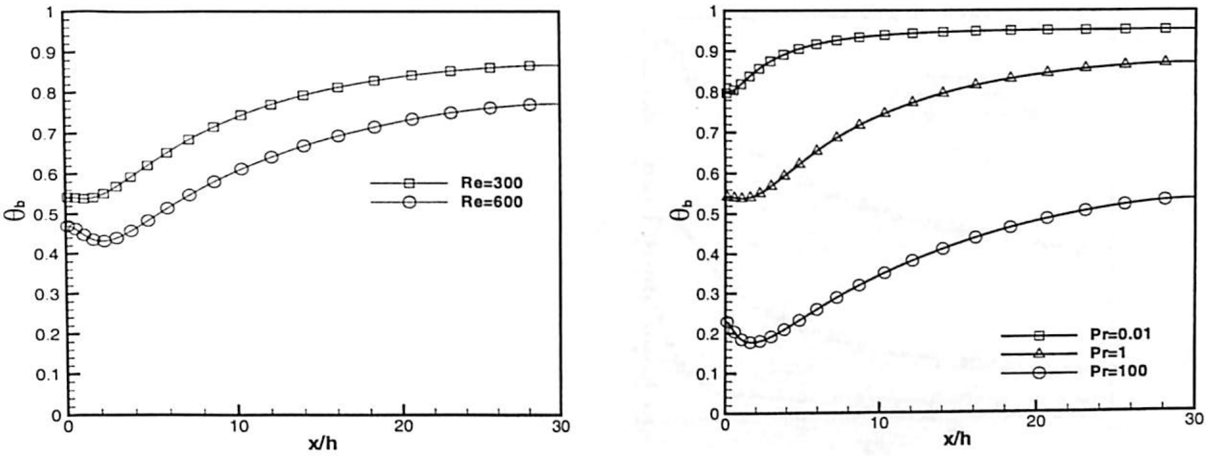

(a) $Pr = 1, S/h = 5, k = 5$

(b) $Re = 300, S/h = 5, k = 5$

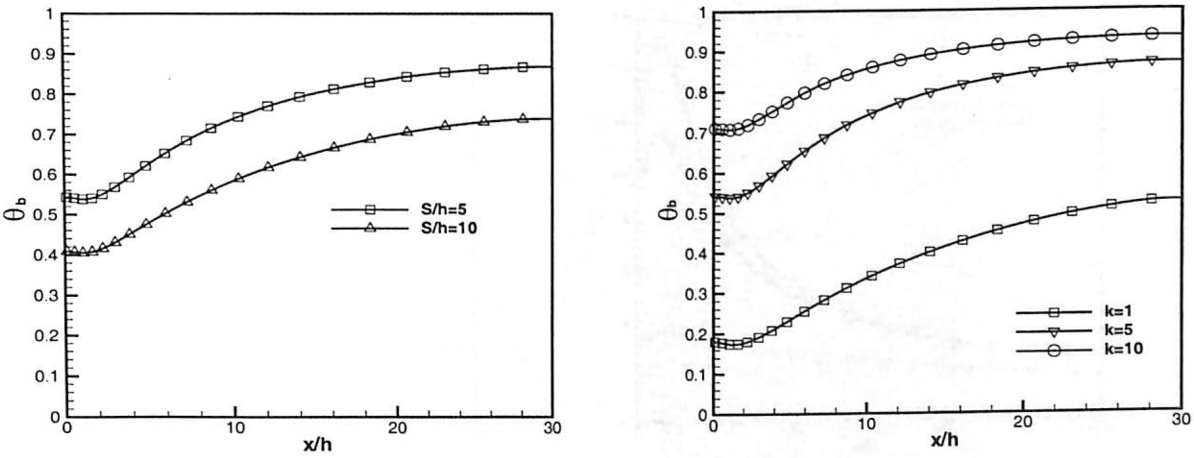

(c) $Re = 300, Pr = 1, k = 5$

(d) $Re = 300, Pr = 1, S/h = 5$

Figure 6.12: Conjugate interface temperature (θ_b): Effect of $Re, Pr, S/h, k$

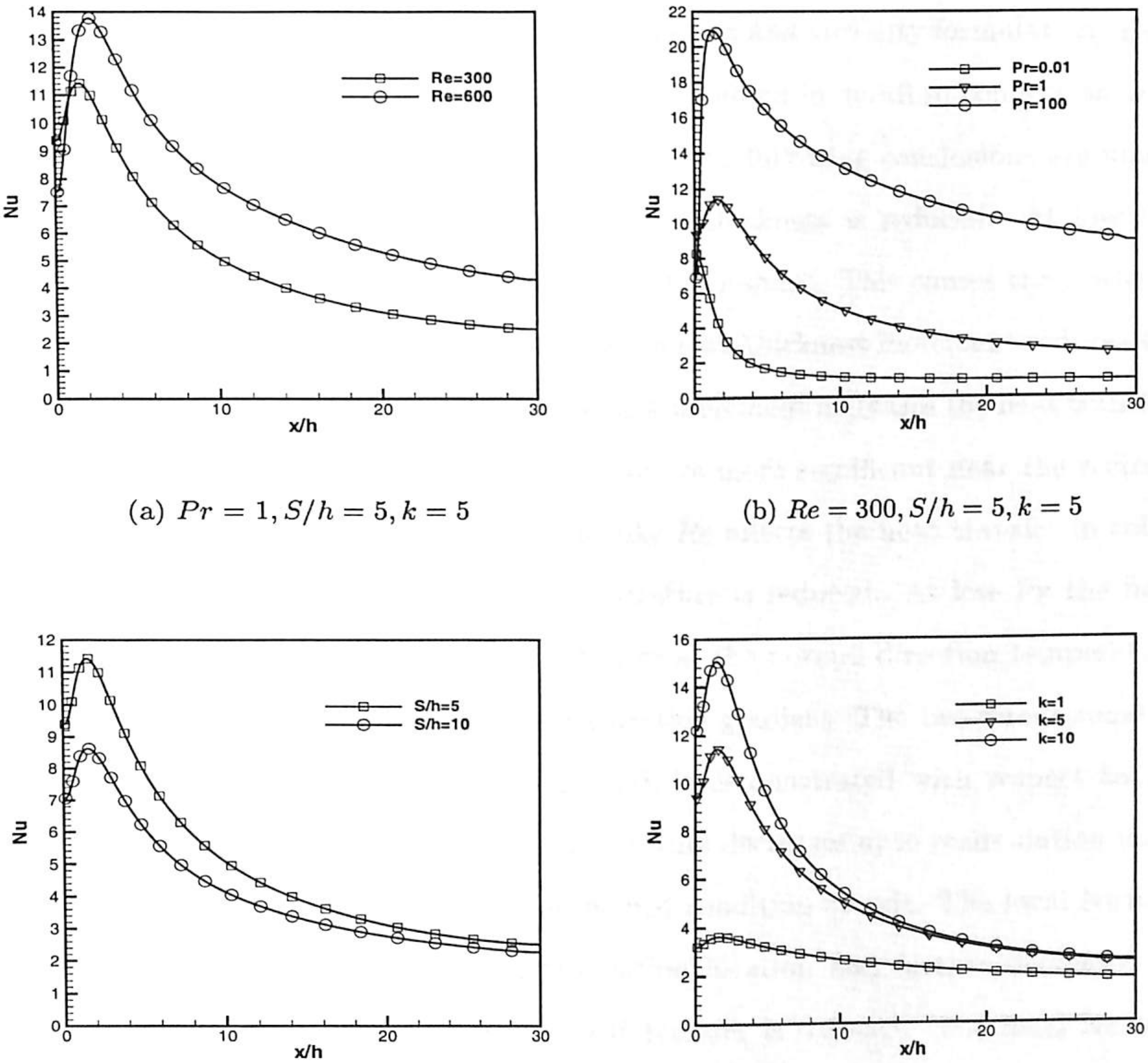

(a) $Pr = 1, S/h = 5, k = 5$ (b) $Re = 300, S/h = 5, k = 5$

(c) $Re = 300, Pr = 1, k = 5$ (d) $Re = 300, Pr = 1, S/h = 5$

Figure 6.13: Local Nusselt number (Nu): Effect of $Re, Pr, S/h, k$

6.5 Conclusions

Conjugate heat transfer study of two-dimensional incompressible nonbuoyant offset jet is solved by unsteady stream function and vorticity formulation. Heat transfer characteristics are systematically studied in detail in connection with four parameters viz. $Re, Pr, S/h$, and k. The following conclusions are made. When Re is increased, the thermal layer thickness is reduced. At low Pr, conduction mode of heat transfer is more dominant. This causes the isotherm to spread well in the domain. Increase in slab thickness increment reduces the magnitude of the heat transfer whereas k increment increases the heat transfer. In solid slab the effect four parameters are more significant near the recirculation region. The property of fluid like Re affects the heat transfer in solid. When Re is increased the slab temperature is reduced. At low Pr the heat transfer across the slab is more. At low k, the normal direction temperature gradient is higher than streamwise direction gradient. The two-dimensionality nature of heat transfer within the slab is demonstrated with respect to Pr and k. The conjugate interface temperature decreases upto recirculation location and further increases to a developed condition at exit. The local Nusselt number is maximum at the recirculation location and further decreased in the downstream direction where heat transfer is reduced. The local Nusselt number is increased when Re is increased and the peak Nu is shifted in downstream direction. With increase in the fluid property Pr, Nu is increased. The relative increase is more from 1 to 100 compared to 0.01 to 1. For low Pr, Nu becomes developed (constant) very close to the jet inlet (i.e. at recirculation region). The variation of Nu value is more sensitive near the recirculation region. Average Nu is increased when Re, Pr and k are increased. It is decreased when solid wall thickness is increased.

Acknowledgement

The present results are accepted for publication in *Numerical Heat Transfer, Part A: Application*. The helpful comments of the reviewers of the journal are sincerely acknowledged.

Chapter 7

Study of Wall Jet Over Backward-facing Step

7.1 Introduction

This chapter discusses the hydrodynamic study of plane wall jet flow over backward-facing step. The flow emanating from a two-dimensional (2D) plane wall jet is shown in Fig. 7.1(a) where the main features and regions of interest are depicted. Fluid is discharged from a slot along vertical wall into the ambient near a horizontal solid boundary parallel to the inlet jet direction. The jet flow features are different in various regions. In the near-field upto step from the point of discharge, the jet behaves like plane wall jet. Further the jet expands across the step. Due to entrainment between the solid wall and the jet there is a reduction of pressure in this region forcing the jet to deflect towards the boundary and eventually attach with it. This is called Coanda effect. In the region around the attachment point, that is, the impingement region and part of the recirculation region, the jet can be partly characterized as an impingement jet. The jet becomes a wall jet in the far field. Other factors like free-stream velocity, ambient stratification, buoyancy (density difference), discharge orientation etc. further complicate the jet-boundary interaction and the behavior of an wall jet.

Wall jet flow over step occurs in many industrial situations like electronics cooling, refrigerated air curtain, paper industry, electrical motor cooling etc. The understanding of the flow behavior of wall jet under step is important in engineering practices. If attachment is not desired for more mixing, a knowledge of calculation and design is required to prevent it. For a case where attachment is desirable, study of the involved variables is required so that a precise location of the attachment point and the containment of the flow can be established.

The effect of channel length in the backward-facing step is studied by Barton [35]. For similar geometry for the pulsatile inlet condition heat transfer results reported by Valencia and Hinojosa [71]. Jacob *et al* [72] investigated the sound radiation by a backward facing step under a plane wall jet.

Though many studies have been conducted on wall jet, the available literature on theoretical simulation of plane laminar wall jet under step jet flow is not carried by anybody. The case of an entraining jet located near the jet discharge, which occur in several practical applications, has not been studied. In the present study, a time marching incompressible flow solver has been applied for simulating the flow features of wall jet for a range of aspect ratios and Reynolds number.

7.2 Mathematical Formulation

An incompressible two-dimensional laminar wall jet under backward-facing step jet flow is considered. The surrounding medium of wall jet may be quiescent or co-flow or counter-flow depending upon the applications. In the present case, the surrounding is considered to be quiescent. For the sake of simplicity, the jet is assumed to be isothermal and having the same density as the ambient fluid. Also, the velocity profile at the jet inlet is taken as parabolic. The governing equations in non-dimensional form (Eq. 2.8 and Eq. 2.9) are solved.

The boundary conditions needed for the numerical simulation have been prescribed. For an wall jet with entrainment, the following dimensionless conditions have been enforced as shown in Fig. 7.1(b). The inlet slot height is assumed as, $h = 0.05$.

At the jet inlet, along AG (Fig. 7.1(b)),

$$u(y) = 120y - 2400y^2; \quad \omega(y) = 4800y - 120; \quad \psi(y) = 60y^2 - 800y^3 \tag{7.1a}$$

Along FG, AB, BC and CD due to no-slip condition,

$$u = v = 0 \tag{7.1b}$$

Along EF,

$$\frac{\partial u}{\partial x} = 0 \tag{7.1c}$$

At downstream boundary, the condition of zero first-derivative has been applied for velocity components. This condition implies that the flow has reached a developed condition. Thus, at (DE),

$$\frac{\partial u}{\partial x} = \frac{\partial v}{\partial x} = 0 \tag{7.1d}$$

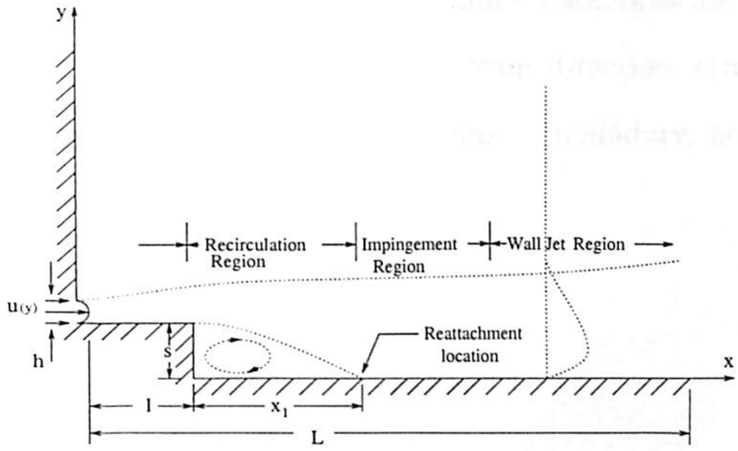

(a) Schematic diagram of plane wall jet under step

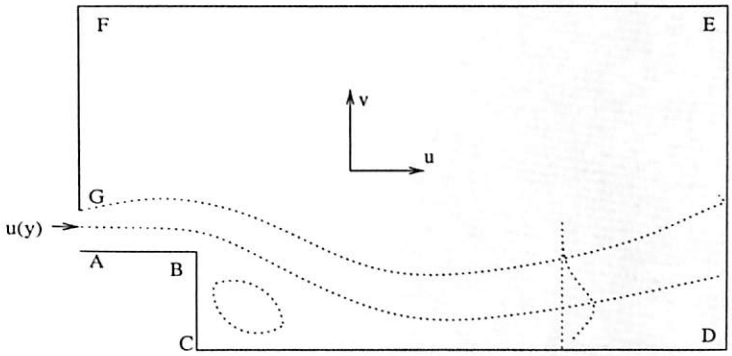

(b) Computational domain

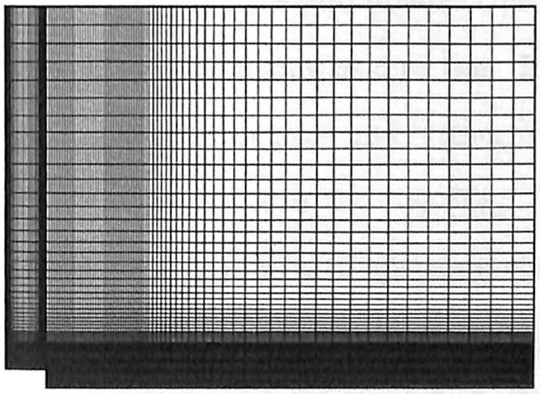

(c) Grids used for the computation

Figure 7.1: Schematic diagram and boundary conditions in a wall jet under backward-facing step problem

At the bottom wall and the left side wall, constant stream lines are assumed based on inlet flow. At the outlet in the downstream direction, stream-wise gradients are assumed to be zero. At the entrainment boundary, normal velocity gradient is zero [58].

The detailed boundary conditions are,

along FE (Fig. 7.1(b)),

$$\omega(y) = \frac{2(\psi_w - \psi_{w+1})}{\triangle x_1 * \triangle x_1};\ \psi = 0.05 \tag{7.2a}$$

along BA,

$$\omega(y) = \frac{2(0 - \psi_{w+1})}{\triangle x_1 * \triangle x_1};\ \psi = 0 \tag{7.2b}$$

along BC,

$$\omega(x) = \frac{2(0 - \psi_{w+1})}{\triangle y_1 * \triangle y_1};\ \psi = 0 \tag{7.2c}$$

The computational domain considered here are clustered cartesian grids. In Eq. 2.11 $\kappa = 0.7$ is used for generating the grid points. Upto $x = l$, $\vartheta = 2\pi$ is used and further $\vartheta = \pi$ is used in the streamwise direction. In normal direction upto slot inlet height uniform grids are used and further $\vartheta = \pi$ clustering is followed. Thus more grids are clustered near the step (Fig. 7.1(c)). Similar grids used to solve backward-facing step flow with upstream channel problem. It is presented in Appendix F. The unsteady vorticity transport equation (2.9) in time is solved by Alternate Direction Implicit scheme (ADI). For the computation, time step 0.0001 is used. The convergence criteria is set as sum of vorticity error in Eq. 2.22 is reduced to either $\varepsilon < 10^{-4}$ or large total time.

7.3 Validation of the Code

Wall jet flow over backward-facing step flow consists sudden expansion in the downstream direction, reattachment and further expansion in streamwise direction. To validate this simulation two split domain problems are solved. L shape lid driven cavity flow is solved and the velocity profiles are compared with Oosterlee et al. [60]. The computed results are presented in Appendix E. For inflow and outflow condition backward-facing step flow with upstream channel is solved and the reattachment length is compared with Barton [35]. Backward-facing step with different expansion ratios are tested and reattachment length is compared with Valencia and Hinojosa [71] and Thangam and Knight [73] (Appendix F). There is a good agreement between the present simulation and benchmark results.

7.4 Grid Independent Study

The domain has chosen as $25\times h$ in streamwise direction from the step and $20\times h$ in normal direction. For grid independence study reference case considered is $Re = 400, l = 2h$ and $s = 1h$. Four grid systems 61×51, 71×61, 97×85 and 127×125 are considered. The variation in the reattachment length is less than 2.5% and 97×85 grid system is used for the entire computation. The grids are clustered near the step and solid walls. Uniform grids are followed for inlet to ensure that parabolic velocity profile falls exactly at inlet slot. Typical grids are shown in Fig. 7.1(c)

7.5 Results and Discussion

The parabolic profile, issuing from inlet slot, and spreads over a plane wall and further expands across a backward-facing step. It reattaches on the bottom wall due to Coanda effect and spreads along the wall (Fig. 7.1(a)). The length between the step and the reattachment point is called reattachment length (x_1, Fig. 7.1(b)). The flow in the domain has the nature of wall jet, recirculation, developing and wall jet at far downstream. Before flow expands from the step, it behaves like a plane wall jet. However due to entrainment, self similarity nature is not obtained at this length. To understand the flow physics of the present situation three parameters considered here are $Re(=\overline{U}h/\nu)$, step length (l) and step height (s). Results are presented here for $l = 1h, 2h, 3h$ and $s = 0.5h, 1h, 2h$. Since at low Re the jet has difficulty to overcome the downstream friction [26], Re has been chosen between 300 to 600. The clustered grids are used for the computations. *Tecplot* 9.0 [66] is used for extracting the values for any particular location.

Figure 7.2 shows the streamline contours for a range of the parameters Re, l and s. The streamline contours illustrate the main jet flow, recirculation and entrainment flow. When Re increases from 300 to 600, the main flow is confined towards the bottom wall. Particularly after the step, the jet deflects towards the bottom wall (Fig. 7.2(a) and Fig. 7.2(b)). The size of the recirculation eddy is increased considerably. At low *Re* the jet spreads more in the normal direction which causes the reduction in ambient fluid flow. It is noticed that increase in length of the step reduces the reattachment length (Fig. 7.2(c) and Fig. 7.2(d)). When height of the step is increased the main flow deflects towards the bottom wall. Recirculation eddy size is increased (Fig. 7.2(e) and Fig. 7.2(f)). At exit, the streamlines become parallel and thus the assumption for fully developed flow is satisfied. Near the bottom wall, streamlines are less denser in order to satisfy the no-slip conditions along the walls. The effect of these parameters on vorticity is shown in Fig. 7.3. Near the bottom wall u velocity gradient is greater in the normal direction than v velocity gradient in the streamwise direction. It is noticed that when *Re* increases this is magnified (Fig. 7.3(a) and Fig. 7.3(b)). At longer step vorticity values is reduced (Fig. 7.3(c) and Fig. 7.3(d)). However when height of the step is increased u velocity normal direction gradient is increased (Fig. 7.3(e)).

Walls are the sources of vorticity. Here solid walls exist along AB, BC, CD and FG (Fig. 7.1(b)). Effect of *Re* and step geometry on wall vorticity are presented in detail from Fig. 7.4 to Fig. 7.6. Vorticity distributions are shown for vertical walls followed by horizontal walls. The effect of *Re* on vorticity along BC is shown in Fig. 7.4(a). Along step height vorticity is in positive direction and its value is increased when *Re* is increased. However the maximum vorticity is occurred at same height (y=0.833h). It is important to note that along BC there are two singular corner points existing. Roache [54] reported in detail about how to treat these corner singular points. However at high *Re* he concluded that those forms are less efficient. Above inlet, left wall causes vorticity mainly due to the entrainment of the ambient fluid. Vorticity is generated by the left wall upto maximum of $y = 2h$ above the inlet and further it approaches zero (Fig. 7.4(b)). At higher *Re* it increases in negative direction. This is attributed due to high entrainment towards the inlet. The vorticity is generated due to negative v velocity gradient. Along step length vorticity varies exponentially (Fig. 7.4(c)). When *Re* increases it tends towards negative direction because the normal direction u gradient is increased. Along CD wall vorticity varies its direction from positive to negative in downstream direction. From the step it increases in positive direction and decreases. After reattachment its direction is changed to negative direction. Further it increases monotonically (Fig. 7.4(d)). However at far from the reattachment it becomes invariant at high *Re*.

Effect of step length on vorticity is shown in Fig. 7.5. It is noticed that when length of the step is increased, wall vorticity on BC is decreased (Fig. 7.5(a)). However the maximum values is occurred at same height. When length increased left wall vorticity is decreased (Fig. 7.5(b) due to reduction of entrainment. Figure 7.5(c) shows the effect of change in step length on vorticity. It is observed that when length increases the wall vorticity decreased for the same distance. Along length of the step vorticity value tends towards positive direction. It is noticed that the vorticity along CD is affected by the upstream step length (Fig. 7.5(d)). The peak value of the vorticity in any direction is reduced for longer step length. However at far downstream the effect of step length is less significant. The effect of step height is shown in

Fig. 7.6. Along BC the vorticity is increased in positive direction to a maximum value. As the top corner is approached tends towards negative direction. The magnitude is increased when step height is increased (Fig. 7.6(a)) due to large recirculation which causes more positive v velocity gradient. Along FG, magnitude of the vorticity is less affected by the variation in height. However due to more entrainment at high step height negative vorticity is generated at far away from the inlet (Fig. 7.6(b)). The variation in step height does not have significant effect on the vorticity along step length (Fig. 7.6(c). Thus the separation in the flow less significant for the upstream flow wall vorticity. It is noticed that positive direction peak value is higher for $s = 2h$ and negative direction peak value is higher for $s = 0.5h$ (Fig. 7.6(d)).

Wall jet boundary layer thickness (δ) is the normal distance where $u = 0.5u_{max}$. The similarity u velocity profile at different downstream location is compared with experimental [15] and similarity [1] results (Fig. 7.7 for $Re = 400, l = 2h$ and $s = 1h$). The u velocity profiles at locations middle of step length ($x = 1h$), reattachment point ($x = 2.874h$) and inlet are shown in Fig. 7.7(a). Due to entrainment negative direction velocity value is presented. The same at further downstream locations is shown in Fig. 7.7(b). After reattachment, flow is under development to certain distance. Location $x = 5h$ corresponds to the developing region velocity profile. Wall jet region similarity profiles are shown in Fig. 7.7(c). Present computations show excellent agreement with experimental and similarity results for inner region as well as outer region of the wall jet. However at further downstream locations, the jet expands in the normal direction and thus it is not having agreement with similarity solution at entrainment location free shear layer. Whereas the experimental result shown here is chosen from one particular location where it satisfies with the similarity. The length from the step to the wall jet region, *i.e.* where the similarity profiles begins and close form solutions of wall jet can applicable, is measured for different Re and step geometry. It is observed that when the Re is increased due to more entrainment similarity rising distance also increased (Table 7.1). When length increases this distance is reduced due to reduction of entrainment. However this distance is larger for zero step length case (Table 7.2). This is caused by the entrainment. It is observed that when step height increases this distance is reduced (Table 7.3). The effect of the step height on the upstream velocity is shown in (Fig. 7.8). The local u velocity at $x = 1h$ location is compared with different step height. It is noticed that the downstream step height variation does not affect the local u velocity at upstream. The maximum u velocity in the normal direction from the entire downstream direction is presented for different Re are shown in Fig. 7.9. The local normalised (*i.e.* u_{max}/U_{max}) u_{max} is decayed monotonically in downstream direction finally reaching an asymptotic condition. Corresponding normalised y location (*i.e.* y/h) is shown in Fig. 7.9(b). It is noticed that when Re increases jet u_{max} location (y/h) shifts down. The reattachment length of

Table 7.1: Effect of Re on wall jet similarity region distance. $l = 2h, s = 1h$

Re	x/h
300	7.72
400	7.74
500	7.99
600	8.33

Table 7.2: Effect of step length on wall jet similarity region distance. $Re = 300, s = 1h$

Length of the step	x/h
$l = 1h$	8.84
$l = 2h$	7.72
$l = 3h$	6.42
$l = 0h$ [74]	14.24

Table 7.3: Effect of step height on wall jet similarity region distance. $Re = 300, l = 2h$

Height of the step	x/h
$s = 0.5h$	9.65
$s = 1h$	7.74
$s = 2h$	7.56

Table 7.4: Effect of step length on primary vortex reattachment length. Percentage of reduction from $l = 1h$: $s = 1h$

Re	x_1/h for $l = 1h$	% of reduction if $l = 2h$	% of reduction if $l = 3h$
300	2.378	10.51	15.39
400	2.389	6.28	11.01
500	2.514	5.09	10.02
600	2.643	5.15	9.72

Table 7.5: Effect of step height on primary vortex reattachment length. Percentage of variation from $s = 1h$: $s = 1h$

Re	x_1/h for $s = 1h$	% of increment if $s = 2h$	% of reduction if $s = 0.5h$
300	2.128	118.65	58.51
400	2.239	113.31	60.87
500	2.386	104.48	57.88
600	2.507	100.03	55.08

all the cases considered here are presented in Fig. 7.10. It is observed that the increase in step length reduces the reattachment length. However it is noticed that the reattachment length is reduced when the step length is absent [74]. This is mainly due to the heavy entrainment near the expansion of the jet. When step height increases, increase in recirculation length is observed. However the variation in x_1 is very sensitive to step height than step length (Table 7.4 and Table 7.5).

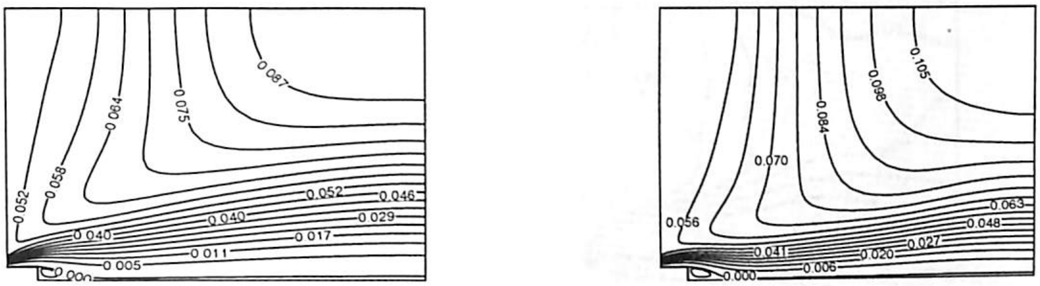

(a) $l = 2h, s = 1h, Re = 300$

(b) $l = 2h, s = 1h, Re = 600$

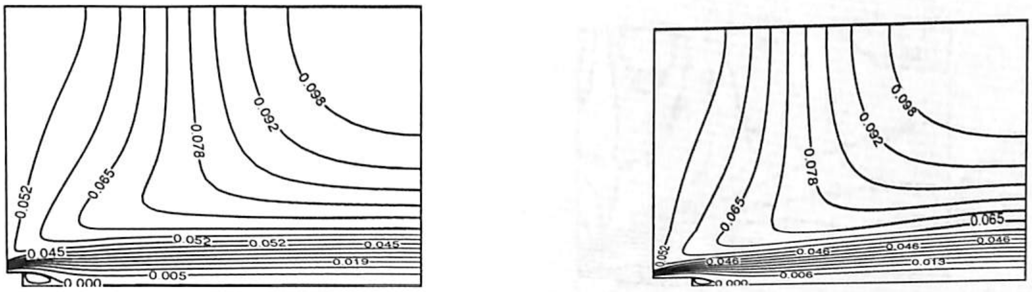

(c) $l = 1h, s = 1h, Re = 400$

(d) $l = 3h, s = 1h, Re = 400$

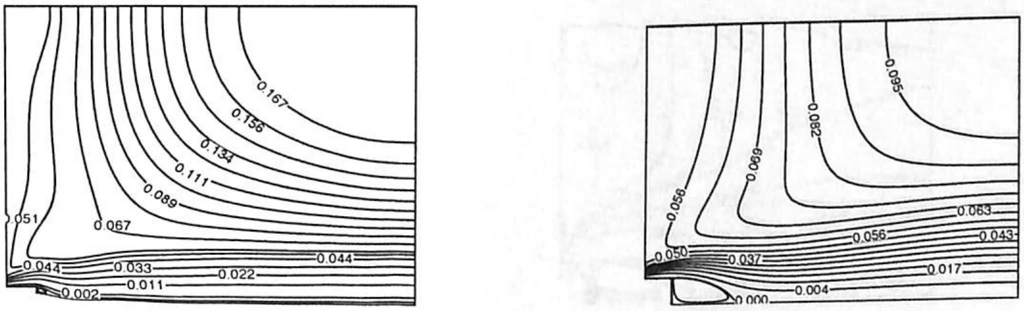

(e) $l = 2h, s = 0.5h, Re = 400$

(f) $l = 2h, s = 2h, Re = 400$

Figure 7.2: Streamline contour

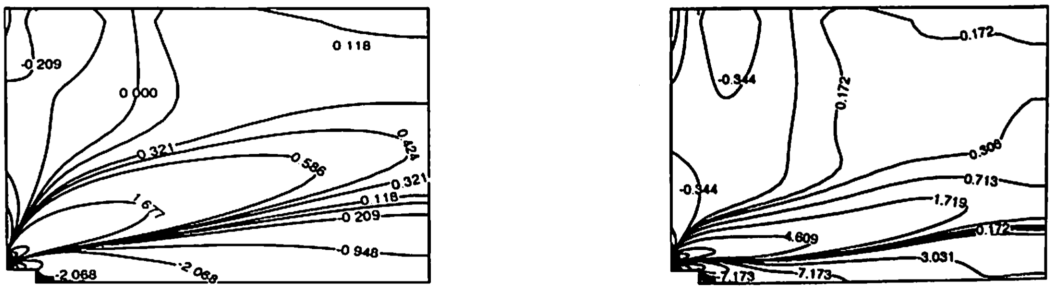

(a) $l = 2h, s = 1h, Re = 300$ (b) $l = 2h, s = 1h, Re = 600$

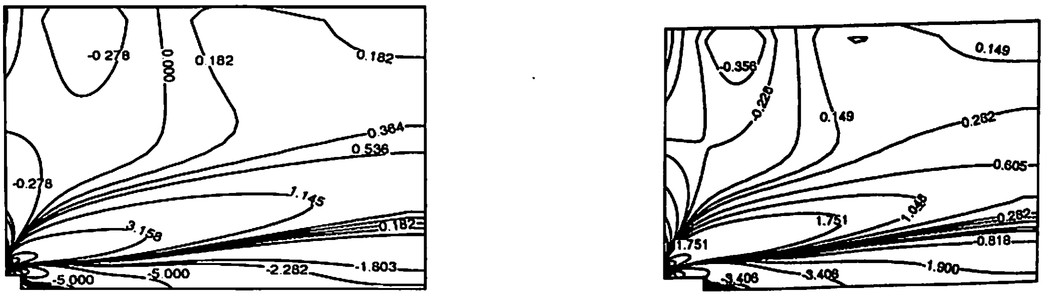

(c) $l = 1h, s = 1h, Re = 400$ (d) $l = 3h, s = 1h, Re = 400$

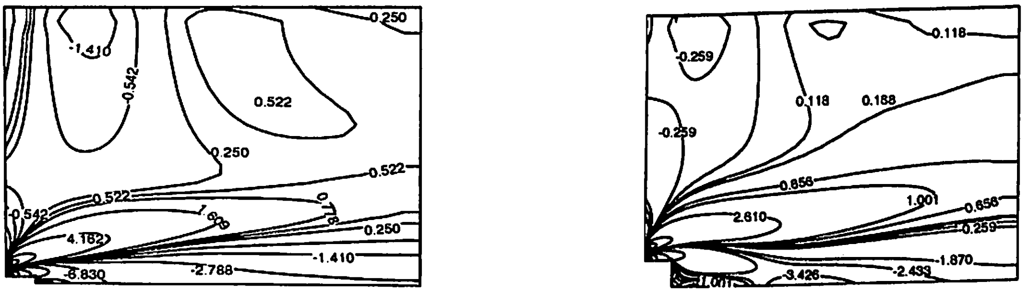

(e) $l = 2h, s = 0.5h, Re = 400$ (f) $l = 2h, s = 2h, Re = 400$

Figure 7.3: Vorticity contour

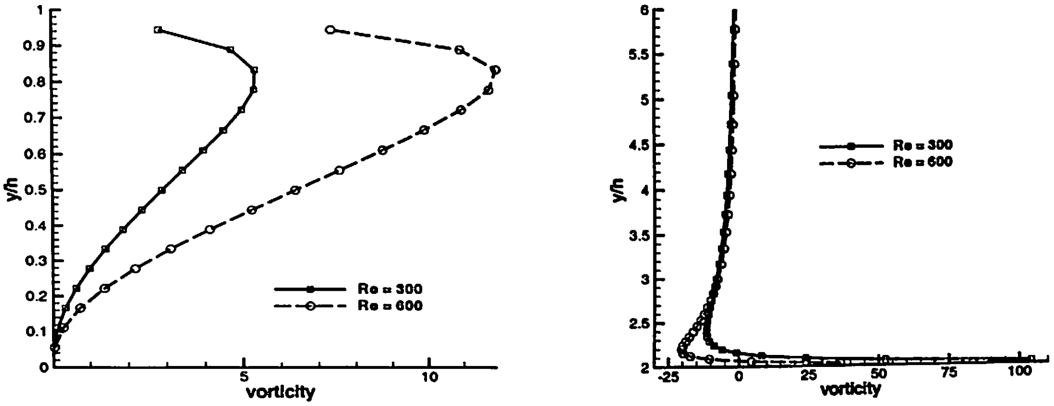

(a) Vorticity along step height, BC

(b) Vorticity along left wall, FG

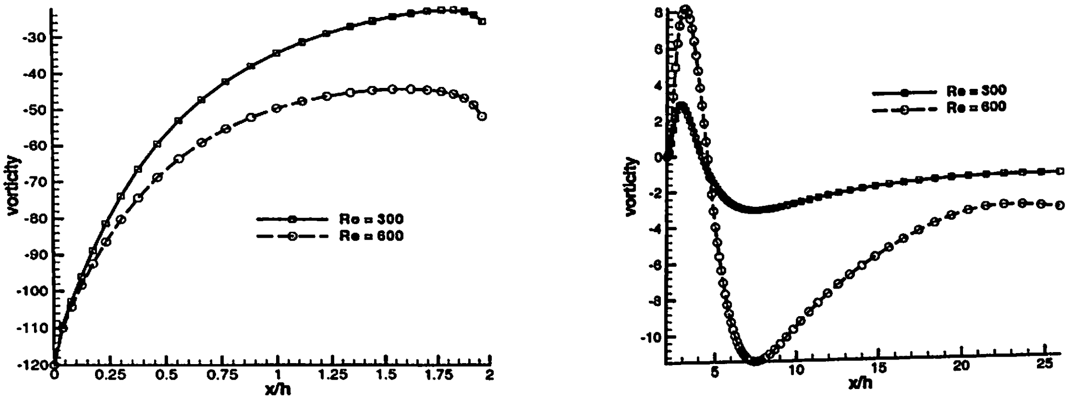

(c) Vorticity along step length, AB

(d) Vorticity along $(L-l)/h$, CD

Figure 7.4: Effect of *Re* on wall vorticity: $l = 2h, s = 1h$

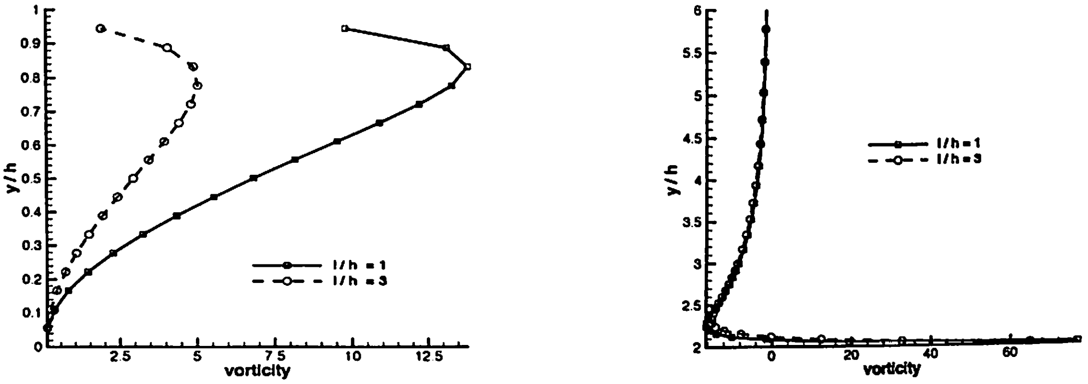

(a) Vorticity along step height, BC

(b) Vorticity along left wall, FG

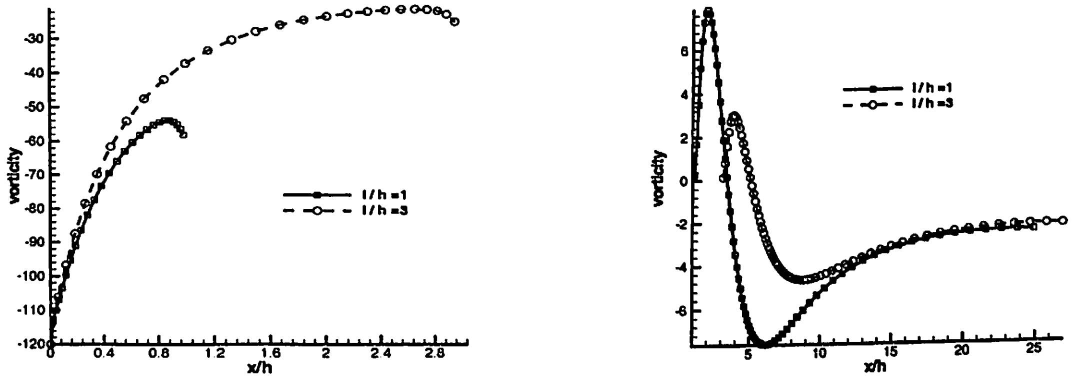

(c) Vorticity along step length, AB

(d) Vorticity along $(L-l)/h$, CD

Figure 7.5: Effect of step length on wall vorticity: $Re = 400, s = 1h$

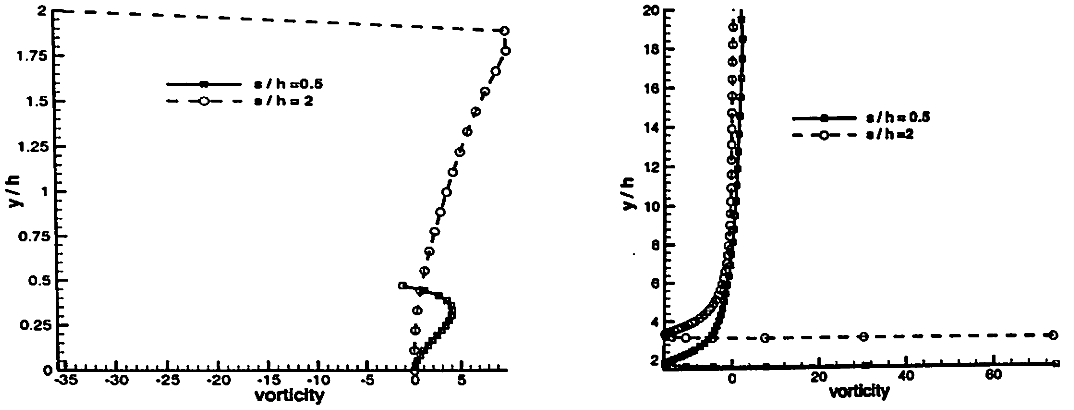

(a) Vorticity along step height, BC

(b) Vorticity along left wall, FG

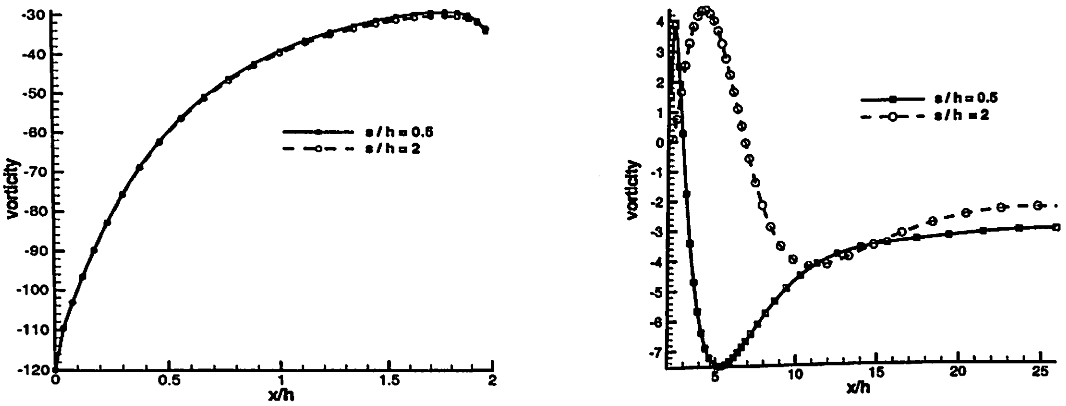

(c) Vorticity along step length, AB

(d) Vorticity along $(L-l)/h$, CD

Figure 7.6: Effect of step height on wall vorticity: $Re = 400, l = 2h$

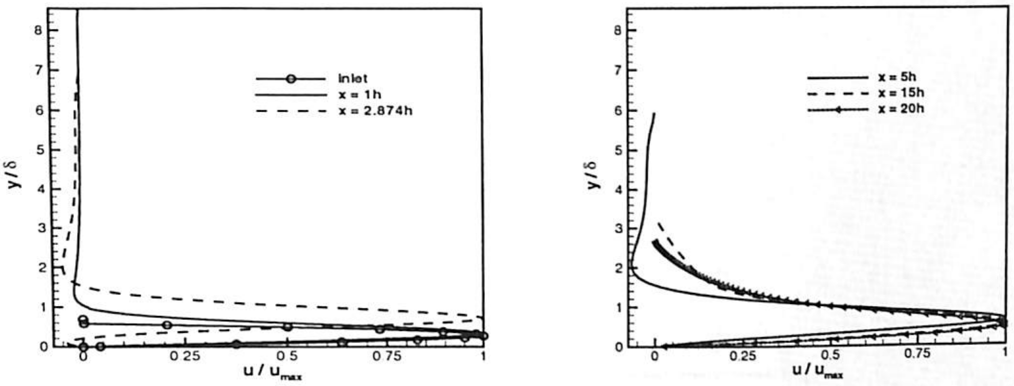

(a) Downstream location u velocity. contd.

(b) Downstream location u velocity. contn.

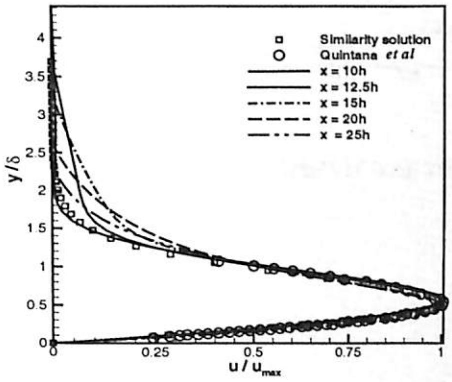

(c) Comparison of u velocity profile: Wall jet region

Figure 7.7: Similarity profile $Re = 400, l = 2h, s = 1h$

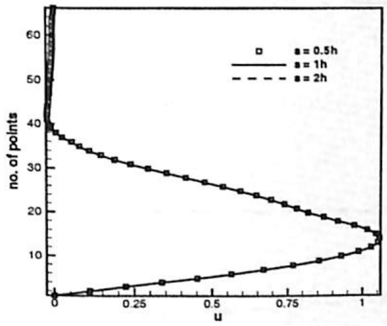

Figure 7.8: Effect of step height on upstream velocity at $x = 1h$: $Re = 400, l = 2h$

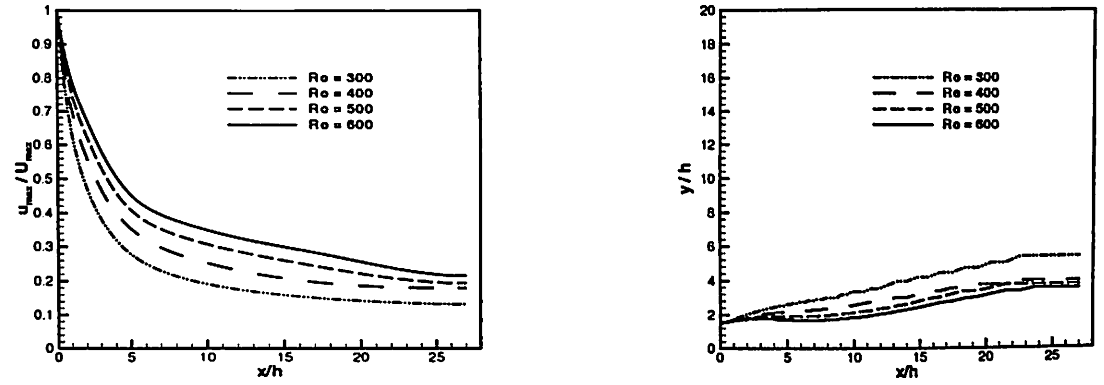

(a) Decay of local u_{max} (b) Location of local u_{max}

Figure 7.9: Local maximum u velocity: $l = 2h, s = 1h$

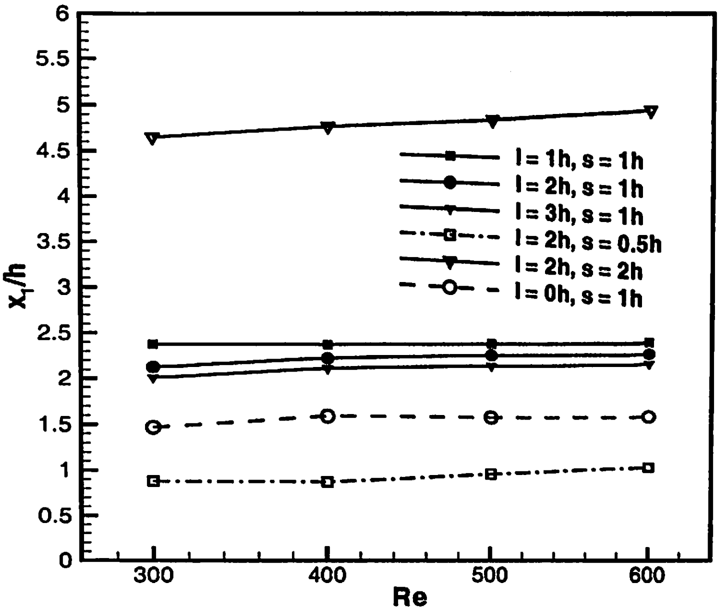

Figure 7.10: Reattachment length for different geometry and Reynolds number: ($l = 0h, s = 1h$ [74])

7.6 Conclusions

Two-dimensional incompressible nonbuoyant laminar wall jet under backward-facing step is solved by stream function and vorticity formulation considering the problem as asymptotic solution to the transient equation. The flow characteristics like strength of recirculation eddy, impingement length, decay of local velocity and wall jet region are studied in details in accordance with flow property and physical property. The entrainment is increased for high *Re* and it is less affected with change in step length. The reattachment length follows almost a linear trend with *Re* and step geometry. However it is more sensitive to step height than length. The upstream flow properties are not affected by expansion in the geometry. Vorticity from solid wall is affected by *Re*. The maximum vorticity location is independent of *Re* and step geometry. Vorticity from the step height is increased for higher *Re* and decreased if step length is increased. From left wall, vorticity is generated to few inlet slot height and further it is independent of *Re* and step geometry. At bottom wall vorticity changes its direction after reattachment point and further it decreases monotonically. The u_{max} location shifts down when *Re* is increased. Similarity is not occurred along step length due to entrainment. Similarity exists for the wall jet at far away from the reattachment. Due to shear of ambient and main flow similarity fails at outer region of wall jet. Similarity profiles formation distance reduced by increasing the step geometry. Whereas *Re* increment increases this distance. The bottom wall vorticity is considerably affected near the impingement region.

Chapter 8

Heat Transfer Study: Wall Jet Flow Over Backward-Facing Step

8.1 Introduction

This chapter discuss the heat transfer characteristics of plane wall jet over backward-facing step flow. The flow emanating from a two-dimensional (2D) plane wall jet under backward-facing step is shown in Fig. 8.1(a) where the main features and regions of interest are depicted.

Although many studies have been conducted on wall jet, the available literature suggests that theoretical simulation of the wall jet under backward facing step has not been carried out by any researcher. In the present study, forced convection heat transfer has been considered. The step length, step height and the bottom wall are maintained at constant higher temperature whereas the wall jet is at ambient temperature. The isotherm and Nusselt number variation are studied for a range of Re, Pr and step geometry.

8.2 Mathematical formulation

An incompressible two-dimensional laminar wall jet under backward-facing step jet flow is considered. In the present case, the surrounding is considered to be quiescent. For the sake of simplicity, the jet is assumed to be isothermal and having the same density as the ambient fluid. Also, the velocity profile at the jet inlet is taken as parabolic. The step is assumed to be adiabatic condition. The governing equations are in non-dimensional form Eq.2.8, Eq.2.9 and Eq. 2.10 are solved. The unsteady vorticity transport equation (2.9) in time is solved by Alternate Direction Implicit scheme (ADI). The details of ADI is presented in Chapter 3.3. The unsteady energy equation (2.10) in time is solved by Alternate Direction Implicit scheme (ADI). .

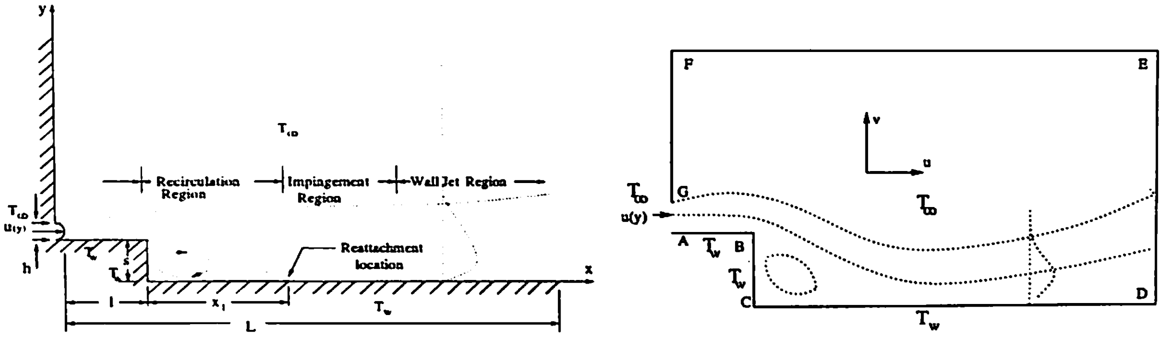

(a) schematic of the problem (b) Computational domain

Figure 8.1: Schematic diagram and boundary conditions in a wall jet under backward-facing step problem

The boundary conditions needed for the numerical simulation have been prescribed. For an wall jet with entrainment under backward-facing step, the following dimensionless conditions have been enforced as shown in Fig. 8.1(b). The inlet slot height (AG) is assumed as, $h = 0.05$.

At the jet inlet, along AG (Fig. 8.1(b)),

$$u(y) = 120y - 2400y^2; \quad \omega(y) = 4800y - 120; \quad \psi(y) = 60y^2 - 800y^3 \quad (8.1a)$$

Along GF, AB, BC and CD due to no-slip condition,

$$u = v = 0 \quad (8.1b)$$

Along EF,

$$\frac{\partial u}{\partial x} = 0 \quad (8.1c)$$

Along AB, BC and CD

$$\theta = 1 \tag{8.1d}$$

Along GF adiabatic,

$$\frac{\partial \theta}{\partial x} = 0 \tag{8.1e}$$

Along FE and AG ambient condition is assumed for θ. At downstream boundary the condition of zero first-derivative has been applied for velocity components. This condition implies that the flow has reached a developed condition. Thus, at DE,

$$\frac{\partial u}{\partial x} = \frac{\partial v}{\partial x} = \frac{\partial \theta}{\partial x} = 0 \tag{8.1f}$$

The detailed boundary conditions are,

along GF (Fig. 8.1(b)),

$$\omega(y) = \frac{2(\psi_w - \psi_{w+1})}{\Delta x_i * \Delta x_{i-1}};\ \psi = 0.05 \tag{8.1g}$$

along BC,

$$\omega(y) = \frac{2(0 - \psi_{w+1})}{\Delta x_i * \Delta x_{i-1}};\ \psi = 0 \tag{8.1h}$$

along AB and CD,

$$\omega(x) = \frac{2(0 - \psi_{w+1})}{\triangle y_j * \triangle y_{j-1}};\ \psi = 0 \tag{8.1i}$$

The Nusselt number expression is given by,

along AB,

$$Nu(x) = -\frac{\partial \theta}{\partial y}|_{y=1} \tag{8.2a}$$

along CD,

$$Nu(x) = -\frac{\partial \theta}{\partial y}|_{y=0} \tag{8.2b}$$

along BC,

$$Nu(y) = -\frac{\partial \theta}{\partial x}|_{x=2} \tag{8.2c}$$

The solution of the velocity field is done initially (Chapter 7). Using this velocity field, the energy equation is solved by ADI method. For the computation time step 0.001 is used for $Pr = 1.0, 100.0$, whereas for $Pr = 0.01$, time step 0.0001 is used. At steady state, the error reaches the asymptotic behavior. Here it is set as sum of temperature error from consecutive iteration reduced to either the convergence criteria (Eq. 2.23, $\varepsilon < 10^{-4}$) or large total time.

Table 8.1: Grid independence study: Value of $\overline{Nu}$: $Re = 400, Pr = 1.0, l = 2h$

	$\overline{Nu}$	
Grids	$s = 1h$	$s = 2h$
61 x 51	3.7201	3.5327
71 x 61	5.2815	4.9737
97 x 85	8.5249	7.9895
127 x 125	8.4397	7.9268

8.3 Grid Independence Study

The domain has been chosen as $25\times h$ in streamwise direction and $20\times h$ in normal direction. Systematic grid refinement study is carried out with 61×51, 71×61, 97×85 and 127×125 (Table. 8.1). Average Nusselt number variation is less than 1% between the last two grid systems and grid system 97×85 is chosen for the entire computations. The grids are clustered in streamwise direction whereas in normal direction along the inlet height, grids are arranged uniformly and above this region, they are clustered. Typical grids are shown in Fig. 8.2.

8.4 Results and Discussion

Flow spreads along the step length and separates at the corner and reattaches at the bottom of the wall due to Coanda effect. This length is called reattachment length (x_1, Fig. 8.1(a)). The heat transfer study has been done with four parameters considered here. They are Re ($\overline{U}h/\nu$), Pr, step length (l) and step height (s). Results are presented here for Re varying from 300 to 600 in steps of 100. Prandtl number considered are $Pr = 0.01, 1, 100$. The geometry of the step are step length $l = 1h, 2h, 3h$ and step height $s = 1h, 2h$. The detailed

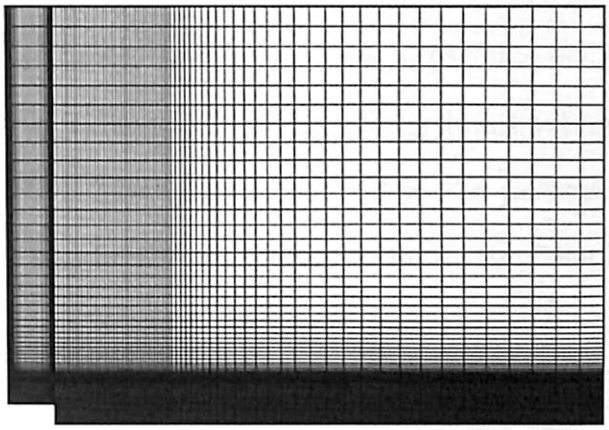

Figure 8.2: Typical grids used for the computation.

heat transfer results are presented for isotherm contour, Nusselt number and average Nusselt number for the four study parameters.

Isotherm pattern

Effect of Re on isotherm lines are shown in Fig. 8.3 for the case $Pr = 1, l = 2h$ and $s = 1h$. When Re increases, the isotherms are concentrated near the bottom wall (Fig. 8.3(a)-8.3(c)). This is attributed to the increment of convection at high Re. From the hydrodynamics solution, it is observed that the jet spread rate in normal direction is decreased at high Re. When Re is increased to 600 (Fig. 8.3(d)), a depression in the isotherms after the step is noticed. This is due to the reattachment of the jet where recirculation is more and the wall jet boundary layer starts developing. The surroundings is assumed to be quiescent at ambient condition. In this region the isotherm values are less than 6.3% of the bottom wall temperature ($\theta = 1$) (Fig. 8.3(a)-Fig. 8.3(d)).

The influence of Pr on the isotherms is shown in Fig. 8.4 for $Re = 400, l = 2h$ and $s = 1h$. At low Pr conduction heat transfer is dominant and at high Pr convection is dominant [37]. The same is evident in the present results (Fig. 8.4). Figure 8.4(a) shows the isotherm of low Pr fluid. Here the heat transfer occurs in the entire solution domain due to diffusion. For the low Pr fluid, since conduction is dominant mode of heat transfer, the heat is transferred to the quiescent medium. At $Pr = 100$ (Fig. 8.4(c), heat transfer occurs in the thin boundary layer of the main flow where the temperature gradient is high. Fig. 8.4(b) shows the intermediate effect of both kinds of heat transfer in the domain.

The effect of step geometry on the isotherm are presented in Fig. 8.5 and Fig. 8.6. The effect of step length is shown in Fig. 8.5 for $Re = 400, Pr = 1, s = 1h$. When length increases to $l = 3h$ (Fig. 8.5(a) - Fig. 8.5(d)) deflection of isotherm contour is reduced near the recirculation region. This is due to the jet expansion as the step length increases. Similar effects are present when step height increases (Fig. 8.6). This is due to large recirculation eddy.

Nusselt number

Local Nusselt number distribution is presented in detail for different cases in Figs. 8.7-8.10. Local Nusselt number distribution along the step length is shown in Fig. 8.7 for the case $Pr = 1, l = 3h, s = 1h$ for various Re. Near the inlet due to entrainment, Nu is very large. It is decreasing continuously in the downstream direction. When Re increases the local Nu along the step length is increasing (Fig. 8.7(a)). Effect of Pr along step length is presented in Fig. 8.7(b). When Pr increases Nu is increased due to the dominant convection heat transfer effect. The effect of Re and Pr on local Nusselt number distribution along the step height is shown in Fig. 8.8. Nu increases from the bottom of the step while reaching the top of the step (Fig. 8.8(a)). This is attributed to the interaction of the recirculation with the main stream. When Pr increases Nu increases sharply along the step height (Fig. 8.8(b)). Local Nu distribution along the bottom wall CD is presented in Fig. 8.9. Nu increases to a maximum and further decreases before reaching a developed state in the downstream direction (Fig. 8.9(a)). When Re increases Nu increases along the bottom wall. Also Nu increases when Pr is increased (Fig. 8.9(b)). The effect of upstream step geometry on the local Nusselt number of the bottom wall are presented in Fig. 8.10. When length of the step increases the local Nusselt number along the downstream bottom wall is reduced. For a case without step length , local Nu is increased along the bottom wall (Fig. 8.10(a)). This is mainly due to the entrainment near the inlet. When the step height increases local peak Nu is reduced. However in the downstream direction local Nu is increased (Fig. 8.10(b)). It is observed that the peak Nusselt number does not coincide with the reattachment location. It is shifted downstream from the reattachment location. Percentage of shift of this distance between reattachment location and peak Nusselt number are tabulated (Table 8.2-Table 8.3). It is observed that when the length is increased the distance is increased upto 52.8% whereas when height is increased the distance is reduced to 25.6%.

Boundary layer profile

The hydrodynamic as well as thermal boundary layer similarity profiles are presented in Fig. 8.11. δ is the wall jet boundary layer thickness, in the normal direction where the local u is equal to half of the local u_{max} [15]. Profiles are shown for locations $x/h = l/2, x_1, 8h$ and $20h$. This covers middle of the step, reattachment location, developing and wall jet region respectively. As the jet expands in downstream direction, the local u_{max} shifts in normal direction (Fig. 8.11(a)). Thermal similarity profile results are presented for different Pr. For low Pr a kink is observed at $x = 1h$ and further downstream it shows a linear trend in the downstream direction (Fig. 8.11(b)). In downstream direction the jet spreads well in the normal direction which causes the reduction of thermal boundary layer thickness ($x = 20h$, Fig. 8.11(b)). At high Pr thermal boundary layer thickness is small and increases in the downstream direction (Fig. 8.11(d)). Intermediate results are observed for $Pr = 1$ (Fig. 8.11(c)). It is observed that the boundary layers overlap with each other downstream of x/h=1.

Average Nusselt number

The variation of average Nusselt number with various parameters are shown in Fig. 8.12. When length of the step increases the average Nusselt number is decreased (Fig. 8.12(a)-Fig. 8.12(c)). However for no length case ($l = 0h$) average Nu is higher. This is due to the large amount of entrainment near the inlet. When Re increases average Nu is increased. The effect of step height on average Nu is presented in Fig. 8.12(d)-Fig. 8.12(f). At low Pr, when step

Table 8.2: Peak Nusselt number: $Re = 400, Pr = 1, s = 1h$

length	x_1/h	Peak Nu	% of shift from x_1/h
$l = 1h$	2.389	12.4212	20.33
$l = 2h$	2.239	9.6840	33.97
$l = 3h$	2.126	8.1315	52.84

Table 8.3: Peak Nusselt number: $Re = 400, Pr = 1, l = 2h$

length	x_1/h	Peak Nu	% of shift from x_1/h
$s = 1h$	2.239	9.684	33.94
$s = 2h$	4.476	7.963	25.62

height is increased average Nu is reduced (Fig. 8.12(d)). When Pr increases to 100 (Fig. 8.12(f), the effects are reversed. This is mainly attributed to the larger recirculation at higher step height.

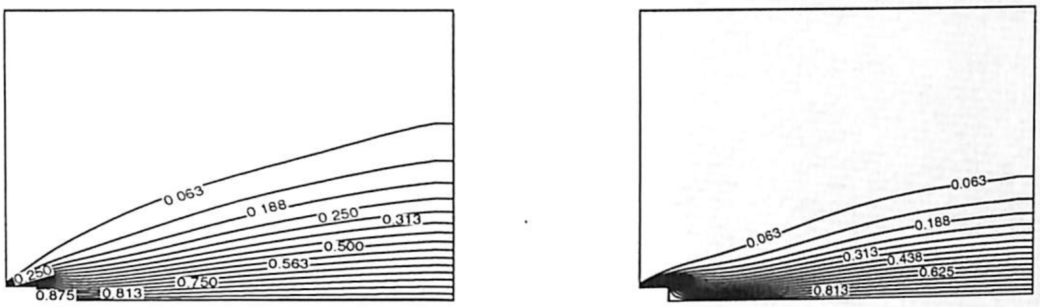

(a) $Re = 300, Pr = 1.0, l = 2h, s = 1h$ (b) $Re = 400, Pr = 1.0, l = 2h, s = 1h$

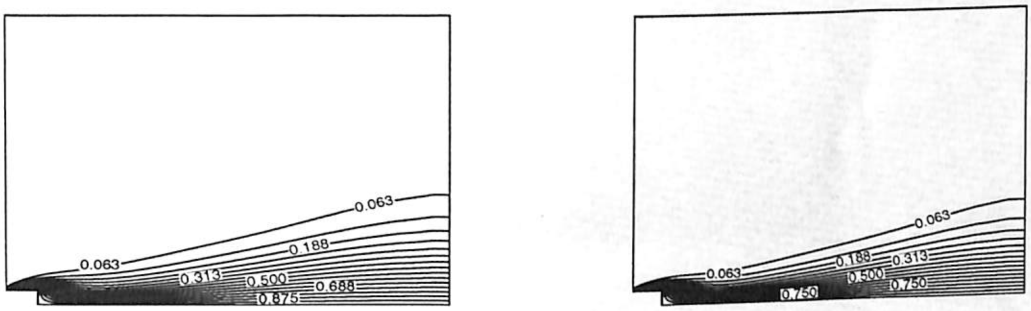

(c) $Re = 500, Pr = 1.0, l = 2h, s = 1h$ (d) $Re = 600, Pr = 1.0, l = 2h, s = 1h$

Figure 8.3: Effect of Re on Isotherm contour:

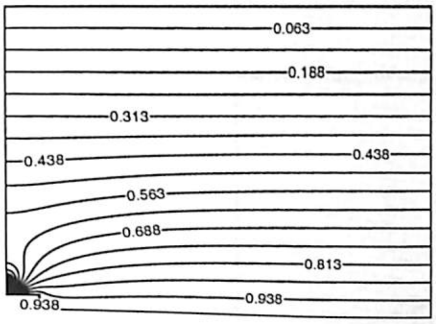

(a) $Pr = 0.01$

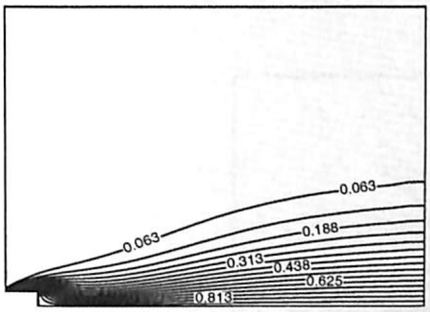

(b) $Pr = 1.0$

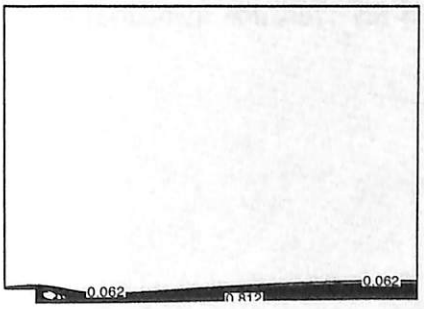

(c) $Pr = 100$

Figure 8.4: Effect of Pr on Isotherm contour:$Re = 400, l = 2h, s = 1h$

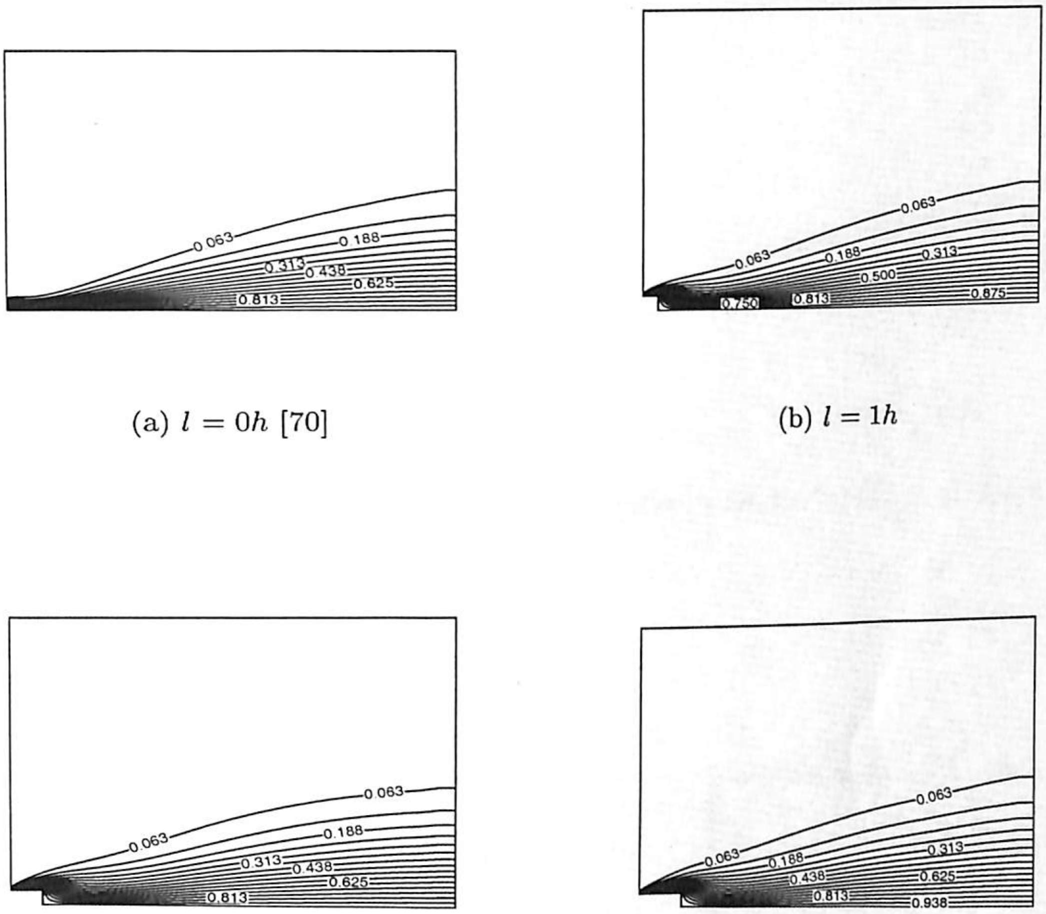

(a) $l = 0h$ [70]

(b) $l = 1h$

(c) $l = 2h$

(d) $l = 3h$

Figure 8.5: Effect of step length on Isotherm contour: $Re = 400, Pr = 1.0, s = 1h$

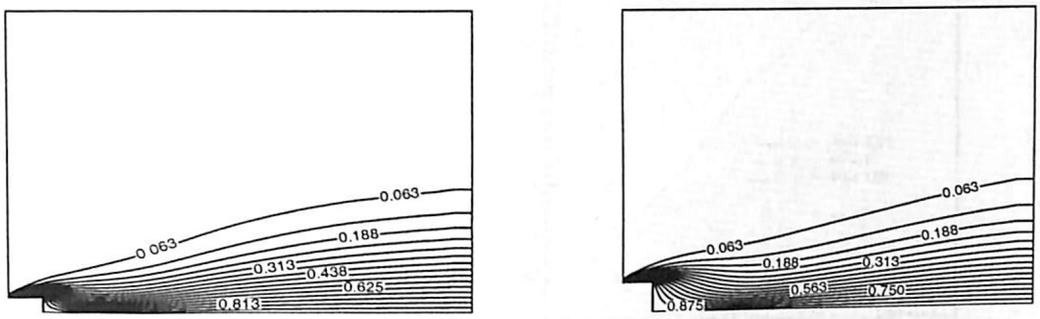

(a) $s = 1h$ (b) $s = 2h$

Figure 8.6: Effect of step height on Isotherm contour: $Re = 400, Pr = 1.0, l = 2h$

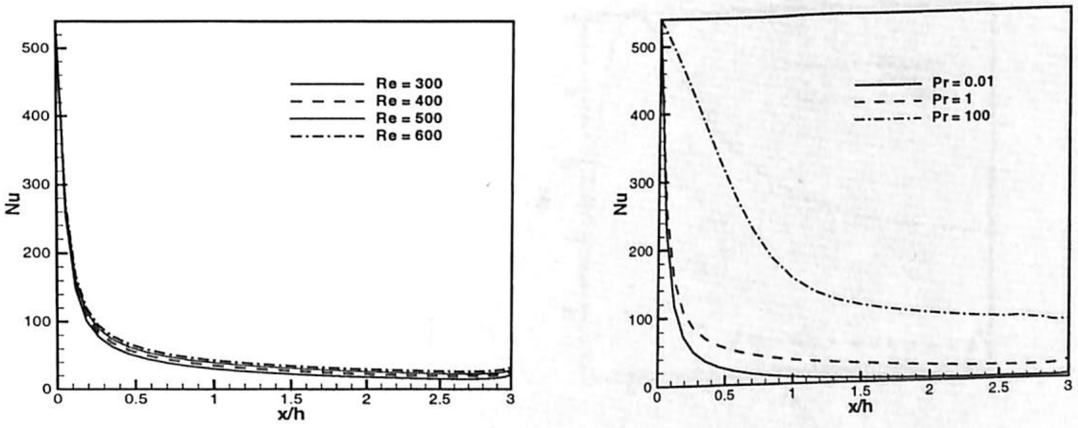

(a) $Pr = 1.0, l = 3h, s = 1h$ (b) $Re = 400, l = 3h, s = 1h$

Figure 8.7: Local Nusselt number distribution along step length, AB

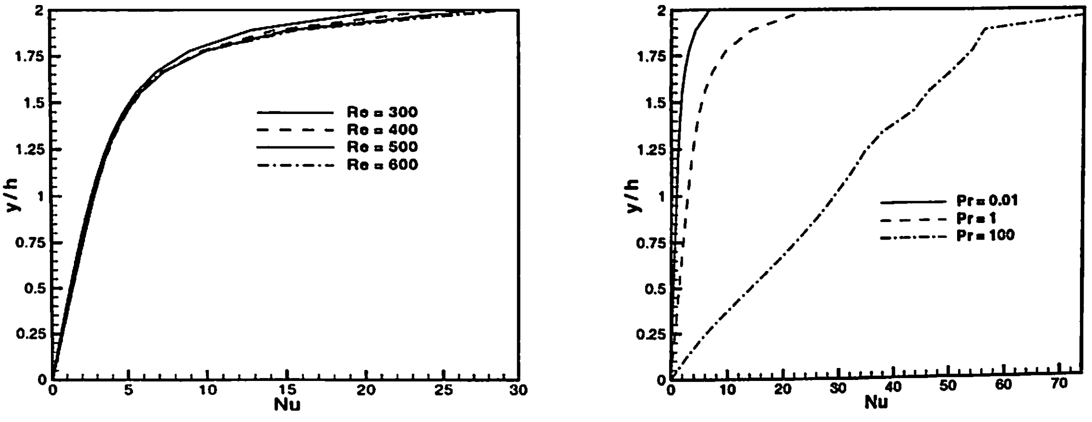

(a) $Pr = 1.0, l = 2h, s = 2h$ (b) $Re = 400, l = 2h, s = 2h$

Figure 8.8: Local Nusselt number distribution along step height, BC

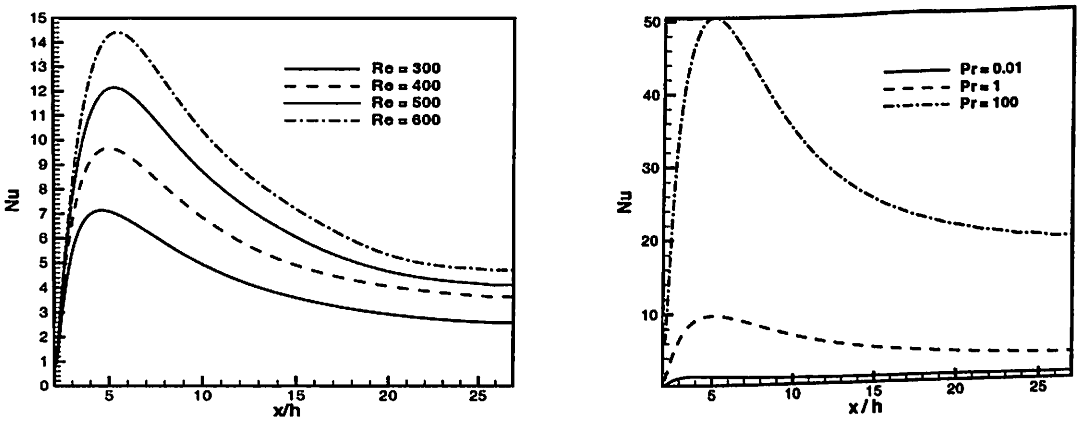

(a) $Pr = 1.0, l = 2h, s = 1h$ (b) $Re = 400, l = 2h, s = 1h$

Figure 8.9: Local Nusselt number distribution along bottom wall, CD

(a) $Re = 400, Pr = 1.0, s = 1h$

(b) $Re = 400, Pr = 1.0, l = 2h$

Figure 8.10: Effect of upstream geometry on local Nusselt number along bottom wall, CD

(a) $Re = 400, l = 2h, s = 1h$

(b) $Re = 400, Pr = 0.01, l = 2h, s = 1h$

(c) $Re = 400, Pr = 1.0, l = 2h, s = 1h$

(d) $Re = 400, Pr = 100.0, l = 2h, s = 1h$

Figure 8.11: Downstream u velocity and temperature similarity profile

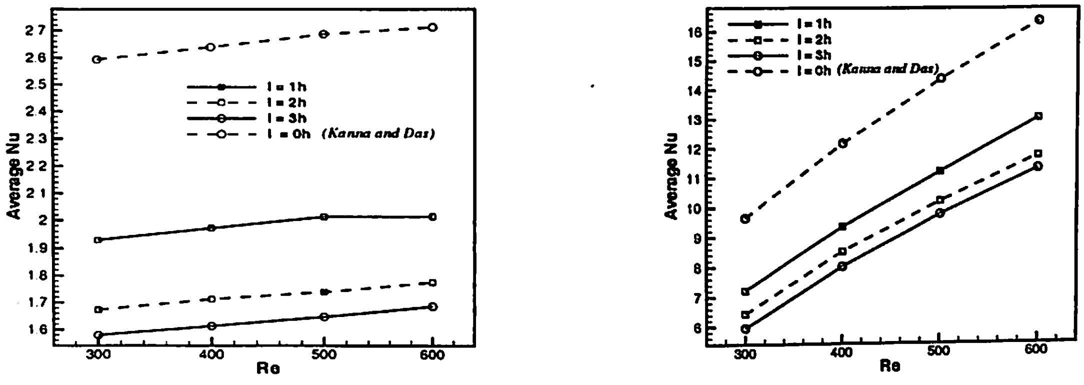

(a) $Pr = 0.01, s = 1h$

(b) $Pr = 1, s = 1h$

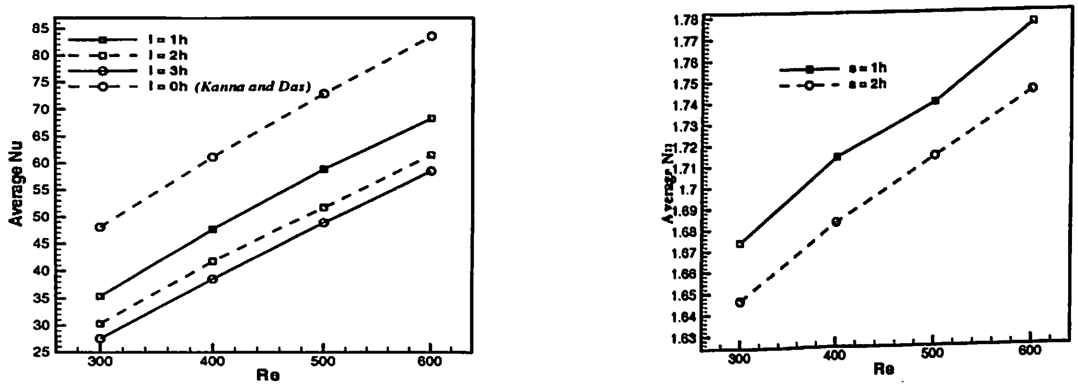

(c) $Pr = 100, s = 1h$

(d) $Pr = 0.01, l = 2h$

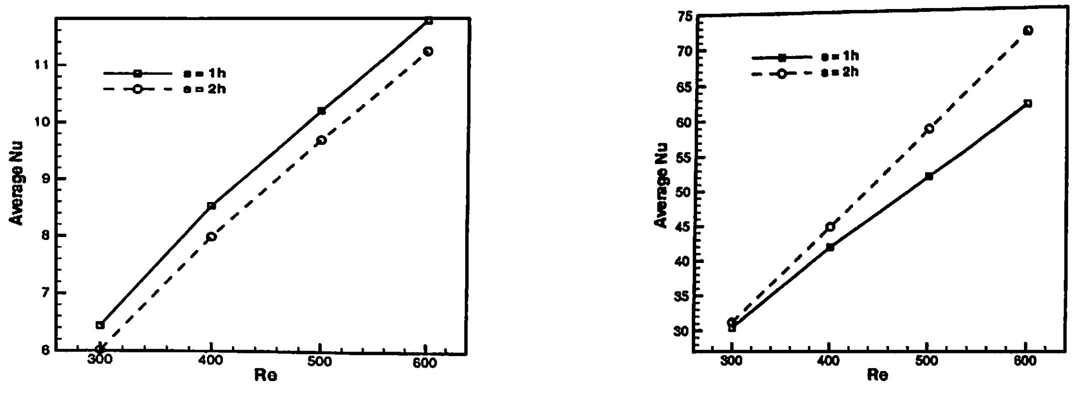

(e) $Pr = 1, l = 2h$

(f) $Pr = 100, l = 2h$

Figure 8.12: Effect of upstream geometry on average Nusselt number

8.5 Conclusions

Heat transfer study of two-dimensional incompressible nonbuoyant wall jet under backward facing step problem is carried out by solving the momentum equation and energy equation using stream function and vorticity formulation. Heat transfer characteristics are systematically studied in detail by varying four parameters viz. Re, Pr,length of the step (l) and height of the step (s) and the following conclusions are obtained.

When Re increases the isotherm deflected near the recirculation and clustered towards the wall. At low Pr conduction mode of heat transfer is dominant and isotherm spreads well over the quiescent medium. Whereas high Pr thin thermal layer is formed. Peak Nusselt number is occurred near the inlet due to entrainment. Second peak Nusselt number is occurred after the recirculation. This second peak Nusselt number always exist downstream of the reattachment location. When Re increases the local Nusselt number along the bottom wall is increasing to a peak value and monotonically reduced in the downstream direction. Increment in step height reduces the peak Nusselt number but increases the local Nusselt number in downstream direction. Average Nusselt number shows linear trend to Re and Pr. When the step length increases average Nu decreases. However it is noticed that zero step length causes higher average Nu. For high Pr, step height favour to high average Nu.

Chapter 9

Conjugate Study: Wall Jet Flow Over Backward-Facing Step - Part 1

9.1 Introduction

This chapter discusses the conjugate heat transfer study of wall jet over backward-facing step. The flow emanating from a two-dimensional plane wall jet over backward-facing step is shown in Fig. 9.1(a) where the main features and regions of interest are depicted.

Wall jet over step flow occurs in many engineering applications such as environmental discharges, heat exchangers, fluid injection systems, cooling of combustion chamber wall in a gas turbine, automobile demister and others. In electronics cooling the prediction of Nusselt number distribution along the step as conjugate situation is very important in thermal design point of view.

Although many studies on non-conjugate and conjugate heat transfer have been conducted on wall jet, the available literature suggests that theoretical simulation of the wall jet over backward facing step as conjugate case has not been carried out by any researcher. In the present study, forced convection heat transfer has been considered. The bottom wall is maintained at constant higher temperature whereas the wall jet is at ambient temperature. The temperature at interface (separating fluid from the slab) is obtained by satisfying the conjugate boundary condition criteria. The isotherm and Nusselt number variation are studied for a range of Re, Pr and conductivity ratio (k). The experimental study on laminar plane wall jet is presented in Bajura and Szewczyk [2]. Based on jet exit Reynolds number they reported laminar wall jet results upto $Re = 770$. Bhattacharjee and Loth [20] reported the early transition is begun about $Re = 700$ for plane wall jet. The present laminar study restricted to fall within this Reynolds number range.

9.2 Mathematical Formulation

An incompressible two-dimensional laminar wall jet under backward-facing step is considered. For the sake of simplicity, the jet inlet temperature is assumed to be isothermal and having the same density and temperature as the ambient fluid. Also, the velocity profile at the jet inlet is taken as parabolic. The solid slab bottom is kept at constant temperature and side walls of the slab are insulated. The step is assumed to be adiabatic condition. The solid slab bottom is kept at constant temperature and side walls of the slab are insulated. The governing equations are in non-dimensional form Eq. 2.8, Eq.

2.9, Eq. 2.10 and Eq. 2.24 are solved.

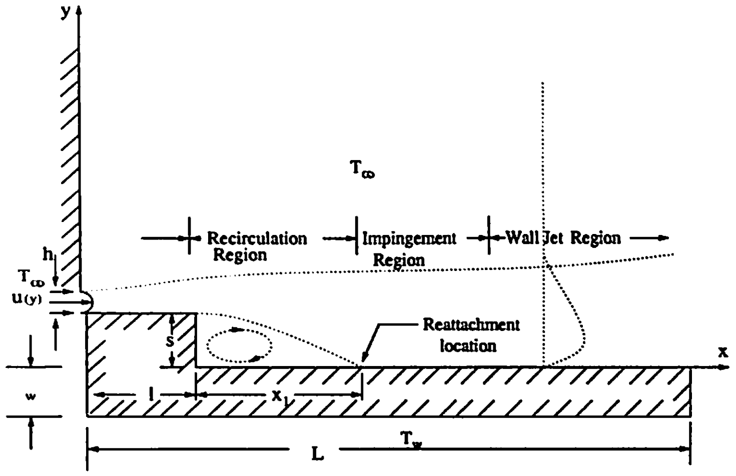

(a) schematic of the problem

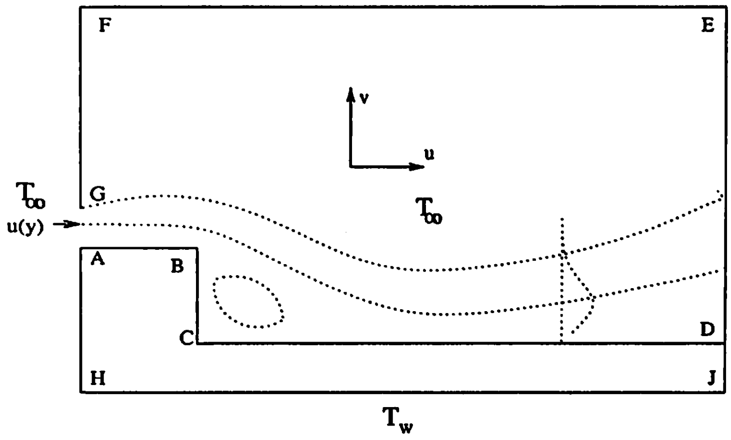

(b) Computational domain

Figure 9.1: Schematic diagram and boundary conditions in a wall jet over backward-facing step problem

The boundary conditions needed for the numerical simulation have been prescribed. For a wall jet with entrainment, the following dimensionless conditions have been enforced as shown in Fig. 9.1(b). The inlet slot height is assumed as, $h = 0.05$.

At the jet inlet, along AG (Fig. 9.1(b)),

$$u(y) = 120y - 2400y^2; \quad \omega(y) = 4800y - 120; \; \psi(y) = 60y^2 - 800y^3 \quad (9.1a)$$

Along AB, BC, CD and FG due to no-slip condition,

$$u = v = 0 \quad (9.1b)$$

Along entrainment boundary FE,

$$\frac{\partial v}{\partial y} = 0 \quad (9.1c)$$

Along HJ,

$$\theta = 1 \quad (9.1d)$$

Along AH, DJ and FG (adiabatic condition),

$$\frac{\partial \theta}{\partial x} = 0 \quad (9.1e)$$

Along FE and AG ambient condition is assumed for θ. At downstream boundary the condition of zero first-derivative has been applied for velocity components. This condition implies that the flow has reached a developed condition. Similar type of boundary condition have been used by Angirasa [75] and Kand and Grief [58]. The justifications about using these flow and thermal boundary condition for FE and DE are given in details in Kanna and Das [74].

Thus, at DE,

$$\frac{\partial u}{\partial x} = \frac{\partial v}{\partial x} = \frac{\partial \theta}{\partial x} = 0 \tag{9.1f}$$

9.2.1 Interface boundary condition

The conjugate boundary condition along AB,

$$k_s \left(\frac{\partial \theta_s}{\partial y}\right)_{y=1} = k_f \left(\frac{\partial \theta_f}{\partial y}\right)_{y=1} \quad \text{and} \quad \theta_f = \theta_s \quad \text{at interface} \quad y = 1, \quad 0 < x \leq 2 \tag{9.2a}$$

The conjugate boundary condition along CD,

$$k_s \left(\frac{\partial \theta_s}{\partial y}\right)_{y=0} = k_f \left(\frac{\partial \theta_f}{\partial y}\right)_{y=0} \quad \text{and} \quad \theta_f = \theta_s \quad \text{at interface} \quad y = 0, \quad 2 < x \leq 25 \tag{9.2b}$$

The conjugate boundary condition along BC,

$$k_s \left(\frac{\partial \theta_s}{\partial x}\right)_{x=2} = k_f \left(\frac{\partial \theta_f}{\partial x}\right)_{x=2} \quad \text{and} \quad \theta_f = \theta_s \quad \text{at interface} \quad x = 2, \quad 0 < y \leq 1 \tag{9.2c}$$

From Taylor series expansion the temperature gradients are evaluated and substituted in equations (2.10), (2.24) and (9.2). Simplifying, the conjugate interface temperature at new time step for streamwise direction is,

$$
\begin{aligned}
\theta_{i,j}^{t+\Delta t} &= \theta_{i,j}^{t} + \frac{2\Delta t}{RePr(\Delta y_f + k\Delta y_s)}\Bigg[\frac{1}{2}(\Delta y_f + k\Delta y_s) \\
&\quad \left(\frac{\theta_{f,i+1,j} - 2\theta_{f,i,j} + \theta_{f,i-1,j}}{\Delta x_i * \Delta x_{i-1}}\right) - k\frac{\theta_{s,i,j} - \theta_{s,i,j-1}}{\Delta y_s} \\
&+ \frac{\theta_{f,i,j+1} - \theta_{f,i,j}}{\Delta y_f}\Bigg]^t
\end{aligned} \tag{9.3a}
$$

Similarly in the normal direction is,

$$
\begin{aligned}
\theta_{i,j}^{t+\Delta t} &= \theta_{i,j}^{t} + \frac{2\Delta t}{RePr(\Delta x_f + k\Delta x_s)}\Bigg[\frac{1}{2}(\Delta x_f + k\Delta x_s) \\
&\quad \left(\frac{\theta_{f,i,j+1} - 2\theta_{f,i,j} + \theta_{f,i,j-1}}{\Delta y_j * \Delta y_{j-1}}\right) - k\frac{\theta_{s,i,j} - \theta_{s,i-1,j}}{\Delta x_s} \\
&+ \frac{\theta_{f,i+1,j} - \theta_{f,i,j}}{\Delta x_f}\Bigg]^t
\end{aligned} \tag{9.3b}
$$

The Nusselt number expressions are given by,

along AB,

$$Nu(x) = -\frac{\partial\theta}{\partial y}|_{y=1} \tag{9.4a}$$

along CD,

$$Nu(x) = -\frac{\partial\theta}{\partial y}|_{y=0} \tag{9.4b}$$

along BC,

$$Nu(y) = -\frac{\partial\theta}{\partial x}|_{x=2} \tag{9.4c}$$

The computational domain considered here are clustered cartesian grids. In Eq. 2.11 $\kappa = 0.7$ is used for generating the grid points. Upto $x = l$, $\vartheta = 2\pi$ is used and further $\vartheta = \pi$ is used in the streamwise direction. In normal direction upto slot inlet height uniform grids are used and further $\theta = \pi$ clustering is followed. Thus more grids are clustered near the step (Fig. 9.2). Similar grids used to solve backward-facing step flow with upstream channel problem. It is presented in Appendix F.

With known hydrodynamic solution (Chapter 7), the energy equations in fluid region as well as solid region are solved simultaneously. The energy equation (Eq. 2.10) is discretised with central difference scheme for both convective and diffusive terms. It is solved by ADI method. The unsteady solid slab energy equation (Eq. 2.24) is discretised by central difference scheme and solved by Gauss-Seidel method. For particular time step, Eq. 2.24 is solved with guess interface value. Then the interface Eq. 9.3 is solved with new slab temperature values. Then the calculated interface value is used to compute fluid energy Eq. 2.10.

Solution approaches steady-state asymptotically while the time reaches infinity. The energy equations in fluid regime and solid regime are solved simultaneously. For the computation, time step 0.01 is used for $Pr = 1.0, 100.0$, whereas for $Pr = 0.01$, time step 0.0001 is used. Here it is set as sum of temperature error from consecutive iteration reduced to either the convergence criteria in Eq. 2.27 or large total time. At steady state, the error reaches the asymptotic behavior. For $Pr = 0.01$ the convergence criteria ϵ is set as 10^{-4} and for higher Pr, it is set as 10^{-6}.

9.3 Grid Independent Study

The domain has been chosen as 25 × h in streamwise direction from the step and 20 × h in normal direction. Systematic grid refinement study is carried out with the grids in the fluid region as 61×51, 71×61, 97×85 and 127×125. Sahoo and Sharif [68] have used average Nusselt number as a criteria for grid independent study for impinging confined slot jet problem. Similar way the variation in $\overline{Nu}$ is less than 1.5% grid system. So a grid of 97×85 is used for the entire computation (Table. 9.1). Within solid slab 36 grid points are arranged in normal direction. The grids are clustered in streamwise direction whereas in normal direction up to 3×h height, grids are arranged uniformly and above this region, they are clustered. Typical grids are shown in Fig. 9.2. Since the interface is common for solid as well as fluid region, in both direction the same size of clustered grids are used along the interface. The energy equations are solved for fluid region, solid region and conjugate interface simultaneously.

Table 9.1: Grid independence study: Value of $\overline{Nu}$. ($Re = 400, Pr = 1, l = 2h, s = 1h, w = 1h$)

Grids	$\overline{Nu}(k = 5)$	$\overline{Nu}(k = 50)$
61 × 51	3.5293	5.4823
71 × 61	4.8012	6.740125
97 × 85	7.64481	8.269212
127 × 125	7.55307	8.153443

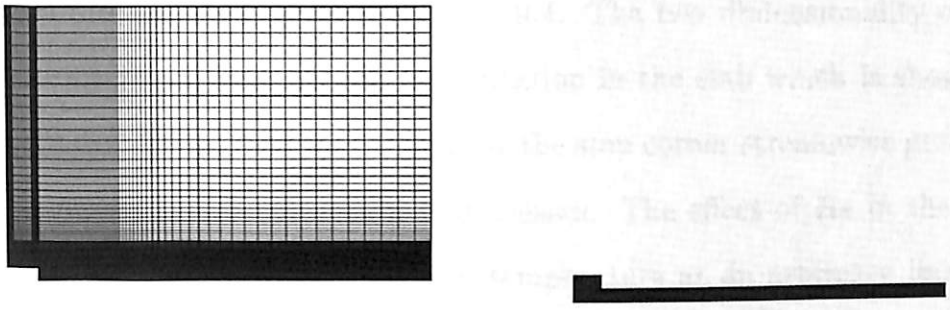

(a) Fluid region

(b) Solid region

Figure 9.2: Clustered grids used for the computation.

9.4 Results and Discussion

The conjugate heat transfer study has been done with three parameters considered here. They are Re, Pr and conductivity ratio (k). Results are presented for values of $Re = (300, 400, 500, 600)$, $Pr = (0.01, 1, 100)$ and $k = (1, 5, 10, 20, 50)$. The detailed conjugate heat transfer results are presented in terms of isotherm contour, conjugate interface temperature, Nusselt number (Nu) and average Nusselt number ($\overline{Nu}$) for the above cases.

The effect of flow property (Re), fluid property (Pr) and thermal conductivity ratio of solid region to fluid region (k) are reported in detail. Isotherm contours are presented for fluid region as well as solid region in Figs. 9.3 - 9.8. At low Re, jet spreads more in normal direction because the momentum flux is small compared to downstream direction frictional forces. Since the surrounding is quiescent, the jet spreads more at $Re = 300$ than at $Re = 600$.

This is reflected on heat transfer (Fig. 9.3). Thermal boundary layer thickness for *Re* = 300 is higher than for *Re* = 600 (Fig. 9.3(c)). Influence of *Re* on solid wall heat transfer is shown in Fig. 9.4. The two dimensionality of the geometry is captured well by the computation in the slab which is shown in isotherm contour. It is observed that near the step corner streamwise gradient is more. At downstream direction it decreases. The effect of *Re* in the slab is demonstrated with normal direction temperature at an arbitrary location $x = 10h$ (Fig. 9.4(c)) and streamwise direction temperature at $y = 0.5h$ (Fig. 9.4(d)). The slab heat transfer has linear relationship with *Re* in normal direction whereas along streamwise direction temperature reduces to a minimum value and further it increases and near the end of the slab it decreases. When *Re* increases the gradient increases in both directions. For low *Pr*, thermal diffusivity is more and conduction mode of heat transfer is dominant. Heat penetrates within the quiescent fluid region at low *Pr* number (Fig. 9.5(a)). For high *Pr* fluid, thermal boundary layer thickness is small (Fig. 9.5(c)) due to convection mode of heat transfer and *Pr* = 1 case lies in between these two values (Fig. 9.5(b)). The similarity temperature profile for different *Pr* is shown in Fig. 9.5(d). It is observed that when *Pr* increases the thermal layer thickness is reduced. The influence of *Pr* in solid slab is shown in Fig. 9.6. At low *Pr* the slab temperature approaches bottom wall temperature (Fig. 9.6(d)). In the streamwise direction the slab temperature at $y = 0.5h$ is presented in (Fig. 9.6(e)). It is noticed that it decreases to a minimum value and further increases. This fluctuation is high at high *Pr*.

The effects of conductivity ratio (k) are demonstrated in Fig. 9.7 - 9.8.

Increment in k will increase heat transfer in fluid region as expected. It is observed that in the fluid region, the effect of increment in k is reflected on the isotherm of the fluid region (Fig. 9.7(a)- Fig. 9.7(d)). Isotherms having magnitude less than 6.5% of bottom wall temperature are not shown in the figure. The similarity temperature profile for different k at $x = 10h$ is shown in Fig. 9.7(e). When k is increased the heat transfer in fluid region is increased. However the rate of increase is reduced at higher k values. The influence of k in solid wall is shown in Fig. 9.8. At high k values it is observed that the gradient in the streamwise direction is reduced and it approaches the bottom wall temperature value. Streamwise temperature at $y = 0.5h$ is shown in Fig. 9.8(d). At lower k values temperature decreases to a minimum value and further increases. When k increases this fluctuation is reduced and it approaches a constant value.

The conjugate interface temperature viz. AB, BC, CD presented in Fig. 9.9 - Fig. 9.11. The influence of *Re* on interface temperature is presented in Fig. 9.9(a)-Fig. 9.9(c). Along AB the interface temperature decreases non-linearly. It is observed that this is less sensitive to *Re*. Along BC when in the positive y direction interface temperature is reduced non-linearly. This is attributed by large recirculation near the step. The influence of *Re* on interface temperature is very significant along the CD. It decreases to a minimum value and further increases monotonically (Fig. 9.9(b)). The decrement in the temperature is attributed by the recirculation eddy. The minimum value locates downstream of the reattachment point. It shifts further when *Re* is increased. When *Re* increases temperature value is decreased in the entire downstream direction. The effect of Pr on interface temperature is presented in Fig. 9.10. The interface temperature decreases along AB. When Pr increases from 0.01 to 100 the temperature values is decreased. However while approaching the expansion it is less sensitive to Pr. Along CD the interface temperature reduce to a minimum value and further it increases monotonically. At low Pr this variations are very less and it magnifies when Pr increases (Fig. 9.10(b)). It is observed that the location of minimum temperature value occurs in CD is shifted in downstream direction when Pr is increased. Along BC the interface temperature value is decreased in the normal direction. BC is laid between recirculation eddy and solid wall. This situation causes the conduction is dominant mode of heat transfer which leads to higher interface value for low Pr (Fig. 9.10(c)). The influence of conductivity ratio on interface temperature is presented in Fig. 9.11. It is observed that the k is sensitive to the entire interface. Along AB the interface temperature is increased non-linearly to k. However it is noticed that the increment rate is reduced at higher k values. Along CD the interface temperature value is decreased to a minimum value and further increases monotonically. At hight k value it becomes almost constant value (Fig. 9.11(b)). Along BC interface temperature value is decreased in positive y direction. It is noticed that when increasing k interface temperature value is increasing.

The local Nusselt number distribution is presented in detail in Fig. 9.12 - Fig. 9.14. The influence of Re is shown in Fig. 9.12. Along AB due to entrainment Nu value is large near the inlet and further it decreases in the downstream direction. When Re increases Nu is increased due to the increment in thermal gradient (Fig. 9.12(a)). Along CD, Nu is increased to a maximum value and further decreases monotonically. It is observed that the peak Nu is falling downstream of the reattachment location and it shifts down when Re is increased (Fig. 9.12(b)). Along BC the Nusselt increases to a maximum value and further it decreases to small value and further it increases (Fig. 9.12(c)). This trend in Nusselt number is attributed by the conjugate effect between recirculation eddy and solid wall near the corner. This effect demonstrated earlier in the isotherm contour (Fig. 9.4). When Re increases Nu is increased. The effect of Pr is presented in Fig. 9.13. Along AB convection is dominant region due to jet entry as well as ambient entrainment. This attributed for high Nu for high Pr (Fig. 9.13(a)). Along CD Nu increases to a maximum and decreases monotonically in the downstream direction (Fig. 9.13(b)). When Pr increases Nu is increased. The peak Nusselt number occurs due to recirculation. However the peak Nu location shifts down when Pr increases. Along BC Nu increases to a maximum value and decreases further it increases. Due to recirculation the Nusselt number is increased for high Pr (Fig. 9.13(c)). The effect of k in local Nusselt number is shown in Fig. 9.14. The thermal resistance in the solid wall can be overcome with high k. An isothermal interface heat transfer study [76] is compared to validate this point. Along AB when k is increasing Nu is increased Fig. 9.14(a). It approaches the non-conjugate value at downstream. Near the corner a kink is observed. Along CD the Nu distribution is shown in Fig. 9.14(b). It increases to a peak value and further downstream decreases monotonically. When k increases the location of peak value shifts down. It is observed that at high k value the Nusselt number distribution along CD is higher than non-conjugate case. In

Table 9.2: Average Nusselt number: Effect of *Re*. ($Pr = 1, k = 5, l = 2h, s = 1h, w = 1h$)

Re	$\overline{Nu}$	Non-conjugate	% difference from non-conjugate
300	5.808317	6.441137	9.82
400	7.644812	8.524984	10.32
500	9.079950	10.212431	11.09
600	10.341680	11.767634	12.12

downstream direction the jet expands and bottom wall is isothermal. Whereas in conjugate case the wall temperature is variant (Fig. 9.11(b)). Along BC the Nu is increasing to maximum value and further reduces and increases in the normal direction. When k increases Nu increases.

Table 9.3: Average Nusselt number: Effect of *Pr*. ($Re = 400, k = 5, l = 2h, s = 1h, w = 1h$)

Pr	$\overline{Nu}$	Non-conjugate	% difference from non-conjugate
0.01	2.165427	1.714043	-26.33
1	7.644812	8.524984	10.32
100	30.719183	41.852650	26.60

Table 9.4: Average Nusselt number: Effect of *k*. ($Re = 400, Pr = 1, l = 2h, s = 1h, w = 1h$)

k	$\overline{Nu}$
1	5.968452
5	7.644812
10	7.913072
20	8.179786
50	8.269212
non-conjugate	8.524984

The summary of all the results are presented as variation of average Nusselt number ($\overline{Nu}$), shown in Table 9.2 - Table 9.4. The influence of *Re* is shown in Table. 9.2. When *Re* increases average Nusselt number is increased. Conjugate values always less than non-conjugate average Nusselt number. Effect of *Pr* is shown in Table 9.3. It is observed that when *Pr* increases the average Nusselt number is increasing. When it is compared with non-conjugate values at low *Pr* non-conjugate ($\overline{Nu}$) is less than conjugate case. At low *Pr* conduction is dominant mode of heat transfer. In conjugate case heat transfer in solid is coupled with fluid heat transfer. Which causes this higher ($\overline{Nu}$) than non-conjugate ($\overline{Nu}$). It is observed that when *k* increases the ($\overline{Nu}$) values is increased (Table 9.4). At higher *k* value it approaches the non-conjugate value. It is point worth to note that though the local Nusselt number distribution for conjugate case at higher *k* along BC is higher than non-conjugate (Fig. 9.14), the average Nusselt number of non-conjugate is higher than conjugate case. This is mainly due to the entrainment near the inlet and recirculation eddy.

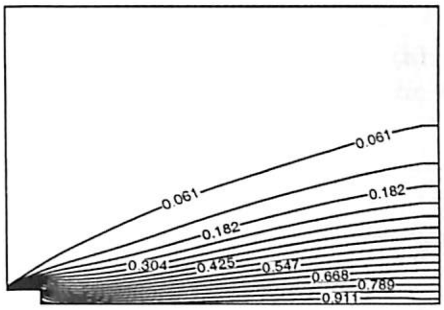

(a) Isotherm contour: $Re = 300$

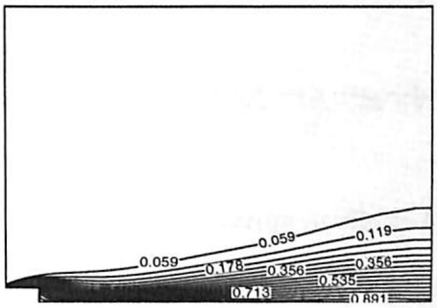

(b) Isotherm contour: $Re = 600$

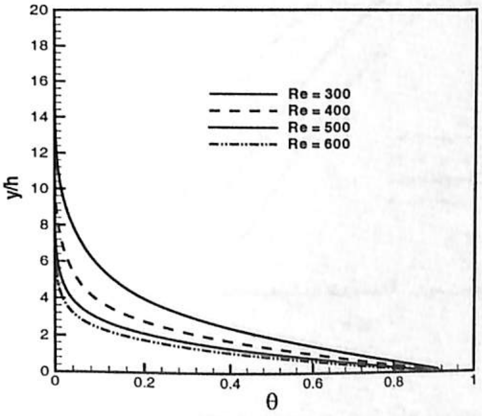

(c) Temperature profile at $x = 10h$

Figure 9.3: Effect of Re in fluid region ($Pr = 1, k = 5, l = 2h, s = 1h, w = 1h$).

(a) Isotherm contour in the slab: $Re = 300$ (A part of the domain)

(b) Isotherm contour in the slab: $Re = 600$ (A part of the domain)

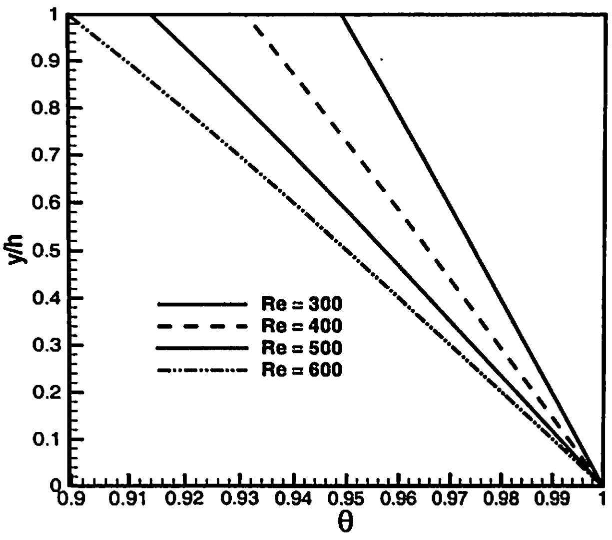

(c) Temperature profile at $x = 10h$

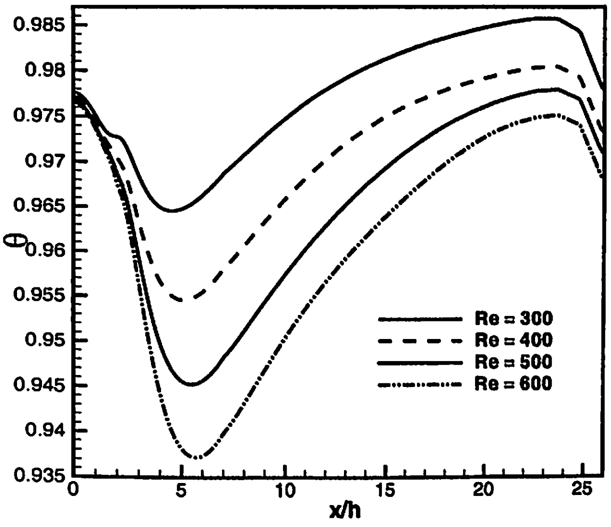

(d) Temperature profile at $y = 0.5h$

Figure 9.4: Effect of Re in solid wall ($Pr = 1, k = 5, l = 2h, s = 1h, w = 1h$).

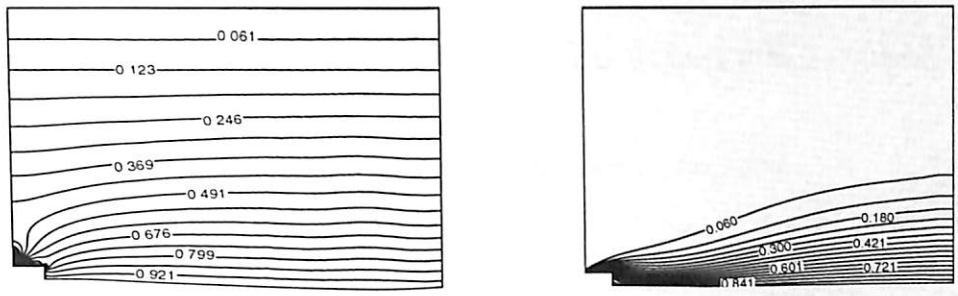

(a) Isotherm contour: $Pr = 0.01$

(b) Isotherm contour: $Pr = 1$

(c) Isotherm contour: $Pr = 100$

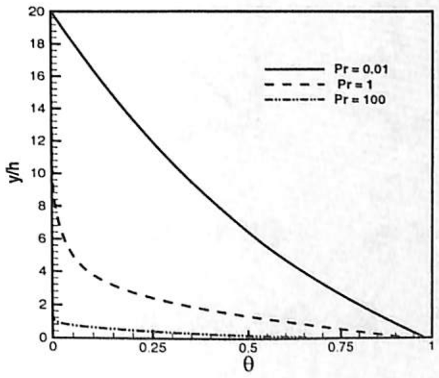

(d) $x = 10h$

Figure 9.5: Effect of Pr in fluid region ($Re = 400, k = 5, l = 2h, s = 1h, w = 1h$).

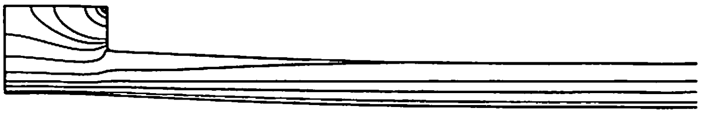

(a) Isotherm contour: $Pr = 0.01$

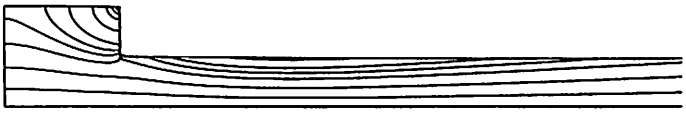

(b) Isotherm contour: $Pr = 1$

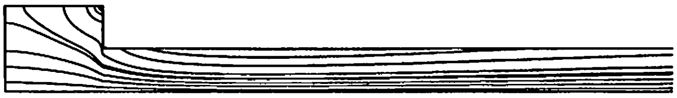

(c) Isotherm contour: $Pr = 100$

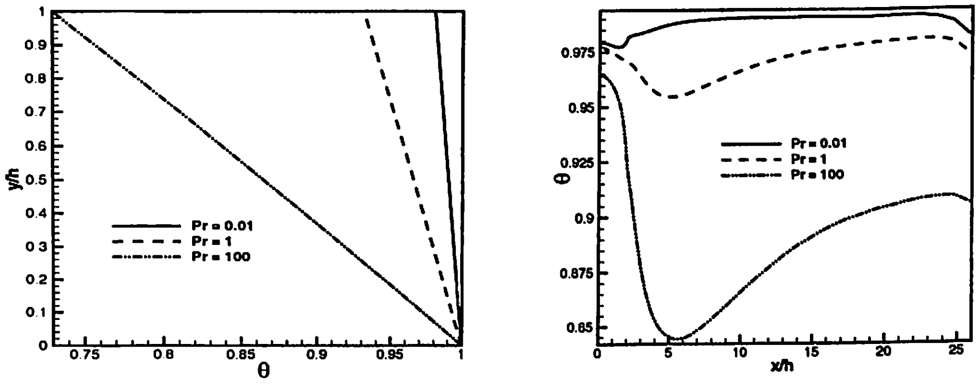

(d) Temperature profile at $x = 10h$ (e) Temperature profile at $y = 0.5h$

Figure 9.6: Effect of Pr in solid wall. ($Re = 400, k = 5, l = 2h, s = 1h, w = 1h$).

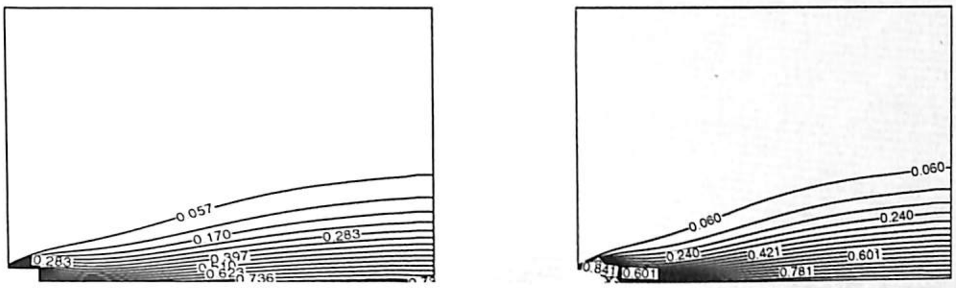

(a) $k = 1$ (b) $k = 5$

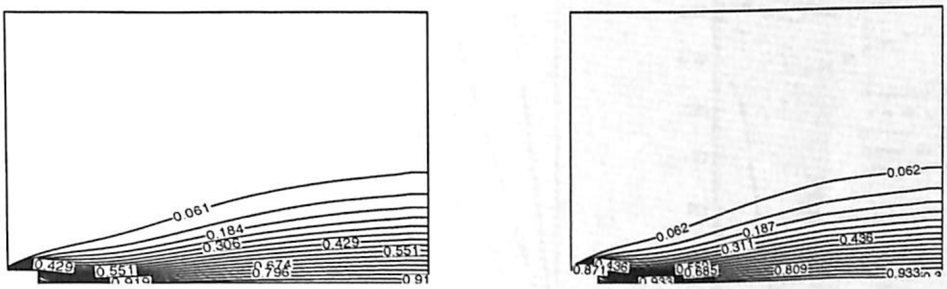

(c) $k = 10$ (d) $k = 50$

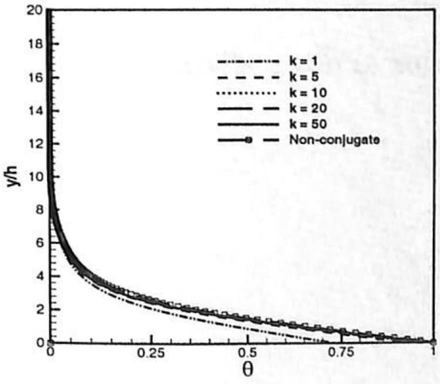

(e) $x = 10h$

Figure 9.7: Isotherm contour: Effect of conductivity ratio in fluid region ($Re = 400, Pr = 1, l = 2h, s = 1h, w = 1h$).

(a) Isotherm contour: $k = 1$

(b) Isotherm contour: $k = 50$

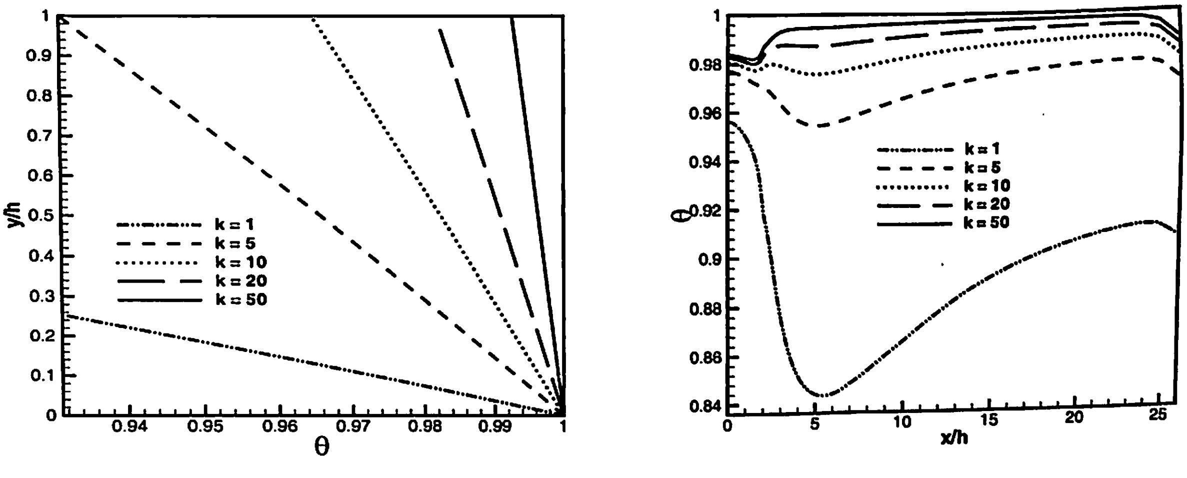

(c) Temperature profile at $x = 10h$

(d) Temperature profile at $y = 0.5h$

Figure 9.8: Effect of conductivity ratio in solid wall ($Re = 400, Pr = 1, l = 2h, s = 1h, w = 1h$).

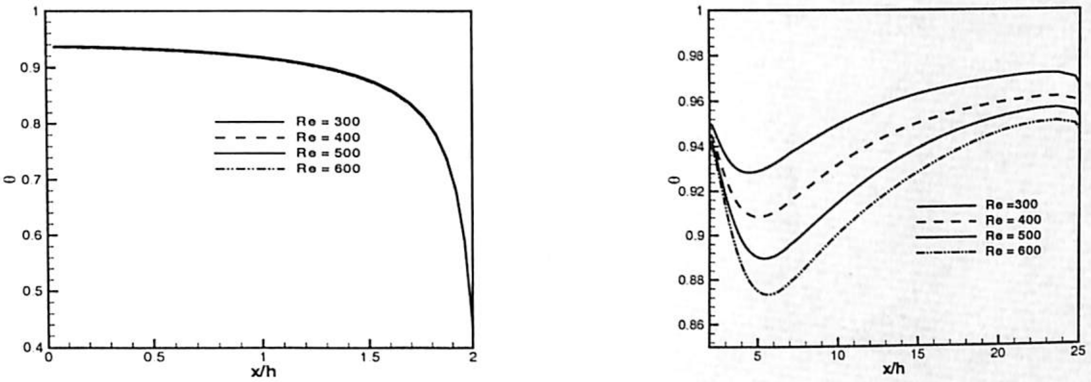

(a) Along AB

(b) Along CD

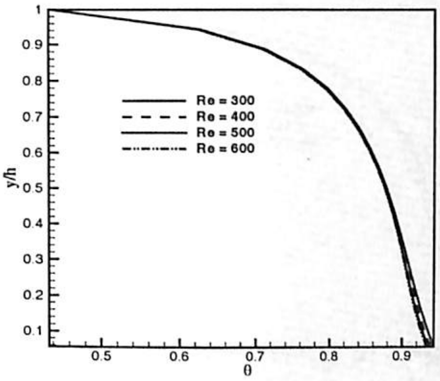

(c) Along BC

Figure 9.9: Conjugate interface temperature: Effect of Re. ($Pr = 1, k = 5, l = 2h, s = 1h, w = 1h$)

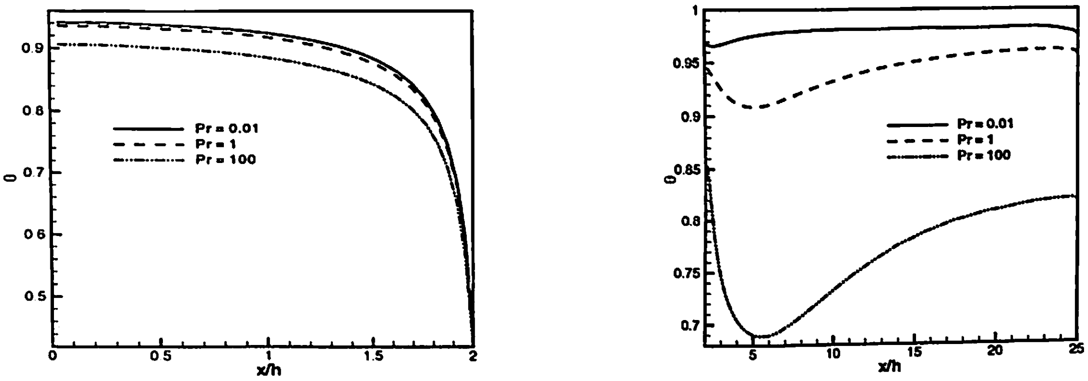

(a) Along AB

(b) Along CD

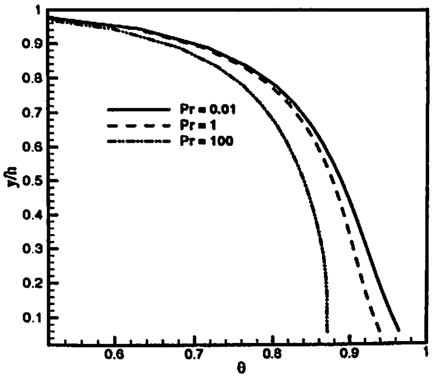

(c) Along BC

Figure 9.10: Conjugate interface temperature: Effect of Pr. ($Re = 400, k = 5, l = 2h, s = 1h, w = 1h$)

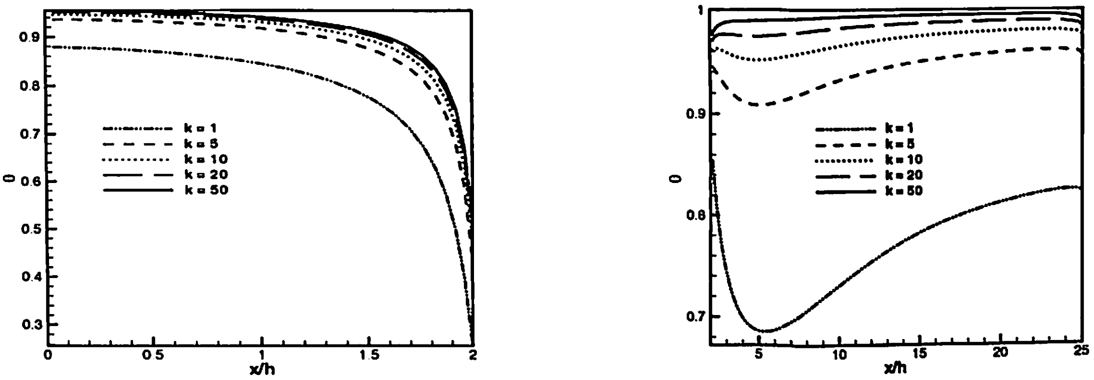

(a) Along AB

(b) Along CD

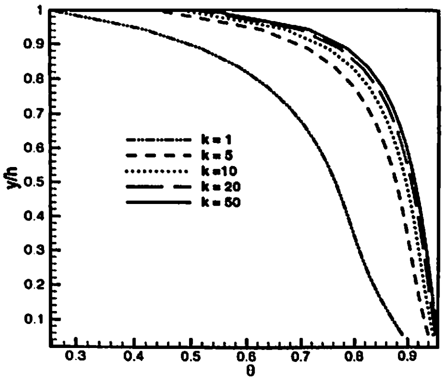

(c) Along BC

Figure 9.11: Conjugate interface temperature: Effect of k. ($Re = 400, Pr = 1, l = 2h, s = 1h, w = 1h$)

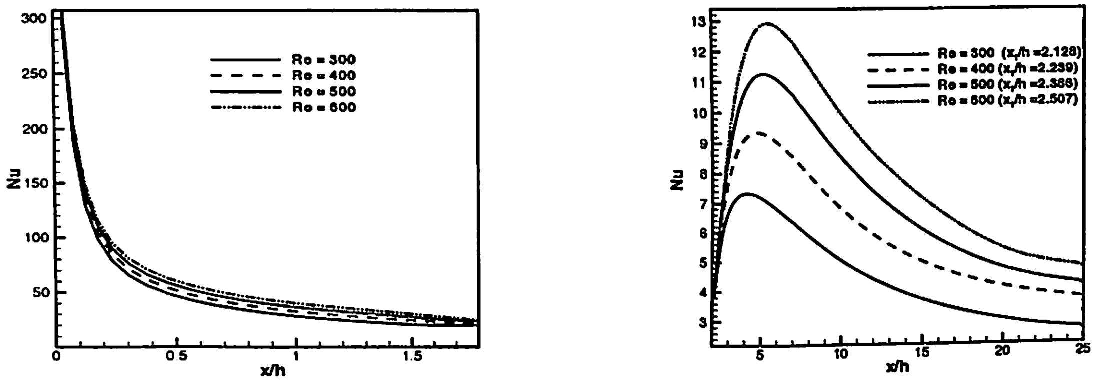

(a) Along AB

(b) Along CD

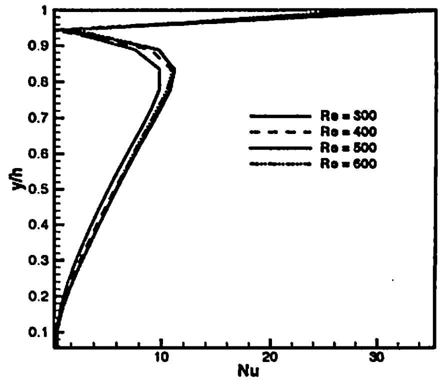

(c) Along BC

Figure 9.12: Local Nusselt number: Effect of Re. ($Pr = 1, k = 5, l = 2h, s = 1h, w = 1h$)

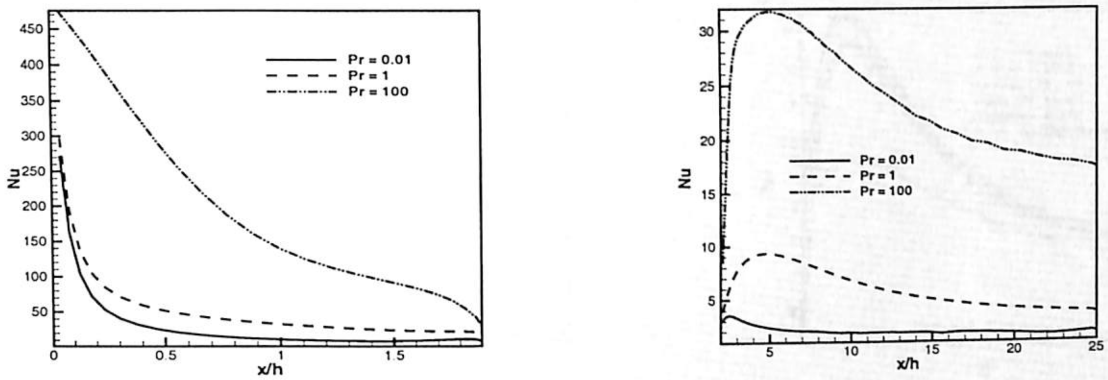

(a) Along AB (b) Along CD

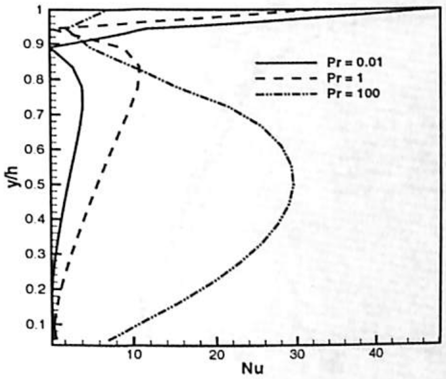

(c) Along BC

Figure 9.13: Local Nusselt number: Effect of Pr. ($Re = 400, k = 5, l = 2h, s = 1h, w = 1h$)

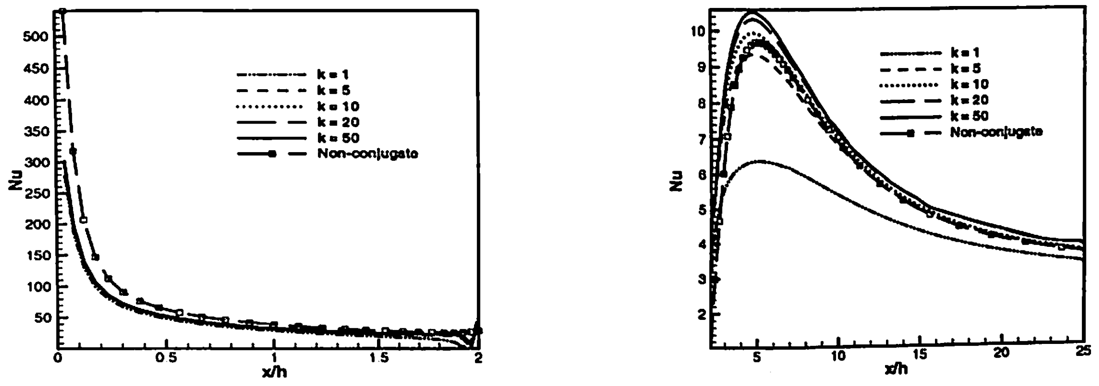

(a) Along AB

(b) Along CD

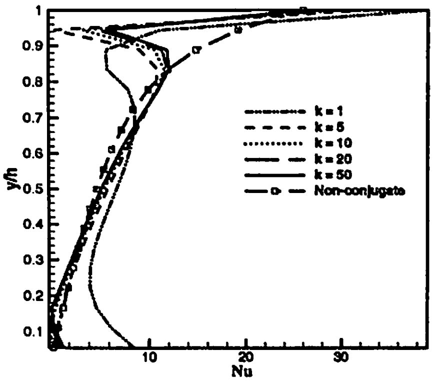

(c) Along BC

Figure 9.14: Local Nusselt number: Effect of k. ($Re = 400, Pr = 1, l = 2h, s = 1h, w = 1h$). Non-conjugate study - [76]

9.5 Conclusions

Conjugate heat transfer study of two-dimensional incompressible nonbuoyant wall jet under backward facing step problem is carried out by solving the streamfunction vorticity equations and energy equations in fluid and solid regions. Heat transfer characteristics are systematically studied for flow property (Re), fluid property (Pr) and the conductivity ratio (k) and the following conclusions are obtained.

The conjugate interface temperature value decreases along the step length and height. After expansion from the step its value is reduced to a minimum value followed by an increase. The minimum Nu falls after reattachment location. The interface temperature value decreases when Re is increased. Also, it decreases for higher Pr. However the interface temperature increases for higher k. Local Nusselt number has peak value near the inlet due to entrainment and second peak occurs after reattachment of the jet. Increment in Re, Pr and k increases Nu. At low Pr non-conjugate $\overline{Nu}$ is smaller than conjugate $\overline{Nu}$.

$\overline{Nu}$ for non-conjugate case is 12.12% higher compared to conjugate case for $Re = 600$. For low Pr (=0.01), $\overline{Nu}$ for non-conjugate case is lower by -26.33%. whereas for high Pr (=100), the trend reverses and it is higher by 26.6%. As k is increased, $\overline{Nu}$ for conjugate case behavior is close to that of non-conjugate case and the difference is 3%.

Chapter 10

Conjugate Study: Wall Jet Flow Over Backward-Facing Step - Part 2

10.1 Introduction

This chapter discusses the conjugate heat transfer study of wall jet over backward-facing step in connection with effect of geometry involved in heat transfer. Conjugate heat transfer study on offset jet is carried out by Kanna and Das [77]. They studied the conjugate heat transfer characteristics with four parameters viz. Re, Pr, S and $k = \frac{k_s}{k_f}$. They found that fluid properties are affecting the heat transfer in the solid slab. When Re is increased the slab temperature is reduced. At low Pr the heat transfer across the slab is more. It is decreased when slab thickness is increased. The conjugate interface temperature is decreased upto recirculation region and further increased close to a developed condition.

Wall jet under step flow occurs in many engineering applications such as environmental discharges, heat exchangers, fluid injection systems, cooling of combustion chamber wall in a gas turbine, automobile demister and others. In electronics cooling the prediction of Nusselt number distribution along the step as conjugate situation is very important in thermal design point of view. Kanna and Das [78] have reported the flow characteristics of wall jet flow over a step. Reattachment length, local u velocity decay are reported for different step geometry. The heat transfer study is carried out by the same authors [76]. They found that the peak Nusselt number occurs due to entrainment as well as recirculation. Step height enhances the average Nusselt number. Similarity velocity profiles from different downstream locations are presented.

Kanna and Das [79] have numerically investigated the effect of properties involved in the conjugate heat transfer in wall jet over backward-facing step flow. The conjugate heat transfer characteristics are studied with flow property (Re), fluid property (Pr) and solid to fluid conductivity ratio (k). They noticed that the fluid properties are affecting the heat transfer in the solid slab. The conjugate interface temperature decreases along the step. Two peak Nusselt number occurs due to entrainment and recirculation eddy. As k is increased, average Nusselt number is increased and at higher k, it approaches a non-conjugate value. It is worthwhile to note that the conjugate heat transfer is affected by the geometry of the solid slab involved in heat transfer with fluid medium.

Although many studies have been conducted on wall jet, the available literature suggests that the study concerning the effect of geometry of wall jet over backward facing step as conjugate case has not been carried out by any researcher. In the present paper, conjugate heat transfer study is focused to find the effect of the step length, step height and the bottom wall thickness on the isotherm, conjugate interface temperature, local Nusselt number distribution and average Nusselt number distribution.

10.2 Results and Discussion

Conjugate heat transfer study of two-dimensional incompressible nonbuoyant wall jet over backward facing step problem is carried out by solving the momentum equation and energy equation using stream function and vorticity formulation for the fluid region and conduction equation in the solid. The conjugate heat transfer characteristics are systematically studied for flow property (Re), fluid property (Pr) are and the conductivity ratio (k) are reported in details in [79]. In the present investigation, attention is given to the effect of geometry on the conjugate heat transfer. The details of governing equations and boundary conditions for the present case are illustrated in section 9.2. The grid independent study is presented in section 9.3. It is noticed that for $w = 10h$ case the $\overline{Nu}$ variation is less than 2% with 72 grid points in the normal direction of solid slab.

The effect of geometry on the conjugate heat transfer has been studied with three parameters considered here. They are: length of the step (l), height of

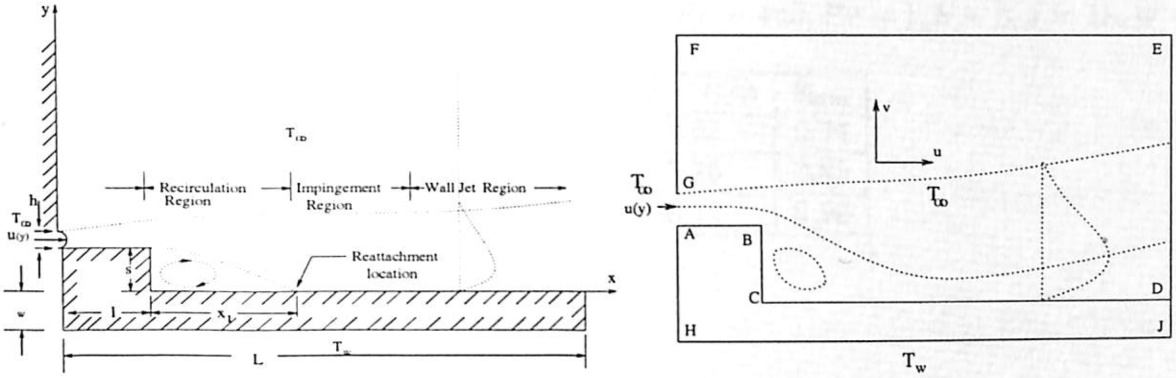

(a) schematic of the problem (b) Computational domain

Figure 10.1: Schematic diagram and boundary conditions

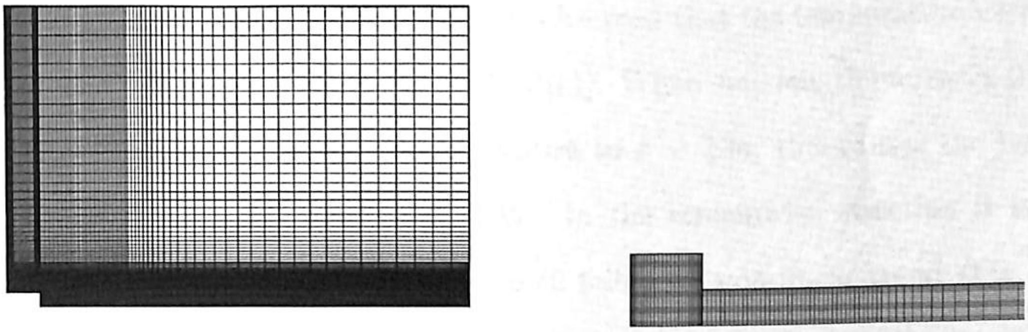

(a) Fluid region (b) Close view of part of the solid region

Figure 10.2: Clustered grids used for the computation.

the step (s) and thickness of the solid slab (w). Results are presented for different geometry sizes. Flow property, fluid property and thermal property are fixed as follows: $Re = 400, Pr = 1$ and $k = 5$. The detailed conjugate heat transfer results are presented in terms of isotherm contour, interface temperature, Nusselt number (Nu) and average Nusselt number ($\overline{Nu}$).

Table 10.1: Minimum temperature. ($Re = 400, Pr = 1, k = 5, s = 1h, w = 1h$)

l/h	$(x-l)/h$	θ_{min}
1	3.91	0.94
2	5.15	0.95
3	6.12	0.96

The effect of geometry on isotherm contour inside the solid slab is shown in Figs. 10.3 - 10.5. Isotherm contour is presented in streamwise direction at mid height ($y = w/2$) of the slab and in normal direction at $x = 10h$ from where u velocity similarity profile is observed [78]. Fig. 10.3(a)-10.3(b) shows the effect of the step length on the isotherm contour. The two-dimensionality is captured well in the slab. It is observed that the temperature varies linearly in the normal direction (Fig. 10.3(c)). When step length increases the location of recirculation eddy comes closure to $x = 10h$; this causes the temperature to be decreased near $x = 10h$. In the streamwise direction it is observed that the temperature at $y = w/2$ follows a non-linear trend (Fig. 10.3(d)). In streamwise direction temperature is decreased to a minimum value (Table 10.1) and further it is increased in the downstream direction. When length increases the temperature value is increased. It is observed that the effect of the step length is significant only upto development region and after the wall jet region ($x > 10h$) temperature becomes less sensitive to step length variation. Effect of step height is presented in Fig. 10.4. The isotherm contour in the slab is shown in Figs. 10.4(a)-10.4(b). It is observed that when the step height is increased, the non-dimensional temperature is decreased in the normal direction (Fig. 10.4(c)). This is due to the larger recirculation eddy at higher s value. In the streamwise direction, the temperature follows a non-linear trend. For $s = 1$ (Fig. 10.4(d)), the temperature decreases to a minimum value and further downstream direction it attains an asymptotic value. For $s = 2$, the temperature contour increases to a local maximum value ($\theta = 0.9686, x/h = 3.192$); further downstream, it decreases to a minimum value ($\theta = 0.9585, x/h = 7.306$) and finally it reaches to the same asymptotic value of case $s = 1$. Beyond the development region ($x > 5h$), both the cases $s = 1$ and $s = 2$ have the common trend. The effect of slab thickness (w) is presented in Fig. 10.5 for $w = 1, 2, 5$ and $w = 10$. The isotherm contour is shown for $w = 1$ in Fig. 10.5(a) and for $w = 10$ in Fig. 10.5(b). It is observed that a two-dimensionality nature of isotherms exists near the interface for the slab thicknesses. The temperature distribution in the normal direction is plotted for $x = 10h$ and it shows a linear trend (Fig. 10.5(c)). In the streamwise direction it is plotted for $y = w/2$ and a non-linear trend is observed (Fig. 10.5(d)). It is noticed that when w is increased the temperature gradient is decreased (Fig. 10.5(c)). In streamwise direction, the temperature decreases to a local minimum value and further increases in the downstream direction (Fig. 10.5(d)). It is observed that when w is increased the magnitude of temperature is decreased and the minimum value is shifted ($w = 1, x/h = 5.046; w = 2, x/h = 5.794; w = 5, x/h = 6.393; w = 10, x/h = 7.591$) in the downstream direction. This is attributed to the thermal resistance inside the slab which is increased when w is increased.

The effect of geometry on the interface temperature is presented in Figs. 10.6-10.8. The interface is divided into three lengths viz. AB (step length), BC (step height) and CD$(L-l)$ (Fig. 10.1(b)). The interface temperature decreases gradually upto a certain length followed by a sharp drop (Fig. 10.6(a)). The temperature at mid step length is ($\theta = 0.83$ for $l = 1$, $\theta = 0.92$ for $l = 2$ and $\theta = 0.95$ for $l = 3$). It is observed that when l increases interface temperature is increased. As k_s is greater than k_f, more heating process takes place when l is increased. The interface temperature decrement is continued along BC and is shown in Fig. 10.6(b). For all the three cases, the variations are close to each other with maximum difference of $\theta = 0.031$ at $y/h = 0$ (i.e. point C). Along CD the interface temperature decreases to a minimum value and finally it reaches an asymptotic value in the downstream direction (Fig. 10.6(c)). This trend is due to the recirculation eddy and development of the wall jet after the reattachment point. The effect of step height on the interface temperature is presented in Fig. 10.7. The interface temperature decreases gradually and falls down near the convex corner of the step (Fig. 10.7(a)). When s is increased the interface temperature value is reduced since the size of the recirculation eddy is increased. Fig. 10.7(b) shows the interface temperature along the step height BC. It decreases through the entire length in non-linear fashion. The interface temperature along CD is shown in Fig. 10.7(c). When $s = 1$ it decreases to a local minimum value and further downstream direction it increases to a near asymptotic value. For $s = 2$ it increases to a local maximum value and decreases to a local minimum value; finally it attains a steady value of $\theta = 0.96$. Effect of slab thickness w on interface temperature is shown in Fig. 10.8. Along AB (Fig. 10.8(a)), interface temperature decreases in the streamwise direction. When w increases interface temperature value is decreased. This is due to reduction of temperature inside the slab at higher slab thickness. A boundary layer type profile is observed where the interface temperature from an asymptotic value is dropping sharply near the location at $x/h = 2$. Along BC it increases with an opposing nature to that AB (Fig. 10.8(b)). Along CD the interface temperature is shown in Fig. 10.8(c). It decreases to a local minimum value and further increases in the downstream direction. It is noticed that when w is increased the interface temperature is decreased. It is observed that the minimum value is shifted in the downstream direction when w is increased (for $w = 1$, x/h=5.01, $w = 2$, x/h=5.49, $w = 5$, x/h=6.05 and $w = 10$, x/h=6.54).

The local Nusselt number distribution is presented in Figs. 10.9 - 10.11. The effect of step length is shown in Fig. 10.9. Along AB, due to entrainment, Nu is very large and it is decreasing in the downstream direction. When l is increased a small increment in Nu is observed (for $l = 1$, $Nu = 46.93$; for $l = 2$, $Nu = 51.62$ and for $l = 3$, $Nu = 53.31$ at $x/h = 0.5$) (Fig. 10.9(a)). This is caused due to the variation in the entrainment near the inlet. However this variation is reduced along the downstream of the step length. Fig. 10.9(b) shows the Nu distribution along BC. Nu increases to a maximum value and decreases in the direction of B to C (-ve y direction). When l is increased the maximum value is decreased ($l = 1, Nu = 13.865; l = 2, Nu = 10.903; l = 3, Nu = 8.365$). Nu distribution along CD is presented in Fig. 10.9(c). Nu increases to a maximum value and decreases to a near-steady value in the downstream direction. It is noticed that when l is increased its magnitude is decreased and the peak Nu value is shifted ($l = 1, x = 3.679h, Nu = 11.769; l = 2, x = 4.746h, Nu = 9.352; l = 3, x = 5.678h, Nu = 8.501$) in the downstream direction. Effect of step height is shown in Fig. 10.10(a). Along AB, Nu is decreased in the downstream direction. When s is increased, Nu is decreased (for $s = 1$, $Nu = 51.66$ and for $s = 2$, $Nu = 42.16$ at $x/h = 0.5$). Along BC, Nu is decreased to certain height and increases to a maximum value and then further it is decreased (Fig. 10.10(b)). This trend is magnified at higher step height. Along CD, Nu is increased to a maximum value and decreases to a near-steady value (Fig. 10.10(c)). When s is increased, Nu is decreased and the peak value is shifted downstream direction (for $s = 1$, $Nu = 9.35$ at $x/h = 4.76$ and $s = 2$, $Nu = 8.43$ at $x/h = 7.25$). This is attributed by the large size of recirculation eddy. The effect of slab thickness is presented in Fig. 10.11. Along AB, Nu is sensitive to w (for $w = 1$, $Nu = 51.66$; for $w = 2$, $Nu = 50.87$; for $w = 5$, $Nu = 47.62$ and for $w = 10$, $Nu = 39.35$ at $x/h = 0.5$). It is observed that when w is increased, Nu is decreased (Fig. 10.11(a)). Along BC (Fig. 10.11(b)) Nu is increased to a maximum value and is decreased and further increased (for $w = 1, 2$ and 5). At higher slab thickness (at $w = 10$), the trend is slightly different such that near the corner it is decreased. Along CD, Nu increases to a maximum value (at $x/h = 4.73$ for $w = 1$, $Nu = 9.35$; $w = 2$, $Nu = 8.35$; $w = 5$, $Nu = 7.10$ and $w = 10$, $Nu = 5.28$) and decreased gradually to a near-steady value. When w is increased Nu is decreased. It is observed that the peak value location does not vary for different w (Fig. 10.11(c)). It is observed from the entire study that the singularity is arisen at step corner B and the buffer zone effect is reflected at the exit region results [18].

The bulk mean property in terms of the average Nusselt number ($\overline{Nu}$) are presented in Table 10.2 - Table 10.4. When length of the step is increased, the average Nusselt number is decreased (Table 10.2). At higher step height, the average Nusselt number is decreased (Table 10.3). Table 10.4 shows the effect of slab thickness in $\overline{Nu}$. It is noticed that when slab thickness is increased the average Nusselt number is decreased.

Table 10.2: Average Nusselt number: Effect of l. $(Re = 400, Pr = 1, k = 5, s = 1h, w = 1h)$

l	$\overline{Nu}$	% change
1	8.675017	-
2	7.644812	-11.88
3	6.908958	-20.35

Table 10.3: Average Nusselt number: Effect of s. $(Re = 400, Pr = 1, k = 5, l = 2h, w = 1h)$

s	$\overline{Nu}$	% change
1	7.644812	-
2	7.066061	-7.57

Table 10.4: Average Nusselt number: Effect of w. $(Re = 400, Pr = 1, k = 5, l = 2h, s = 1h)$

w	$\overline{Nu}$	% change
1	7.644812	-
2	7.239326	-5.30
5	6.683218	-12.57
10	5.400715	-29.35

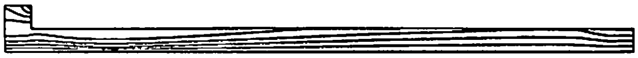

(a) $l = 1h$

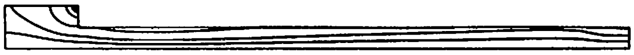

(b) $l = 3h$

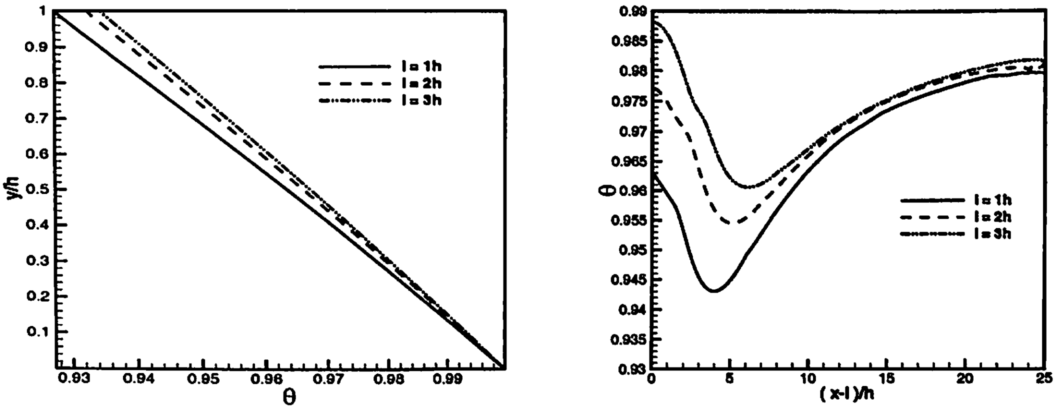

(c) Temperature inside the slab at $x = 10h$

(d) Temperature inside the slab at $y = w/2$

Figure 10.3: Temperature in the solid region: Effect of l. ($Re = 400, Pr = 1, k = 5, s = 1h, w = 1h$).

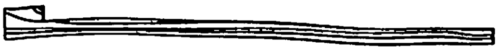

(a) $s = 1$

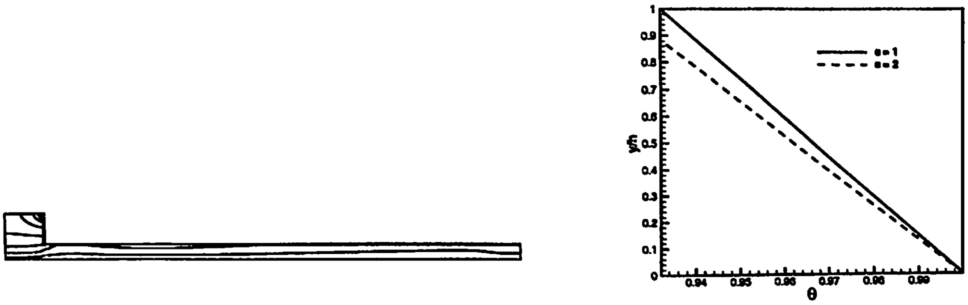

(b) $s = 2$

(c) Temperature inside the slab at $x = 10h$.

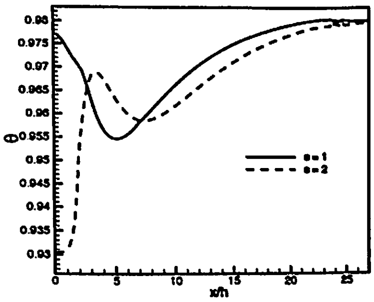

(d) Temperature inside the slab at $y = w/2$.

Figure 10.4: Temperature in the solid region: Effect of s. ($Re = 400, Pr = 1, k = 5, l = 2h, w = 1h$).

(a) $w = 1h$

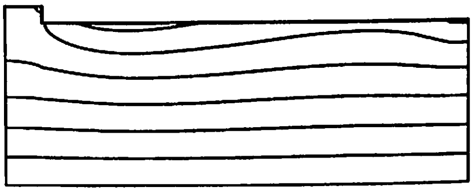

(b) $w = 10h$

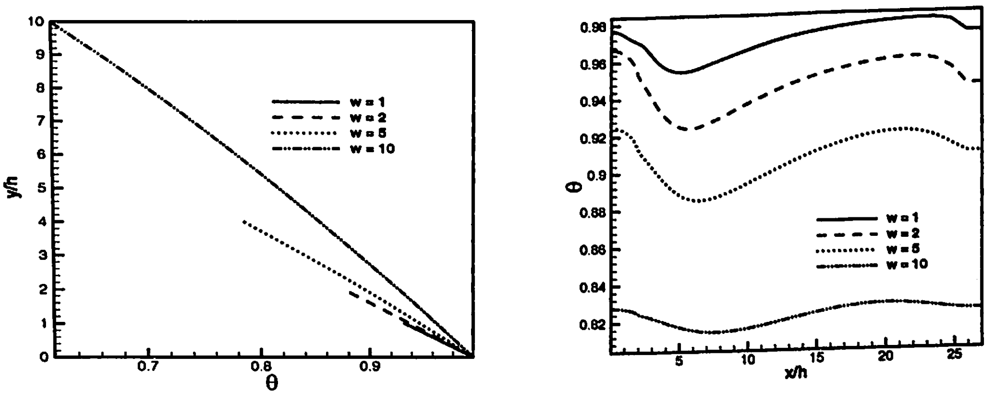

(c) Temperature inside the slab at $x = 10h$.

(d) Temperature inside the slab at $y = w/2$.

Figure 10.5: Temperature in the solid region: Effect of w. ($Re = 400, Pr = 1, k = 5, l = 2h, s = 1h$).

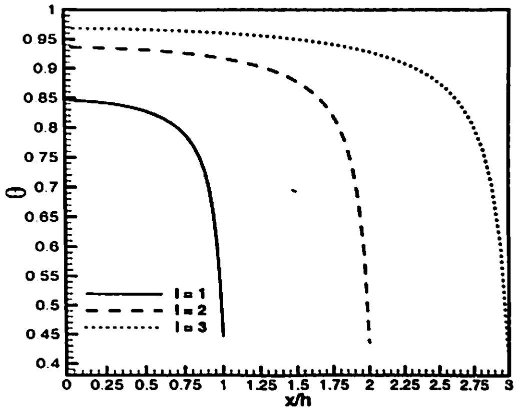

(a) Along AB

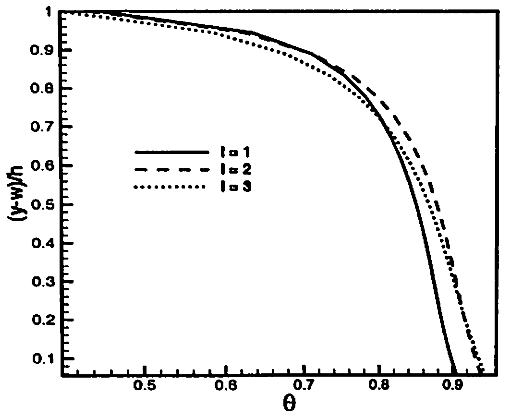

(b) Along BC

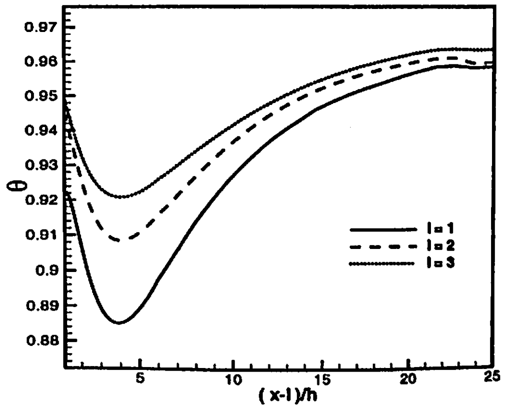

(c) Along CD

Figure 10.6: Conjugate interface temperature: Effect of l. ($Re = 400, Pr = 1, k = 5, s = 1h, w = 1h$).

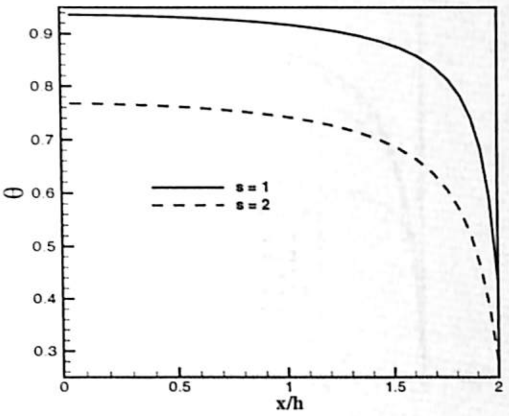

(a) Along AB

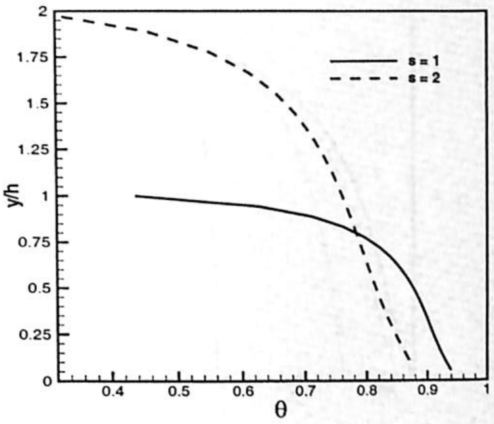

(b) Along BC

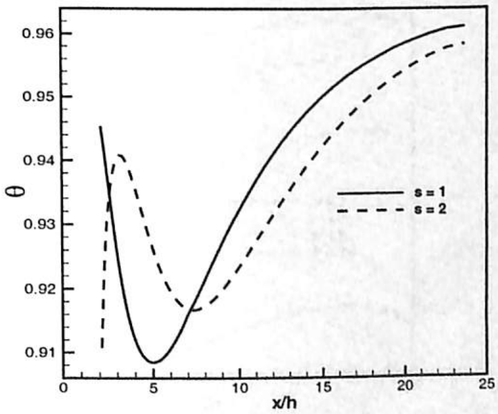

(c) Along CD

Figure 10.7: Conjugate interface temperature: Effect of s. ($Re = 400, Pr = 1, k = 5, l = 2h, w = 1h$).

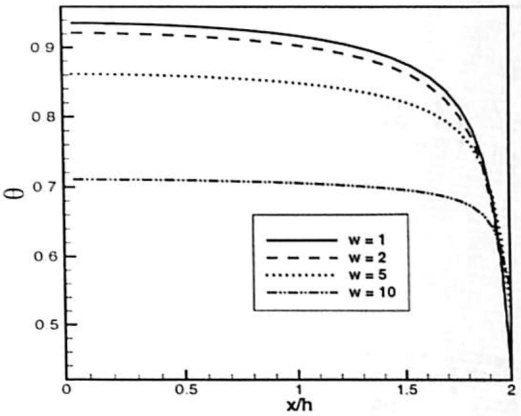

(a) Along AB

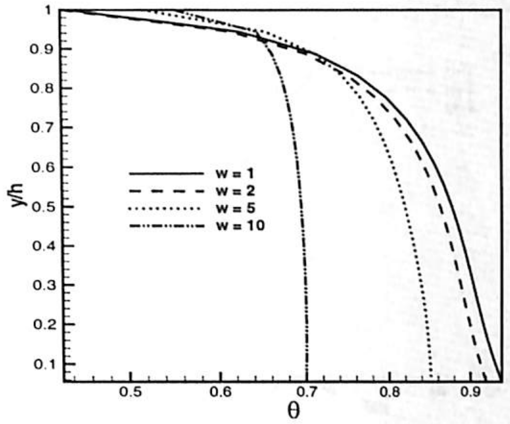

(b) Along BC

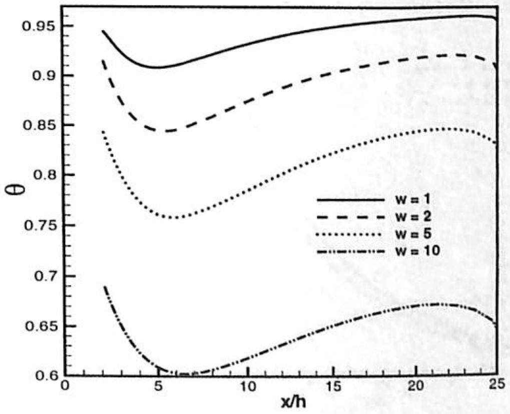

(c) Along CD

Figure 10.8: Conjugate interface temperature: Effect of w. ($Re = 400, Pr = 1, k = 5, l = 2h, s = 1h$).

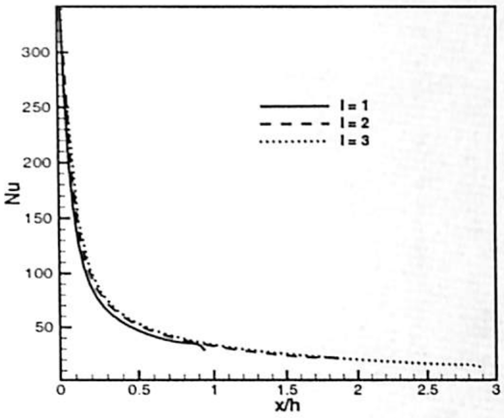

(a) Along AB

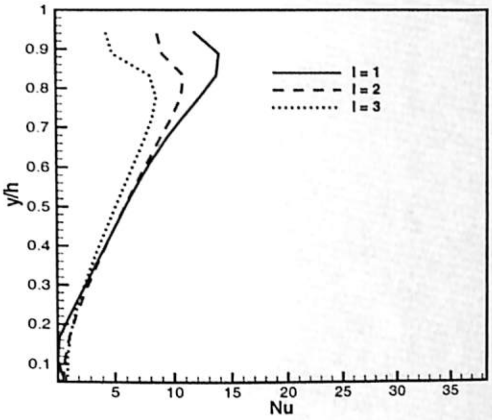

(b) Along BC

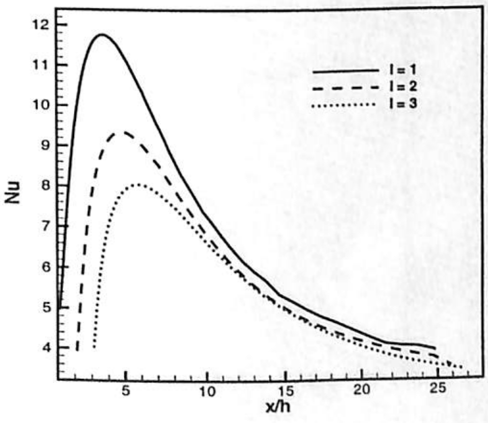

(c) Along CD

Figure 10.9: Local Nusselt number distribution: Effect of l. ($Re = 400, Pr = 1, k = 5, s = 1h, w = 1h$).

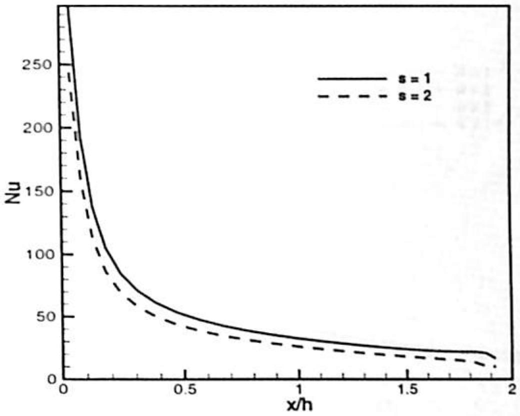

(a) Along AB

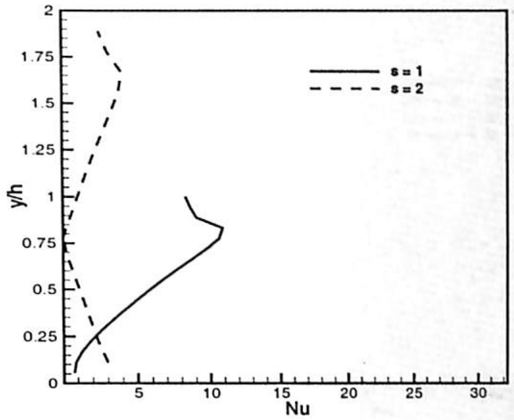

(b) Along BC

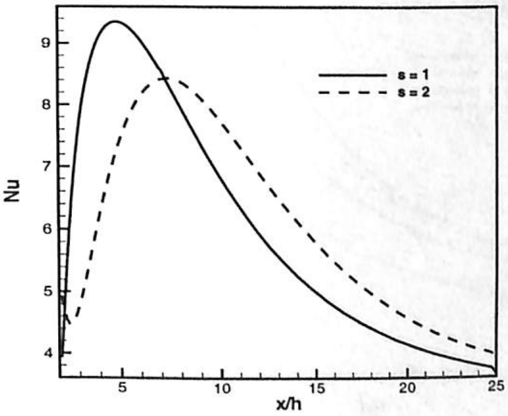

(c) Along CD

Figure 10.10: Local Nusselt number distribution: Effect of s. ($Re = 400, Pr = 1, k = 5, l = 2h, w = 1h$).

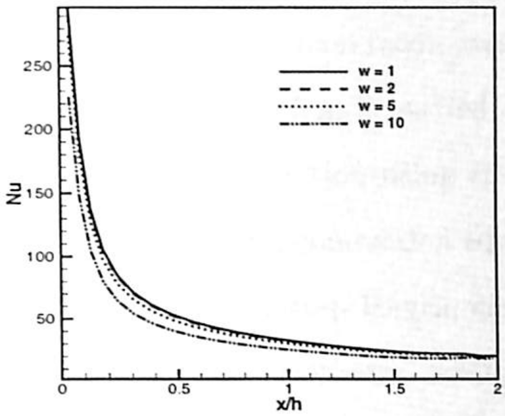

(a) Along AB

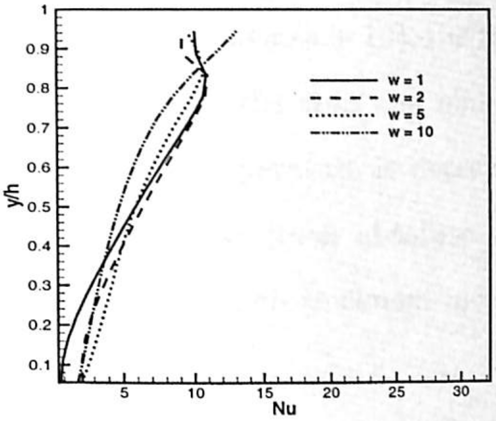

(b) Along BC

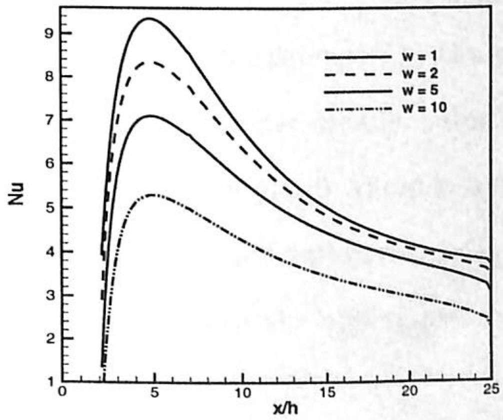

(c) Along CD

Figure 10.11: Local Nusselt number distribution: Effect of w. ($Re = 400, Pr = 1, k = 5, l = 2h, s = 1h$).

10.3 Conclusions

Conjugate heat transfer study of two-dimensional incompressible non-buoyant wall jet over backward facing step flow problem is carried out by solving the vorticity transport equation and energy equation using stream function and vorticity formulation for the fluid region and conduction equation for the solid region. Parametric study is carried out for step length, step height and slab thickness. Results are presented in terms of isotherm, conjugate interface temperature, local Nusselt number and average Nusselt number. Study is carried with $Re = 400, Pr = 1$ and $k = 5$. The following conclusions are drawn.

- Inside the slab in normal direction (at $x/h = 10$), the temperature follows a linear trend for different size of the step and slab thickness. When length of the step is increased temperature is decreased in the normal direction. Higher step height causes lower absolute temperature in the normal direction. Increase in the slab thickness increases the absolute temperature in the normal direction.
- In streamwise direction, the temperature follows a non-linear trend. Upto a certain downstream distance solid temperature (at $y = w/2$) decreases and further it increases to a near-steady value.
- Conjugate interface temperature is decreased in the downstream direction and further it increases to a near-steady value. When length of the step is increased interface temperature value is increased. When the step height is increased the interface temperature is decreased. However within the reattachment length the effects are reversed. When the

slab thickness is increased the interface temperature is decreased in the downstream direction further it is increased.

- Near the inlet, Nusselt number is larger due to entrainment and further it is decreased. Along CD it is increased to a maximum value and further decreases to a near-steady value monotonically. When l is increased, it is decreased. Similarly, w is increased Nu is decreased.

- Average Nusselt number is decreased upto 20.35% when length of the step is increased to 3. It is observed that for higher step height ($s = 2$) reduces the $\overline{Nu}$ by 7.5%. The increment in slab thickness from 1 to 10 reduces the average Nusselt number by 29.35%.

Chapter 11

Conclusion and Scope for the Future Work

Wall bounded jet flows are having industrial significance for many applications. Conjugate heat transfer study is a subject of interest for the past few decades. The present work is aimed at gain some of the insight of the topics considered.

11.1 Summary

Chapter 3 presented closed form solutions for laminar plane wall jet flow as conjugate case. Closed form expressions are presented for local Nusselt number, interface temperature and average Nusselt number in connection with four parameters (Re, Pr, λ, k). The model is validated with numerical prediction and it is found that the model is having good agreement for low Pr and $k \leq 5$.

Chapters 4, 5 and 6 discuss the flow, heat transfer and conjugate heat transfer study of two dimensional incompressible laminar offset jet flow. The transient results are presented to demonstrate the nature of vortex generation, movement with respect to time and disappearance while reaching steady state. The downstream wall jet region is showing agreement with similarity solution of wall jet flow. Non-conjugate heat transfer study of offset jet is discussed in chapter 5. It is found that the increment in offset ratio increases the average Nusselt number. The local Nusselt number increases to a maximum value and further decreases in the downstream direction. From the conjugate heat transfer study it is found that the interface temperature decreases upto recirculation location and further increases to a developed condition at exit. It is noticed that the property of flow like Re affects the heat transfer in solid.

The hydrodynamic study of plane wall jet over backward facing step is reported in chapter 7. Here the upstream flow to the step is different from offset jet case. In the present situation plane jet is expanded along the step whereas parabolic profile is expanded in offset jet flow. The reattachment length is reduced while increasing the step length. Reattachment length is increasing when Re and OR is increased.

Chapters 8, 9 and 10 discuss the heat transfer characteristics of wall jet over backward facing step flow as non-conjugate and conjugate case. Non-conjugate heat transfer results are compared with zero step length flow i.e. offset jet flow. It is found that when a step is presented, the average Nusselt number is reduced. Also it is noticed that when the length is increased average Nusselt number is decreased. Conjugate heat transfer study is carried out in connection with the effect of property of solid medium as well as fluid medium and effect of solid step geometry. It is noticed that when *Re* increases the isotherms are deflected near the recirculation and clustered towards the wall and thermal boundary layer thickness is reduced. At low *Pr* conduction mode of heat transfer is dominant and isotherm spreads well over the quiescent medium. At low *Pr*, non-conjugate $\overline{Nu}$ is smaller than conjugate $\overline{Nu}$. Near the inlet *Nu* is larger due to entrainment and further it is decreased. It is observed that the increase in the step height reduces the $\overline{Nu}$.

11.2 Scope for the Future work

In the present work plane wall jet and offset jet are studied in detail. The similar study can be carried out for impinging jet. It is observed that the closed form model for conjugate heat transfer of plane wall jet is having discrepancy between the model and prediction for high Prandtl number. The model can be reformulated for high *Pr* and high conductivity ratio. An empirical relation can be investigated for reattachment length in connection with *Re* and *OR* for offset jet. It is important to find out the length from which the similarity region of wall jet in the downstream of offset jet flow holds good. After this length the closed form solutions of wall jet flow are applicable.

The developed solver can be used to find an empirical relation for location of peak Nusselt number in an offset jet flow problem for both non-conjugate and conjugate cases. This is important for design of cooling of thermal devises.

Buoyancy effects are neglected in this entire study. The work can be extended to understand the effect of buoyancy in the geometry and problems considered here.

Appendix A

Lid Driven Cavity Problem

The lid driven cavity flow is a standard benchmark problem for testing a numerical code. Here the top wall is moving with uniform velocity. The computational domain along with the boundary conditions are given in Fig. A.1. The streamlines are constant along impermeable walls and set as zero value. No-slip conditions are assumed along the walls. The test case considered is two dimensional laminar incompressible viscous flow for steady state solution. Other properties are constant. The clustered grids are used for the computations and generated by equation (2.11). The governing equation (2.9) is solved by ADI method. The center line u and v velocity components are compared with benchmark results of Ghia et al. [59] and Rek and Skerget [80] (Figs. A.2-A.3) for various Re. The moving wall vorticity is compared with Ghia [59] (Fig. A.4). The left wall vortex separation points are compared with Barragy and Carey [81] and is shown in Figure A.5. The agreement is good even at high Reynolds numbers. The minimum stream function at primary vortex center is within 2.4% error with benchmark results for Re=10000.

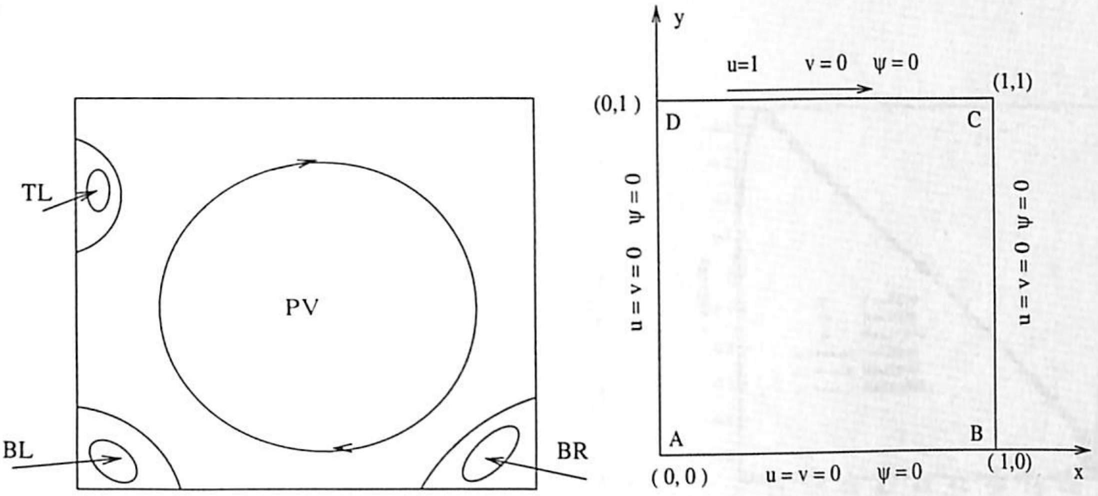

(a) (b)

Figure A.1: Schematic diagram with boundary condition of lid driven cavity problem. PV-Primary vortex, BL-Bottom left vortex, BR-Bottom right vortex, TL-Top left vortex.

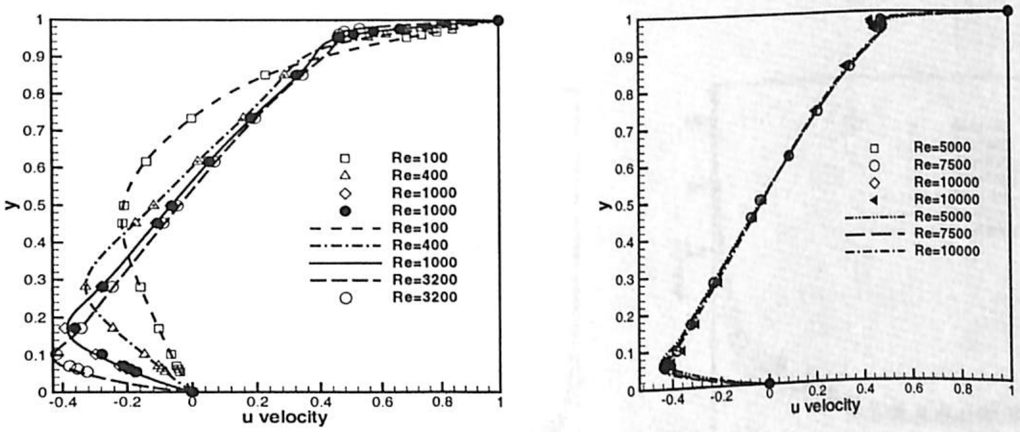

(a) (b)

Figure A.2: Vertical centerline u- velocity passing through geometric center. Open symbols [59], close symbol [80] and line patterns are present results

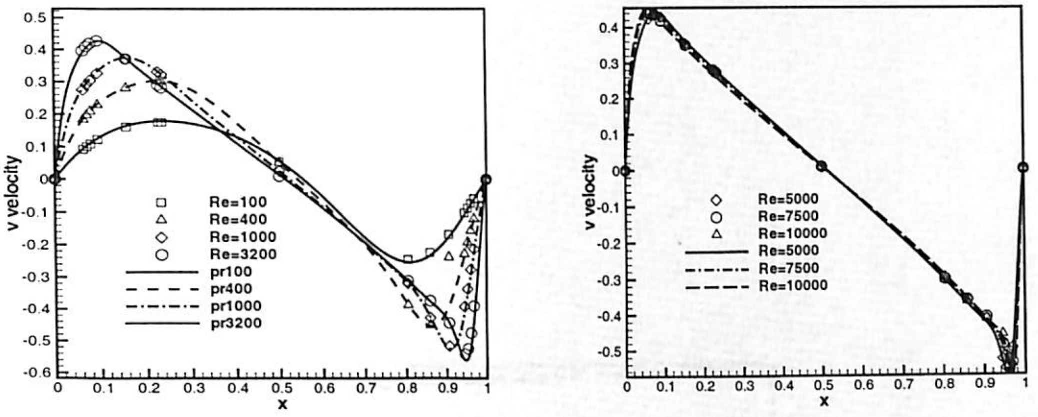

(a) (b)

Figure A.3: Horizontal centerline v- velocity passing through geometric center. Open symbols [59], close symbol [80] and line patterns are present results

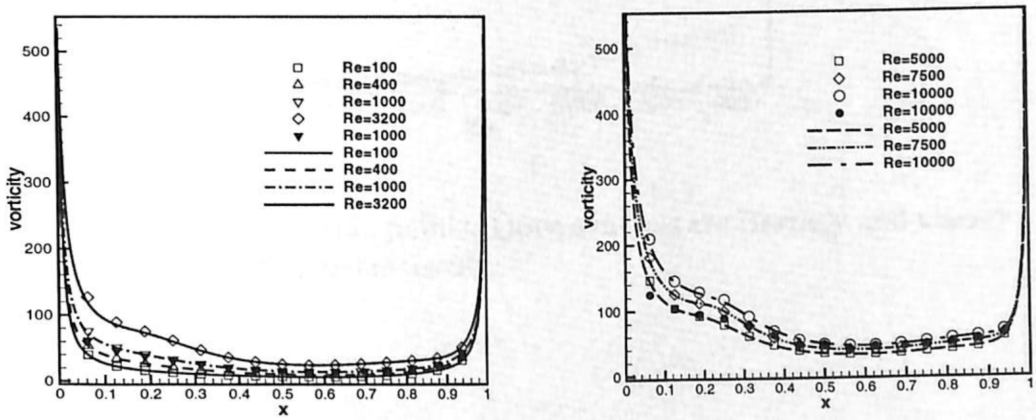

(a) (b)

Figure A.4: Moving wall vorticity. Open symbols [59], close symbol [80] and line patterns are present results

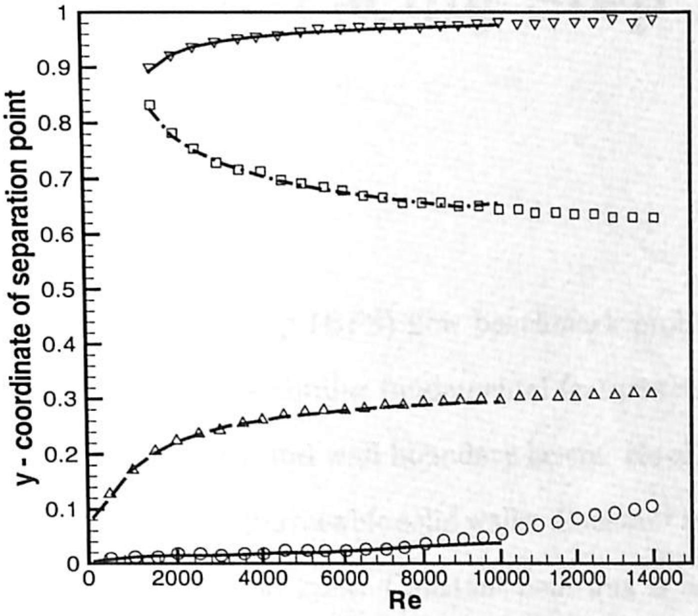

Figure A.5: Left wall separation points. Open symbols are Barragy and Carrey [81] and line patterns are present results

Appendix B

Backward-Facing Step Flow Problem

The backward-facing step (BFS) flow benchmark problem is described in the Fig. B.1. The flow has similar fundamental features as that of plane wall jet flow i.e. free-shear flow and wall boundary layers. No-slip boundary conditions were applied on the impermeable solid walls. Constant streamlines are assumed along the walls based on inlet. Constant heat flux is assumed at bottom and top of the wall. The problem considered here is two dimensional incompressible laminar viscous flow backward-facing step problem.

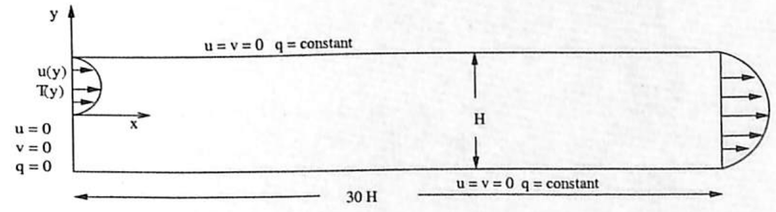

Figure B.1: Schematic diagram and boundary conditions in a BFS problem

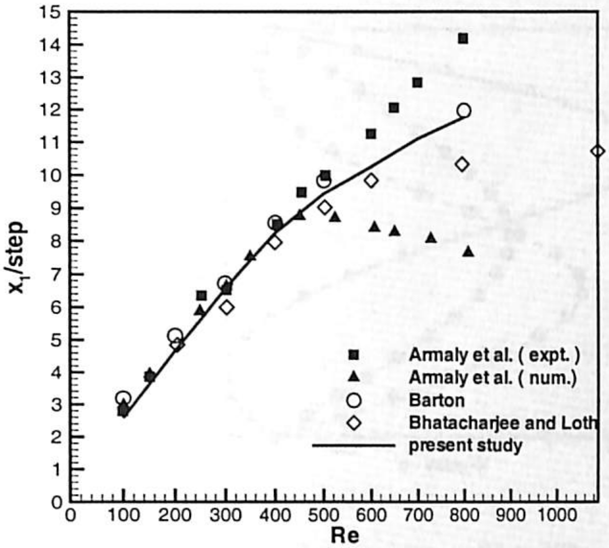

Figure B.2: Primary vortex reattachment length for various *Re*.

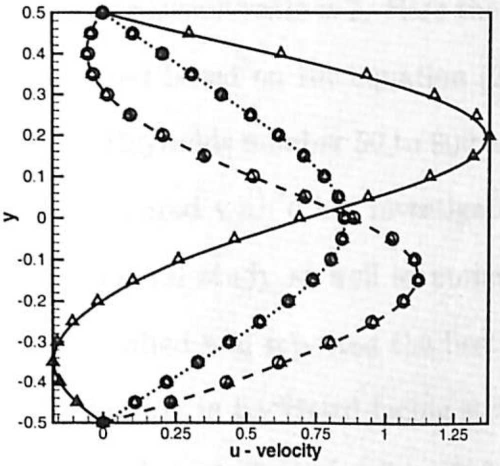

(a) u-velocity: $Re = 800$

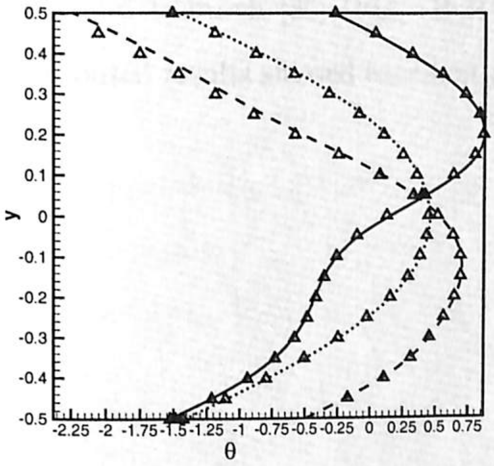

(b) temperature: $Re = 800, Pr = 0.7$

Figure B.3: Comparison of numerical solution with benchmark results. O - Gartling [34], Δ -Dyne and Heinrich [36] and present: —— x=3, - - - x=7, ... x=15

Parabolic velocity profile is assumed at inlet. Stream wise gradients are assumed to be zero at exit. The inlet profile is taken from Dyne and Heinrich [36]. Reynolds number based on step height is used for the calculations. The step height is 0.5H, thus the expansion ratio is 2. Here the grid points are clustered near the wall and clustered based on the equation (2.11). The governing equation (2.9) is solved for Reynolds number 50 to 800 and the primary vortex reattachment length is compared with other investigators (Fig. B.2). Armaly et al. [33] carried experimental study as well as numerical investigations. Gartling [34] numerically studied and reported the best exit boundary condition. The interesting investigation in backward-facing step flow problem for many authors ([82], [30], [83]) is the case study for $Re = 800$. In the present validation the study is carried out at $Re = 800$ and the u velocity is compared with Gartling [34] and Dyne and Heinrich [36] (Fig. B.3(a)) and energy solution is compared with Dyne and Heinrich [36] (Fig. B.3(b)) at different downstream location. This computed results showed excellent agreement with them.

Appendix C

Plane Wall Jet Flow Problem

The laminar plane wall jet problem (Fig. C.1(a)) has been solved and the computed velocity profiles are compared with the similarity solutions of Glauert [1] and the experimental results of Quintana et al. [15] in a similar way as represented by Seidel [18] (Fig. C.1(b)). It is observed that at different downstream locations x/h, a good agreement amongst them has been obtained. The non-conjugate heat transfer case has been solved for Pr=1.4 and 100 and compared in a similar way for five downstream locations (Figs. C.1(c), C.1(d)).

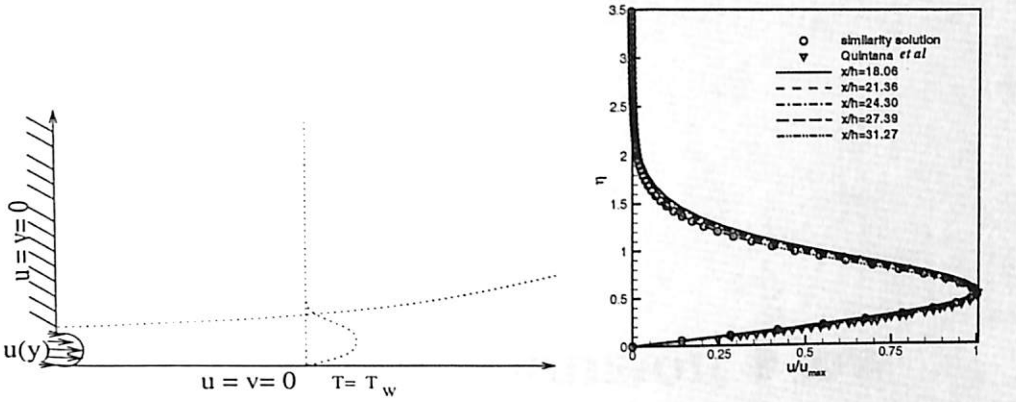

(a) Schematic of plane wall jet flow

(b) Comparison of horizontal velocity profile

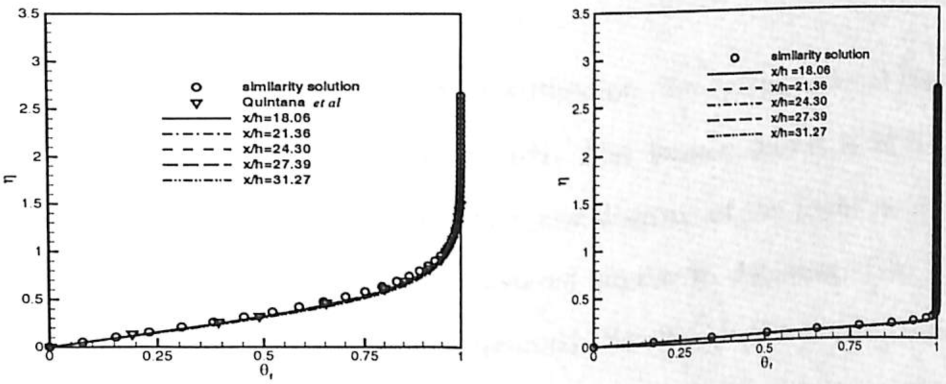

(c) Comparison of temperature profile, $Pr = 1.4$

(d) Comparison of temperature profile, $Pr = 100$

Figure C.1: Comparison of results with similarity solution for $Re = 500$: Plane Wall jet flow.

Appendix D

Sudden Expansion Flow Problem

For sudden expansion flow investigation, the computational domain reported by Durst et al. [28] is considered. The domain chosen is $50H$ in length and expansion ratio is 2. The schematic diagram of the problem is shown in Fig. D.1(a). Grids have been clustered similar to Alleborn et al [84]. At inlet, parabolic velocity profile is assumed. No-slip conditions are assumed along the solid walls. At exit, streamwise gradients are assumed as zero for the vorticity and u velocity component [54]. For different Re, the u velocity component at various downstream locations is compared with experimental and numerical prediction of Durst et al. [28]. For $Re = 70$, the flow is symmetric. Flow separates at the corner of the inlet and reattaches at the top and bottom of the solid wall (Fig. D.1(b)). Results are having good agreement at locations $x/H = 3.6$ and $x/H = 14$, whereas at $x/H = 5$ along the symmetry line there are some deviations (Fig. D.2). For Re=610, the comparisons of the axial velocity profiles are shown in Fig. D.3. The present numerical predictions are closure to their predicted values at downstream locations ($x/H = 14, x/H = 29$) and ($x/H = 44$). The present computations captures the formation of second recirculation at top wall for this *Re*, which is consistent with Durst et al. [28] and Alleborn et al. [84].

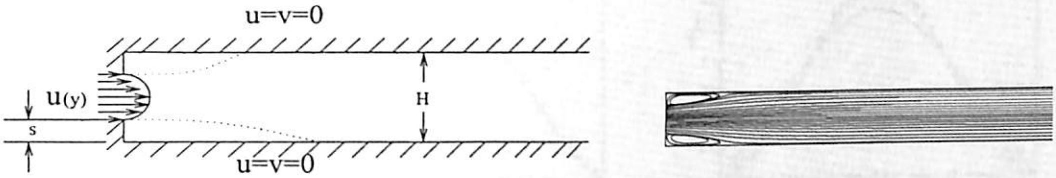

(a) Schematic diagram and boundary conditions

(b) Stream line contour $Re = 70$

Figure D.1: Plane sudden-expansion flow problem: a part of the domain, Durst et al. [28]

Sarma et al. [25] validated their result for a critical *Re*=190 with a critical $Re = 187$ of Battaglia et al. [85]. Here no such attempt has been made to compare the results with an adjustment of *Re*. The deviations in the results of the present study and those of the earlier investigations may be attributed to the differences in the numerical scheme and the round-off/discretisation errors [25].

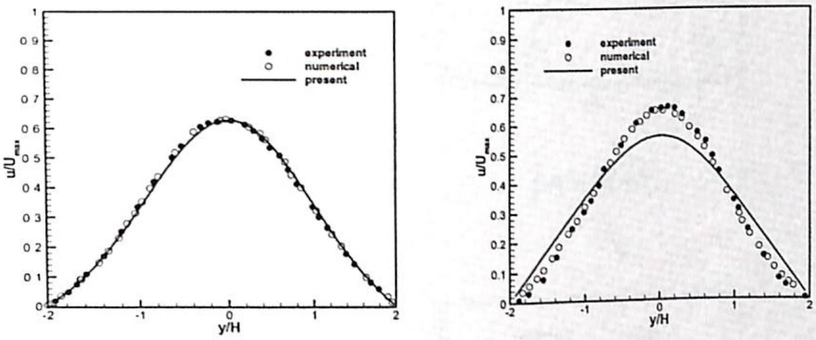

(a) x/H=3.6

(b) x/H=5

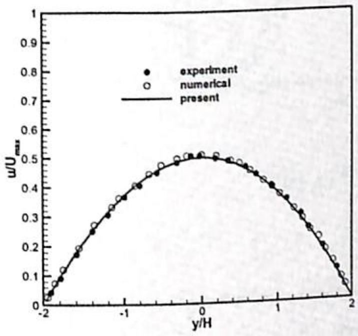

(c) x/H=14

Figure D.2: Comparison of normalised u velocity profiles for $Re = 70$, Durst et al. [28]

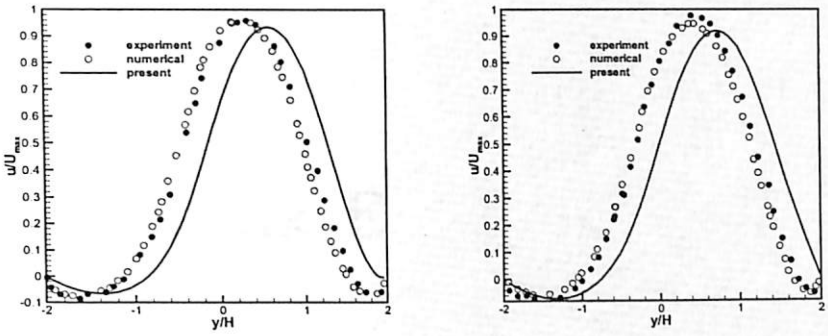

(a) x/H=3.6 (b) x/H=5

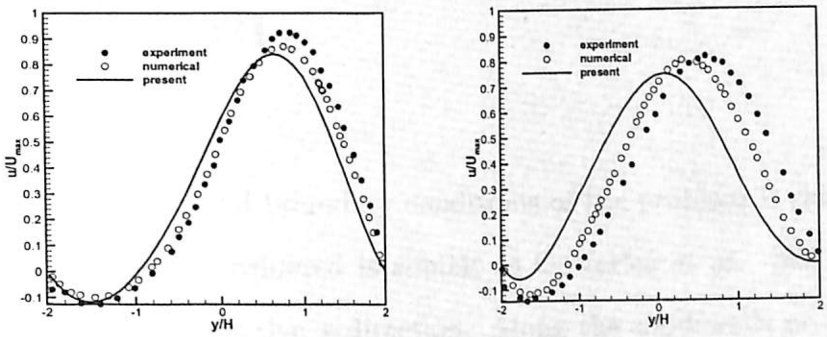

(c) x/H=14 (d) x/H=20

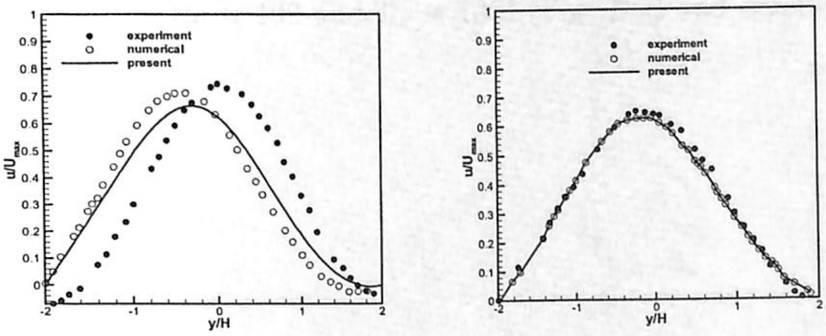

(e) x/H=29 (f) x/H=44

Figure D.3: Comparison of normalised u velocity profiles for $Re = 610$, Durst et al. [28]

Appendix E

L- Shape Lid Driven Cavity Problem

The schematic and boundary conditions of the problem is shown in Fig. E.1. The geometry considered is similar to Oosterlee *et al.* [60]. The top lid is moving in the positive x-direction. Along the solid walls no-slip condition is applied. Results are compared at two locations named CL1 and CL2 (Fig. E.1). u- velocity and v- velocity components at these locations are compared with [60] for $Re = 100$ and $Re = 1000$ (Fig. E.2) and excellent agreement is obtained.

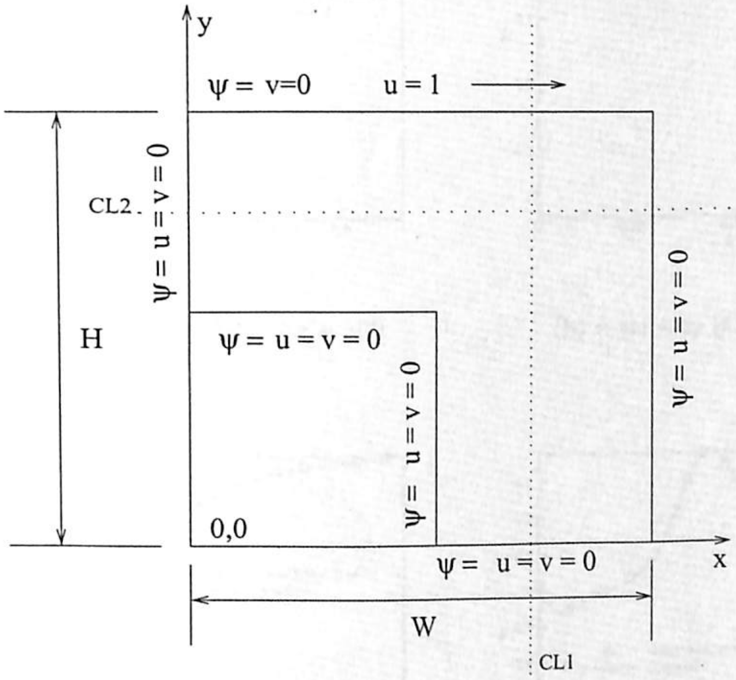

Figure E.1: Schematic diagram and boundary conditions of L-shape lid driven cavity flow problem [60].

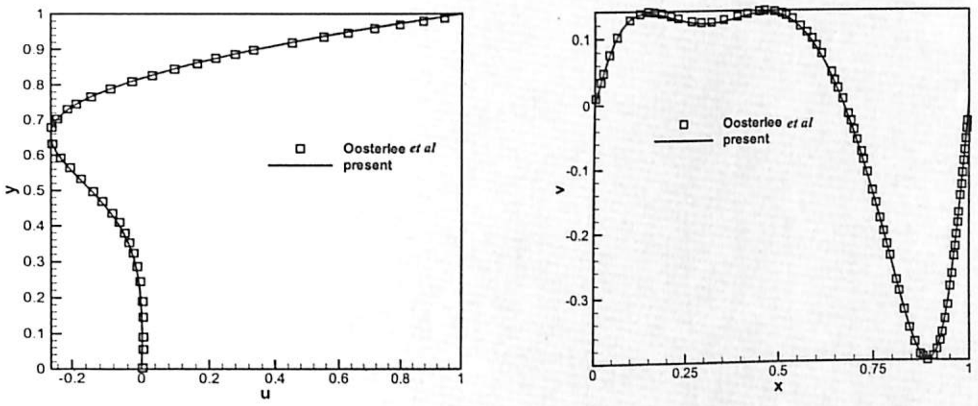

(a) u-velocity (CL1), $Re = 100$

(b) v-velocity (CL2), $Re = 100$

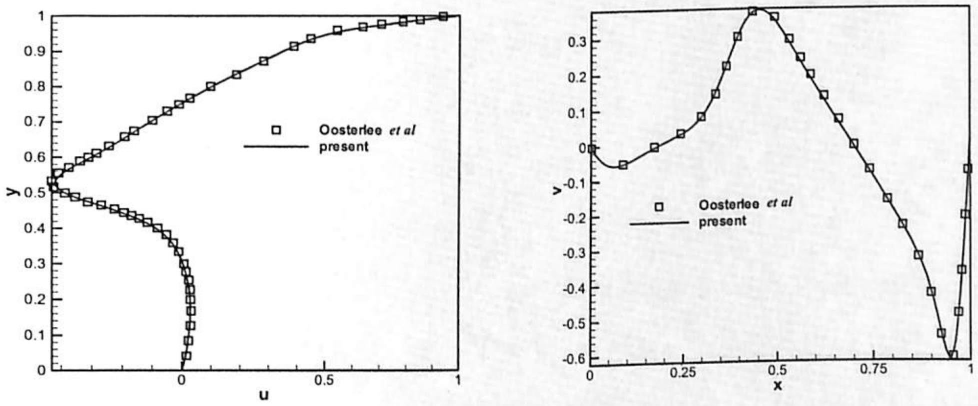

(c) u-velocity (CL1), $Re = 1000$

(d) v-velocity (CL2), $Re = 1000$

Figure E.2: Velocity profiles along CL1 and CL2.

Appendix F

Backward-Facing Step Flow with Upstream Channel

Backward-facing step with upstream channel flow is the problem of interest for the study of sudden expansion flows. Armaly *et al.* [33] have reported the experimental results in which the geometry has a long inlet channel and fully developed flow is expected at the expansion. To simulate the experimental situation, inlet channel is considered in the numerical computation also. Kondoh *et al* [37] reported heat transfer study on backward-facing step flow with upstream channel geometry. They considered various expansion ratios. However their reattachment length (ER=2.0, $Re = 100, x_1/h = 4.8$) is larger than the other published work ($x_1/h = 2.8$, [33], [71]). Barton studied in detail the effect of inlet channel [35]. He has reported the reattachment length by setting the inlet at different upstream locations in the channel for various Reynolds numbers. Thangam and Knight [73] studied the effect of step height in the sudden expansion flow.

The geometry considered here is similar to the one considered by Barton [35], which is having $10 \times h$ as upstream channel length. The schematic diagram of the problem and boundary conditions are shown in Fig. F.1(a). Clustered grids are used near the step which is shown in Fig. F.1(b). At inlet, parabolic velocity profile is assumed and at exit fully developed condition is assumed. Expansion ration (ER) is defined as h/H. The streamline contour and velocity vector are shown in Fig. F.1(c) and F.1(d) respectively for $Re = 500$ and $ER = 0.5$. The effect of ER=0.75 is considered to visualise the effect of ER. Results are shown for $Re = 200$, ER=0.75 in Fig. F.1(e) and Fig. F.1(f). For large values of Re the primary vortex reattachment length is compared with [33] and [35] (Fig. F.2). The present computations show excellent agreement with computational results and upto $Re = 400$ with experimental results. Backward-facing step with different expansion ratios are tested and the reattachment length is compared with the published results and good agreement is obtained (Table F.1-Table F.2).

Table F.1: Primary vortex reattachment length: (ER=0.25,Re=500)

[73]	[71]	present
0.84628	1.1158	1.0707

Table F.2: Primary vortex reattachment length: (ER=0.75,Re=200)

[73]	[71]	present
6.4868	7.0261	7.1469

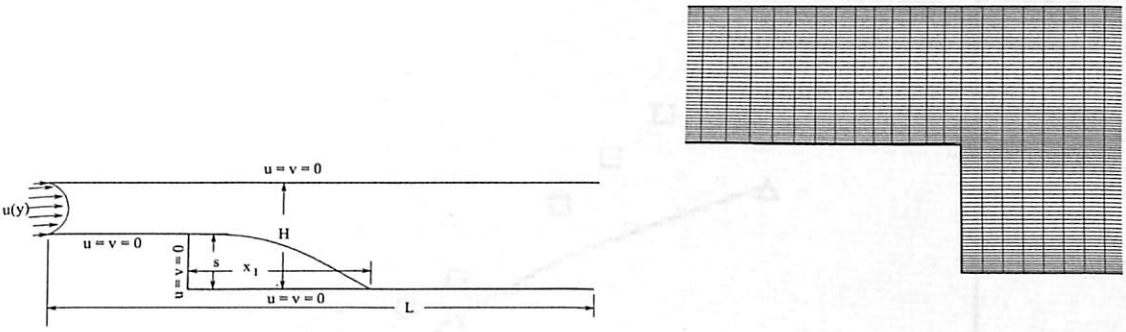

(a) Schematic diagram

(b) Clustered grids used near the step: ER=0.5

(c) *Re* = 500, ER=0.5. Streamline contour

(d) *Re* = 500, ER=0.5. Velocity vector

(e) *Re* = 200, ER=0.75. Streamline contour

(f) *Re* = 500, ER=0.75. Velocity vector

Figure F.1: Backward-facing step flow with upstream channel problem. (Domain shown near the step)

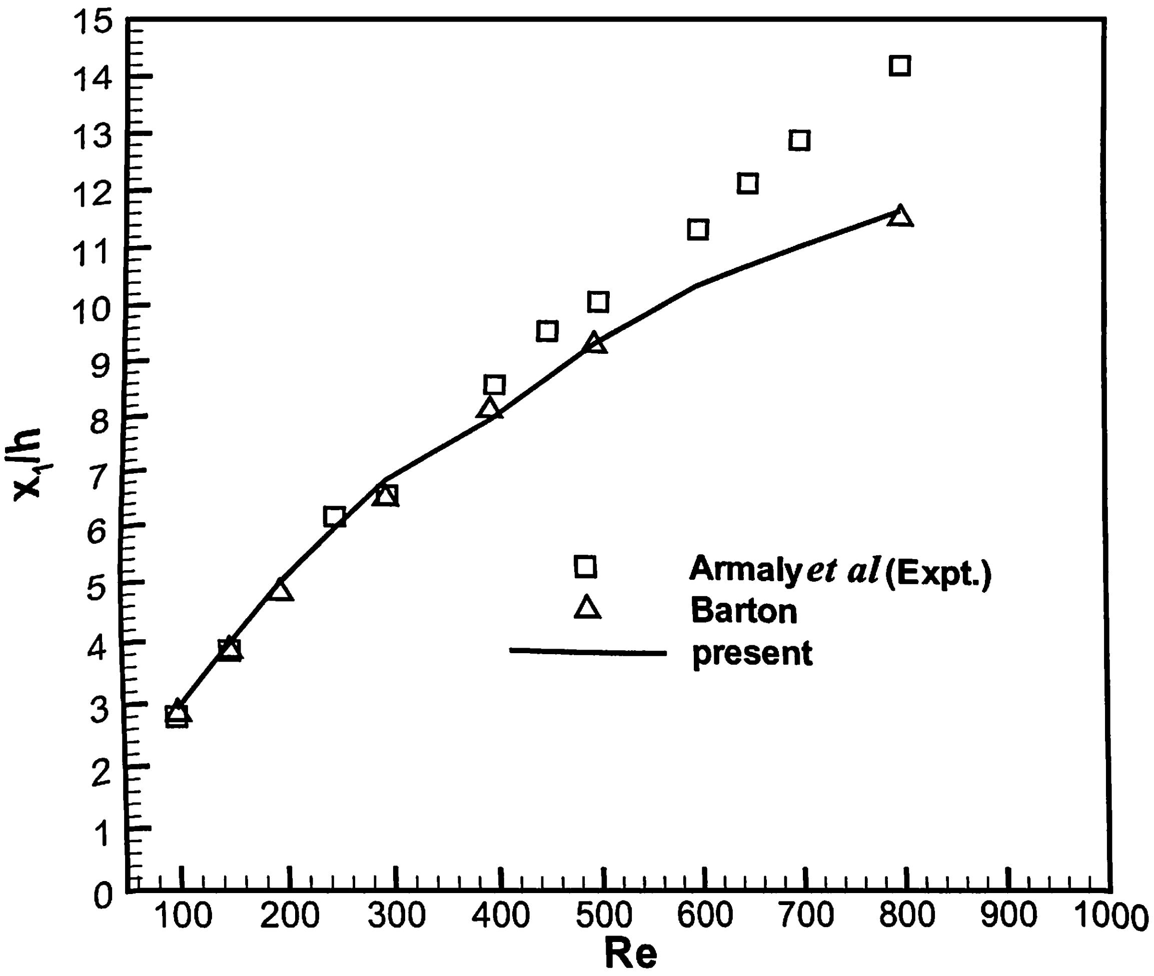

Figure F.2: Reattachment length for different Reynolds number: Parabolic inlet profile

Bibliography

[1] M.B. Glauert. The wall jet. *Journal of Fluid Mechanics*, 1(1):1–10, 1956.

[2] R.A. Bajura and A.A. Szewczyk. Experimental investigation of a laminar two-dimensional plane wall jet. *The Physics of Fluids*, 13:1653–1664, 1970.

[3] D.J. Tritton. *Physical Fluid Dynamics*, pages 284–286. Von Norstrand Reinhold, UK, 1977.

[4] R.A. Seban and L.H. Back. Velocity and temperature profiles in a wall jet. *International Journal of Heat and Mass Transfer*, 3:255–265, 1961.

[5] W.H. Schwarz and B. Caswell. Some heat transfer characteristics of the two-dimensional laminar incompressible wall jet. *Chemical Engineering Science,*, 16:338–351, 1961.

[6] D.H. Chun and W.H. Schwarz. Stability of the plane incompressible viscous wall jet subjected to small disturbances. *The Physics of Fluids*, pages 911–915, 1967.

[7] R.S.R. Gorla. Unsteady heat transfer characteristics of two dimensional laminar wall jet. *International Journal Engineering Science*, 11:841–851, 1973.

[8] R.A. Bajura and M.R. Catalano. Transition in a two-dimensional plane wall jet. *Journal of Fluid Mechanics*, 70:773–799, 1975.

[9] Y. Tsuji, Y. Morikawa, T. Nagatani, and M. Sakou. The stability of a two-dimensional wall jet. *Aeronautical Quarterly*, 28:235–246, 1977.

[10] A.B. Paige. *An experimental study of a laminar wall-jet in the presence of a uniform external flow.* PhD thesis, Institute for Aerospace Studies, The University of Toronto, USA, 1988.

[11] C. Shih and S. Gogineni. Experimental study of perturbed laminar wall jet. *AIAA Journal*, 33:559–561, 1994.

[12] H. Oguz. On the relaxation of laminar jets at high Reynolds numbers. *The Physics of Fluids*, 10:361–367, 1998.

[13] M. Amitay and J. Cohen. Instability of a two-dimensional plane wall jet. *Journal of Fluid Mechanics*, 344:67–94, 1997.

[14] J. Cohen, M. Amitay, and B.J. Bayly. Laminar-turbulent transition of wall-jet flows subjected to blowing and suction. *Physics of Fluids*, 4:283–289, 1992.

[15] D.L. Quintana, M. Amitay, A. Ortega, and I.J. Wygnanski. Heat transfer in the forced laminar wall jet. *Journal of Heat Transfer*, 119:451–459, 1997.

[16] K.O. Homan and S.L. Soo. The steady horizontal flow of a wall jet into a large-width cavity. *Journal of Fluids Engineering*, 120:70–75, 1998.

[17] A. Tumin and L. Aizatulin. Instability and receptivity of laminar wall jets. *Theoretical Computational Fluid Dynamics*, 9:33–45, 1997.

[18] J. Seidel. *Numerical investigations of forced laminar and turbulent wall jets over a heated surface.* PhD thesis, Faculty of the department of Aerospace and Mechanical Engineering. The Graduat College, The University of Arizona, USA, 2001.

[19] S. Marzouk, H. Mhiri, S.E. Golli, and G.L.Palec. Numerical study of momentum and heat transfer in a pulsed plane laminar jet. *International Journal of Heat and Mass Transfer*, 46:4319 – 4334, 2003.

[20] P. Bhattacharjee and E. Loth. Simulations of laminar and transitional cold wall jets. *International Journal of Heat and Fluid Flow*, 25:32–43, 2004.

[21] H. Sato. The stability and transition of a two-dimensional jet. *Journal of Fluid Mechanics*, 7:53–80, 1960.

[22] H. Sato and F. Sakao. An experimental investigation of the instability of a two-dimensional jet at low Reynolds numbers. *Journal of Fluid Mechanics*, 20:337–352, 1964.

[23] G.K. Batchelor and A.E. Gill. Analysis of the stability of axisymmetric jets. *Journal of Fluid Mechanics*, 14:529–551, 1962.

[24] J. Cohen and I. Wygnanski. The evolution instabilities in the axisymmetric jet. part 1. the linear growth of disturbances near the nozzle. *Journal of Fluid Mechanics*, 176:191–219, 1987.

[25] A.S.R. Sarma, T. Sundararajan, and V. Ramjee. Numerical simulation of confined laminar jet flows. *International Journal for Numerical Methods in Fluids*, 33:609–626, 2000.

[26] V.A. Chiriac and A. Ortega. A numerical study of the unsteady flow and heat transfer in a transitional confined slot jet impinging on an isothermal surface. *International Journal of Heat and Mass Transfer*, 45:1237–1248, 2002.

[27] H. Chattopadhyay. Numerical investigations of heat transfer from impinging annular jet. *International Journal of Heat and Mass Transfer*, 47:3197–3201, 2004.

[28] F. Durst, J.C.F. Pereira, and C. Tropea. The plane symmetric sudden-expansion flow at low Reynolds numbers. *Journal of Fluid Mechanics*, 248:567–581, 1993.

[29] J.T. Holland and J.A. Liburdy. Measurements of the thermal characteristics of heated offset jets. *International Journal of Heat and Mass Transfer*, 33:69–78, 1990.

[30] J. Kim and P. Moin. Application of a fractional-step method to incompressible Navier-Stokes equations. *Journal of Computational Physics*, 59:308–323, 1985.

[31] R. Gu. Modelling two-dimensional turbulent offset jets. *Journal of Hydraulic Engineering*, 122(11):617–624, 1996.

[32] S. H. Cho and S. O. Park. Steady and unsteady computation of a two-dimensional upwash jet. *International Journal for Numerical Methods for Heat Fluid Flow*, 8:64–82, 1998.

[33] B.F. Armaly, F. Durst, J.C.F. Pereira, and B. Schonung. Experimental and theoretical investigation of backward-facing step flow. *Journal of Fluid Mechanics*, 127:473–496, 1983.

[34] D.K. Gartling. A test problem for outflow boundary conditions-flow over a backward-facing step. *International Journal for Numerical Methods in Fluids*, 11:953–967, 1990.

[35] I.E. Barton. The entrance effect of laminar flow over a backward-facing step geometry. *International Journal for Numerical Methods in Fluids*, 25:633–644, 1997.

[36] B.R. Dyne and J.C. Heinrich. Flow over a backward-facing step: A bench mark problem for laminar flow with heat transfer. *Benchmark problems for heat transfer codes*, HTD-V 222:73–76, 1992.

[37] T. Kondoh, Y. Nagano, and T. Tsuji. Computational study of laminar heat transfer downstream of a backward-facing step. *International Journal of Heat and Mass Transfer*, 36(3):577–591, 1993.

[38] G. Biswas, M. Breuer, and F. Durst. Backward-facing step flows for various expansion ratios at low and moderate reynolds numbers. *Journal of Fluids Engineering*, 126:362–374, May 2004.

[39] H.I. Abu-Mulaweh, B.F. Armaly, and T.S. Chen. Measurements in buoyancy-opposing laminar flow over a vertical forward-facing step. *International Journal of Heat and Mass Transfer*, 39:1805–1813, 1996.

[40] A.V. Luikov, V.A. Aleksashenko, and A.A. Aleksashenko. Analytical methods of solution of conjugated problems in convective heat transfer. *International Journal of Heat and Mass Transfer*, 14:1047–1056, 1971.

[41] A.V. Luikov. Conjugate convective heat transfer problems. *International Journal of Heat and Mass Transfer*, 17:257–265, 1974.

[42] P. Payvar. Convective heat transfers to laminar flow over a plate of finite thickness. *International Journal of Heat and Mass Transfer*, 20:431–433, 1971.

[43] I. Pop and D.B. Ingham. A note on conjugate forced convection boundary layer flow past a flat plate. *International Journal of Heat and Mass Transfer*, 36:3873–3876, 1993.

[44] A. Pozzi and M. Lupo. The coupling of conduction with forced convection over a flat plate. *International Journal of Heat and Mass Transfer*, 32:1207–1214, 1989.

[45] M. Vynnycky, S. Kimura, K. Kanev, and I. Pop. Forced convection heat transfer from a flat plate: the conjugate problem. *International Journal of Heat and Mass Transfer*, 41:45–59, 1998.

[46] W. K.S. Chiu, C. J. Richards, and Y. Jaluria. Experimental and numerical study of conjugate heat transfer in a horizontal channel heated from below. *Journal of Heat Transfer*, 123:688–697, August 2001.

[47] C.G. Rao, C. Balaji, and S.P. Venkateshan. Conjugate mixed convection with surface radiation from a vertical plate with a discrete heat source. *Journal of Heat Transfer*, 123:698–702, August 2001.

[48] G. Jilani, S. Jayaraj, and M. A. Ahmad. Conjugate forced convection-conduction heat transfer analysis of a heat generating vertical cylinder. *International Journal of Heat and Mass Transfer*, 45:331–341, 2002.

[49] Gh. Juncu. Conjugate heat/mass transfer from a circular cylinder with an internal heat/mass source in laminar crossflow at low reynolds numbers. *International Journal of Heat and Mass Transfer*, 48:419–424, 2005.

[50] Gh. Juncu. Unsteady conjugate heat/mass transfer from a circular cylinder in laminar crossflow at low reynolds numbers. *International Journal of Heat and Mass Transfer*, 47:2469–2480, 2004.

[51] H. Schlichting and K. Gersten. *Boundary Layer Theory, p 215-218*. Springer, 8th revised edition, 2000.

[52] J.C. Tannehill, D.A. Anderson, and R.H. Pletcher. *Computational fluid mechanics and Heat transfer*. Taylor & Francis, Taylor & Francis,Washington, DC20005-3521, second edition edition, 1997.

[53] R.A. Kuyper, Th.H. Van Der Meer, C.J. Hoogendoorn, and R.A.W.M. Henkes. Numerical study of laminar and turbulent natural convection in an inclined square cavity. *International Journal of Heat and Mass Transfer*, 36(11):2899–2911, 1993.

[54] P.J. Roache. *Fundamentals of Computational Fluid Dynamics, chapter-3*. Hermosa, USA, 1998.

[55] M. Napolitano, G. Pascazio, and L. Quartapelle. A review of vorticity conditions in the numerical solution of the $\zeta - \psi$ equations. *Computers and Fluids*, 28:139–185, 1999.

[56] H. Huang and B.R. Wetton. Discrete compatibility in finite difference methods for viscous incompressible fluid flow. *Journal of Computational Physics*, 126:468–478, 1996.

[57] G. Comini, M. Manzan, and C. Nonino. Finite element solution of the streamfunction-voriticity equations for incompressible two-dimensional flows. *International Journal for Numerical Methods in Fluids*, 19:513–525, 1994.

[58] S.H. Kang and R. Greif. Flow and heat transfer to a circular cylinder with a hot impinging air jet. *International Journal of Heat and Mass Transfer*, 35(9):2173–2183, 1992.

[59] U. Ghia, K.N. Ghia, and C.T. Shin. High Re solutions for incompressible flow using the Navier-Stokes equations and multigrid method. *Journal of Computational Physics*, 48:387–411, 1982.

[60] C.W. Oosterlee, P. Wesseling, A. Segal, and E. Brakkee. Benchmark solutions for the incompressible Navies-Stokes equations in general coordinates on staggered grids. *International Journal for Numerical Methods in Fluids*, 17:301–321, 1993.

[61] H.S. Carslaw and J.C. Jaeger. *Conduction of Heat in Solids, p 73-74*. Clarendon Press,Oxford, 1959.

[62] *Maple 7.00.* Waterloo Maple Inc, Waterloo, Canada, 2001.

[63] N.V. Chandrasekhara Swamy and P. Bandyopadhyay. Mean and turbulent characteristics of three-dimensional wall jets. *Journal of Fluid Mechanics*, 71(3):541–562, 1975.

[64] S.A. Al-Sanea. Convection regimes and heat transfer characteristics along a continuously moving heated vertical plate. *International Journal of Heat and Fluid Flow*, 24:888–901, 2003.

[65] S.A. Al-Sanea. Mixed convection heat transfer along a continously moving heated vertical plate with suction or injection. *International Journal of Heat and Mass Transfer*, 47:1445–1465, 2004.

[66] Amtec Engineering Inc. *TecPlot Version:9.0-0-9*, 2001.

[67] M.M. Rahman, A.J. Bula, and J.E. Leland. Conjugate heat transfer during free jet impingement of a high prandtl number fluid. *Numerical Heat Transfer, Part B*, 36(2):139–162, 1999.

[68] D. Sahoo and M.A.R. Sharif. Mixed-convective cooling of an isothermal hot surface by confined slot jet impingement. *Numerical Heat Transfer: Part A*, 45:887–909, 2004.

[69] P.R. Kanna and M.K. Das. Conjugate forced convection heat transfer from a flat plate by laminar plane wall jet flow. *International Journal of Heat and Mass Transfer*, 48:2896–2910, 2005.

[70] P.R. Kanna and M.K. Das. Heat transfer study of two-dimensional laminar incompressible offset jet flows. *Heat and Mass Transfer.* Revised manuscript submitted.

[71] A. Valencia and L. Hinojosa. Numerical solution of pulsating flow and heat transfer characteristics in a channel with backward-facing step. *Heat and Mass Transfer*, 32:143–148, 1997.

[72] M.C. Jacob, Alain Louisot, Daniel Juve, and Sylvie Guerrand. Experimental study of sound generated by backward-facing steps under wall jet. 39(7):1254–1260, 2001.

[73] S. Thangam and D.D. Knight. Effect of step height on the separated flow past to backward facing step. *The Physics of Fluids*, 1:604–606, 1989.

[74] P.R. Kanna and M.K. Das. Numerical simulation of two-dimensional laminar incompressible offset jet flows. *International Journal for Numerical Methods in Fluids.* Article in press.

[75] D. Angirasa. Interaction of low-velocity plane jets with buoyant convection adjacent to heated vertical surfaces. *Numerical Heat Transfer, Part A*, 35:67–84, 1999.

[76] P.R. Kanna and M.K. Das. Heat transfer study of two-dimensional laminar incompressible wall jet flow over step. *Numerical Heat Transfer: Part A.* submitted.

[77] P.R. Kanna and M.K. Das. Conjugate heat transfer study of two-dimensional laminar incompressible offset jet flows. *Numerical Heat Transfer: Part A.* Article in press.

[78] P.R. Kanna and M.K. Das. Numerical simulation of two-dimensional laminar incompressible wall jet over backward-facing step flows. *Journal of Fluids Engineering.* submitted.

[79] P.R. Kanna and M.K. Das. Conjugate heat transfer study of two-dimensional laminar incompressible wall jet over backward-facing step. *Journal of Heat Transfer.* Revised manuscript submitted.

[80] Z. Rek and L. Skerget. Boundary element method for steady 2d high-Reynolds-number flow. *International Journal for Numerical Methods in Fluids*, 19:343–361, 1994.

[81] E. Barragy and G.F. Carey. Stream function-vorticity driven cavity solution using p finite elements. *Computers and Fluids*, 26(5):453–468, 1997.

[82] G.A. Osswald, K.N. Ghia, and U. Ghia. Study of incompressible separated flow using implicit time dependent technique. *In: AIAA Sixth CD Conefence, Davers, MA*, pages 686–692, 1983.

[83] A. Kaiktsis, L.G.E. Karniadakis, and S.A. Orsag. Onset of three dimensionality, equilibria and early transition in flow over a backward-facing step. *Journal of Fluid Mechanics*, 231:501–528, 1991.

[84] N. Alleborn, K. Nandakumar, H. Raszillier, and F. Durst. Further contributions on the two-dimensional flow in a sudden expansion. *Journal of Fluid Mechanics*, 330:169–188, 1997.

[85] F. Battaglia, S.J. Tavener, A.K. Kulkarni, and C.L. Merkle. Bifurcation of low Reynolds number flows in symmetric channels. *AIAA*, 35:99–105, 1997.